Influence of thermal and mechanical aspects on deformation behaviour of NiTi alloys

Pauline Schlosser Rebeiz

Université Joseph Fourier de Grenoble - Grenoble Universités

N° attribué par la bibliothèque :

| | | | | | | | | | |

THÈSE

pour obtenir le grade de

DOCTEUR DE UNIVERSITE JOSEPH FOURIER GRENOBLE

Spécialité : Spécialité : « Matériaux, Mécanique, Génie Civil, Electrochimie »

préparée au laboratoire Sols, Solides, Structures - Risques
dans le cadre de ***l'Ecole Doctorale « I-MEP2 : Ingénierie - Matériaux, Mécanique, Environnement, Energétique, Procédés, Production »***

présentée et soutenue publiquement
par

Pauline SCHLOSSER

le 3 décembre 2008

Influence des aspects mécaniques et thermiques sur les mécanismes de déformation d'alliages NiTi

Influence of thermal and mechanical aspects on deformation behaviour of NiTi alloys

JURY

M. Y. Liu	Professeur	Rapporteur
M. F. Hild	Directeur de recherche	Rapporteur
M. D. Favier	Professeur	Directeur de thèse
M. H. Louche	Maître de Conférences	Co-directeur
M. L. Orgéas	Chargé de recherches	Co-directeur
M. A. Deschamps	Professeur	Examinateur
M. J. Van Humbeeck	Professeur	Examinateur

Résumé

La transformation martensitique thermoélastique apparaissant dans les alliages à mémoire de forme (AMF) de type Nickel-Titane (NiTi) est un mécanisme de déformation conférant à ces matériaux des propriétés remarquables de plus en plus utilisées, par exemple dans des applications biomédicales (stents, cathéters,....). Les forts phénomènes de localisation des déformations lors d'essais de traction superélastique remettent en cause l'utilisation de cet essai pour bâtir des lois de comportement, alors que d'autres essais comme la torsion et le cisaillement apparaissent comme plus homogènes. Ce travail de thèse est dédié à l'analyse des mécanismes de déformation des AMF NiTi. Les comportements homogènes et localisés ont été étudiés en fonction des géométries d'échantillons (tubes et plaques minces), des types de sollicitations (traction et cisaillement simple) et des conditions d'essais (vitesse de déformation, quasi-isotherme, quasi-adiabatique, cyclage). L'originalité de cette étude est d'utiliser deux méthodes de mesures de champs : (i) la corrélation d'images afin d'obtenir les champs cinématiques et d'observer les localisations de déformation ; (ii) la thermographie infrarouge pour mesurer les champs de température et analyser les phénomènes de changement de phase. Afin d'utiliser ces techniques simultanément, des outils de recalage spatial et temporel des données ainsi que des techniques d'estimation de sources de chaleur à partir des mesures de température ont été développés. Lors d'essais superélastiques, cette étude a permis d'une part de mettre en évidence la présence de changement(s) de phase homogène en début de charge et de décharge, d'autre part de caractériser de manière quantitative les différentes morphologies de localisation. Les outils développés sont une première tentative pour disposer, à l'issue de ce travail, d'une DSC locale sous chargements mécaniques.

Mots Cléfs
Alliages à mémoire de forme, NiTi, Changement de phase, Champs cinématiques et thermiques, Estimation de source de chaleur, DSC locale.

Abstract

NiTi alloys are widely used notably as a biomaterial (stents for heart artery). Recent studies have shown that the conventional understanding of nominal stress-strain curve during super elastic tensile test was, assuming homogeneity, not sufficient to model the behaviour of such a material. In fact NiTi SMAs exhibit localized phases transformations and are influenced by many factors.
This work is dedicated to the study of these phase transformations and especially when they are localized. Two types of samples are used, namely, thin tubes in tensile tests and thin plates in tensile and shear tests. Two measurement techniques are used, namely, digital image correlation for strain field measurements and infrared thermography for temperature field measurements. The first one allows to observe strain localization and the second one allows to monitor phase transformations. The use of these two techniques needs special analysis tools, which have been developed during this work, as (i) spatial and temporal synchronisation for both strain and temperature fields, (ii) heat sources estimations from the noisy temperature field measurements.
The analysis of the performed tests led to the following conclusions: (1) The homogeneous stage at the beginning of tensile loading, commonly assumed to be pure elastic deformation, exhibits homogeneous phase transformations that started as soon as the test starts. Up to 9 % of martensite fraction was estimated when the alloys only presented an A-M phase transformation. (2) The localization morphologies are unpredictable and induce variation of the local strain and stress that influences the macroscopic stress. (3) The latent heat of phase transformation induced by temperature, commonly obtained by differential scanning calorimetry, is lower than the latent heat induced by stress. (4) Localization phenomena are emphasized by heat source and heat energy estimations. The positions of the heat source peaks correspond to phase transformation areas. Energy estimation allows one to perform local DSC during mechanical test. (5) Shear test seems to be more appropriate to model NiTi SMA since under such loading the phase transformation seems almost homogeneous.

Key words
Shape memory alloy, NiTi, Martensitic phase transformation, Heat sources estimation, Digital image correlation.

Remerciements

This report represents the end of four years (my master and thesis) within three laboratories: the laboratory 3S-R in Grenoble, where I spent most of my time, the laboratory SYMME in Annecy where I have done most of my experiments and finally, the School of Mechanical Engineering in Perth (Australia) where I spent six months thanks to the Explora'doc scholarship. I would like to thank all the members of these different laboratories that always gave me a wonderful welcome. Doing this thesis in various laboratories was very interesting and rich in experience.

I would like to thank Alexis Deschamps with whom I enjoyed teaching and who agreed to be the president of my jury.

I would like to thank my two reporters Pr. Yinong Liu and Pr. François Hild who have accepted this difficult task, for their constructive and detailed reports.

Thank you, Pr Yinong Liu for all the discussions we had together. Most of them were about the understanding of NiTi behaviour but not all of them. Thank you for the wonderful welcome you gave me in Australia, making sure that everything was fine for me. I also have to thank you for agreeing to follow-up my defence via videoconference.

Thank you, Pr. François Hild, for the discussions we had every time we met at conferences. Thanks to you I have avoided loosing a lot of time on "experimental tricks".

Thank you Pr. Jan Van Humbeeck for having been an examiner of my jury; I was very impressed to meet you at my thesis defence after having heard a lot about you from my thesis supervisor Pr. Denis Favier.

Doing this thesis with three thesis supervisors (Pr. Denis Favier, Dr. Hervé Louche and Dr. Laurent Orgéas) was not always easy since I was often pushed into three different directions, but it gave me the opportunity to investigate various approaches of the understanding of NiTi behaviour. I would like to thank all of you for your availability especially in reviewing so many times my thesis report in English.

Un Grand merci au "M. NiTi" du laboratoire : Denis Favier. J'ai encore en mémoire notre premier échange par email du Bénin lorsque je cherchais un sujet de master2. C'est par ton enthousiasme vis à vis des alliages à mémoire de forme (il est resté intact depuis) et grâce à

mon ignorance de la météo à Grenoble en hiver que cette grande aventure a commencé. Merci pour toutes les discussions que nous avons eues ensemble, pour avoir orienté en douceur mes travaux de recherche. Je garderai surtout en mémoire ce regard émerveillé devant un essai de traction de NiTi mais aussi cette capacité à retrouver des papiers qui ne sont même pas sur le web pour agrémenter ma bibliographie.

Un Grand merci au “M. thermographie” : Hervé Louche. Merci de m'avoir donné toutes les ficelles de la thermographie infrarouge et du calcul de sources via Matlab. Merci pour ta réactivité à toute épreuve même à 22h un samedi soir !

Un Grand merci à Laurent Orgéas. Face à Denis et Hervé, la place à occuper restait bien mince, merci de l'avoir occupée notamment lors des relectures (nombreuses) des publications et de ma thèse. Merci pour ces nombreuses remarques qui bien que parfois dures à accepter étaient pertinentes et vraiment constructives.

Mes remerciements vont également à la société Minitubes S.A., représentée par MM. Philippe Poncin et Philippe Comte-Gaz, Fabien Gruez et Seng Vong, qui ont soutenu et motivé cette étude.

Une thèse n'est rien sans les autres thésards. Je tiens donc à remercier les thésards du laboratoire 3S (nouvellement 3S-R et Gscop) : mes nombreux co-bureaux Thibault devenu breton depuis ; Vincent, promis, on viendra te voir au Gite de La Villette ; Luc toi qui a été à mes cotés tout au long de ces trois années qui nous a quitté trop tôt et trop brutalement et bien-sûr Mumu et Olivier. Mais aussi Maria, Rosalinda, Prof, les deux Nico, Max, JP, Jeff, Barth, Guilherme, Mamadou, Stéphane, Thomas, Hannen, Pierre... J'en oublie c'est sûr. Je garderai en mémoire ces moments de détente à la pause café avec la machine italienne de Rosalinda. Le pique-nique le midi qui se transformait très souvent en BBQ l'été, les sorties randos et bières surtout.

I'd like to thank also the PhDs of UWA who welcomed me especially Andy, Shoey, Nando and Brent. Thanks to you four, I spent a great time in UWA.

Je tiens également à remercier ma famille. Parmi eux je pense particulièrement à ma soeur et ex-colloc Caro avec qui j'ai passé une super année. Mon père, qui m'a beaucoup soutenue en fin de thèse sur la dernière ligne droite. Christopher pour sa présence et confiance de chaque instant.

Enfin, je tiens à remercier tous ceux qui de près ou de loin ont participé et étaient à mes cotés durant cette thèse dont Sophie, Barbara, Karine et Marie.

Contents

Notations

SHORT CUT

A	Austenite
DIC	Digital Image Correlation
DSC	Differential Scanning Calorimetry
FFT	Fast Fourier Transform
LVDT	Linear Variable Differential Transducer
M	Martensite
NETD	Noise Equivalent Temperature Difference
NUC	Non Uniformity Correction
SMA	Shape Memory Alloys
SME	Shape Memory Effect
LDB	Localised Deformation Bands
BB	Band Boundary

NOTATIONS

Thermodynamic analysis of the martensite transformation

ΔH_c	Difference of specific chemical enthalpies between the austenite and martensite phase $\Delta H_c = H_c^M - H_c^A$ (J.g^{-1})
ΔS_c	Difference of specific chemical enthalpies between the austenite and martensite phase $\Delta S_c = S_c^M - S_c^A$ (J.g^{-1}.K^{-1})
f_m	Mass fraction of martensite inside the elementary volume dV constituted of a mass dm_A of austenite and a mass dm_M of martensite $f_m = \frac{dm_M}{dm_M + dm_A}$ with $0 \leq f_m \leq 1$
δE_{el}	Elastic energy stored in the elementary volume by an infinitesimal step df_m of the transformation at the stage corresponding to f_m (J.g^{-1})
δE_{ir}	Irreversible energy dissipated by the infinitesimal step df_m of transformation at the stage corresponding to f_m; $\delta E_{ir} = \delta E_{iq} + \delta E_{iw}$ (J.g^{-1})
δE_{iq}	Heat component of the Irreversible energy (J.g^{-1})
δE_{iw}	Non-heat component of the Irreversible energy (J.g^{-1})
δW_{mech}	External mechanical work during the infinitesimal step df_m of transformation at the same stage (J.g^{-1})
q	Heat energy (J.g^{-1})
$s_i, \dot{q}$	Heat sources per unity volume (W.m^{-3}), per unity mass (W.g^{-1})

Material parameters

C	Specific heat ($J.kg^{-1}.K^{-1}$)
ρ	Mass density (kg. m^{-3})
k	Thermal conductivity ($W.m^{-1}.K^{-1}$)

DSC measurements

$T(A-M)_s$	Starting temperature for A→M transformation
$T(A-M)_f$	Finishing temperature for A→M transformation
$T(M-A)_s$	Starting temperature for M→A transformation
$T(M-A)_f$	Finishing temperature for M→A transformation

Sample geometry

L_0	Gauge length of the sample (m)
l_0	Distance between two extreme points (labelled A and B) of the image correlation grid (m)
R	Mean radius of the tube (m)
e	Thickness of the sample (m)

Mechanical data

t_{0mech}	Beginning of the test = time given by the testing machine (s)
f_{mech}	Mechanical data acquisition frequency (Hz)
$F(t)$	Axial load (N)
$U(t)$	Cross-head displacement (m)
$l(t), \Delta l$	Current length l and displacement Δl deduced from measurements of the displacements of the two extreme particles A and B (m), $\Delta l = l - l_0$
ε_0	$= U/L_0$, global nominal axial strain
$\dot{\varepsilon}_0$	$= \dot{U}/L_0$, global nominal axial strain rate (s^{-1})
ε	$= \Delta l/l_0$ Local axial strain

Coordinate system

P	Particle (or material point)
(X, Y)	Coordinate of the particle P at initial time
(x, y)	Coordinate of the particle P at time t
(NX, NY)	Coordinate of the particle P having an integer pixel value at initial time
(Nx, Ny)	Coordinate of the particle P having an integer pixel value at time t

Spatial and temporal synchronisation

$\underline{\underline{\mathbf{v2ir}}}$	Transformation matrix to go from the visible to the infrared description
$\underline{\underline{\mathbf{ir2v}}}$	Transformation matrix to go from the infrared to the visible description
$\overrightarrow{T}$	$= (T_x, T_y)$, Vector of translation from the visible to the infrared description
α	Rotation angle from the visible to the infrared description
k	Homothetic transformation coefficient from the visible to the infrared description

Kinematic parameters

t_{0v}	Beginning of visible image acquisition (s)
f_v	CCD camera frame rate (Hz)
$\overrightarrow{u}$	Displacement field measured by DIC
E_{xx}, E_{yy}, E_{xy}	Green Lagrange plane strain fields

Thermal parameters

t_{0IR}	Beginning of infrared image acquisition (s)
f_{IR}	Infrared frame rate (Hz)
T_a	Ambient temperature (K)
T_{fuild}	Temperature of the heat transfer fluid circulating inside the tube (K)
DL	Digital Level measured by the infrared camera
$T(P,0)$	Temperature of the particle P at initial time
$T(P,t)$	Temperature of the particle P at time t
ϵ	Emissivity
$\theta^0(Nx,Ny,t)$	$= T(Nx,Ny,t) - T(Nx,Ny,0)$ Temperature variation of one pixel of the IR camera
$\theta(P,t)$	$= T(P,t) - T(P,0)$ Temperature variation of a particle P. If the initial coordinates of P are (X,Y), then $\theta_t(P) = T(Nx,Ny,t) - T(X,Y,0)$

NiTi parameters

This table summarises the NiTi material parameters used.

Elasticity of the crystalline network (Young's modulus)	$E = 110$ GPa	Rajagopalan et al. (2005)
Specific heat	$C = 500$ J.kg^{-1}.K^{-1}	Faulkner et al. (2000)
Mass density	$\rho = 6400$ kg.m^{-3}	
Austenite thermal conductivity	$k_A = 18$ W.m^{-1}.K^{-1}	
Martensite thermal conductivity	$k_M = 8.6$ W.m^{-1}.K^{-1}	
Transformation strains in shear and tension for a polycrystalline NiTi	$\Delta\gamma_{tr} = 12\%$, $\Delta\varepsilon_{tr} = 8\%$	Orgéas and Favier (1998)

General introduction

Like all other Shape Memory Alloys (SMAs), nearly equiatomic polycrystalline NiTi alloys exhibit a reversible martensitic transformation that gives them specific thermomechanical behaviour. They are being increasingly used in a large number of applications in the fields of aeronautical, structural engineering and biomedical applications (e.g., human implants and surgical instruments). The applications based on these peculiar properties are generally designed using finite element simulation in which three-dimensional constitutive equations are implemented to model the thermomechanical behaviour of these alloys.
A large number of applications use the superelastic properties of these NiTi alloys. In this case, the constitutive equations are mostly based on simple understanding of nominal stress strain curve during superelastic tensile test. However, intensive experimental investigations that have been carried out in recent decades to characterize and understand deformation mechanisms associated with the superelasticity of SMAs have established that uniaxial tensile superelastic deformation of polycrystalline NiTi SMAs often exhibits localised Lüders-like deformation modes (Miyazaki et al., 1981; Leo et al., 1992; Shaw and Kyriakides, 1995, 1997; Orgéas and Favier, 1998; Favier et al., 2001; Gadaj et al., 2002; Sun and Li, 2002; Iadicola and Shaw, 2002b; Brinson et al., 2004; Ng and Sun, 2006). Those localization phenomena cannot be easily detected from a simple stress strain curve. Most of these studies have been achieved in tension using wires, strips or bone-shaped samples. The complex localization phenomena have been studied using qualitative optical observations (Miyazaki et al., 1981; Shaw and Kyriakides, 1997; Sun and Li, 2002; Gadaj et al., 2002; Brinson et al., 2004), multiple extensometers (Leo et al., 1992; Shaw and Kyriakides, 1995; Orgéas and Favier, 1998; Favier et al., 2001) and temperature fields (Shaw and Kyriakides, 1997; Iadicola and Shaw, 2002b; Gadaj et al., 2002). Those studies have shown that the localization phenomena depend on many parameters such as materials characteristics, sample geometries and loading conditions (Shaw and Kyriakides, 1995; Orgéas and Favier, 1998; Sun and Li, 2002).
With the recent development of full field measurement techniques, it is now possible to measure simultaneously on the surface of a deformed sample: (i) temperature fields using infrared cameras and (ii) strain fields obtained by Digital Image Correlation (DIC) post processing (Vacher et al., 1999; Coudert, 2005; Hild and Roux, 2006). The observation of strain fields allows one to observe and quantify strain localization but does not give any information on the strain field nature. Temperature measurements allow to detect the phase

transformation since it is either exothermic or endothermic. The simultaneous use of those two techniques gives a unique opportunity to observe and better analyse the complex thermal and mechanical behaviour and their coupling present during homogeneous and heterogeneous NiTi behaviour. This is what is aimed at in this thesis. By combining temperature and strain field measurements, the superelastic or the shape memory effect of NiTi alloys can be investigated more precisely. The influence of the type of mechanical loading (tension, shear), the sample geometry (tube, plate), the thermomechanical boundary conditions (temperature, macroscopic strain rate) will be analysed. Within this context, the present thesis report is structured in six chapters.

The **first chapter** presents generalities on martensitic transformation and its consequence on the thermomechanical behaviour of SMAs. Among the SMAs presenting reversible martensitic transformation, nearly equiatomic NiTi alloys will be used. Hence, the specificity of this alloy and especially localization phenomena observed during mechanical tests will be presented in more details. Finally, the thermodynamic framework of the thermoelastic transformations that will be used in chapters 4 to 6 to analyse the experiments will be presented.

The tools that have been developed and used to observe and analyse the complex thermal and mechanical behaviour present in NiTi SMAs are presented in **second chapter**. The full field measurement techniques used to obtain the strain and temperature fields are first described. In order to use simultaneously these two techniques and analyse properly the data, a spatial synchronisation software, which has been developed, will be explained. Since the observation of a temperature variation is only the consequence of the presence of internal or external heat sources, another software has been developed in order to estimate 2D heat sources from temperature fields measured either on thin plate or tube samples.

To study NiTi behaviour under different loading conditions, several materials and experimental set-up are used and will be presented in the **third chapter**. In this chapter, the materials that have been used are first described. They are of two types, namely, first thin tubes, second thin plates. In order to perform tensile test on the tube specimens, a special gripping system developed to perform tensile test on tubes of various diameters and impose the temperature during the test will be detailed. Finally, we will discuss on the possibilities to perform strain field measurements during a shear test.

The last three chapters report experimental results and analysis deduced from the different mechanical tests performed on these materials.

Chapter four concerns tests performed on tubular samples. The analysis of simultaneous observation of both strain and temperature fields during a superelastic NiTi under tension is first presented. Then, the influence of parameters such as macroscopic strain rate and temperature are studied.

Chapter five is devoted to tests performed on the plate samples. These samples present only austenite and martensite phases (and no R-phase) and allow an easier analysis of the phase transformation behaviour. Homogeneous, then localised stages during tensile test loadings, are successively analysed with both spatial synchronisation and heat source estimation tools. The influence of the type of loading is then studied by performing simple shear tests.

Chapter six presents heat source estimation on tubular sample during the localised stages. In these cases the analysis is more complicated since the specimen exhibits martensite phase transformation and R-phase transformation on loading.

CHAPTER 1

Bibliography on NiTi

Table of contents

1.1 Martensitic transformation in SMA

Shape Memory Alloys (SMAs) exhibit thermo-mechanical behaviours that are very different from usual metallic alloys. Deformed at "cold" temperatures, the alloy experiences large irreversible deformation after a mechanical loading (see ferroelastic behaviour in Figure 1.1.a) but recovers its original shape and dimension upon heating. This phenomenon is called Shape Memory Effect (SME) and was first observed in gold-cadmium alloys (AuCd) in 1932 by the Swedish scientist Olander (1932). In the following decades, 40 different alloys have been discovered to exhibit the shape memory effect.

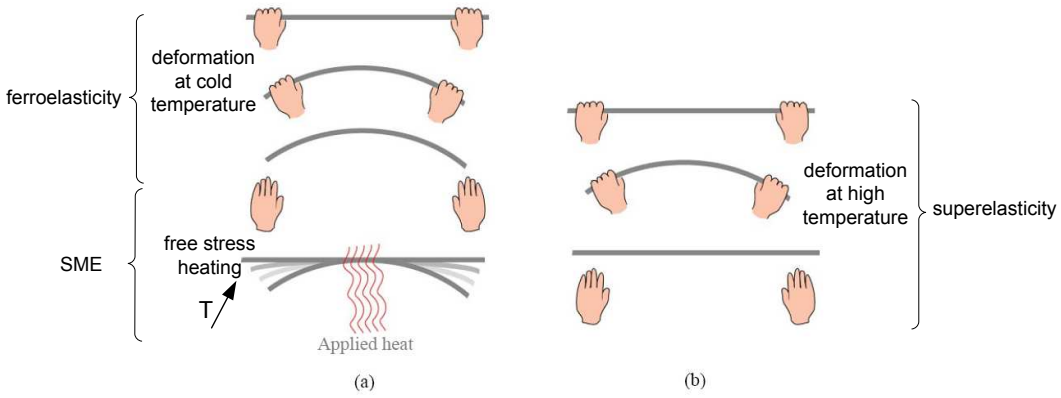

Figure 1.1: *Illustration of (a) feroelasticity, shape memory effect and (b) pseudoelasticity.*

Another property of SMAs (widely used in commercial applications) is the pseudo-elasticity or superelasticity: at "high" temperature, SMAs can undergo large deformations (bending, twisting and pulling) and then instantly revert back to their original shapes when removing the load (Figure 1.1.b).

1.1.1 Crystallography of Martensitic Transformations

SMAs owe their unusual thermomechanical behaviour to a solid-solid phase transformation between a parent austenite (A) phase and a product martensite (M) phase having different atomic structure. As presented schematically in Figure 1.2.b-c, the less symmetric martensite variants are either oriented along a particular direction (often the loading direction in a mechanical test) or self-accommodated one to another over all the possible martensite variants in order to minimise the internal elastic energy (Ortin and Planes, 1988).

The martensitic transformation is considered as:

- a diffusionless process of displacive lattice distortion, namely, the atoms move cooperatively, the displacements being small (1/10 of the inter atomic distance).
- crystalographically reversible in SMAs since very few irreversible defects such as dislocations are introduced during its occurrence

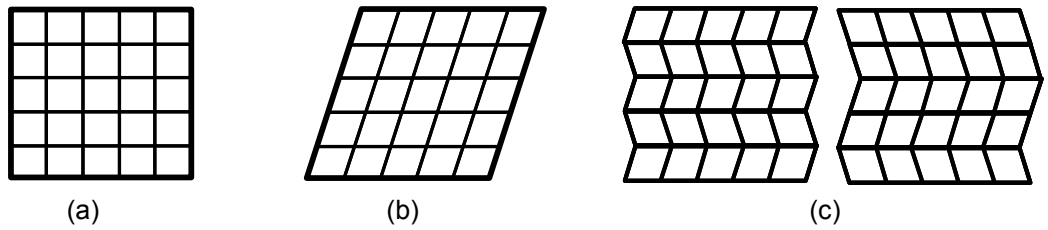

Figure 1.2: *Scheme of SMAs structures. (a) Austenite A. (b) Oriented martensite M. (c) examples of self accommodated martensite.*

Such martensitic transformation can also occur by rapidly cooling down carbon steel and induce large volume variation. Therefore, many defects are created and the transformation is not reversible. In the case of SMAs, the transformations are reversible at a macroscopic scale by heating and proceed with almost no volume change.

1.1.2 Thermomechanical behaviour

1.1.2.1 Introduction

As shown in Figure 1.3, lattice distortion induced by martensitic transformation produces a finite deformation of the crystal. Martensitic transformation is both a mechanical process and a phase transformation that is strongly correlated with thermal effects. The martensitic phase transformation is either induced by thermal or mechanical variations. Furthermore, many factors, such as the microstructure (composition, transformation crystallography, texture, grain size, dislocation, precipitates morphology), and external thermomechanical loading conditions (temperature, strain rate and stress state) affect the transformation.

To better understand the behaviour of SMAs, different schematic thermal and mechanical behaviours induced by testing conditions (temperature and load variation) are presented in Figure 1.3.a.

Structure A represents austenite, B represents self-accommodate martensite and C, oriented martensite. Several behaviours are possible:

- **A→B:** martensite transformation is temperature-induced from initial austenite state when decreasing the temperature. The martensite variants are in different directions and self-accommodated among the possible variants to minimise the stored elastic energy;
- **B→A:** the reverse transformation is also thermally induced by increasing the temperature;
- **A→C:** under a sufficient external load at a given temperature, austenite transforms into oriented martensite. The macroscopic deformation is produced by the phase transformation named *stress-induced martensite transformation*;
- **B→C:** self accommodated martensite will become oriented under sufficient external load. The macroscopic deformation is produced by a change of orientation of the martensite variants. This path is therefore called *martensite reorientation*;

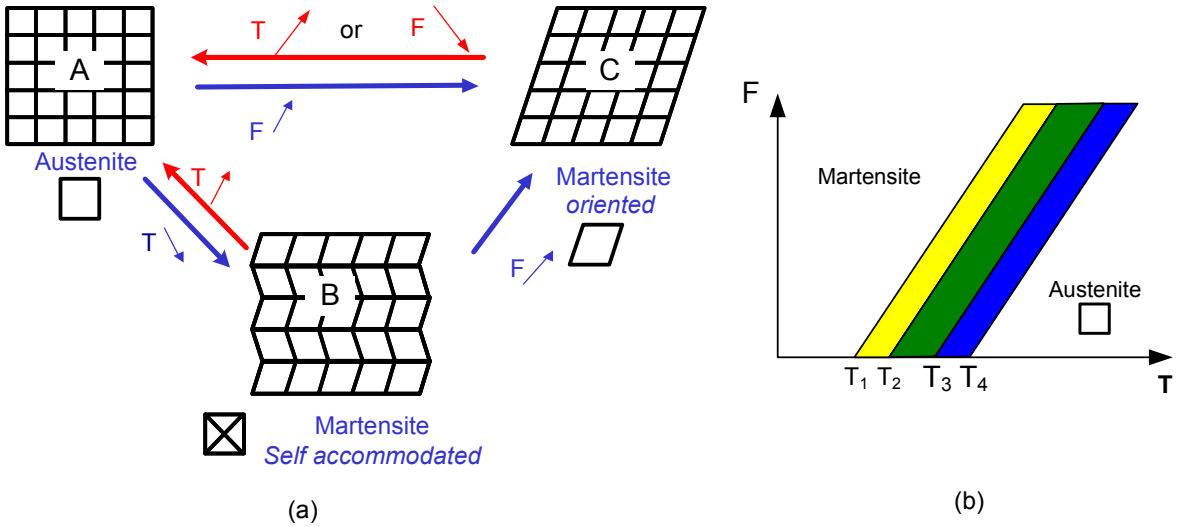

Figure 1.3: *a) Illustration of influence of variation of load (F) or temperature (T) on phase transformation. b) Load-temperature SMA phase diagram. In this diagram* $T(A-M)_f$, $T(M-A)_s$, $T(A-M)_s$, $T(M-A)_f$ *are respectively labelled* T_1, T_2, T_3, T_4.

- C→**A:** two thermomechanical conditions produce the reverse martensite transformation. (i) If the martensite is stable at the ambiant temperature, the reverse transformation is produced by a temperature increase. (ii), if the martensite is not stable at the ambiant temperature, stress-induced martensite C transforms back to austenite when reducing the load F.

At zero load we can define the temperature of phase transformation starts and ends: upon cooling, A→M starts at temperature $T(A-M)_s = T_3$ and ends at temperature $T(A-M)_f = T_1$. Upon heating, the reverse transformation M→A starts at temperature $T(M-A)_s = T_2$ and ends at temperature $T(M-A)_f = T_4$.

The existing phase can be expressed in the load-temperature (F - T) phase diagram presented in Figure 1.3.b. Depending on the (F - T) loading, Shape Memory Alloys can have different mechanical behaviours such as superelastic, the shape memory effect, ferroelasticity. The following sections will present these behaviours in more details.

1.1.2.2 Stress induced behaviour

Superelasticity ($\mathbf{A \rightarrow C_1 \rightarrow A}$)

If the temperature is above $T_4 = T(M-A)_f$ (the alloy is initially in austenitic state A), stress-induced martensitic transformation induces oriented martensite (A→C_1, Figure 1.4.a). At the end of loading, martensite plates formed are all oriented in the same direction (loading direction). For NiTi polycrystalline alloys, accumulation of the lattice distortion can induce a macroscopic transformation strain up to 8% in tension or 12% in shear (Orgéas and Favier, 1998). Yet the martensitic phase is not stable at the test temperature. When the stress is removed, reverse M→A transformation occurs (C→A, Figure 1.3), the alloy recovers its original shape. This behaviour is named superelasticity or pseudoelasticity.

As shown in Figure 1.4.b, the superelastic curve is usually divided into six parts. On loading, a first linear part (1) associated with the elastic strain of A; a second one (2) associated with the transformation A→M occurring along an upper stress plateau and then a third one (3) associated with the elastic deformation of oriented martensite variants. When the load is progressively removed, the reverse transformation M→A occurs along a lower stress plateau (5) after an initial linear stage (4) associated with the elastic unloading of the oriented martensite. The complete reverse transformation is followed by the elastic unloading of A during stage (6).

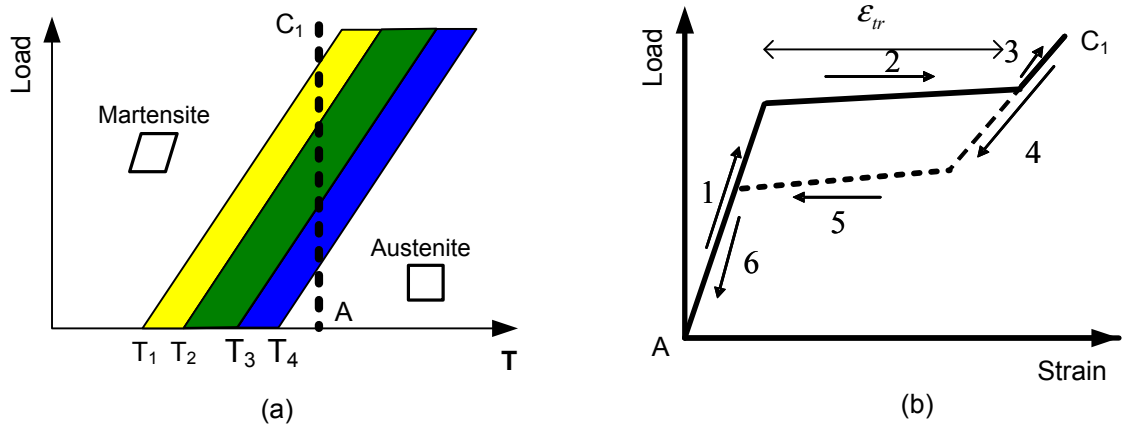

Figure 1.4: *a) Load-temperature SMAs phase diagram. b) Simplified superelastic SMAs strain-stress curve corresponding to the path $A \rightarrow C_1 \rightarrow A$ plotted in (a). Conventional understanding: (1) elastic deformation of austenite; (2) austenite to oriented martensite transformation; (3) and (4) elastic deformation of oriented martensite. (5) Oriented martensite to austenite reverse transformation; (6) elastic deformation of austenite.*

Ferroelasticity ($\mathbf{B \rightarrow C_2 \rightarrow C'_2}$)

If the alloy is in initial self accommodated martensite state ($T < T(A-M)_f = T_1$), reorientation of the martensite plates occurs during loading ($B \rightarrow C_2$ in Figure 1.5).

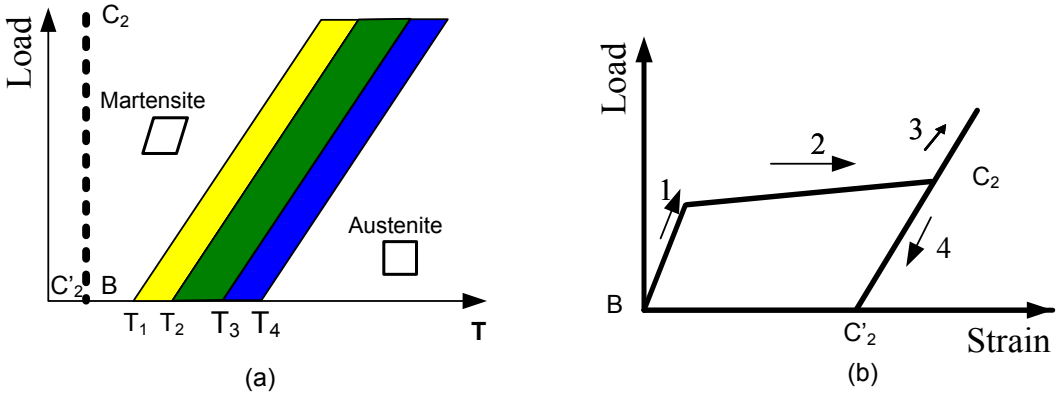

Figure 1.5: *a) Load-temperature SMAs phase diagram. b) Simplified SMAs strain-stress curve corresponding to the path $B \rightarrow C_2 \rightarrow C'_2$ plot in (a).*

When the stress is removed, only the elastic deformation combined with possible detwinning

phenomena is recovered ($C_2 \rightarrow C_2'$).

Conventional understanding of the mechanical behaviour of ferroelasticity schematically shown in Figure 1.5.b, is divided into 4 parts: (1) elastic deformation of M, (2) stress plateau associated with martensite reorientation $B \rightarrow C_2$ (3) and (4) elastic deformation of oriented martensite and detwinning. At the end of unloading, martensite plates remain preferentially oriented in the loading direction.

When the initial temperature is between $\mathbf{T(A-M)_f = T_1}$ and $\mathbf{T(M-A)_f = T_4}$

Both austenite and martensite phase can co-exist initially (see Figure 1.6.a). During the loading depending on the initial state, martensite reorientation or stress induced martensite tranformation behaviour occur. At the end of loading (C_3), the sample is fully or partially in oriented martensite (see Figure 1.6.b). As the stress is removed, since martensite phase is stable at ambiant temperature, only the elastic deformation of oriented martensite will be recovered ($C_3 \rightarrow C_3'$).

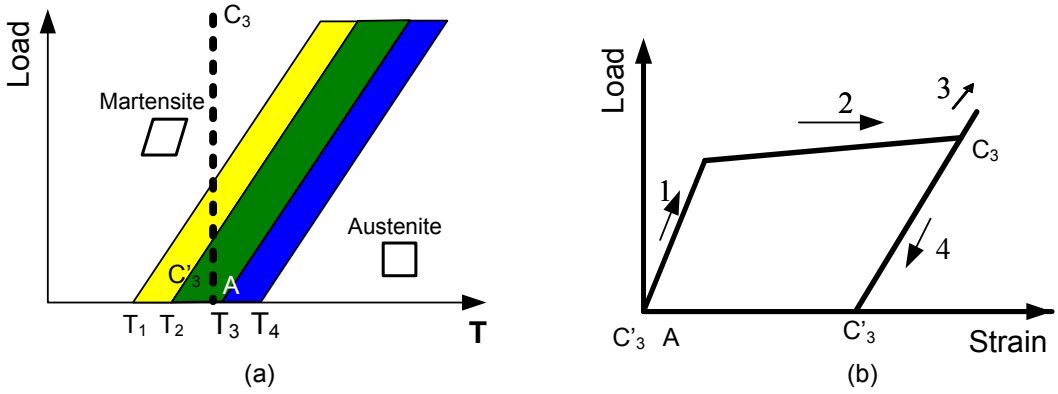

Figure 1.6: *a) Load-temperature SMAs phase diagram. b) Simplified SMAs strain-stress curve corresponding to the path $A_3 \rightarrow C_3 \rightarrow C_3'$ plot in (a).*

1.1.2.3 Shape memory effect

The sample in oriented martensite state ($C_3' \rightarrow A$ or $C_2' \rightarrow A$) will recover its original form via reverse M $\rightarrow$A phase transformation by heating the material to above $T(M-A)_f = T_4$. This phenomenon is called shape memory effect (see Figure 1.7).

1.2 Specificity of NiTi SMAs

1.2.1 Nearly equiatomic NiTi properties and applications

Among all SMAs, near-equiatomic NiTi alloys, which were discovered by Chang and Read in 1951 (Chang and Read, 1951), were the first to be used in 1963. The first application was in the military field (cryogenic couplings used by the US-Navy for F-14 air planes in the 70s).

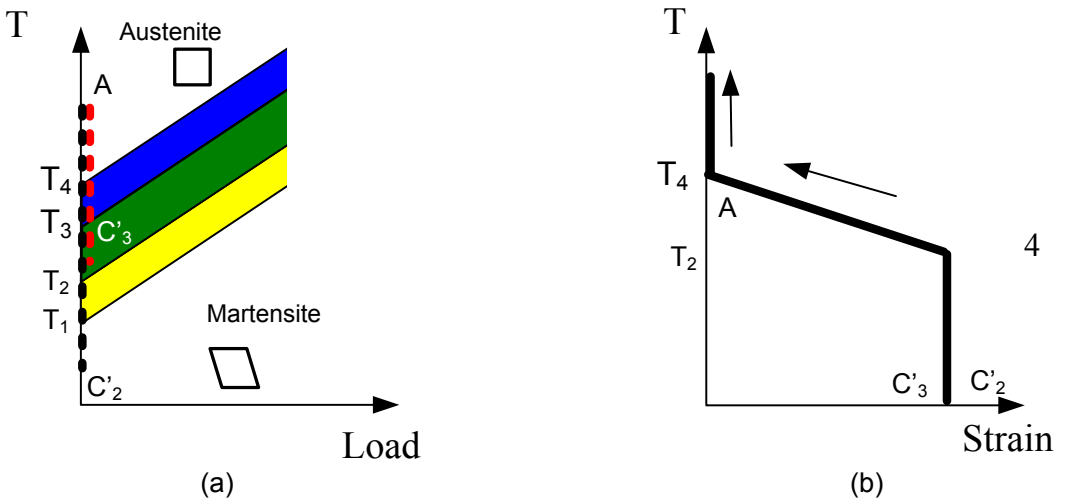

Figure 1.7: *a) temperature-Load SMAs phase diagram. b) Simplified SMAs strain-stress curve corresponding to the path $C_3' \rightarrow A$ and $C_2' \rightarrow A$ plot in (a).*

Nowadays, NiTi SMAs are used in many commercial applications. They are found to provide the most desirable combination of material properties for many engineering and technological applications mostly based on the superelastic properties of SMAs. Comparison of stress strain curves for different materials is presented in Figure 1.8. NiTi recoverable strain amplitudes are much higher than those of standard steel material, human hair or tendon. But stress needed is much higher than those for living tissues and is close to that of steel. Finally, NiTi SMAs exhibit a stress plateau like human hair or tendon.

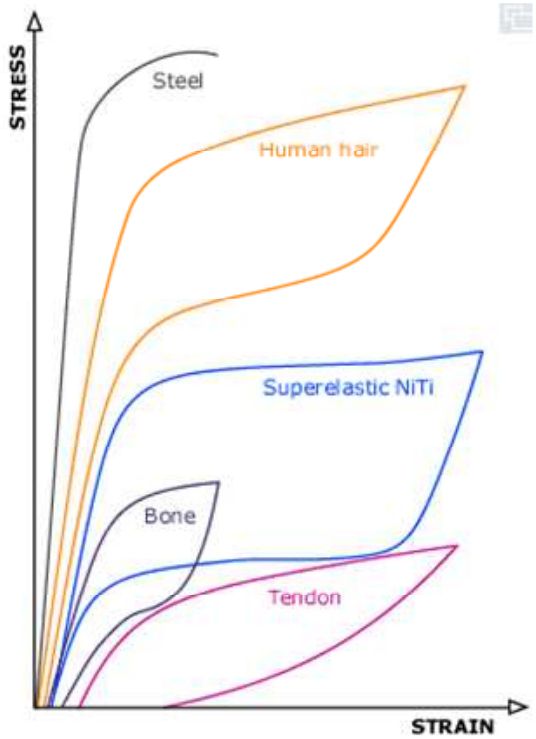

Figure 1.8: *Comparison the typical stress strain curve of different materials.*

Nowadays, owing to their outstanding superelastic behaviour at human body temperature and

to their rather good biocompatibility, NiTi SMAs are being increasingly used for biomedical applications:

- Superelastic NiTi wires have found wide use as orthodontic wires (Figure 1.9.a).
- Nickel-Titanium alloy has also revolutionised endodontic instruments. The bending flexibility of NiTi while rotating makes it an ideal material for use to clean the root canal during a crown-down as represented in Figure 1.9.b.

Figure 1.9: *a) Example of NiTi orthodontic wires (after: www.memry.com), b) Example of NiTi endodontic instruments (after: http://www.micro-mega.com)*

- One of the current largest applications for NiTi SMAs is the Stent (Figure 1.10). Stents are often used to alleviate diminished blood flow to organs and extremities beyond an obstruction in order to maintain an adequate delivery of oxygenated blood.

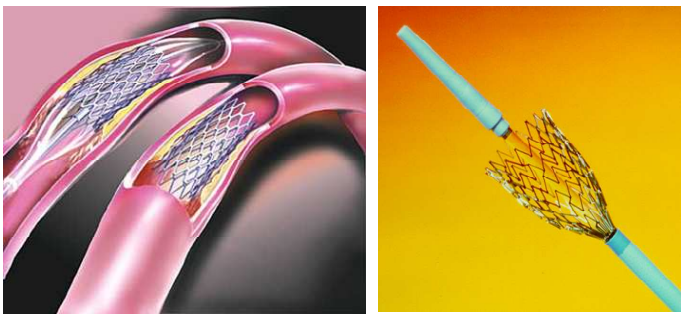

Figure 1.10: *Example of Stent.*

Many other applications also exist in other fields such as electrically manipulated actuators, in robotics, in remote control devices, in micro-electromechanical systems and smart structures...

1.2.2 Crystallographic microstructure

Near-equiatomic NiTi alloys exhibit three phases in the solid state:

- a B2 cubic austenite (A) that is stable at high temperatures. The crystal structure of austenite is presented in Figure 1.11.a,

- a B19' monoclinic martensite (M) appearing at low temperatures (Figure 1.11.b),
- a rhombohedral R-phase (R) that can appear under certain structural conditions, between the austenite and the martensite (Figure 1.11.c).

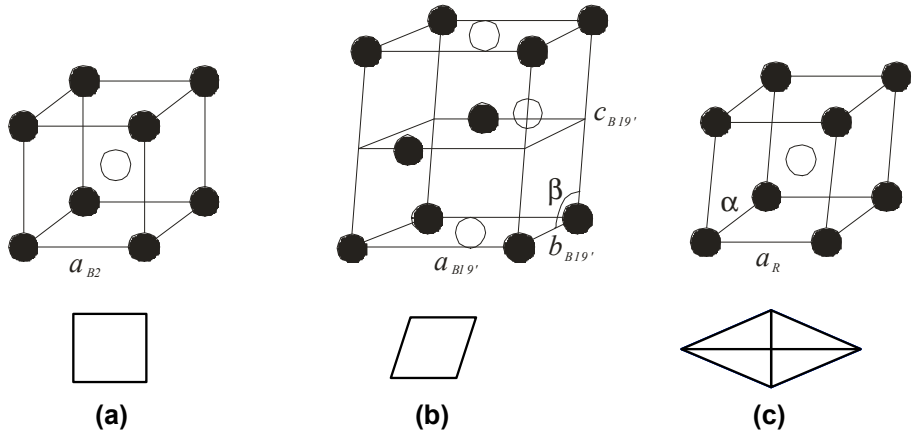

Figure 1.11: *The crystal structures of NiTi alloys. (a) Cubic austenite parent B2 structure. (b) Monoclinic B19' martensite structure, c) R-phase (Otsuka et al., 1971).*

1.2.3 Localization phenomena in NiTi SMAs

Most of the commercial applications are based on the superelasticity of NiTi alloys. In that case, the constitutive equations are mostly based on simple understanding of the nominal stress-strain curve during superelastic tensile test presented in Section 1.1.2. Within the past decades, intensive experimental investigations have been carried out to characterise and understand deformation mechanisms associated with the superelasticity of SMAs. Those studies have established that polycrystalline NiTi SMAs often exhibits localized Lüders-like deformation modes (Miyazaki et al., 1981; Leo et al., 1992; Shaw and Kyriakides, 1995, 1997; Orgéas and Favier, 1998; Favier et al., 2001; Gadaj et al., 2002; Sun and Li, 2002; Iadicola and Shaw, 2002b; Brinson et al., 2004; Ng and Sun, 2006) under tensile loading and that the localization phenomena depend on many parameters such as materials characteristics, sample geometries and loading conditions (Shaw and Kyriakides, 1995; Orgéas and Favier, 1998; Sun and Li, 2002).

1.2.3.1 First observations of localization on a thin wire in tension

The first observations of localization phenomena on superelastic NiTi alloys were made during tensile tests performed at low strain rate on thin wires (Leo et al., 1992). In Leo *et al.* experiment, four extensometers (E1 to E4), were put at different positions along the gauge length of the NiTi wire, as represented in Figure 1.12.a. The temporal evolution of each extensometers and the nominal stress are presented in Figure 1.12.b. This figure brings the following comments:

- during stage 1 the mechanical response presented a first increase. At the same time, the four extensometers gave the same responses: in this stage, the strain field was uniform;

- in stage 2, the stress became constant. A plateau was observed. The responses of the extensometers change. One after another, their strains jumped from $\varepsilon = 1\%$ to $\varepsilon = 6\%$ and stabilised again. This second stage shows the existence of strong strain localization;
- reverse phenomena were observed during unloading.

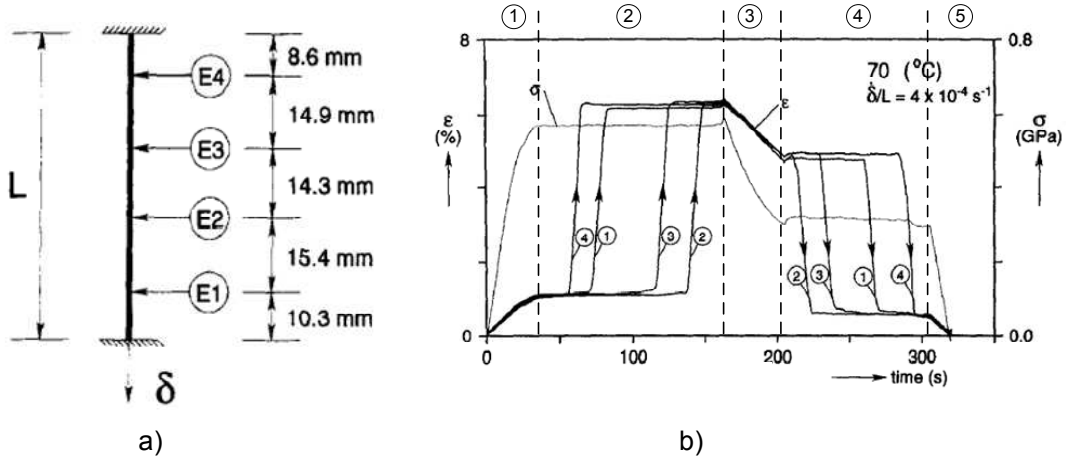

Figure 1.12: *a) Schematic of the set-up used on NiTi thin wire to observe localization phenomena with the presence of four extensometers. b) Temporal evolution of the nominal stress and strain, estimated from four extensometers (Leo et al., 1992).*

1.2.3.2 Different methods to observe localization

Several methods can be used to monitor the localization phenomena in NiTi alloys.

- Historically, the use of several extensometers in different areas of the sample as presented in the previous subsection has been most frequently used (Shaw and Kyriakides, 1995; Orgéas and Favier, 1998; Li and Sun, 2002; Liu et al., 1998).
- One simple method consists in taking advantage of strong strain gradients induced during localisation, by coating the sample with material that breaks during the occurrence of a high strain gradient (Miyazaki et al., 1981; Shaw and Kyriakides, 1997; Iadicola and Shaw, 2002a; Brinson et al., 2004; Ng and Sun, 2006). Such material can be a thin layer of inelastic paint, glaze or even the natural oxide layer that often forms in NiTi alloy. This second method is more qualitative but allows one to observe the initiation, propagation and morphologies of the localization phenomena as presented in Figure 1.13.a.
- Another technique consists in measuring the evolution of the surface morphology using a profilometer (Li and Sun, 2002). Since the martensitic phase transformation occurs without volume change, the longitudinal strain variation will induce a reduction of the thickness of the sample as presented in Figure 1.14.
- Since the martensitic transformation is exothermic, heat will be locally released during the phase transformation. Therefore, observation of local temperature changes can bring precious information on the martensitic transformation. In 1992, localization was observed using thermocouples on a thin NiTi wire (Leo et al., 1992). With the

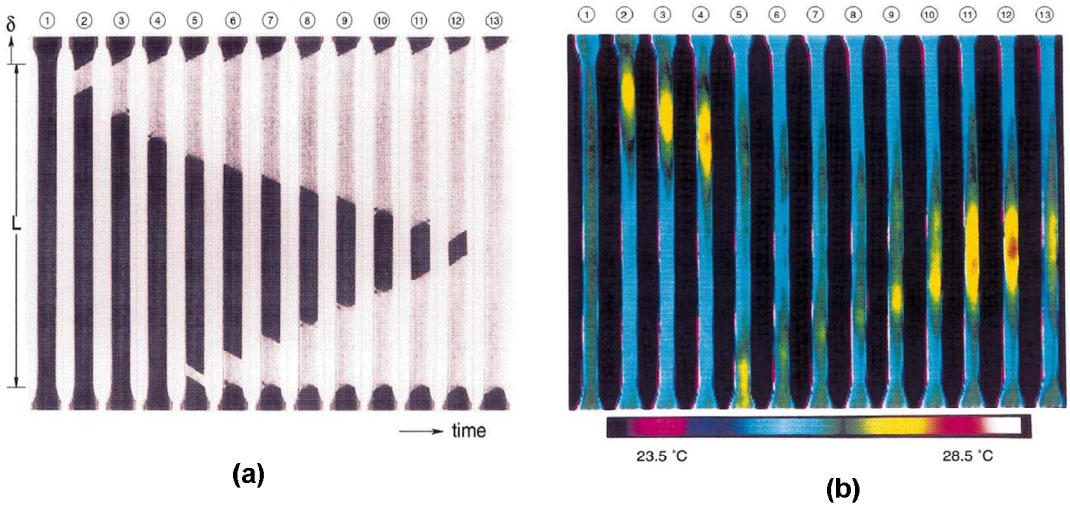

Figure 1.13: *Observation of localised A→M phase transformation during a tensile test, performed at* $\dot{\delta}_f/L = 10^{-4}s^{-1}$ *at ambiant temperature, by taking a) visible photo and b) temperature fields measured by an infrared camera (Shaw and Kyriakides, 1997).*

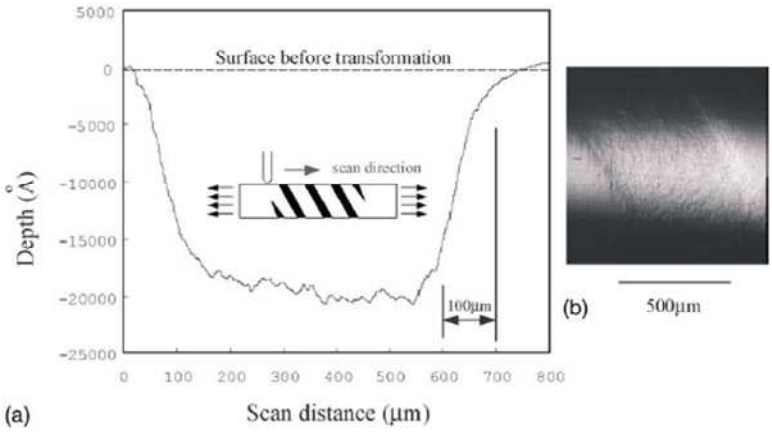

Figure 1.14: *Example of detection of the localization using profilometer on a NiTi thin tube (Li and Sun, 2002).*

recent development of infrared cameras, many studies have established the correlation between localization morphologies and temperature fields, (see Figure 1.13 and (Shaw and Kyriakides, 1997; Gadaj et al., 2002; Iadicola and Shaw, 2002a; Pieczyska et al., 2004)).

However, due to conduction phenomenon, analysis of temperature fields remains difficult and may only lead to qualitative information on localization phenomena. Heat source estimation takes into account the heat diffusion and brings quantitative information on the causes.

- Nowadays, displacement and strain fields can be estimated using for example Digital Image Correlation (DIC) software. This technique has proved its efficiency to observe and analyse localised phenomena (Louche et al., 2007). However so far this technique has not been used to study NiTi.

1.2.3.3 Influence of loading path on NiTi

Within the past decades, intensive experimental investigations have been carried out to characterise and understand deformation mechanisms associated with the superelasticity of SMAs. Depending on the loading type, the thermomechanical history of the alloy as well as the sample geometry, several behaviours have been observed:

- **Tensile tests:** Nowadays, shape memory alloy behaviours are mostly characterised using simple tensile tests. Despite strong localization phenomena during the stress plateau (stage (2) in Figure 1.4), most constitutive equations used to design NiTi applications assume homogeneous deformation of the specimens during tensile loading. Many studies (Miyazaki et al., 1981; Shaw and Kyriakides, 1995; Liu and McCormick, 1996; Shaw and Kyriakides, 1997; Orgéas and Favier, 1998; Sun and Li, 2002; Brinson et al., 2004; Ng and Sun, 2006) have been achieved to characterise stage (2). Comparatively, the other stages (1), (3), (4) and (6) have been less studied. However, Brinson et al. (2004) present some results showing clearly the occurrence of several deformation mechanisms other than elastic distortion of the crystalline structure during each of these stages.

- **Tension-torsion tests:** Using surface morphology analysis, Sun and Li (2002) have qualitatively observed NiTi tubes under combined tension and torsion loading. Under pure tensile loading, the tube exhibited localised phase transformation. As torsion loading was added, localisation became diffuse and even disappeared under sufficient torsion. Figure 1.15 shows the change of the surface morphology depending on the loading.

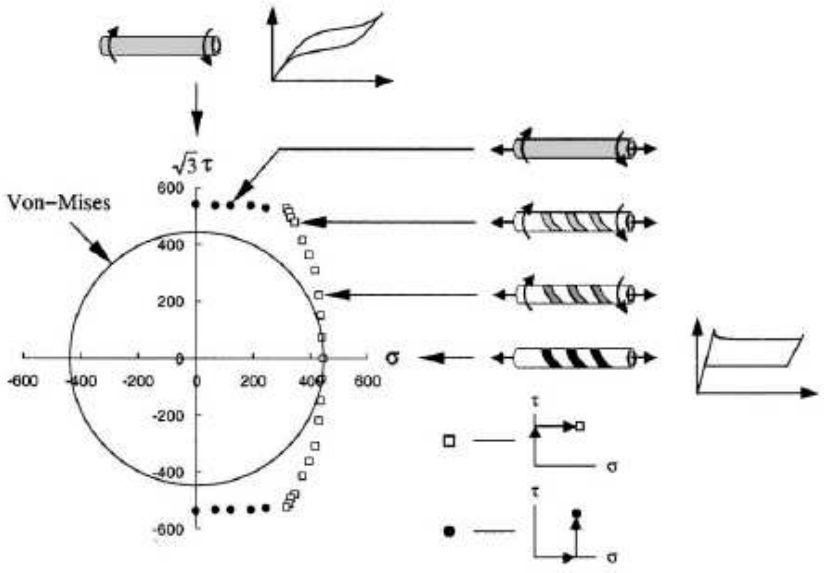

Figure 1.15: *Stress locus at the start of transformation: (□) tension under fixed torsion, (•) torsion under fixed tension (Sun and Li, 2002).*

- **Compression tests:** Compression tests are very difficult to perform on wire, plate and thin tubes, since the specimens tend to buckle. Therefore only few studies exist for this type of loading (Jacobus et al., 1996; Orgéas and Favier, 1998; Grabe and Bruhns, 2008). Among them, Orgéas and Favier have designed a compression device

that avoids this phenomenon and have shown, using extensometers homogeneous deformation under compression loading. Moreover, it has been shown that for Ni-Ti alloys the transformation deformation $\Delta\varepsilon_{tr}$ was lower in compression than in tension.

- **Shear test:** Like compression test, shear test seems to be homogeneous (Orgéas and Favier, 1998), but no full field measurements have been performed for this kind of loading.

1.3 Thermodynamic analysis of thermoelastic martensitic transformation

1.3.1 Thermodynamic framework

Several thermodynamic frameworks have been proposed to describe the thermomechanical behaviour of shape memory alloys. Some of these frameworks provide empirical based thermodynamic description that aims to account for complex state behaviour of polycrystalline SMAs, including thermomechanical coupling (McNichols et al., 1987; Chrysochoos et al., 1996). Others are based on the pioneering work of Cohen and his collaborators (Patel and Cohen, 1953; Salzbrenner and Cohen, 1979). In these last approaches, the martensitic transformation is considered as diffusionless first order reversible transformations. Many authors have investigated the link between the local equilibrium conditions (temperature, local stress) at individual austenite-martensite interfaces and thermodynamics analysis of thermoelastic martensitic transformation of an elementary volume of polycrystalline (Patel and Cohen, 1953; Ortin and Planes, 1988, 1989; Orgéas, 1997; Zhang et al., 2004). Among them, one will find in Orgéas (1997) the different steps and assumptions necessary to go from one to another scale.

We have decided to use this last approach with the framework developed by Ortin and Planes (Ortin and Planes, 1988, 1989, 1991) expressed at a macroscopic level.

Occurence of a thermoelastic martensitic transformation is determined where $\mathrm{d}G = 0$ by the free energy (G) balance at equilibrium for the transformation. For a thermoelastic martensitic transformation in a polycrystalline matrix the free energy per unit mass change over an infinitesimal step df_m of transformation is expressed as (Ortin and Planes, 1989; Wollants et al., 1993):

$$\mathrm{d}G = (\Delta H_c - T\Delta S_c)df_m + \delta E_{el} + \delta E_{ir} - \delta W_{mech} = 0 \tag{1.1}$$

or in derivative form as:

$$G' = \Delta H_c - T\Delta S_c + E'_{el} + E'_{ir} - W'_{mech} = 0, \tag{1.2}$$

where:

- G' is defined by $\mathrm{d}G = (\partial G/\partial f_m)\, df_m = G' df_m$
- ΔH_c is the difference between the two chemical specific enthalpies of the martensite and austenite phase: $\Delta H_c = H_c^M - H_c^A$;

- ΔS_c is the difference between the two chemical specific entropies of the martensite and austenite phase: $\Delta S_c = S_c^M - S_c^A$;
- f_m is the mass fraction of martensite defined in the elementary volume;
- T is the temperature;
- $\delta E_{el} = (\partial E_{el}/\partial f_m)\ df_m = E'_{el} df_m$ is the elastic energy stored in the elementary volume by an infinitesimal step df_m of the transformation at the stage corresponding to f_m;
- $\delta E_{ir} = (\partial E_{ir}/\partial f_m)\ df_m = E'_{ir} df_m$ is the irreversible energy dissipated by the infinitesimal step df_m of transformation at the same stage; $\delta E_{ir} > 0$;
- $\delta W_{mech} = (\partial W_{mech}/\partial f_m)\ df_m = W'_{mech} df_m$ is the external mechanical work per unit mass elementary volume during the infinitesimal step of transformation at the same stage.

All the terms are expressed as energy per unit mass of transformation in $\mathrm{J.g^{-1}}$ and are algebraic values; in full austenite $f_m = 0$ and in full martensite, $f_m = 1$; at every infinitesimal step, $0 \leq f_m \leq 1$. The infinitesimal martensite mass fraction step (df_m) is positive during the forward transformation and negative during the reverse transformation.

Enthalpy and entropy changes ΔH_c and ΔS_c originate from the difference in atomic arrangement between the two phases involved. ΔH_c and ΔS_c are considered constant for given transformation in a given alloy system. We assume that the heat capacities of austenite and martensite are equal (Ortin, 1992; Wollants et al., 1993). For the A→M martensite phase transformation $\Delta H_c = H_c^M - H_c^A < 0$ and $\Delta S_c = S_c^M - S_c^A < 0$; since austenite and martensite have different atomic arrangements (McCormick et al., 1993):

$$H_c^M < H_c^A, \tag{1.3}$$

$$S_c^M < S_c^A. \tag{1.4}$$

Elastic strain energy δE_{el} includes both the elastic strain energy, which is associated with the shape and volume changes of the transformation, and the interfacial energy which is also reversible. This energy is stored in the system during the forward transformation ($\delta E_{el} \geq 0$) and progressively released with the reversion of martensite to the parent phase ($\delta E_{el} \leq 0$). Tong and Wayman (1974) have shown that for a thermally induced transformation in a CuZn single cristal, the ratio $E'_{el}/\Delta H_c$ was of the order of 2 %.

Irreversible energies δE_{ir} is the sum of all irreversible energies dissipated, such as the emission of acoustic waves, the storage of lattice energy by the production of crystalline defects, and energy consumed in moving dislocations and interfaces. δE_{ir} is always dissipated and thus is always positive. δE_{ir} is dissipated both as heat ($\delta E_{iq} = (\partial E_{iq}/\partial f_m)\ df_m = E'_{iq} df_m$) and as non-heat components ($\delta E_{iw} = (\partial E_{iw}/\partial f_m)\ df_m = E'_{iw} df_m$) (Ortin, 1992; Favier and Liu, 2000):

$$\begin{array}{rcccc} \delta E_{ir} = & \delta E_{iq} & + & \delta E_{iw} \\ = & E'_{iq}\ df_m + & & E'_{iw}\ df_m \\ & > 0 & & > 0 \end{array} \tag{1.5}$$

The heat component of the irreversible energy δE_{iq} is dependent on a number of factors, including the actual path of the transformation, temperature, the metallurgical conditions and the mechanical properties of the matrix. It is often assumed in the literature (Ortin and Planes, 1988, 1991) that δE_{iq} has equal values during forward and reverse processes of a transformation: $|\delta E_{iq}^{A-M}| = |\delta E_{iq}^{M-A}|$. However, considering that internal stresses are created during the forward transformation and relaxed during the reverse transformation, it seems more reasonable to assume that more irreversible work is dissipated during the forward process than during the reverse transformation $|\delta E_{iq}^{A-M}| > |\delta E_{iq}^{M-A}|$. Tong and Wayman (1974) have shown that for a stress induced transformation in a CuZn single cristal, the ratio $E'_{iq}/\Delta H_c$ was of the order of 6 %.

Mechanical work δW_{mech} is the mechanical work performed by the external forces on the elementary volume to obtain the transformation. In continuum mechanics at the level of the elementary volume, the mechanical work is expressed as function of the macroscopic strain and stress tensors. The mechanical work per unit mass is expressed as:

$$\delta W_{mech} = \frac{1}{\rho}\underline{\underline{\sigma}} : \underline{\underline{\mathbf{D}}} dt = \frac{1}{\rho}\underline{\underline{\sigma}} : \underline{\underline{\mathbf{d}\varepsilon}}, \tag{1.6}$$

where ρ is the density. $\underline{\underline{\sigma}}$, $\underline{\underline{\mathbf{D}}}$, $\underline{\underline{\mathbf{d}\varepsilon}}$ represent respectively the stress, strain rate and macroscopic strain increment tensors at time t.

For a tensile and shear test the mechanical work is expressed as:

$$\delta W_{mech} = \frac{1}{\rho}\sigma d\varepsilon_{tr} \quad \text{for tensile loading,} \tag{1.7}$$

$$\delta W_{mech} = \frac{1}{\rho}\tau d\gamma_{tr} \quad \text{for shear loading,} \tag{1.8}$$

where $\mathrm{d}\gamma_{tr} = \Delta\gamma_{tr} df_m$ and $\mathrm{d}\varepsilon_{tr} = \Delta\varepsilon_{tr} df_m$ if we assume that the increment of the transformation strain is proportional to the infinitesimal step df_m. $\Delta\gamma_{tr}$ and $\Delta\varepsilon_{tr}$ are respectively the shear and tension transformation strains for a complete transformation. Orgéas and Favier have shown that for a complete transformation $\Delta\gamma_{tr} = 12\%$ and $\Delta\varepsilon_{tr} = 8\%$ (Orgéas and Favier, 1998).

Therefore, eq. (1.2) reads

$$G' = \Delta H_c - T\Delta S_c + E'_{el} + E'_{iq} + E'_{iw} - \frac{1}{\rho}\sigma\Delta\varepsilon_{tr} = 0 \quad \text{for tensile loading,} \tag{1.9}$$

$$G' = \Delta H_c - T\Delta S_c + E'_{el} + E'_{iq} + E'_{iw} - \frac{1}{\rho}\tau\Delta\gamma_{tr} = 0 \quad \text{for shear loading.} \tag{1.10}$$

If we define the transformation heat sources:

$$\begin{aligned} \dot{q}_{tr} &= -T\Delta S_c \frac{\mathrm{d}f_m}{\mathrm{d}t} + E'_{iq}\frac{\mathrm{d}f_m}{\mathrm{d}t} \\ &= \dot{q}_{tr\,chem} + \dot{q}_{tr\,diss} \end{aligned} \tag{1.11}$$

with $\dot{q}_{tr} = \mathrm{d}q_{tr}/\mathrm{d}t$ the specific heat sources that include both chemical $\dot{q}_{tr\,chem}$ and dissipative $\dot{q}_{tr\,diss}$ components. With eq. (1.1) and (1.5), $\dot{q}_{tr}$ becomes:

$$\dot{q}_{tr} = \left(-\Delta H_c - E'_{el} - E'_{iw} + W'_{mech}\right)\frac{\mathrm{d}f_m}{\mathrm{d}t}. \tag{1.12}$$

Heat effect associated with martensitic transformation consists of four components, namely, the chemical enthalpy change of the transformation (ΔH_c), the elastic energy stored or released during the process of the transformation ($E'_{el}df_m$), all the irreversible energies excluding heat ($E'_{iw}df_m$) and the mechanical work ($W'_{mech}df_m$) during the process of the transformation. Depending on the loading conditions, eq. (1.12) becomes for tensile loading

$$\begin{aligned} \dot{q}_{tr} &= \left(-\Delta H_c - E'_{el} - E'_{iw} + \frac{1}{\rho}\sigma\Delta\varepsilon_{tr}\right)\frac{\mathrm{d}f_m}{\mathrm{d}t} \\ &= \Delta H_{tr}^{tensile}(f_m)\frac{\mathrm{d}f_m}{\mathrm{d}t} \end{aligned} \tag{1.13}$$

and for shear loading

$$\begin{aligned} \dot{q}_{tr} &= \left(-\Delta H_c - E'_{el} - E'_{iw} + \frac{1}{\rho}\tau\Delta\gamma_{tr}\right)\frac{\mathrm{d}f_m}{\mathrm{d}t} \\ &= \Delta H_{tr}^{shear}(f_m)\frac{\mathrm{d}f_m}{\mathrm{d}t}. \end{aligned} \tag{1.14}$$

ΔH_{tr} is often called the latent heat of phase transformation. The above expressions show that its value is influenced by the loading conditions; therefore; $\Delta H_{tr}^{tensile} \neq \Delta H_{tr}^{shear}$. Moreover, its value ($\Delta H_{tr} = -\Delta H_c - E'_{el} - E'_{iw}$) estimated during a temperature induced phase transformation (e.g. in a DSC) is lower than during a stress induced transformation (Liu and Favier, 2001). It is worth noting that E'_{el} and E'_{iw} are functions of f_m and other factors.

Clausius Clapeyron relation under stress induced martensite transformation

Since ΔH_c is constant, temperature differentiation of eq. (1.9) and eq. (1.10) become:

$$\frac{\mathrm{d}\sigma}{\mathrm{d}T} = \frac{\rho}{\Delta\varepsilon_{tr}}(-\Delta S_c + \frac{\partial E'_{el}}{\partial T} + \frac{\partial E'_{iq}}{\partial T} + \frac{\partial E'_{iw}}{\partial T}) \quad \text{for tensile loading,} \tag{1.15}$$

$$\frac{\mathrm{d}\tau}{\mathrm{d}T} = \frac{\rho}{\Delta\gamma_{tr}}(-\Delta S_c + \frac{\partial E'_{el}}{\partial T} + \frac{\partial E'_{iq}}{\partial T} + \frac{\partial E'_{iw}}{\partial T}) \quad \text{for shear loading.} \tag{1.16}$$

The Clausius-Clapeyron equation is then obtained assuming that $\frac{\partial E'_{el}}{\partial T} \approx 0$, $\frac{\partial E'_{iw}}{\partial T} \approx 0$ and $\frac{\partial E'_{iq}}{\partial T} \approx 0$:

$$\frac{\mathrm{d}\sigma}{\mathrm{d}T} = \frac{-\rho\Delta S_c}{\Delta\varepsilon_{tr}} \tag{1.17}$$

1.3.2 Estimation of the total heat from two martensite fractions

We will first present for a general case for the total heat over a transformation between two martensite fraction states ($f_{m1} \rightarrow f_{m2}$). Then, we will present the case of cyclic loading ($f_{m1} \rightarrow f_{m2} \rightarrow f_{m3}$) when some residual martensite is retained at the end of the cycle ($f_{m1} \neq f_{m3}$) and when all martensite has transformed back ($f_{m3} = f_{m1}$). For all three cases, the total heat will be presented as function of the mechanical work and as function of the temperature. Possible simplification during isothermal transformation will also be presented for every case.

1.3.2.1 General case

Figure 1.16 represent an evolution between two distinct martensitic states f_{m1} to f_{m2} (Figure). At f_{m1} and f_{m2}, the temperature is T_1 and $T_2 = T_1 + \theta$ respectively. θ is the temperature variation and is dependent on the thermomechanical coupling. In the following we will express the temperature as a function of the temperature variation $T = T_1 + \theta$.

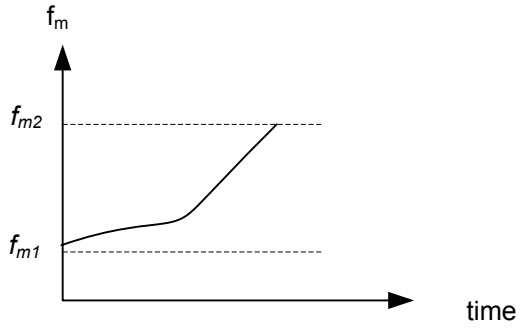

Figure 1.16: *Oversimplified scheme of the evolution of the martensite fraction during a thermomechanical test 1-2*

The total heat presented in eq. (1.11) and (1.12) over a finite range of transformation is expressed as:

$$\begin{aligned} q_{tr}^{1-2} &= \int_{f_{m1}}^{f_{m2}} [-T\Delta S_c + E'_{iq}]\, df_m \\ &= \int_{f_{m1}}^{f_{m2}} [-(T_1+\theta)\Delta S_c + E'_{iq}]\, df_m \\ &= -T_1\Delta S_c(f_{m2} - f_{m1}) - \Delta S_c \int_{f_{m1}}^{f_{m2}} \theta\, df_m + \int_{f_{m1}}^{f_{m2}} E'_{iq}\, df_m \end{aligned} \tag{1.18}$$

Introducing the notation:

$$\Delta_1^2\, \xi = \int_{f_{m1}}^{f_{m2}} \xi'\, df_m \tag{1.19}$$

eq. (1.18) becomes,

$$q_{tr}^{1-2} = -T_1\Delta S_c(f_{m2} - f_{m1}) - \Delta S_c \int_{f_{m1}}^{f_{m2}} \theta\, df_m + \Delta_1^2\, E_{iq}, \tag{1.20}$$

where $-\Delta S_c \int_{f_{m1}}^{f_{m2}} \theta\ df_m$ represents the thermomechanical coupling. When expressed as a function of the enthalpy variation and the mechanical work, q_{tr}^{1-2} reads:

$$\begin{aligned} q_{tr}^{1-2} &= \int_{f_{m1}}^{f_{m2}} \left(-\Delta H_c - E'_{el} - E'_{iw} + W'_{mech}\right) df_m \\ &= -\Delta H_c(f_{m1} - f_{m1}) - \Delta_1^2\, E_{el} - \Delta_1^2\, E_{iw} + \Delta_1^2 W_{mech}. \end{aligned} \tag{1.21}$$

where $\Delta_1^2\, E_{el} = \int_{f_{m1}}^{f_{m2}} E'_{el}\ df_m$ is the total elastic energy stored in the matrix, $\Delta_1^2\, E_{iw} = \int_{f_{m1}}^{f_{m2}} E'_{iw}\ df_m$ is the sum of the irreversible energies excluding heat dissipated and $\Delta_1^2 W_{mech} = \int_{f_{m1}}^{f_{m2}} W'_{mech}\ df_m$ is the total mechanical work from f_{m1} to f_{m2}.

For an isothermal transformation

The temperature stays at $T = T_1$ during the process of the transformation, therefore, $\theta = 0$. The heat sources in eq. (1.18) are expressed as:

$$q_{tr}^{1-2} = -T_1 \Delta S_c (f_{m2} - f_{m1}) + \Delta_1^2 E_{iq}. \tag{1.22}$$

1.3.2.2 Case of cyclic loading

During a cyclic loading, the martensite fraction at the beginning of loading, at the end of loading and at the end of the test of the cyclic loading, are respectively labelled f_{m1}, f_{m2} and f_{m3} as presented in Figure 1.17 with $f_{m1} \leq f_{m3} < f_{m2}$. If the martensitic transformation is not totally reversible, some martensite is stabilised and $f_{m3} > f_{m1}$.

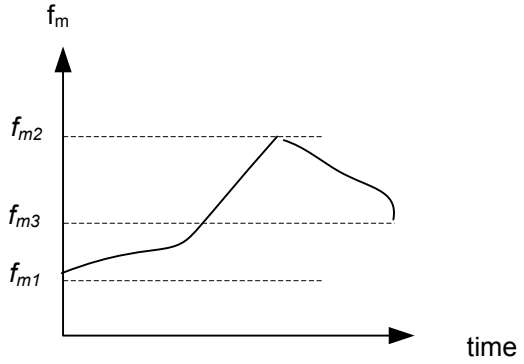

Figure 1.17: *Schematic view of the evolution of the martensite fraction during a thermomechanical test 1-2-3*

The heat associated with the cyclic transformation q_{tr}^{1-2-3} is expressed as:

$$\begin{aligned} q_{tr}^{1-2-3} &= \left(-\Delta H_c (f_{m2} - f_{m1}) - \Delta_1^2 E_{el} - \Delta_1^2 E_{iw} + \Delta_1^2 W_{mech}\right) \\ &+ \left(-\Delta H_c (f_{m3} - f_{m2}) - \Delta_2^3 E_{el} - \Delta_2^3 E_{iw} + \Delta_2^3 W_{mech}\right). \end{aligned} \tag{1.23}$$

The elastic energy stored is positive during the forward transformation, and negative during the reverse transformation. The irreversible energy is always positive:

$$\begin{aligned} \Delta_1^2 E_{el} \geq 0, \quad \Delta_1^2 E_{iw} \geq 0 \\ \Delta_2^3 E_{el} \leq 0, \quad \Delta_2^3 E_{iw} \geq 0 \\ \text{and} \quad \Delta H_c = H_c^M - H_c^A < 0 \end{aligned}$$

Therefore, eq. (1.23) reads:

$$q_{tr}^{1-2-3} = -\Delta H_c (f_{m3} - f_{m1}) - \oint_{123} E'_{el} df_m - \oint_{123} E'_{iw} df_m + \oint_{123} W'_{mech} df_m \tag{1.24}$$

By assuming the decomposition of the strain ε into elastic strain (ε_{el}) and phase transformation strain (ε_{tr}), it is possible to estimate the mechanical work during a mechanical test from the stress-strain curve. It corresponds to stress-strain curve hysteresis area (see Figure 1.18)

during a cycle:

$$\oint_{123} W'_{mech} df_m = \frac{1}{\rho}\oint_{123} \sigma \Delta\varepsilon_{tr} df_m = \frac{1}{\rho}\oint_{123} \sigma d\varepsilon_{tr} \approx \frac{1}{\rho}\oint_{123} \sigma d\varepsilon \quad \text{in tension,} \tag{1.25}$$

$$= \frac{1}{\rho}\oint_{123} \tau \Delta\gamma_{tr} df_m = \frac{1}{\rho}\oint_{123} \tau d\gamma_{tr} \approx \frac{1}{\rho}\oint_{123} \tau d\gamma \quad \text{in shear,} \tag{1.26}$$

where σ, and τ are the normal and shear stresses, ε and γ are the axial and shear strains measured on the mechanical curve.

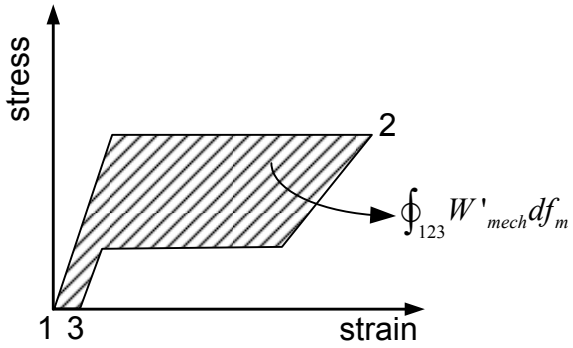

Figure 1.18: *Schematic view of the mechanical work during a mechanical test.*

The final expression is:

$$q_{tr}^{1-2-3} = -T_1 \Delta S_c (f_{m3} - f_{m1}) - \Delta S_c \left(\int_{f_{m1}}^{f_{m2}} \theta \, df_m + \int_{f_{m2}}^{f_{m3}} \theta \, df_m \right) + \Delta_1^2 E_{iq} + \Delta_2^3 E_{iq},$$

$$= -T_1 \Delta S_c (f_{m3} - f_{m1}) - \Delta S_c \oint_{123} \theta \, df_m + \oint_{123} E'_{iq} \, df_m. \tag{1.27}$$

For an isothermal transformation

The temperature remains identical $T = T_1$ during all process of transformation ($\theta = 0$). Therefore the heat sources in eq. (1.27) are expressed as:

$$q_{tr}^{1-2-3} = -T_1 \Delta S_c (f_{m3} - f_{m1}) + \oint_{123} E'_{iq} \, df_m. \tag{1.28}$$

1.3.2.3 Case where $f_{m1} = f_{m3}$

When the martensite formed during forward transformation is totally recovered during reverse transformation, eq. (1.22) and (1.27) are simplified:

$$q_{tr}^{1-2-1} = -\oint_{121} E'_{iw} df_m + \oint_{121} W'_{mech} df_m, \tag{1.29}$$

and

$$q_{tr}^{1-2-1} = -\Delta S_c \oint_{121} \theta \, df_m + \oint_{121} E'_{iq} \, df_m. \tag{1.30}$$

For an isothermal transformation

When the temperature is constant $T = T_1$ during all process of transformation ($\theta = 0$), the heat sources in eq. (1.30) are expressed as:

$$q_{tr}^{1-2-1} = \oint_{121} E'_{iq}\, df_m. \tag{1.31}$$

The integration of the heat sources over an isothermal reversible phase transformation cycle at a constant temperature directly allows one to estimate the heat component of the irreversible dissipated energy.

This formalism will be used for different loading conditions. Clausius Clapeyron relationship will be investigated under quasi-isothermal condition in Section 4.4. Finally, cycling during homogeneous loading of tensile and shear tests will be investigated in Chapter 5.

CHAPTER 2

Full field kinematic and thermal measurements during mechanical tests

Table of contents

2.1 Introduction

Kinematic and thermal full-field measurement techniques are useful for studying thermal and mechanical coupling of materials and structures by using respectively visible light and infrared cameras. These full-field measurements have been used to study localized phenomena associated with plasticity (Lüders or Portevin Le Châtelier bands (Chrysochoos and Louche, 2000; Louche et al., 2005; Besnard et al., 2006; Avril et al., 2008), necking (Chrysochoos and Louche, 2000; Wattrisse et al., 2002)), with phase transformation (Pieczyska et al., 2004) and fracture. With these fields, it is possible to characterise the localisation (e.g., type, position, orientation, intensity, kinematics), and to analyse the physical mechanisms of these heterogeneities depending on the mode of deformation, velocity of the loading, and thermal condition during mechanical testing.

Although these two techniques seem very easy to implement with good cameras and image correlation software, quantitative measurements are not so easy to obtain. Many tricks, and small details can affect the image qualities and the numerical post processing. The aim of this section is to study most of them in order to help the future experimentalists and to justify quantitative measurements that will be given in Chapters 4 and 5. Kinematic full field measurement techniques and more specially Digital Image Correlation (DIC) will first be presented in Section 2.2. Then, an overview to allow for temperature measurements using

an infrared camera will be detailed in Section 2.3. Since these two techniques are used simultaneously, Section 2.4 presents tools we have developed to allow a temporal synchronisation of the data acquisitions (testing machine, infrared camera, visible camera) and a spatial synchronisation between kinematic and thermal fields. Finally, Section 2.5 presents a numerical software developed to estimate the heat sources from the temperature fields.

2.2 Displacement and strain fields measurements

Historically, displacement and strain fields measurements of SMAs have started using either multiple extensometers or a brittle coating. This oxide layer will then break in high deformation areas as presented in Figure 2.1. This technique is easy to use but gives only qualitative information,and is limited to loading.

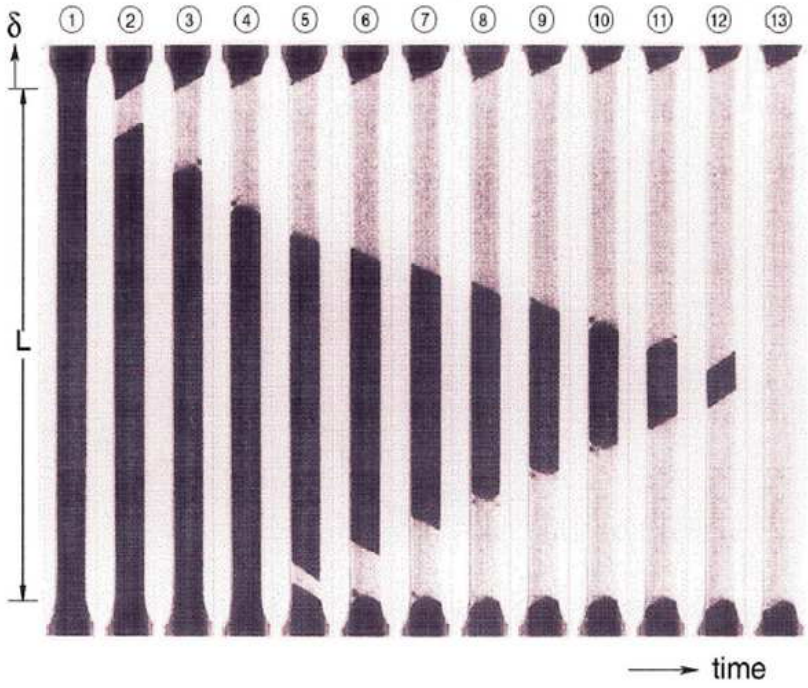

Figure 2.1: *Example of qualitative evolution of a localised strain field during a tensile test on shape memory alloys by taking photographies. The oxide layer coated on the material surface broke when the local strain was higher than 2 % (Shaw and Kyriakides, 1995)*

2.2.1 A brief review of strain field measurement techniques

Several kinematic full field measurement techniques exist and cover a wide range of applications. The choice of a technique is a compromise between several criteria such as experimental conditions, data expected (displacement, strain), range of measure (nano scale to kilometric ones), temporal and spatial resolutions, accuracy, method with or without contact, price, difficulty to setup.

Those techniques are especially useful in mechanical applications when the displacement and strain fields are heterogeneous (localisation, fracture). They can be classified by:

- the texture, natural or added on the surface,
- the algorithm to detect displacement or strain,
- the compromise between the resolution and the spatial resolution to be obtained.

2.2.1.1 Method using periodic textures

Those techniques, also called grid methods, use an identical texture (points or lines) repeating itself periodically on the surface. Depending on the method, it enables one to obtain the displacement field or even directly the strain field (spectral analysis). The main advantage of these techniques is that the spatial resolution is directly linked to the grid step.

Several algorithms are possible:

- The periodic textures can be analysed using Fourier transformation on sub domains of the image. Comparing the signal peaks before and after deformation enables to obtain the strain field components and solid rigid rotation for each sub-domain (Rajaona and Sulmont, 1985; Brémand et al., 1992; Rotinat et al., 2001). Such a method is semi-global since it allows to obtain local deformation without estimating the displacement field of the sub-domain. The strain field of the image is then obtained by scanning series of sub-domains.
- Another technique consists of using the moiré phenomena (Amidror, 1999). The moiré is an interference pattern created, for example, when two grids superimpose themselves and have a mesh size slightly different or are set with a small angle (Figure 2.2).

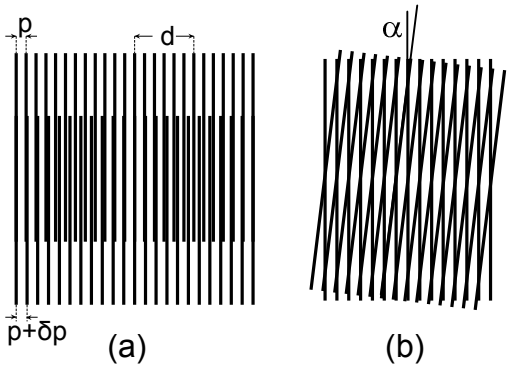

Figure 2.2: *Examples of moiré pattern for two sets of parallel lines. a) The two sets are parallel and the first set has a grid step of length p, the second set $p + \delta p$. b) The two sets have the same grid step p, one is inclined by a small angle with the other.*

The grids are made of lines usually parallel in mechanical applications (Parks, 1993). One of the grid is usually linked to the sample surface, the second one is fixed and transparent. Moiré fringes are then observed during deformation or rotation of the sample. They represent the isovalue of the strain field. This technique, very easy and

quick to set up, is still semi-global. The deformation is either obtained by counting the fringes manually or by using algorithm that increases the resolution.

The moiré phenomena can also use interferometry. The spatial resolution is higher especially when used with a phase-shift algorithm in post processing. But these techniques are difficult to use during in situ mechanical tests and need a vibration insulation and a complex optical setup.

2.2.1.2 Method using random patterns

Speckle pattern interferometry

Interferometry can also be used with random speckles. A coherent light (usualy laser light) reflecting on the surface in all directions will create interferometric figures, the comparison of these figures prior and after deformations enables to estimate displacement fields. These techniques are called electronic speckle pattern interferometry (EPSI) or holography. Once again, they are very sensitive to vibrations and most of the time they do not need any surface preparation.

Digital Image Correlation (DIC) method

The most common techniques using random texture are based on Digital Image Correlation (DIC), (Peters and Ranson, 1981; Sutton et al., 1983; Chu et al., 1985) see also the review in (Hild and Roux, 2006)). This method measures displacements on an object surface by comparing the surface morphology (grey levels) of two digital images prior and after deformation. The texture is either natural or created by spraying paint of different colors on the surface. In order to have a better accuracy, a small pattern (typically 4 to 50 pixels) called "subset" is taken instead of one pixel. The new position of the subset will be tracked by minimising a correlation factor C which is for example taken in 7D software (Vacher et al., 1999) as:

$$C = 1 - \frac{\sum_{i \in D} f(\underline{X_i}).g(\underline{x_i})}{\sqrt{\sum_{i \in D}(f(\underline{X_i}))^2}.\sqrt{\sum_{i \in D}(g(\underline{x_i}))^2}} \tag{2.1}$$

with:

- $\underline{X_i}$ the coordinates in the reference image of pixel number i
- $x_i = \phi(\underline{X_i})$ the coordinates in the image to correlate
- $f(\underline{X_i})$, $g(\underline{x_i}) = g(\phi(\underline{X_i}))$ the grey level respectively in the reference image and the image to correlate.
- D the subset domain. The initial shape of this domain is generally square.

To increase the accuracy, an iteration process is then implemented. The grey level interpolation that is chosen in the software 7D was bicubic and the strain fields were computed on the basis of bilinear expressions of the displacement distribution in the space that allows one to move and deform the subset during the iterative process, as presented in Figure 2.3.

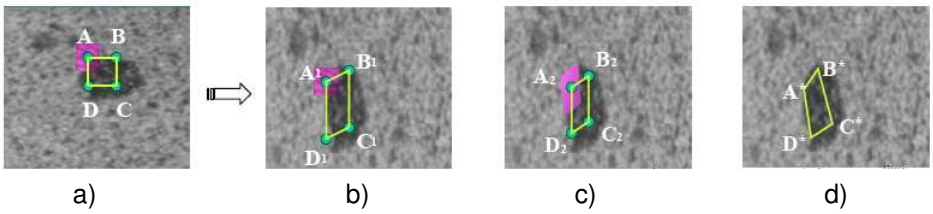

Figure 2.3: *Iteration process controlling the deformation of the subset: a) Initial image.b) Deformed image, 1^{st} iteration. c) Deformed image, 2^{nd} iteration. d) Deformed image, n^{th} iteration (Coudert, 2005).*

Each subset acts then like a small extensometer which is glued on the sample surface. Its gauge length is the subset size l_s. The subsets (up to 10,000) are usually set on a regular grid of step l_g, typically 10 to 40 pixels, as represented in Figure 2.4.

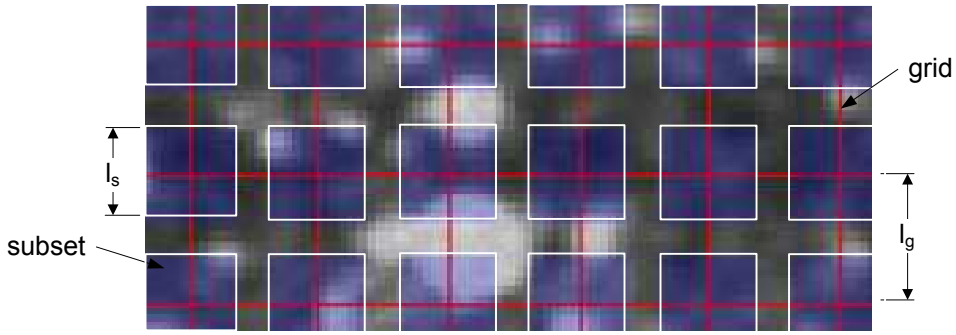

Figure 2.4: *Example of image correlation grid (red) of grid step $l_g = 14$ pixels and the subset (blue) of size l_s=10 pixels used during a DIC estimation.*

The grid (i.e. the positions of the small extensometers) is deformed, following the sample deformation as represented during a shear test in Figure 2.5. The plane component of the displacement $\overrightarrow{u}$ is then obtained for every material points on the subset grid. The Green Lagrange strain tensor $\underline{\underline{E}}$ in the plane is then estimated using:

$$\underline{\underline{\mathbf{E}}} = \frac{1}{2}(\underline{\underline{\mathbf{Grad}}}\ \overrightarrow{u} + \underline{\underline{\mathbf{Grad}}}^T \overrightarrow{u} + \underline{\underline{\mathbf{Grad}}}^T\ \overrightarrow{u} * \underline{\underline{\mathbf{Grad}}}\overrightarrow{u}) \tag{2.2}$$

where $\underline{\underline{\mathbf{Grad}}}$ is the gradient operator with respect to the initial coordinates.

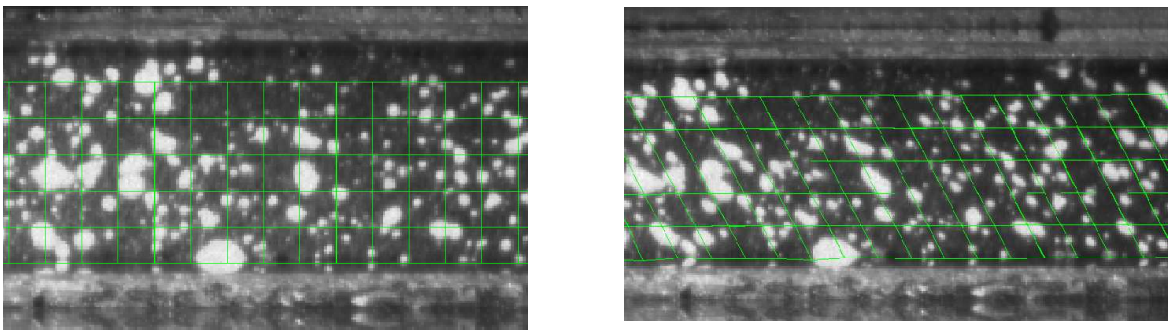

Figure 2.5: *Example of images correlation grid prior (a) and after deformation (b) during a shear test.*

The physical scale can vary from micrometers (Forquin et al., 2004) to meters (Chambon et al., 2005) depending upon the magnification of the images (taken using CCD camera or even standard camera) and the subset size. It is worth noting that the physical scale has a negligible impact on the correlation results.

Well adapted to our sample sizes, the strain amplitudes (0.01 % to 10 %) expected, the temporal resolution of our cameras (about ten or hundred frame per second) and the spatial resolution of the plane surface observed, the DIC method was chosen for its simplicity to use. The software used in all this work was 7D (Vacher et al., 1999; Vacher, 2003; Coudert, 2005).

2.2.2 Main experimental and numerical difficulties

Although this technique is much easier than other ones, special care needs to be taken when preparing samples. Parameters such as texture characteristics, lightening and size of the subset are important. They directly influence the accuracy of the estimated displacement fields.

Sample preparation

Sample preparation is crucial since the quality of the texture (random shape and size of the texture pattern, distribution, adhesion to the surface) directly affects the image correlation accuracy. The texture can be from different origins, namely, random scratches of the surface, grid etched on the material, paint, natural surface morphology of the sample, as presented in Figure 2.6.

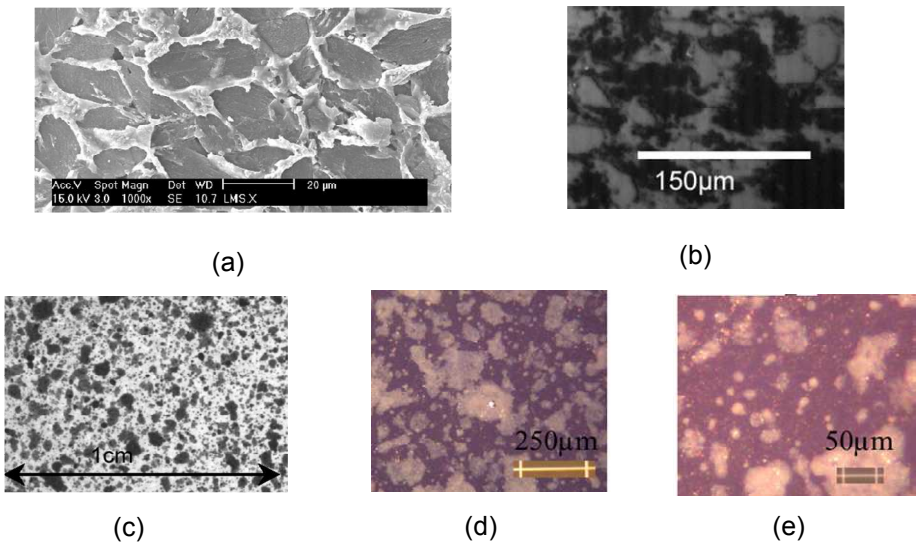

Figure 2.6: *Example of natural and artificial textures. (a) Biphasic Polymer. (b) Rock. (c-e) paint textures.*

Since the DIC software uses grey level color texture, it is important that the texture adheres to the surface during all the test. Therefore, the sample surface needs to be clean before coating (using aceton or white spirit). Because the paint often looses its elasticity after a long drying, the tests need therefore to be achieved soon after the sample preparation.

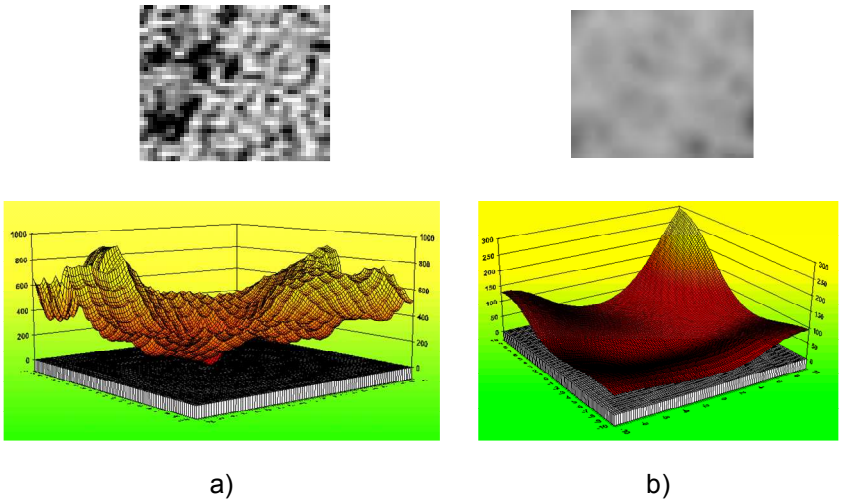

Figure 2.7: *Influence of the contrast on the image correlation factor. a) For an image with too much contrast. b) For an image without enough contrast.*

A special attention is also needed to obtain a well contrasted surface (Figure 2.7). In order to adapt the texture size to the camera resolution (ideally a texture of the size of 4 to 10 pixels), it is necessary to control the texture size. Several methods have been tried and used to obtain different texture sizes including spraying using the spray upside down, breaking the nozzle of the spray to have a bigger texture and using a toothbrush. It is strongly recommended to check the texture's pattern resolution and the image contrast before testing to make sure the image correlation will be able to correlate the images with a good accuracy.

Experimental set-up

The orientation of the visible camera needs to be perpendicular to the surface of the sample. The lightening has to be adjusted to avoid reflection or shadow on the sample (especially for tubular shape) and have a good contrast. Mat paint can be used to reduce reflexion of the light on the surface.

Influence of the subset size

The choice of the pattern size in the DIC software depends of the observed phenomena and the size of the texture. Strain profiles (Green Lagrange axial strain E_{xx}) during a localised tensile test on a NiTi tube obtained with different subset sizes are presented in Figure 2.8. The smaller the subset, the better strain gradient will be described, but with an increase of the uncertainty, as observed with the subset 4×4 in Figure 2.8. Increasing the subset size (subset 40×40) reduces the uncertainties but smoothen sharp strain gradients. Typically, the pattern size was chosen, between 5 to 40 pixels, in our experiments.

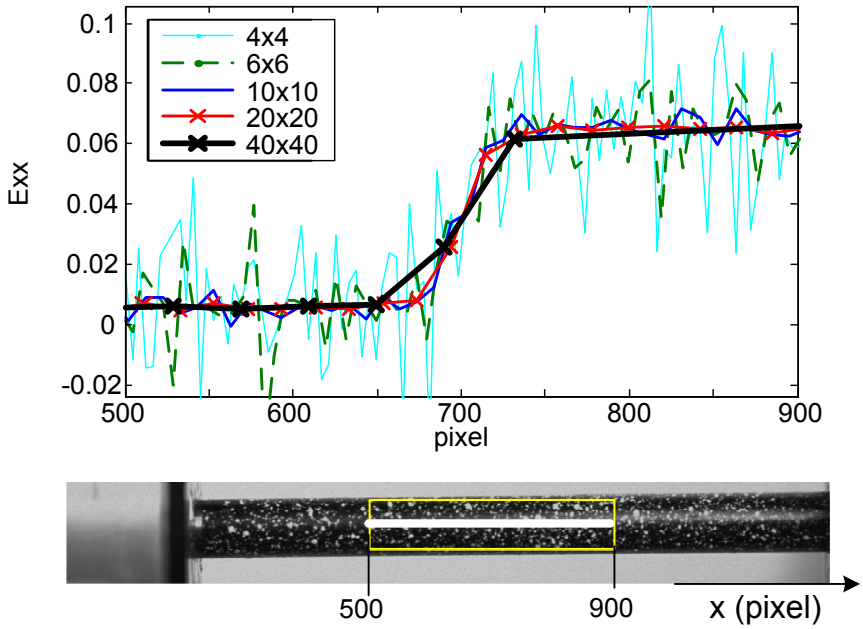

Figure 2.8: *Example of influence of the subset size on the accuracy of the strain. The white line on the picture represents the position of the profile.*

Origin of the uncertainties and consequences on the experimental set-up

The displacement accuracy of the DIC approach is typically 0.01 pixel for strain magnitude under 5% with a subset size of 12×12 pixels (Coudert, 2005; Louche et al., 2007). However, this value depends on many parameters, e.g. image quality, strain gradient and the order of the transformation describing the local deformation. There are different ways of evaluating a correlation accuracy.

a) Creating artificial pictures and applying known displacements to different "markers" of the picture. As all the conditions are known, it is possible to evaluate the error in terms of average, standard deviation. However, these artificial textures are not always representative of real situations.

b) Recording pictures prior to an experiment and applying rigid body motions. The displacement levels are not known. Yet the standard displacement and strain uncertainties can be estimated and should be as low as possible. The latter are usually lower bounds to the actual values (Coudert, 2005).

c) Recording a picture of the considered experiment and applying artificially known displacements. It allows one to estimate the performance associated with actual pictures considered in experiments (Coudert, 2005; Hild and Roux, 2006).

2.2.3 DIC method on tubes

DIC on tubular geometries induce some particular errors. The lighting is especially difficult to adjust. Placed in front of the sample, reflection may disturb the contrast of the image along the middle profile (cf. right endside of the tube in Figure 2.8). Placed on the side, part

of the sample will be in shadow. Moreover, the focus may not be good on the edges of the tube. In these areas, the camera is not perpendicular to the surface, so that the displacement in the radial direction is underestimated. For such sample geometry, stereo correlation or mirror could be used to avoid it.

2.3 Temperature fields measurements

2.3.1 Infrared thermography

As most technologies, infrared camera are based on phenomena discovered nearly 200 years ago. The infrared rays was first discovered by William Herschel in 1800. The first infrared camera was created in 1964 and firstly used for military purpose in the beginning of the 1980. This measurement technique is now more and more used in mechanics of materials to observe phase transformations (Shaw and Kyriakides, 1997; Iadicola and Shaw, 2002a; Pieczyska et al., 2004; Schlosser et al., 2007), plasticity phenomena (Louche, 1999; Chrysochoos and Louche, 2000; Louche and Chrysochoos, 2001; Louche et al., 2005) anf fatigue behaviour (Boulanger and Chrysochoos, 2004; Doudard et al., 2007).

An object at a temperature above 0 K produces a radiation. The radiation is an emission of energy from the surface. The infrared camera sensors measure instantaneously the thermal radiation of a scene and convert into a proportional tension that is then digitised into Digital Levels (DL). The infrared camera is calibrated to convert the measured DL on a black body into temperature (Figure 2.9).

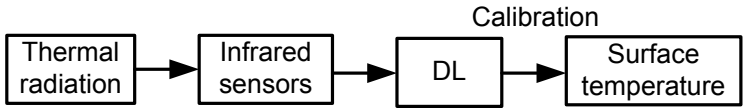

Figure 2.9: *Principle of IR measurement*

As for DIC, quantitative temperature field measurement are not so easy. Several parameters and conditions may disturb the measurement. The following section will present the main experimental and numerical difficulties to measure a temperature as close as possible to the material surface temperature.

2.3.2 Main experimental and numerical difficulties

Sample preparation and emissivity

An infrared camera does not directly measure the temperature from a scene but the radiation that appears to emanate from it. These radiations are due to the scene's self emission, path radiance and reflections that depend on the material surface emissivity. When a radiation is incident on an object the radiation can be either absorbed, transmitted or reflected as presented on the schematic view in Figure 2.10.

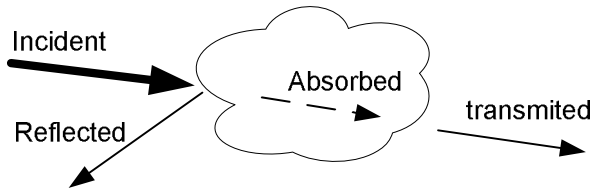

Figure 2.10: *Schematic view of the different forms of radiations.*

The emissivity factor ϵ represents the capacity of a body to absorb the light that fall on him. A black body is an ideal object that absorbs all light that falls on it whichever its wavelength and its direction. A black body has an emissivity of $\epsilon = 1$. Its radiations are only due to the self emission. Any real object would have $\epsilon < 1$. The infrared cameras are calibrated for a black body emissivity.

The emissivity of an object depends on many parameters:

- the chemical composition of the material,
- the wavelength,
- the observation angle of the camera toward the surface,
- the material temperature,
- the surface aspect of the material (polished, roughness, oxidised, painted).

A typical hypothesis (known as the grey body assumption) is to assume that a surface spectral emissivity and absorptivity do not depend on wavelength and on the temperature so that the emissivity is a constant. The Figure 2.11 presents typical emissivities of materials.

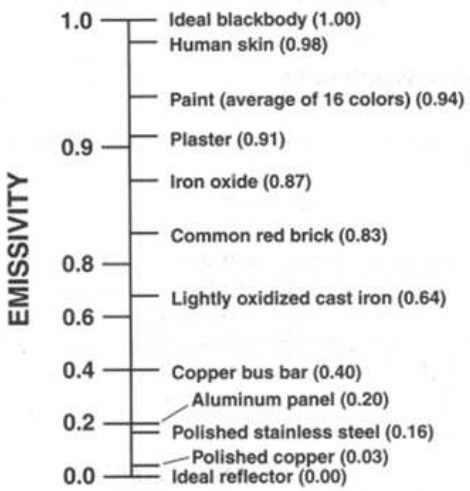

Figure 2.11: *Representatives emissivities. Note the expanded scale from 0.8 to 1 (Holst, 2000).*

In our case, most of the samples are either polished or covered by a thin layer of oxide. Therefore, samples were usually covered with a thin layer of a high emissivity paint before

experiment. This technique, widely used in thermography enables one to obtain grey body property with an emissivity > 0.9.

Moreover, due to our acquisition system, displacement fields (from DIC) also need to be obtained. As presented just above, the samples need to be homogeneously coated using a high emissivity paint, but they also need to present a random texture pattern for the visible images.

In case of a mechanical test, performed on a thin plate, if both deformation and temperature are identical on both sides of the sample and if the gripping system allows it, it is then possible to coat one side with an uniform high emissivity paint for the infrared camera and the other side a surface presenting a random texture (Wattrisse et al., 2002; Louche and Tabourot, 2004) for the visible camera. However, this kind of observation was not possible in our experiment because of the two particular situations:

- for tensile tests performed on NiTi tubular samples, the tube shape and the localised phenomena in NiTi are not adaptated to an observation on the two sides of the sample (Sun and Li, 2002; Favier et al., 2007; Schlosser et al., 2007).
- for shear test, design of the gripping system (Section 3.2.3) was not adapted to such observation.

Therefore, the two cameras observed the same area and the sample was painted using black and white paints.

An experimental procedure to estimate emissivity values and influence of the different coating is explained in Appendix A. This study has shown that: (i) the white paint has an emissivity lower than the black one and its emissivity decreases with the temperature (Figure A.2.d), (ii) a thin white texture on a black homogeneous surface does not affect the infrared measurements. Therefore, before the tensile tests, the samples will be painted in black with a white texture superimposed.

Experimental set-up and data acquisition

During infrared images acquisitions, the measured temperature is influenced by the environment condition (external heat sources, especially when the sample is not a black body) and camera orientation toward the scene. Several precautions need to be taken to limit these influences on the temperature measurement:

- The internal camera temperature that can vary from one test to another could drag the value of the Digital Level (DL). Since this influence is not taken into account in the calibration law of our camera, the camera was turned on at least 2 hours before testing in order to stabilise its temperature.
- Once the sample is mounted on the gripping system, the operator needs to wait until thermal equilibrium is reached again, between the sample and the gripping system, to start the test.
- It is recommended to operate in the dark or using a cold light (ex LEDs).

- Every part of the gripping system close to the sample should be covered with high emissivity paint in order to avoid reflection on the sample.

- The background of the observed area should be uniformed (using a black body or a white or black painted plate).

- The operator must not move behind the camera (the body heat can influence the sample temperature) during the tests.

Temperature measurements on tubes

The camera needs to be, as much as possible, perpendicular to the sample surface. Figure 2.12 presents the emissivity estimated on the radial direction, on a tube of radius r, a) as function of the infrared pixel given by the camera and b) as function of the angle. The emissivity is almost constant as long as the observation angle is below 45°, which agrees with known results (Pajani, 1989). Beyond, it decreases rapidly. In Figure 2.12.a, the edges of the sample are not obvious to detect. In consequence, in all this work, only the temperature of an area limited by an angle between the optical axis and the normal surface less than 45° will be considered.

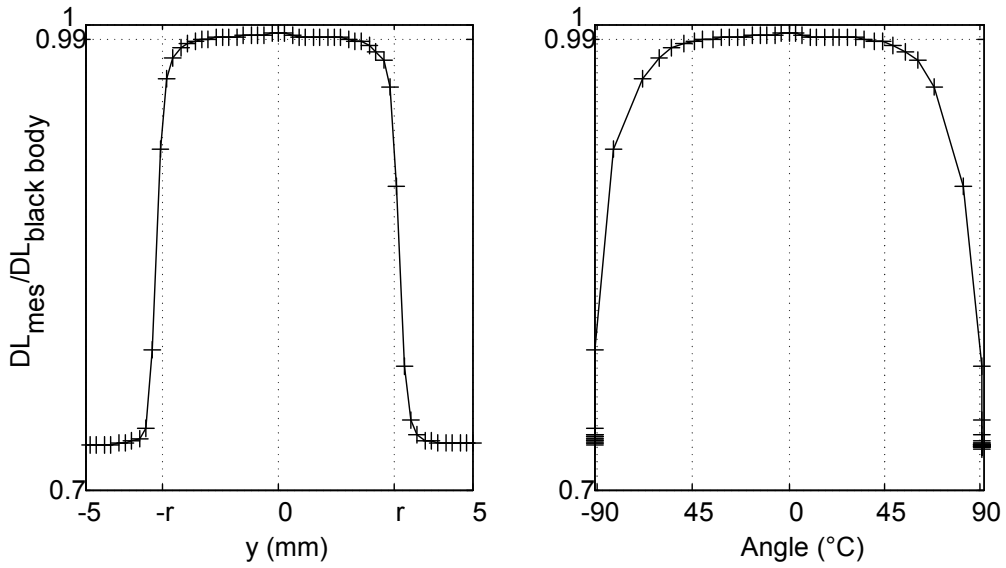

Figure 2.12: *Influence of the angle (between the optical axis and the normal surface) on the emissivity ($\epsilon = DL_{mes}/DL_{BlackBody}$). The tube was covered by a uniform black paint and constant temperature was imposed inside the tube.*

2.4 Simultaneous temperature and strain field measurements

2.4.1 Experimental set-up and issues

During the test, several data were recorded through different acquisition set-ups (Figure 2.13), using different temporal and spatial resolutions.

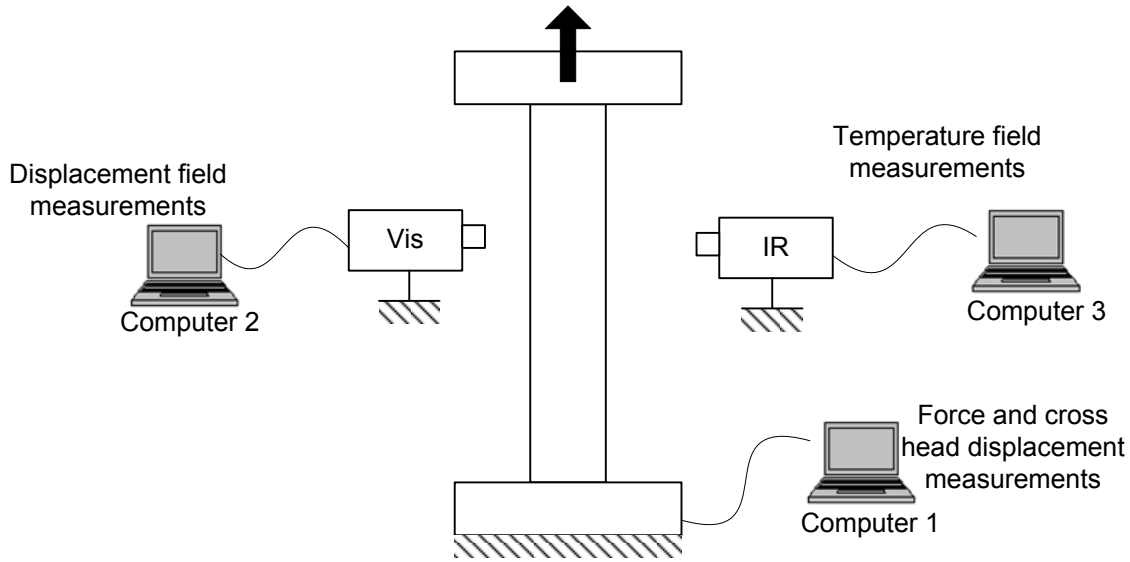

Figure 2.13: *Schematic view of the three acquisition systems.*

Usually, three acquisition systems were used:

- **Computer 1:** Mechanical data (force and cross head displacement) given by the testing machine. It started at the time t_{0mech} (beginning of the test, see Figure 2.4), at an acquisition frequency f_{mech}.
- **Computer 2:** Visible images acquired by a CCD camera. Those images were then used by a DIC software (7D) to obtain the displacement and strain fields. Because the DIC software estimated the displacement fields by reference to an initial image taken before the beginning of the test, the visible camera had either to start at time t_{0V} before the test. The visible image acquisition frequency was denoted by f_V.
- **Computer 3:** Infrared images acquired at frequency f_{IR} by an infrared camera. Once again the camera needed to be started at time $t_{0IR} < t_{0mech}$. At least 10 images have to be recorded before the beginning of the test to estimate initial sample temperature field T_0.

In order to obtain, for material points, at the same time, the kinematic field, the temperature field and the mechanical data, both temporal and spatial synchronisations of the data are necessary. First, the temporal synchronisation needs to be achieved in order to compare the signals at the same time. The method used for this synchronisation will be presented in the following section. Once this temporal synchronisation is achieved, a spatial synchronisation

can also be done to obtain the temperature field for material points. This synchronisation will be presented in Section 2.4.3.

2.4.2 Temporal synchronisation

2.4.2.1 Issue and principles of the temporal synchronisation

The different values for the frequencies and initial times are plotted in Figure 2.14.

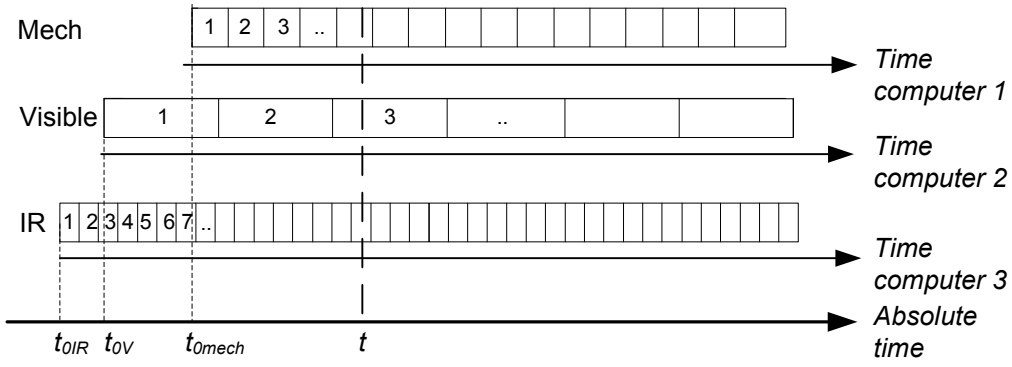

Figure 2.14: *Representation of the three acquisition data, with the time evolution.*

Usually, the time bases of each computer are independent. It was then often difficult to achieve, with a good accuracy, a correspondence between the kinematic field, the temperature field and the usual mechanical data. Moreover, such situation was enhanced if the frequency acquisitions were different from each other and/or transient phenomena were observed.

To get around this problem, two methods are possible. First, a software solution managing non-synchronised data, second, a hardware solution controlling directly the acquisitions.

2.4.2.2 Software synchronisation

Like the synchronisation of images and sound in movies, the software synchronisation was post processed. It synchronised, after the acquisitions, the three time bases. A characteristic event needed to be found both in visible and infrared images (beginning of loading, end of loading, end of the test, beginning of localisation). When the sample frequencies were different, temporal interpolations between the three time bases were necessary to make them correspond (Figure 2.14). The software synchronisation was limited by the difficulty of identifying a characteristic event and the limit of the performances of our visible camera (up to 24Hz) compared with the infrared camera (up to 145Hz). This problem was avoided with the hardware synchronisation presented in the following subsection.

2.4.2.3 Hardware synchronisation

Another computer, set as master, triggered off (via Labview software), the other acquisition systems through a TTL signal (Figure 2.15). As shown in Figure 2.16, two alternatives are then possible:

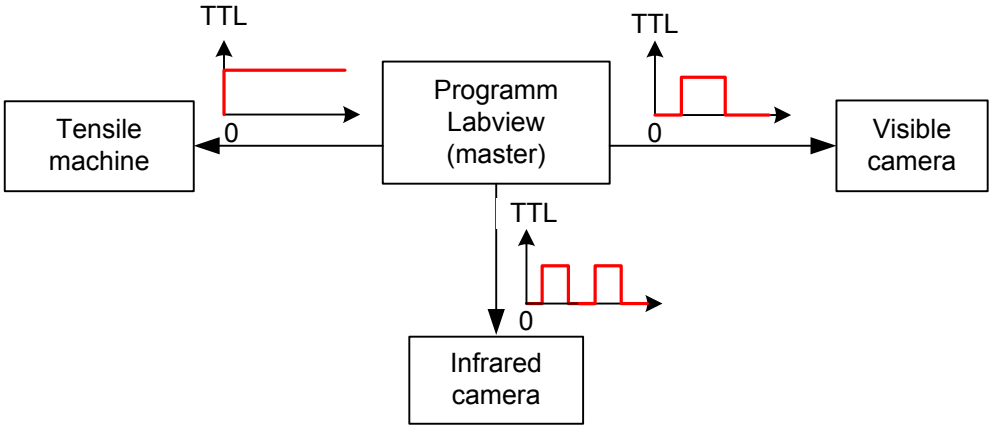

Figure 2.15: *Schematic view of the link between each acquisition with the different TTL signals used to trigger off the different data system from a unique master clock.*

1. starting the three acquisition systems at the same time ($t_{0mech} = t_{0V} = t_{0IR}$) and with the same acquisition frequencies ($f_{mech} = f_V = f_{IR}$) as represented in Figure 2.16.a.

2. starting the three acquisition systems at the same time ($t_{0mech} = t_{0V} = t_{0IR}$) but with different acquisition frequencies ($f_{mech} \neq f_V \neq f_{IR}$) as represented in Figure 2.16.b. In that case, comparison of the data at given time requires an interpolation of the data.

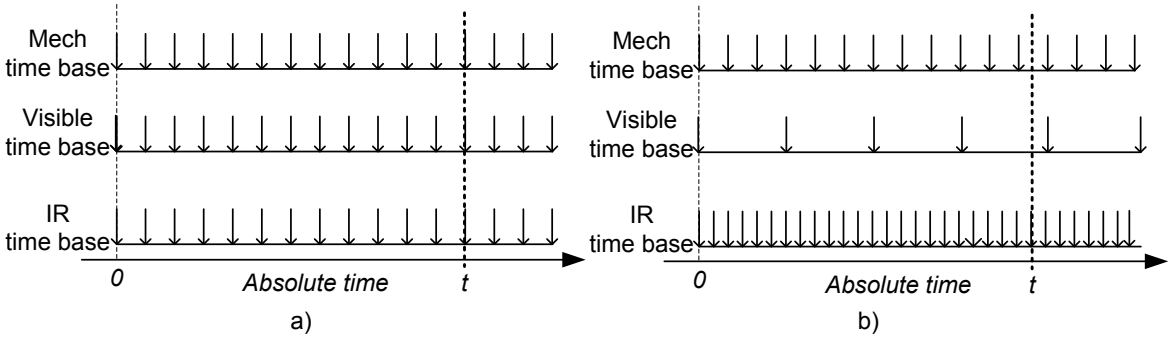

Figure 2.16: *Example of two sets of acquisition synchronisation starting at the same time. a) With the same acquisition frequencies. b) With different acquisition frequencies.*

2.4.2.4 Conclusion on the temporal synchronisation

Whichever the method of temporal synchronisation, the three kinds of data (mechanical, kinematic and thermal fields) could be obtained at the same time. As this temporal synchronisation requires acquisition interpolation, the accuracy of the data is improved by decreasing

the data frequency. In our experimental set-up, the lowest frequency is the visible one. For a time basis with the highest frequency (infrared one), more data will be available but with the risk of error due to temporal interpolations. Choosing one or another time basis depended on the use of the data.

2.4.3 Spatial synchronization

2.4.3.1 Issues and principles of the spatial synchronization

Once the temporal synchronisation was achieved, we now proceed to a spatial synchronisation of the data. The kinematic fields (displacements, strains) are obtained, via the software 7D, on the initial (Lagrangian or material) configuration, or in the final (Eulerian or spatial) configuration. The infrared camera was fixed and observed the material points which can move towards the fixed observation area. The temperature fields were then given as functions of spatial coordinates: $T(Nx, Ny, t)$.

Initially, three coordinates system (or virtual grid) were available :

- **CS-V:** Visible images coordinate system, typically with a resolution of 1280×1024 pixels.
- **CS-7D:** The DIC coordinate system given by 7D. Using a virtual grid on the visible image, every $n = 10$ pixels, the resolution in the two directions was then divided by a factor of n. The maximum resolution was then 128×102 pixels.
- **CS-IR:** The infrared image coordinate system with a maximum resolution of 320×240 pixels.

The kinematic and thermal fields were respectively given in the coordinate system CS-7D and CS-IR. The synchronisation can be achieved by following two routes:

- **The reference coordinates were CS-7D:** The temperature field, at each time, was then projected onto CS-7D frame. The kinematics and temperature fields were then expressed in the CS-7D frame.
- **The reference coordinates were CS-IR:** The displacement and strain fields, at each time, were then projected onto CS-IR frame. The kinematic field and temperature field were then expressed in the CS-IR frame.

The spatial synchronisation in CS-7D is interesting in order to know the temperature evolution of a particle P ($T(P, t)$) which is not possible with only one infrared camera. This is the same as having virtual small thermocouples glued on the surface at the same position than the virtual DIC extensometer. It is especially useful if the sample moves toward the camera (rigid body motion at the beginning of a test), or is deformed (especially in case of large or localised deformations). Figure 2.17 represents the evolution of two selected particles A and B on a typical sample deformed at 8% of strain. The particle A was in the bottom of the sample, close to the gripping system, its vertical displacement is small. The second

particle, (B) was close to the moving grip and its typical vertical displacement could go up to $(u_x)_{maxi} = 23$ pixels (in CS-V) which was not negligible anymore during a 8% strain. At the beginning of loading, a rigid body motion occurred of about $u_x = 4$ pixels and $u_y = -3$ pixels.

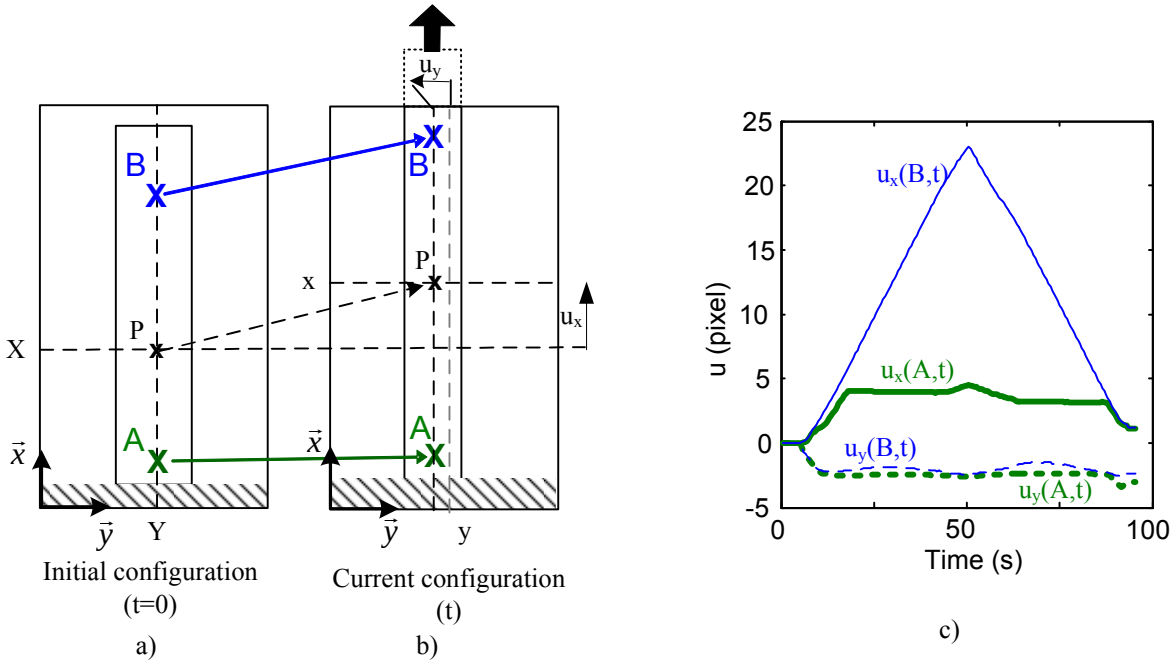

Figure 2.17: *Schematic view of the sample during a tensile test in an initial configuration (a) and on the current configuration (b). The initial and current coordinates of the material points A, B, P are (X,Y) and (x,y) respectively. c) Example of an experimental change of the horizontal (u_y) and vertical (u_x) displacement (in infrared pixel) for points A and B. At the beginning, both points moved together, due to rigid body motion.*

Moreover, with the spatial synchronisation, it is possible:

- To be more accurate when calculating the temperature variation. Without spatial synchronisation, the temperature variation will be estimate using $\theta^0(Nx, Ny, t) = T(Nx, Ny, t) - T(Nx, Ny, 0)$. Initial temperature field on the sample may not be homogenous ($T(x, y, 0) \neq T_0 = cte$) either if a temperature gradient (less than 0.5 K) is observed on the sample (due to the boundary conditions and the griping system); or if the emissivity is not constant (e.g. tube). Moreover, if during the measurement there is a displacement of the material points (rigid body motion or deformation), estimating the temperature variation using $\theta^0(Nx, Ny, 0)$ can induce errors. Indeed, the temperature variation should be estimated for a particle P using $\theta(P, t) = T(P, t) - T(P, 0) = T(x, y, t) - T(NX, NY, 0)$, where NX and NY were the initial coordinates of the spatial point (x, y) observed at instant t.
- To obtain heat sources and corresponding energies, at a material point, by integrating over time (more details are given in Section 2.5).

This section will first present the method used to estimate, for any material point, the strain state, the absolute temperature, and the relative temperature of each initial pixel chosen either on the infrared image or in the visible one. Then, two benchmarks will be presented

to check the validity of the spatial synchronisation. Finally, the limits and the difficulties of this method will be presented.

2.4.3.2 Method used for spatial synchronisation

The two cameras need both to be fixed during the measurement and to observe the sample with the same orientation. Miss orientation could induce error of position during the synchronisation. The two coordinate systems, initially independent, are spatially linked choosing two reference points at the same initiated time $t_0 = 0$, on the visible and on the infrared images.

The initial spatial position of any particle $P(X_V, X_V)$ on the visible image (Figure 2.18.a) can then be linked to its spatial position (X_{IR}, X_{IR}) on the infrared image (Figure 2.18.b) using a rotation of an angle α, a translation vector $\overrightarrow{T} = (T_x, T_y)$, and a homothetic transformation k to change the scale.

The transformation matrix $\underline{\underline{\mathbf{v2ir}}}$ allows to go from the visible to the infrared description with:

$$\begin{pmatrix} X_{IR} \\ Y_{IR} \\ 1 \end{pmatrix} = k. \begin{pmatrix} cos(\alpha) & sin(\alpha) & 0 \\ -sin(\alpha) & cos(\alpha) & 0 \end{pmatrix} . \begin{pmatrix} X_V \\ Y_V \\ 1 \end{pmatrix} + \begin{pmatrix} T_x \\ T_y \\ 0 \end{pmatrix} = \underline{\underline{\mathbf{v2ir}}}. \begin{pmatrix} X_V \\ Y_V \\ 1 \end{pmatrix} \tag{2.3}$$

with:

$$\underline{\underline{\mathbf{v2ir}}} = \begin{pmatrix} k.cos(\alpha) & k.sin(\alpha) & T_x \\ -k.sin(\alpha) & k.cos(\alpha) & T_y \\ 0 & 0 & 1 \end{pmatrix} \tag{2.4}$$

Conversely, the matrix $\underline{\underline{\mathbf{ir2v}}}$ enables one to obtain the position in the visible system from the infrared one:

$$\underline{\underline{\mathbf{ir2v}}} = \underline{\underline{\mathbf{v2ir}}}^{-1} \tag{2.5}$$

Theoretically, only two sets of initial position of two particles on the visible ($V_1 = (X_{V1}, Y_{V1})$, $V_2 = (X_{V2}, Y_{V2})$) and infrared ($IR_1 = (X_{IR1}, Y_{IR1})$, $IR_2 = (X_{IR2}, Y_{IR2})$) images, at the initial time, are necessary to estimate the four parameters (k, α, T_x, T_y) of the transformation matrix. The homothetic transformation k is estimated with the ratio of length:

$$k = \frac{\| \overrightarrow{IR_1IR_2} \|}{\| \overrightarrow{V_1V_2} \|}. \tag{2.6}$$

The transformation angle α is estimated by the angle between the two vectors:

$$\alpha = (\overrightarrow{IR_1IR_2}, \overrightarrow{V_1V_2}) \tag{2.7}$$

Finally the translation vector $\overrightarrow{T} = (T_x, T_y)$ is estimated by solving:

$$\begin{pmatrix} T_x \\ T_y \end{pmatrix} = k. \begin{pmatrix} cos(\alpha) & sin(\alpha) \\ -sin(\alpha) & cos(\alpha) \end{pmatrix} . \begin{pmatrix} X_V \\ Y_V \end{pmatrix} - \begin{pmatrix} X_{IR} \\ Y_{IR} \end{pmatrix} . \tag{2.8}$$

As represented in Figure 2.19, the position (x_{IR}, y_{IR}, t) of a particle P at time t in the infrared coordinate system is achieved in three steps:

1. Link, at the initial time, between the infrared and visible initial coordinates with:

$$\begin{pmatrix} X_V \\ Y_V \end{pmatrix} = \underline{\underline{\mathbf{ir2v}}} \cdot \begin{pmatrix} X_{IR} \\ Y_{IR} \end{pmatrix}. \tag{2.9}$$

2. Link between the first and the current visible image (time t) using DIC. Estimation of the new position of the particle P in the visible coordinate system: $x_V(X, Y, t)$ and $y_V(X, Y, t)$.

3. Link, at the time t, between the final coordinates on the visible image (x_V, y_V) and on the infrared image (x_{IR}, y_{IR}) using the transformation matrix $\underline{\underline{\mathbf{v2ir}}}$.

$$\begin{pmatrix} x_{IR} \\ y_{IR} \end{pmatrix} = \underline{\underline{\mathbf{v2ir}}} \cdot \begin{pmatrix} x_V \\ y_V \end{pmatrix}. \tag{2.10}$$

For example, at time t (Figure 2.19) the axial displacement of the point P_{IR}, in the CS-IR, is 9.5 pixels.

2.4.3.3 Numerical procedure to go from one to another resolution and origin of errors

DIC used herein allows one to estimate displacements only on discrete material points P_{7D} of the DIC grid. With the transformation matrix $\underline{\underline{\mathbf{v2ir}}}$, it is possible to express the initial $(X_{IR}, Y_{IR})_{7D}$ and final $(x_{IR}, x_{IR})_{7D}$ coordinates of P on the infrared image. Quite often, the DIC resolution is less fine than the infrared resolution, as presented in Figure 2.20. The coordinates of the temperature grid $(X_{IR}, Y_{IR})_{IR}$ are then obtained using a linear or bi-cubic interpolation of the extensometer grid $(X_{IR}, Y_{IR})_{7D}$ previously obtained at every acquisition. The temperature field T, and Green-Lagrange strain fields are then known for every material point in both spatial coordinate systems.

2.4.3.4 Verification of the synchronisation using experimental benchmarks

Plate with three white dots

The first experimental benchmark was a plate with three white dots. The emissivity of a white paint is lower than a black paint, therefore the measured temperature of the dots are lower. These white dots can be observed by the visible and by the infrared cameras. The plate was mounted on the upper grip of a tensile machine that moved up at a constant velocity. Figure 2.21 shows the position of these three points at two different times on the visible and infrared images.

Figure 2.22 shows the temperature field projected on the image correlation grid of the visible image, at two different times. The position of the hole in the temperature field corresponded well to the white dots since at these points the image correlation was not possible (no contrast).

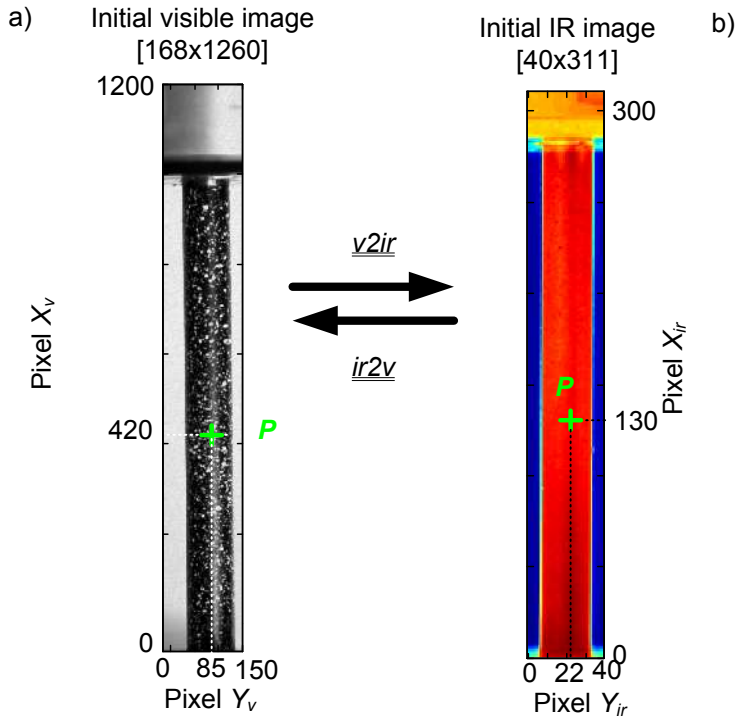

Figure 2.18: *Schematic of the spatial synchronisations at initial time. a) Visible image at initial time. Selection of a particle P of coordinates (X_V, Y_V). b) Infrared image at the same initial time. Representation of the position, of the same particle P, on the infrared image using the transformation matrix* $\underline{\underline{\mathbf{v2ir}}}$ *to go from the visible coordinates to the infrared ones (X_{IR}, Y_{IR}). The resolution was 168×1260 pixels on the visible image and 40×311 pixels on the infrared image.*

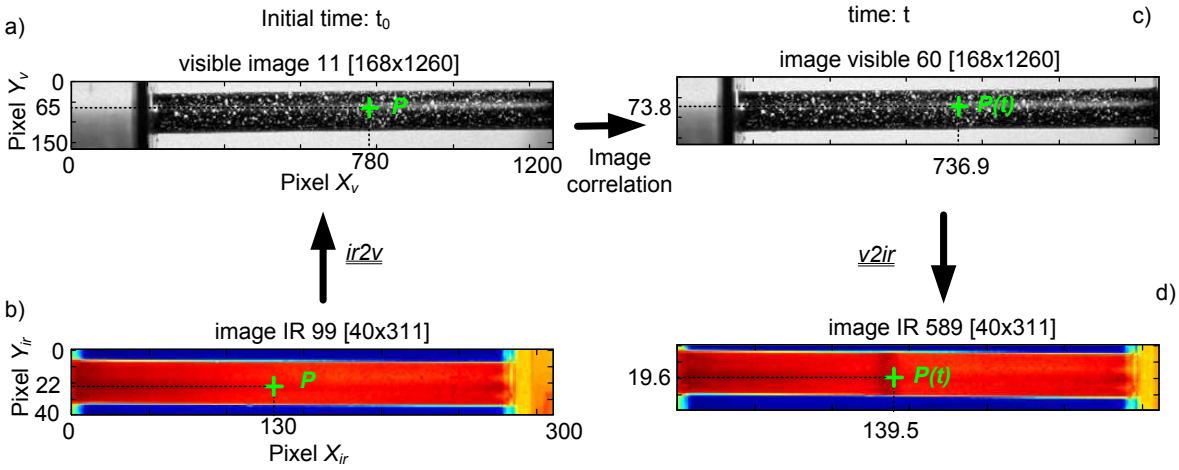

Figure 2.19: *Schematic view of the spatial synchronisation. a) visible image at the initial time corresponding to the frame 11. Selection of particle Pi_{0V}. b) Infrared image at the same initial time corresponding to frame 99. Representation of the position of particle Pi_{0V} on the infrared image using the transformation matrix* $\underline{\underline{\mathbf{v2ir}}}$ *to go from the visible coordinates to the infrared ones. c) Visible image after deformation at the time t corresponding to the visible frame 60. New position of the particle $Pi_V(t)$ obtained using image correlation. d) Infrared frame 599 corresponding to the time t and material position of the particle $Pi_{IR}(t)$ using the transformation matrix $\overline{OPi}_{IR}(t) = \underline{\underline{\mathbf{v2ir}}}\overline{OPi}_V(t)$. The visible images are represented on the visible resolution 168×1260 pixels and the infrared image on the infrared resolution (40×311 pixels)*

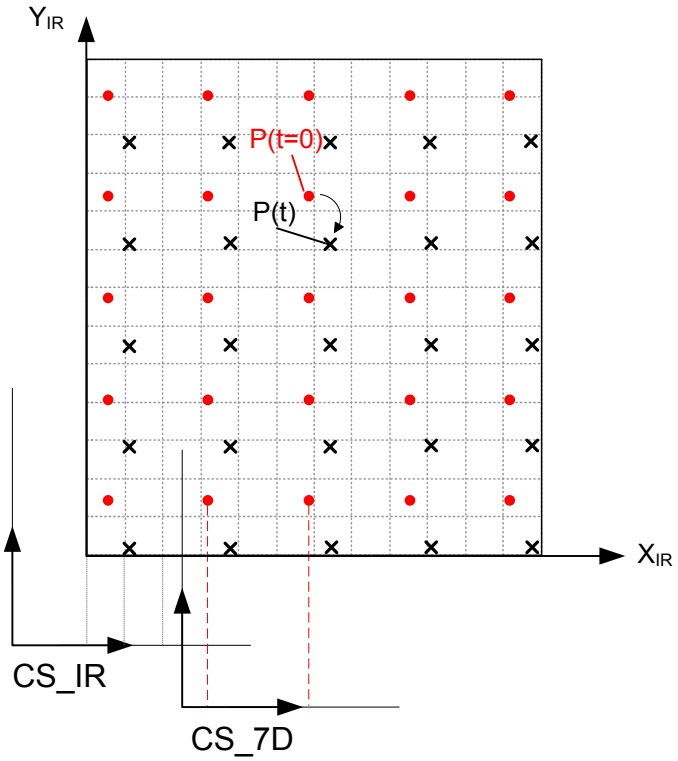

Figure 2.20: *Representation of the discrete motion of point P_{7D} of initial infrared coordinate $(X_{IR}, Y_{IR})_{7D}$ represented with red • and of the final coordinates $(x_{IR}, v_{IR})_{7D}$ represented with black ×. The temperature field is measured at the intersection of the IR grid represented with grey dashed lines.*

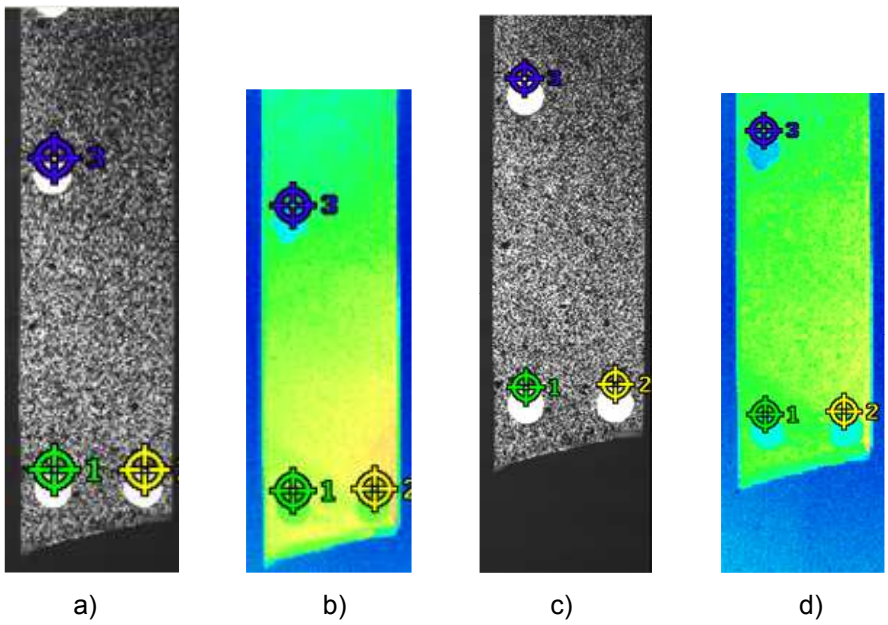

Figure 2.21: *Position of the three characteristic points using white dots having different emissivity (cf section 2.3.2); at the initial time: a) on the visible image and b) on the infrared image; and at a time t, c) and d) respectively.*

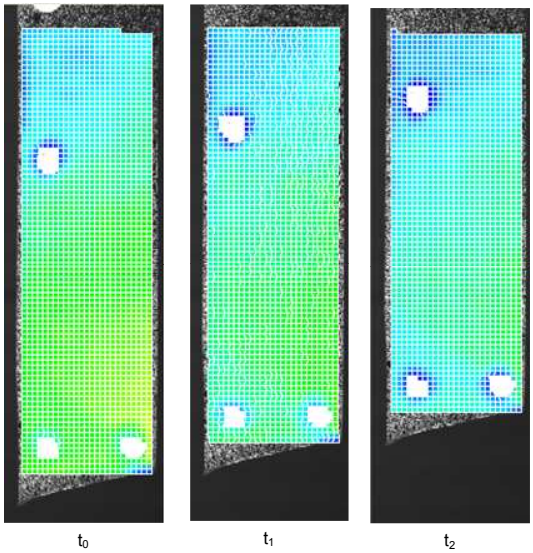

Figure 2.22: *Representation of the temperature field on the visible image at the initial time t_0 and at two other times t_1 and t_2.*

Application of synchronisation on a NiTi SMA tube

A tensile test was performed on a superelastic NiTi tube with hot water (315 K) circulating inside. The experimental set-up is presented in Section 3.2.2.2, the material used in Section 3.1.3.3. During the tensile test, the strain field was strongly localised due to a martensitic phase transformation (e.g. Section 1.2.3). Since martensite phase transformation is exothermic, it increases locally the temperature of the tube. These localised temperature and strain fields induced during this test offered an interesting example to validate the spatio-temporal synchronisation.

Position of characteristic points The choice of characteristic points is crucial for the quality of the spatial synchronisation. The edges of the sample could be used. However in some cases these edges are badly defined in infrared images since the emissivity of the tube decreases as the angle is above 45° (Figure 2.12) and often the gripping system reflects itself into the sample in infrared view. Thus the limit between the sample and the grip is not obvious. We have developed a solution by taking two images prior the test, by using a steel ruler whose graduations are well contrasted on the visible and on the infrared images as presented in Figure 2.23. The positions of characteristic points are estimated using the ruler.

Influence on the estimation of θ Figure 2.24 shows the Green-Lagrange strain component E_{xx} and the temperature variations with and without taking into account the spatial synchronisation, respectively denoted by θ and θ^0. These two last fields were projected onto the image correlation grid. For each spatial point $M(x, y, t)$, of initial coordinate (X, Y), the temperature variation before the spatial synchronisation $\theta^0(t)$ is calculated as:

$$\theta^0(t) = T(x, y, t) - T(x, y, 0) \tag{2.11}$$

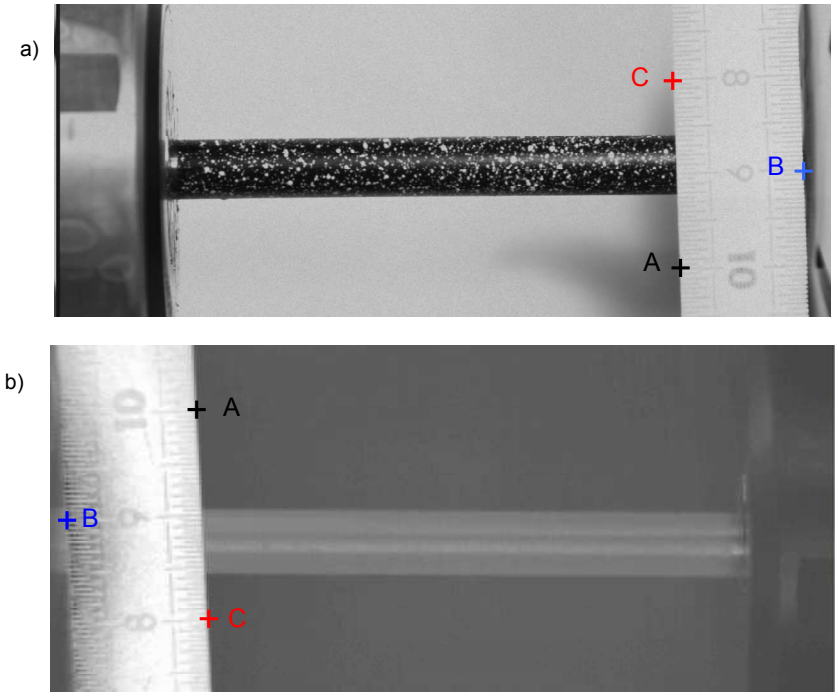

Figure 2.23: *Sample and steel ruler view, prior the test, on the visible image (a) and on the infrared image (b). A grey colormap was used. Three characteristic points (A, B and C) were selected for each image on the ruler. The two images were rotated by 180° due to the position of the two cameras.*

whereas, after the spatial synchronisation θ is given by:

$$\theta(t) = T(x, y, t) - T(X, Y, 0). \tag{2.12}$$

The comparison of the temperature variation in Figure 2.24.b and 2.24.c shows that the temperature peak matches the strain distribution only after the spatial synchronisation and emphasises the importance of this process. To better analyse the influence, two points plotted in green and blue have been selected. The first one (in green) was close to the fixed grip. Its displacement during the tensile test was not very high. The second point (blue) was close to the moving grip. Therefore, its displacement was more important and went up to 20 pixels along the tensile axis as presented in green in Figure 2.25.

Temporal change of displacement and temperature variations of the two selected particles A and B are plotted in Figure 2.26. Since the displacement during the tensile test of the first particle A (green) was not very important (maximum of 5.1 pixels) there was not much difference between the temperature variation of the spatial $\theta^0(t)$ and material $\theta(t)$ points. Both positions and intensity of temperature peaks were similar without and with spatial synchronisation (Figure 2.26.c and 2.26.d respectively). To the contrary, for the particle B (blue) where the displacement is higher, this is not negligible anymore. At the end of the loading, the displacement goes up to 21 pixels. Without any spatial synchronisation, the peak temperature seemed to appear before the strain localisation whereas as the physics will predict it, the temperature peak is expected to appear at the same time. When the spatial synchronisation is used (Figure 2.26.d), both thermal and kinematic phenomena appeared at the same time.

The impact of the spatial synchronisation is not only important to better track the position of the phenomena but also on the estimation of the temperature variation. Even if the sample is

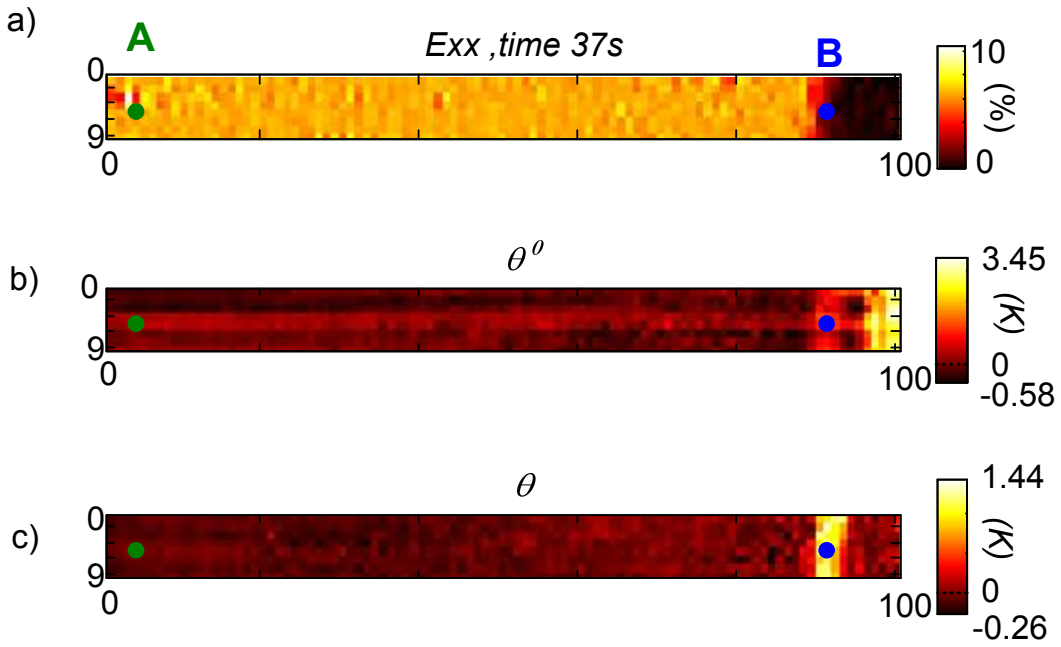

Figure 2.24: *a) Axial component of the Green-Lagrange strain E_{xx} measured at the surface during a tensile test on a NiTi tube sample. Temperature variation at the same time prior to (θ^0, b) and after (θ, c) the spatial synchronisation. The fixed grip was on the left and the moving grip on the right. The fields in images a) to c) are respectively plotted in the initial, final and initial configuration. The round green and blue markers show the fixed positions of the material points in their initial position.*

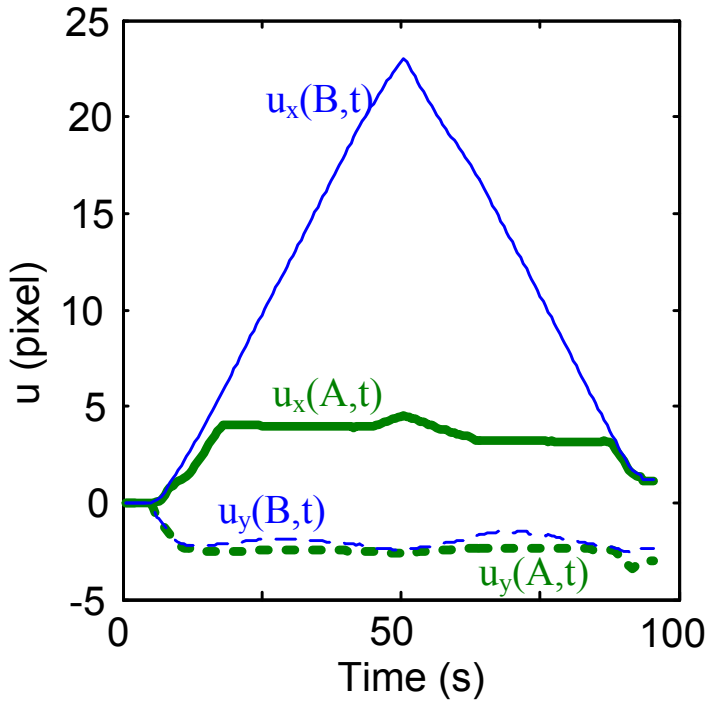

Figure 2.25: *Displacement (in CS-IR) along the tensile axis of the two particles A and B selected in Figure 2.24.a. The green thick line corresponds to A (green), close to the fixed grip, and the blue thin line to the B, close to the moving grip.*

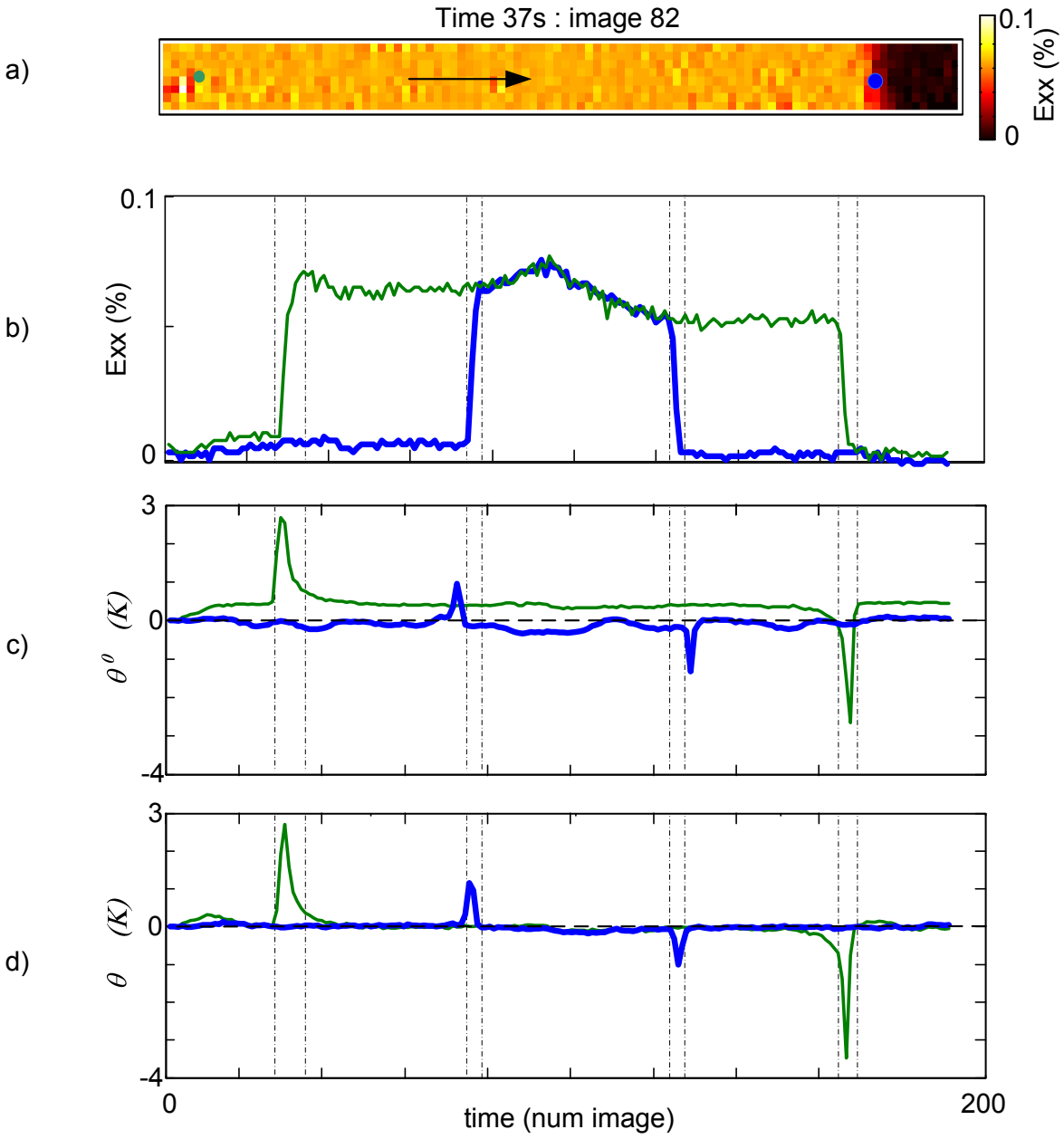

Figure 2.26: *a) Green Lagrange E_{xx} strain field on the tube sample at time 37 s. The fixed grip was on the left, the moving grip on the right. The arrow shows the direction taken by the localisation front during the mechanical loading. b) Time evolution of E_{xx} for the two selected points, one close to the fixed grip (green), the other one close to the moving grip (blue). c) Temperature variation θ^0 of the two selected points without spatial synchronisation (using eq. (2.11)). d) Temperature variation θ of the same points when taking into account the spatial synchronisation (using eq. (2.12)). The vertical lines mark the beginning and the end of the localisation front on the strain field.*

mounted on the grips a long time before starting the experiment, it is very difficult to obtain an homogeneous temperature along the sample. Moreover, for tubular geometries, radial displacement due to rigid body motion at the beginning of the test may induce errors on θ^0 estimation since the temperature field is not constant in the radial direction (emissivity not constant). Therefore $\theta \neq \theta^0$. Figure 2.26 shows that with the spatial synchronisation, the there is no variation of temperature except for the temperature peak, this was not the case without synchronisation. The position of the two peaks superimposed themselves since the abscissa were X_{IR} for θ^0 and x_{IR} for θ.

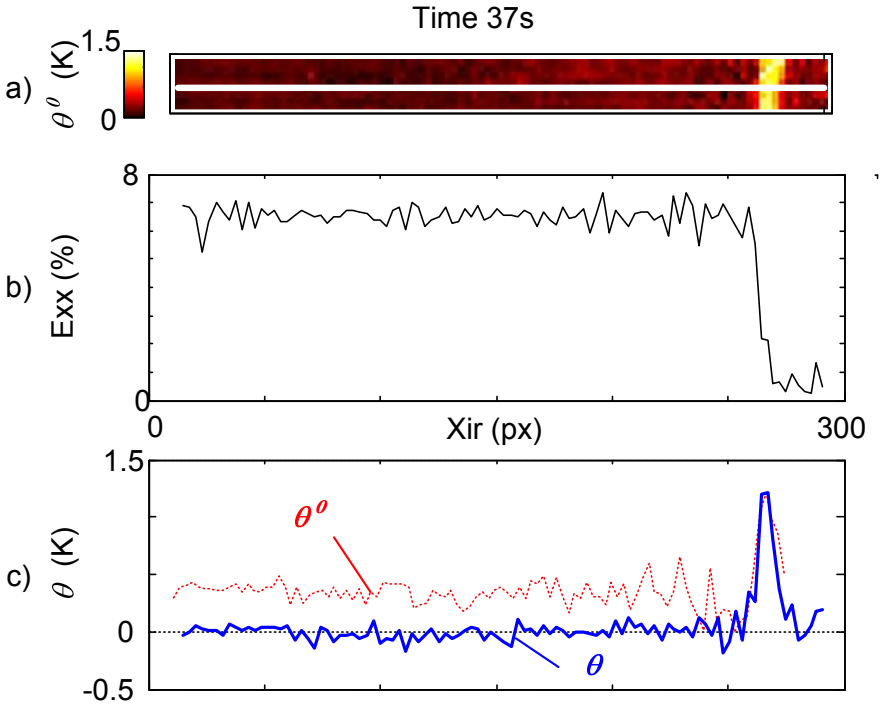

Figure 2.27: *a) Temperature variation estimated with the spatial synchronisation at the same time as Figure 2.26. b) Green-Lagrange strain field along the selected line plot in white on a). c) Temperature variation profile, estimated without spatial synchronisation (spatial points, $\theta^0(x,y,t) = T(x,y,t) - T(x,y,0)$, red dot line), and with the spatial synchronisation (material point, $\theta(x,y,t) = T(x,y,t) - T(X,Y,0)$, blue thick line) as functions of the spatial points.*

2.4.3.5 Factors influencing the accuracy of the measurements

Many parameters may influence the accuracy:

- **position of the cameras:** with our experimental set-up, the two cameras cannot observe the sample from the same orientation. The visible camera has to be perpendicular to the sample to perform DIC. The infrared camera must not be set with an angle higher than 45° to have a constant emissivity. If the two cameras are set with an angle in the x direction some error of position toward the x direction will be made. One solution could be to use semi transparent lens.

- **estimation of v2ir and ir2v:** the position of a point is only known with an accuracy of one pixel. It is not always easy to locate a characteristic point on the infrared images.

To reduce this uncertainty, the estimation of the transformation matrix is done (i) using as many characteristic points as possible and (ii) by averaging the values of the matrix components in order to reduce the errors.

- **DIC estimation:** DIC errors can induce error during the estimation of the displacement of the particle.

- **interpolation error during the temporal interpolation:** in a mechanical test at constant velocity, the displacement is linear except around an area where the strain field is localised. In these cases, linear interpolations, used to estimate the new position of the particle during the mechanical test, may induce some errors especially when the infrared acquisition frequency is higher than the visible one.

- **interpolation errors:** as represented in Figure 2.20, most of the time, the current position of the subset P_{7D} does not correspond to the IR grid. To obtain the temperature of the subset P_{7D}, it is thus necessary to perform another interpolation in space.

2.5 Heat source estimation

2.5.1 Introduction

A temperature change which is induced during the deformation of a solid material can have different causes, namely, elasticity, viscoplasticity, phase transformation, fracture, plastic deformation. Therefore, measuring temperature at the surface of a material during mechanical tests brings a lot of information on its behaviour. Unfortunately, most of these measurements are not easy to interpret since the temperature is only the consequence of the presence of heat sources (internal or external). In order to estimate such heat sources from the heat balance equation and carry up quantitative analyse, an inverse problem needs to be solved.

Hence, the aim of this section is to present the method that has been chosen to estimate heat sources from temperature measurements on two types of sample geometries, namely, plates and tubes. For that purpose, a first set of assumptions is stated in order to write simplified heat balance equation describing heat transfers in solid materials (Subsection 2.5.2). Accounting for the thin thickness of the considered specimen, the heat balance equation can then be simplified, leading to a 2D formulation of the thermal problem (Subsection 2.5.3). Simplifications of the 2D formulation into a 0D formulation is sometimes possible if the observed phenomena are homogeneous. In other cases, a 2D formulation needs to be solved. Such a formulation involves (i) a characteristic time reflecting the natural radial heat loss which is determined experimentally (Subsection 2.5.5.1) and (ii) the estimation of spatial and time derivative of the noisy and discrete temperature fields. The image processing method used to solve the 2D thermal formulation is then described (Subsection 2.5.5.2) for both plates and tubes. Calibration and validation of the method using finite element simulations in the case of tubular samples is presented in Subsection 2.5.5.3. To conclude the section, an estimation of the errors made during such calculations will be presented.

2.5.2 General heat balance equation

The heat balance equation governing heat transfers inside samples is deduced from the first law of thermodynamics applied to continuum media. The heat equation is written either in material or spatial local forms. The spatial local form of the first law combined with the momentum and mass energy balances leads to the energy equation. This equation introduces the specific internal energy e, the mass density ρ, the internal stress power per unit volume p_{int}, the heat flow vector $\mathbf{q}$ per unit area, and distributed external heat sources s_e per unit volume of external origins (radiation here):

$$\rho \dot{e} = -p_{int} + s_e - \text{div } \mathbf{q} \tag{2.13}$$

In the last equation, "div" is the divergence operator, defined with respect to the spatial coordinates x_i and where $\dot{e}$ represents the material time derivative of e. It is assumed that the heat conduction is governed by the standard Fourier's law and that the considered medium is isotropic:

$$\mathbf{q} = -k \, \mathbf{grad} \, T, \tag{2.14}$$

where **grad** is the gradiant operator with respect to the x_i's and k the thermal conductivity. In the following we assume that the thermal conductivity is uniform along the sample and does not change during the test. This may not be always the case especially during localised tensile tests on NiTi SMA exhibiting localised phase transformations. In this case thermal conductivity of austenite (the parent phase) is nearly two times that of martensite. This particular point will be discussed in Section 2.5.6.

Introducing the specific heat C, also assumed uniform and constant, the previous equation is rewritten as a local heat balance equation:

$$\rho C \dot{T} - k \text{ lap } T = s_i + s_e, \tag{2.15}$$

where "lap" stands for the Laplacian operator with respect to the x_i's, and where s_i includes all rates of heat generation per unit of current volume of internal origin such as intrinsic dissipation (Louche, 1999; Chrysochoos and Louche, 2000), or thermoelasticity coupling or latent heat due to solid-solid phase transformation (McCormick et al., 1993). Notice that if the temperature field is expressed as a function of the spatial position M of the particle P, i.e. $T(M,t)$, the material time derivative of the temperature is then given by:

$$\dot{T} = T_{,t} + \mathbf{v}.\mathbf{grad} \, T, \tag{2.16}$$

with $T_{,t} = \partial T / \partial t$ the temperature time derivative, $\mathbf{v}$ being the current velocity of the considered particle at the spatial position M. The second term of the right-hand side of equation (2.16) implies that it is necessary to know simultaneously the thermal and kinematic fields. In the following, this term will be assumed negligible: such a strong assumption should be valid only for low velocities and/or for small temperature gradients and will be further discussed in Section 2.5.6. With all the above assumptions, the local heat conduction equation reads:

$$\rho C T_{,t} - k \text{ lap } T = s_i + s_e \tag{2.17}$$

2.5.3 Thin shell model

The heat balance equation (2.17) clearly shows that heat sources (right-hand side of the equation) can be theoretically deduced if the temperature field and its time and spatial derivatives are known. Unfortunately, the infrared camera allows temperature variation measurements only on the outer sample surface facing the camera, although the heat sources are expressed in the bulk. This inverse problem is then ill posed.

Therefore, further assumptions are required to transform this 3D problem into a 2D problem. This is possible if the sample is a shell with thin thickness (Louche, 1999; Chrysochoos and Louche, 2000). Within this context, the following section will present hypotheses required for thin plates and extend them to thin tubular geometry.

2.5.3.1 2D formulation for thin plates

Using a Cartesian coordinates system (x, y, z) associated with the local reference frame (M, $\mathbf{e_x}$,$\mathbf{e_y}$,$\mathbf{e_z}$) presented in Figure 2.28.a, the Laplacian operator is expressed as:

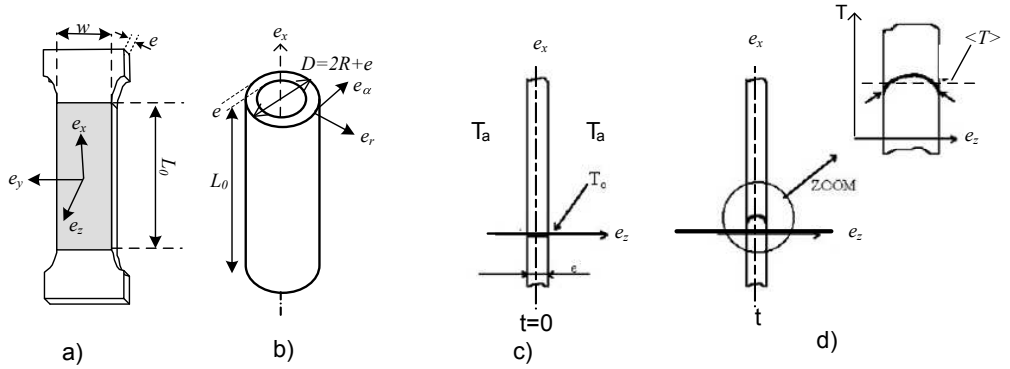

Figure 2.28: *a) Thin plate and b) tube geometries. c) Temperature profile in the thickness at time $t = 0$. d) Temperature profile in the thickness at time t.*

$$\text{lap } T = T_{,xx} + T_{,yy} + T_{,zz}. \tag{2.18}$$

Necessary assumptions are required for a thin plate sample (Figure 2.28.a):

- the thickness of the plate e is small compared to its width w and its height L_0:

$$e \ll w \ll L_0; \tag{2.19}$$

- the heat supply s_e of external origin is considered as time-independent;
- the initial temperature of the plate T_0 is assumed to be uniform and equal to the air temperature T_a ($T_a = T_0$);
- the air temperature T_a is assumed to be constant during the whole tensile test;

- the temperature field T in the plate is expressed as:

$$T(x,y,z,t) = \langle T(x,y,t)\rangle + \delta T(x,y,z,t), \tag{2.20}$$

where in the Cartesian coordinate system

$$\langle \varsigma \rangle = \frac{1}{e}\int_0^e \varsigma dz \tag{2.21}$$

represents the average value of the scalar quantity ς through the thickness of the plate for given transverse position y and axial position x; It is assumed that:

$$\delta T \ll \langle T \rangle. \tag{2.22}$$

- at any given time t, width y and height x, the temperatures on both external surfaces of the plate are supposed to be equal (Figure 2.28.d):

$$T(x,y,0,t) = T(x,y,e,t); \tag{2.23}$$

- introducing the temperature variation $\theta = T - T_0$, so that $\langle\theta\rangle = \langle T\rangle - T_0$, we further assume that:

$$\langle\theta\rangle \ll \langle T\rangle. \tag{2.24}$$

The lower the ratio e/w or e/L_0, the better the assumptions of eq. (2.22) and (2.23). Moreover, eq. (2.24) implies that the heat release or absorption induced by heat sources must be small enough to limit the increase or decrease of $\langle T\rangle$ in the plate.

Therefore, the heat balance eq. (2.17) is integrated in the thickness of the specimen and reads:

$$\rho C\langle T\rangle_{,t} - k\langle \mathrm{lap} T\rangle = \langle s_i\rangle + \langle s_e\rangle \tag{2.25}$$

Accounting for eq. (2.19), the term $k\langle \mathrm{lap}\ T\rangle$ is approximated by:

$$k\langle \mathrm{lap} T\rangle \approx k\langle T\rangle_{,xx} + k\langle T\rangle_{,yy} + \frac{k}{e}[T_{,z}]_0^e \tag{2.26}$$

From eq. (2.23), the last term of the right hand side of eq. (2.26) is estimated from heat exchanges between the considered specimen and air:

$$\frac{k}{e}[T_{,z}]_0^e = -\frac{1}{e}(\mathbf{e}_z \cdot \mathbf{q}_{cond}(x,y,0,t) - \mathbf{e}_z \cdot \mathbf{q}_{cond}(x,y,e,t)) \tag{2.27}$$

where $\mathbf{q}_{cond}(x,y,0,t)$ and $\mathbf{q}_{cond}(x,y,e,t)$ are respectively the conductive heat flow through the two surfaces of the plate. The heat transfers in the external surfaces $z=0$ and $z=e$ are assumed to be induced by natural convection ($\mathbf{q}_{conv}$) and radiation ($\mathbf{q}_{rad}$). Conservation of heat fluxes imposes $\mathbf{q}_{cond} = \mathbf{q}_{conv} + \mathbf{q}_{rad}$ on the external surfaces of the plate of respective normal $\mathbf{e}_z$ and $-\mathbf{e}_z$. The heat flow induced by natural convection ($\mathbf{q}_{conv}$) is expressed as:

$$\begin{aligned} \mathbf{e}_z \cdot \mathbf{q}_{conv}(x,y,e,t) &= h(T(x,y,e,t) - T_a) \\ &\approx h\ \langle\theta(x,y,t)\rangle = h\ \langle\theta\rangle \end{aligned} \tag{2.28}$$

and

$$\begin{aligned} -\mathbf{e}_z \cdot \mathbf{q}_{conv}(x,y,0,t) &= h(T(x,y,0,t) - T_a) \\ &\approx h\ \langle\theta(x,y,t)\rangle = h\ \langle\theta\rangle \end{aligned} \tag{2.29}$$

where h is the heat convection coefficient. The heat transfer induced by radiation on the front face, $\mathbf{q}_{rad}$, is expressed with the Stephan-Boltzmann law. Using eq. (2.22) and (2.24), it can be written as:

$$\begin{aligned} \mathbf{e}_z \cdot \mathbf{q}_{rad}(x,y,e,t) &= \sigma_e \epsilon_m T^4(x,y,e,t) \\ &\approx \sigma_e \epsilon_m \langle T^4 \rangle \\ &\approx \sigma_e \epsilon_m (T_0 + \langle\theta\rangle)^4 \\ &\approx \sigma_e \epsilon_m (T_0^4 + 4T_0^3 \langle\theta\rangle), \end{aligned} \tag{2.30}$$

where $\sigma_e = 5.67051\ 10^{-8}\mathrm{W\ m^{-2}\ K^{-1}}$ and ϵ_m stands for the Stephan-Boltzmann constant and the surface emissivity, respectively. Hence, eq. (2.26) is finally approximated by:

$$k\langle \mathrm{lap} T\rangle \approx -\frac{2}{e}(h_{eq}\langle\theta\rangle + \sigma_e \varepsilon_m T_0^4) + k\ \mathrm{lap}_{2cart}\langle T\rangle, \tag{2.31}$$

where $h_{eq} = h + 4\sigma_e \epsilon_m T_0^3$ and where "lap_{2cart}" represents the 2D Laplacian operator of the scalar averaged quantity $\langle\varsigma\rangle$ in Cartesian coordinate system:

$$\mathrm{lap}_{2cart}\langle\varsigma\rangle = \langle\varsigma\rangle_{,xx} + \langle\varsigma\rangle_{,yy} \tag{2.32}$$

At the equilibrium temperature, *i.e.* for $T = T_0 = T_a$, (2.25) and (2.31) yield

$$\langle s_e\rangle = \frac{2}{e}\sigma_e \varepsilon_m T_0^4 \tag{2.33}$$

This enables one to recast the heat balance equation (2.25) as:

$$\rho C \left(\langle\theta\rangle_{,t} + \frac{\langle\theta\rangle}{\tau_{th}} - d\ \mathrm{lap}_{2cart}\langle\theta\rangle \right) = \langle s_i\rangle, \tag{2.34}$$

where $d = k/(\rho C)$ is the thermal diffusivity and $\tau_{th} = \rho C e/(2h_{eq})$ represents the characteristic time of the heat losses by both convection and radiation in the faces $z = 0$ and $z = e$.

2.5.3.2 2D formulation for thin tubes

Similar developments are used in cylindrical coordinates system (r, α, x) associated with the local reference frame (M, $\mathbf{e_r}$, $\mathbf{e}_\alpha$, $\mathbf{e_x}$). In this case, the Laplacian operator is expressed as:

$$\mathrm{lap}\ T = \frac{1}{r}T_{,r} + T_{,rr} + \frac{1}{r^2}T_{,\alpha\alpha} + T_{,xx}. \tag{2.35}$$

The assumptions to be made on initial and boundary conditions for a thin tube sample (Figure 2.28.b) are expressed as follows:

- The thickness of the tube e is small compared to its mean radius R:

$$e \ll R; \tag{2.36}$$

- the temperature field T in the tube is expressed as:

$$T(r, \alpha, z, t) = \langle T(\alpha, x, t) \rangle + \delta T(r, \alpha, x, t), \tag{2.37}$$

where

$$\langle \varsigma \rangle = \frac{1}{e} \int_{R-e/2}^{R+e/2} \varsigma dr, \tag{2.38}$$

represents the average value of the scalar quantity ς in the thickness of the tube for given angle α and height x. It is assumed that:

$$\delta T \ll \langle T \rangle; \tag{2.39}$$

- at any given time t, angular position α and height x, the temperatures at the internal and external surface of the tube are assumed to be equal:

$$T(R - e/2, \alpha, x, t) = T(R + e/2, \alpha, x, t). \tag{2.40}$$

- and introducing the temperature variation $\theta = T - T_0$, so that $\langle \theta \rangle = \langle T \rangle - T_0$, we further assume that:

$$\langle \theta \rangle \ll \langle T \rangle. \tag{2.41}$$

As for plates, the heat balance equation (2.17) is then integrated in the thickness of the tubes and reads:

$$\rho C \langle T \rangle_{,t} - k \langle \text{lap} T \rangle = \langle s_i \rangle + \langle s_e \rangle. \tag{2.42}$$

The approximation of the term $k\langle \text{lap } T \rangle$ is:

$$k\langle \text{lap} T \rangle \approx \frac{k}{eR} [T]_{R-e/2}^{R+e/2} + \frac{k}{e} [T_{,r}]_{R-e/2}^{R+e/2} + \frac{k}{R^2} \langle T \rangle_{,\alpha\alpha} + k \langle T \rangle_{,xx}. \tag{2.43}$$

From eq. (2.40), the first term of the right hand side of eq. (2.43) is neglected. The second term of the right hand side of eq. (2.43) is estimated from heat exchanges between the considered tube and ambient air:

$$\frac{k}{e} [T_{,r}]_{R-e/2}^{R+e/2} = -\frac{1}{e} \left(\mathbf{e}_r \cdot \mathbf{q}_{cond}(R + e/2, \alpha, x, t) - \mathbf{e}_r \cdot \mathbf{q}_{cond}(R - e/2, \alpha, x, t) \right), \tag{2.44}$$

where $\mathbf{q}_{cond}(R + e/2, \alpha, x, t)$ and $\mathbf{q}_{cond}(R - e/2, \alpha, x, t)$ are respectively the conductive heat flow through the outside and inside surfaces of the tube. As for plates, the heat flow induced by natural convection, $\mathbf{q}_{conv}$, on the external or internal surface of the tube of respective normal $\mathbf{e}_r$ and $-\mathbf{e}_r$, is expressed as:

$$\pm \mathbf{e}_r \cdot \mathbf{q}_{conv}(R \pm e/2, \alpha, x, t) = h(T(R \pm e/2, \alpha, x, t) - T_a), \tag{2.45}$$

where h is a convection coefficient. The heat transfer induced by radiation, $\mathbf{q}_{rad}$, is expressed with the Stephan-Boltzmann law, using eq. (2.39) and (2.41):

$$\begin{aligned} \pm \mathbf{e}_r \cdot \mathbf{q}_{rad}(R \pm e/2, \alpha, x, t) &= \sigma_e \varepsilon_m T^4(R \pm e/2, \alpha, x, t) \\ &\approx \sigma_e \varepsilon_m (T_0^4 + 4T_0^3 \langle \theta \rangle), \end{aligned} \tag{2.46}$$

As for plates, it is possible to recast the heat balance equation (2.42) at the equilibrium temperature to obtain a 2D heat diffusion equation:

$$\rho C \left(\langle\theta\rangle_{,t} + \frac{\langle\theta\rangle}{\tau_{th}} - d \, \mathrm{lap}_{2cyl}\langle\theta\rangle \right) = \langle s_i \rangle, \tag{2.47}$$

where $d = k/(\rho C)$ is the thermal diffusivity, τ_{th} represents the characteristic time of the radial heat loss by convection and radiation in the internal and external surfaces and $\mathrm{lap}_{2cyl}\langle\theta\rangle$ represents the 2D Laplacian operator of the scalar averaged quantity $\langle\theta\rangle$, in cylindrical coordinate system:

$$lap_{2cyl}\langle\theta\rangle = \frac{1}{R^2}\langle\theta\rangle_{,\alpha\alpha} + \langle\theta\rangle_{,xx}. \tag{2.48}$$

Estimation of each term of the left hand side of eq. (2.47) and (2.34) is necessary to obtain the local heat sources. Unfortunately, the temperature field is both discrete and noisy. Depending on the observed phenomena, estimation of the time and spatial derivative operator is not obvious.

In cases of uniform temperature and heat sources fields, some simplifications of the thermal model can be made. This uniform thermal model is presented in the next section. When the observed phenomena are heterogeneous in the two spatial directions, the estimation of heat sources from a 2D model (eq. (2.47) or (2.34)) must be resorted (cf Section 2.5.5).

2.5.4 Simplified thermal model: uniform heat sources

Quite often, 2D formulations eq. (2.47) or (2.34), can be written in a simpler form when the specific heat sources (in W/m^3) are uniformly distributed ($\langle s_i(x,y,t)\rangle = \langle s_i(t)\rangle$) in a specimen surrounded by ambient medium at a temperature T_0 and when specimen temperature is not too far from thermal equilibrium (Chrysochoos et al., 1996; Chrysochoos and Louche, 2000). Hence, at any point of the specimen surface, the Laplacian is linearised as follows:

$$-k \, \mathrm{lap}\langle\theta(x,y,t)\rangle \approx \rho C \frac{\langle\theta(x,y,t)\rangle}{\tau_{eq}}. \tag{2.49}$$

Therefore, this simplified model reads:

$$\rho C \left(\frac{\partial\langle\theta(x,y,t)\rangle}{\partial t} + \frac{\langle\theta(x,y,t)\rangle}{\tau_{eq}} \right) = \langle s_i(t)\rangle, \tag{2.50}$$

where $\langle s_i(t)\rangle$ are the uniform heat sources. The parameter τ_{eq} represents a characteristic time reflecting heat losses both by convection through the specimen surfaces (back and front surfaces for plates, inner and outer surfaces for tubes) and by conduction towards the grip's zones:

$$\tau_{eq} = \tau_{th} + \tau_{grip}. \tag{2.51}$$

Estimation of τ_{eq}

Prior using the uniform model eq. (2.50), an estimation of τ_{eq} is necessary and can be experimentally estimated (Chrysochoos et al., 1989; Chrysochoos and Belmahjoub, 1992).

One method to estimate this parameter is to observe the natural temperature decrease of the sample at the end of a loading by holding the specimen in its deformed configuration. During the natural temperature decrease following the loading, heat sources are assumed to be zero (no phase transformation, thermoelasticity, plasticity, external heat sources). τ_{eq} is then estimated by solving the following equation:

$$\frac{\partial \langle\, \theta \,\rangle}{\partial t} + \frac{\langle\, \theta \,\rangle}{\tau_{eq}} = 0. \tag{2.52}$$

Figure 2.29 illustrate how τ_{eq} was estimated in case of a NiTi tube deformed in tension and stopped at the end of the loading by holding the specimen at constant displacement during 35 s ($h^- h^+$). Negligible transformation was assumed during this resting time. The natural temperature decrease $\theta \approx \langle\, \theta \,\rangle$ was then recorded. The two thick and thin curves in Figure 2.29.a represent time evolutions of temperature variations on two points of the tube sketched in Figure 2.29.b. As shown by the continuous lines plotted in Figure 2.29.a, the modelling of this natural decrease using eq. (2.52) shows that the natural decrease is well modelled with eq. (2.52) by taking $\tau_{eq} = 22 \pm 1s$.

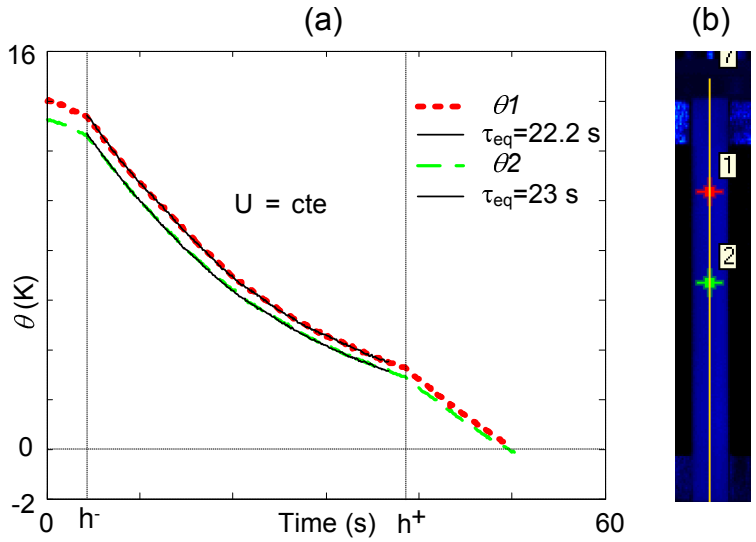

Figure 2.29: *Estimation of τ_{eq} on a NiTi thin tube at the end of a tensile loading (time h^-) for 35s ($h^- h^+$) before unloading at time h^+. The dashed curves represent the time evolutions of the temperature variations θ_1 and θ_2 of points 1 and 2 shown on the specimen in b). The solid curves show the modelling of these evolutions using eq. (2.52) by taking $\tau_{eq} = 22$ s, assuming a zero heat sources during the period $h^- h^+$.*

2.5.5 Estimation of heat sources from 2D measurements

If no simplification is made, the process to estimate the heat source fields is based on the left hand side estimation of the 2D formulation of the heat balance equation (2.47) or (2.34):

$$\rho C \left(\theta_{,t} + \frac{\theta}{\tau_{th}} - d \,\mathrm{lap}_2\, \theta \right) = \langle s_i \rangle, \tag{2.53}$$

by noting:

$$\mathrm{lap}_2\, \theta = \theta_{,xx} + \theta_{,yy} \quad \text{for plates (in Cartesian coordinate system)} \tag{2.54}$$

$$\mathrm{lap}_2\, \theta = \frac{1}{R^2}\, \theta_{,\alpha\alpha} + \theta_{,xx} \quad \text{for tubes (in Cylindrical coordinate system)} \tag{2.55}$$

The experimental temperature variation fields $\theta \approx \langle\, \theta \,\rangle$ are discrete and noisy data, obtained on the outer surface ($z = e$ for plates or $r = R + e/2$ for tubes) of the sample.

The experimental estimation of the characteristic time τ_{th} is first necessary and will be presented in Section 2.5.5.1. The estimation of the time derivative and the 2D Laplacian operator using image processing filtering and its validation will be presented in Section 2.5.5.2 and 2.5.5.3, respectively.

2.5.5.1 Estimation of τ_{th}

As presented in (Louche, 1999) in case of thin plates, it is possible to estimate the characteristic time τ_{th} of the radial heat loss by convection and radiation only for a sample of gauge length l_0, by taking a second specimen of total length equal to the gauge length of the first sample $L_0 = l_0$. The second specimen, which is held by a non-conductive rope, is first heated up to a uniform temperature T_{heat} above T_a, the ambient temperature. From this initial state, the specimen's natural cooling is then analysed with the IR camera as presented in Figure 2.30.b. Under such condition, eq. (2.53) is approximated by an uniform thermal model:

$$\theta_{,t} + \frac{\theta}{\tau_{th}} = 0, \tag{2.56}$$

whose analytical solution is:

$$\begin{aligned} \theta &= (T_0 - T_a) e^{-\frac{t-t_0}{\tau_{th}}} \\ &= \theta_0 e^{-\frac{t-t_0}{\tau_{th}}}. \end{aligned} \tag{2.57}$$

A value of τ_{th}=35 s was estimated when comparing successfully the model (eq. (2.57)) with experimental data measured on a Ti-50.6 at% Ni plate sample (described in Section 3.1.2) of dimension 3 mm × 30 mm × 0.5 mm (Figure 2.30).

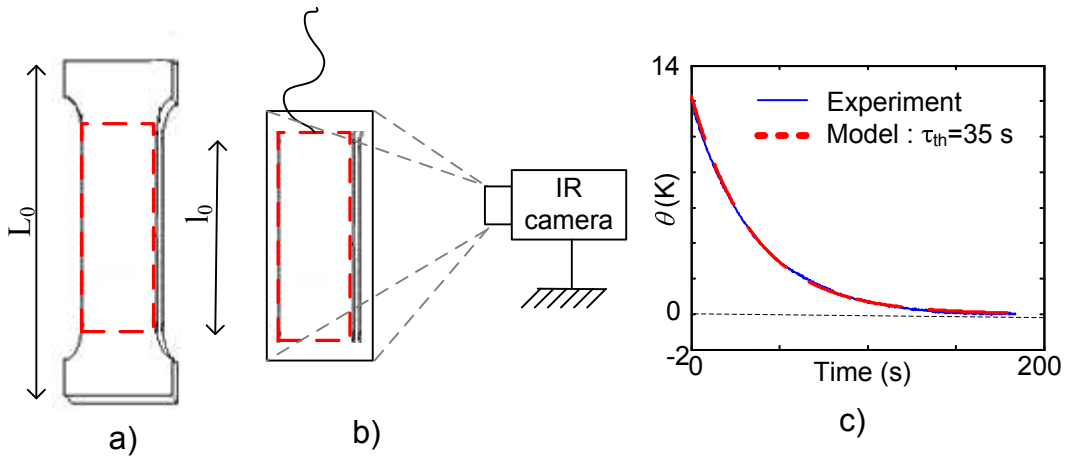

Figure 2.30: *Experimental estimation of the characteristic heat losses τ_{th}. a) Original sample of total length L_0 and gauge length l_0. b) Sample cut of total length l_0, heated up and hold by an insulated rope during natural cooling. The temperature change is recorded by the infrared camera. c) Natural cooling measured and obtained by the model eq. (2.57) with τ_{th}=35 s.*

2.5.5.2 Image processing and filtering

Choice of the filtering process

Due to the important noise, it is not possible to estimate properly (using finite difference method for instance) the time derivative and the Laplacian operators involved in eq. (2.53). Filtering the noisy and discrete temperature fields in time and space is therefore necessary. Several filtering procedures are available, mainly depending on the signal characteristics and the amount of data to analyse. In our case:

- The signal is noisy (Noise Equivalent Temperature Difference (NETD)=20 mK). This noise is random, ergodic and stationary.
- Our tensile and shear test samples have rectangular shape with one dimension much smaller than the other. In this direction, only few pixels describe the phenomena.
- Localisation phenomena observed in NiTi tensile test induce strong localisation of temperature variation (up to 8 K in few pixels).

A lot of filtering techniques are available. Some of them are briefly presented here:

- **Temporal average.** Applying a temporal mean on n images can strongly reduce the noise by a factor $\sqrt{n}$. The limit of such a method stands in the time evolution of the temperature field toward the sample rate. On a quasistatic or stationary scene, such an operation is efficient. If the time evolution of the temperature is fast or non linear between the first and last image (n), mean time function will induce some error (Bouc and Nayroles, 1985).
- **Spatial average.** Mean space function (using square of $n \times n$ pixels) has been used in infrared image processing before estimating differential operator by Dupré (2002). The main difficulty of this technique is the choice of the value of the parameter n and the occurrence of strong edge effects (reduction of the image size).
- **Low-pass filter using discrete Fast Fourier Transform (FFT).** This method was developed by (Chrysochoos and Louche, 2000) to estimate heat sources by removing high frequency noise. It is well adapted to discrete data and time efficient. The main disadvantage of such filtering is that low frequency noise remain after the filtering. Moreover, FFT works well on periodic signal, otherwise the low pass filtering of the image will induce strong edge effects.
- **Wiener filtering.** It is a non linear filter proposed by Norbert Wiener during the 1940s. Its purpose is to reduce the amount of noise in a signal by comparison with an estimation of the desired noiseless signal. This filtering process is based on a statistical approach.
- **Median filtering.** Like Wiener filtering, it is a non linear filter. This filtering replaces the pixel value with the median of neighboring pixel values (window of odd number of pixel wide). The median is calculated by first sorting all the pixel values from the surrounding neighborhood into numerical order and then replacing the pixel being considered with the middle pixel value.

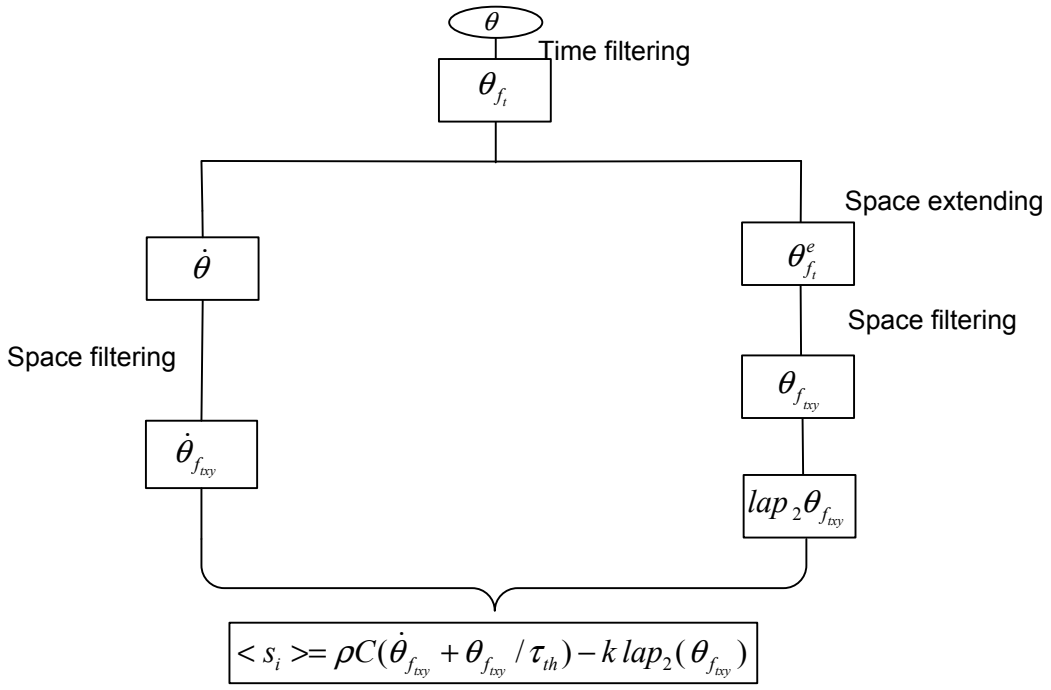

Figure 2.31: *Image processing procedure to estimate local heat sources.*

- **Polynomial smoothing.** Such filtering techniques have been used by Pastor et al. (2008) and consist in approximating the data by a polynomial function (1D or 2D). Once again, the size of the interpolation domain as well as the polynomial degree are parameters whose values should depend on the signal characteristics.

In the following, low-pass FFT method will be used (Louche, 1999).

Image processing procedure

The filtering and operator estimations are summarised in the scheme sketched in Figure 2.31. The temperature variation fields are first filtered in time using an FFT low pass filter to reduce the noise ($\theta \rightarrow \theta_{ft}$). Each image is extended ($\theta_{ft} \rightarrow \theta^e_{ft}$) to a periodic image in the two spatial directions. This operation prepares the data before the next spatial FFT low pass filtering pixels and enables to reduce edge effects. Once extended, a spatial low pass filter and windowing is applied ($\theta^e_{ft} \rightarrow \theta_{ftxy}$). Temporal and lLaplacian operator are estimated using central finite differences (see bellow). More details on the filtering procedure are presented in (Louche, 1999; Chrysochoos and Louche, 2000).

One major difficulty of such an image processing is that the sensitivity of this method depends on the values of the cutoff frequencies of the low-pass filters. Small values are better for operator estimations but they reduce the intensity of the gradients of the unknown heat sources. An increase of these cutoff frequencies enhances the heat sources detection but strongly increases the noise due to the estimation of the operators. In classical signal processing, the critical frequency is the so-called Nyquist frequency, which is half the sample frequency. In the case of a Laplacian estimation, the critical frequency needs to be smaller. Typical values of 15% of Nyquist frequencies are taken (example of various filters are de-

tailed in the next section; Figure 2.40). For such cutoff frequencies and a spatial resolution of 0.4 mm, heat sources of wavelength < 5.3 mm will be underestimated, i.e. the amplitude will be reduced. Moreover, this reduction will be associated with a spatial spreading of the heat sources. Higher values for the cutoff frequencies would lead to significant noise in the Laplacian estimation.

Another difficulty is the estimation of the Laplacian operator near the edges of the thermal images. The spatial periodic extension reduces the range of these edge effects (inherent to FFT filtering of a non periodic image). However, edge effects of finite length exist and will be discussed in Section 2.6.

Laplacian operator estimation

After filtering operations, the Laplacian operator was calculated using a second-order central finite differences scheme. On plates samples, $\text{lap}_{2cart}\theta$ is estimated with constant discretisation steps in the two spatial directions.

In case of tubes, the infrared camera does not directly measure the spatial point M, of cylindrical coordinates (x_i,α_j), but measures its projection (x_i,y_j) as presented in Figure 2.32. The current axial and transverse discrete coordinates of a spatial point M are noted (x_i,y_j) in a orthogonal Cartesian coordinate system and (x_i,α_j) in a cylindrical system. The spatial resolution $\Delta x = x_{i+1} - x_i$ and $\Delta y = y_{j+1} - y_j$ are the pixel sizes, of the infrared camera. At the time t_k, the measured temperature of a spatial point can be expressed in the two coordinate systems:

$$\theta(x_i, y_j, R + e/2, t_k) = \theta(x_i, \alpha_j, R + e/2, t_k) \tag{2.58}$$

with the relationship (see Figure 2.32):

$$y_j = R \sin(\alpha_j). \tag{2.59}$$

Consequently, only the vertical axis x will be estimated with constant discretisation steps

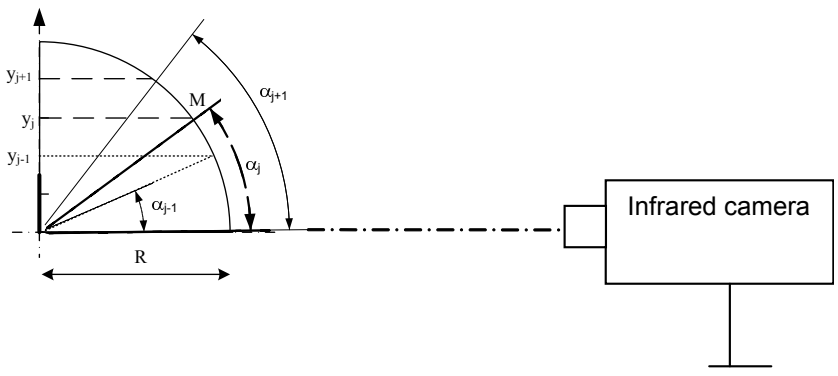

Figure 2.32: *Link between the pixel y_j and the angle α_j.*

on tube samples. A non-constant step estimation will be used in the α-direction:

$$\frac{\partial^2\theta}{\partial\alpha^2}(x_i, \alpha_j, t_k) = \frac{(\alpha_j - \alpha_{j-1})\theta^k_{j+1} - (\alpha_{j+1} - \alpha_{j-1})\theta^k_j + (\alpha_{j+1} - \alpha_j)\theta^k_{j-1}}{(\alpha_j - \alpha_{j-1})(\alpha_{j+1} - \alpha_{j-1})(\alpha_{j+1} - \alpha_j)} \tag{2.60}$$

where α_j represents the angle of the pixel (x_i,y_j) viewed by the IR camera, and $\theta_j^k = \theta(x_i, y_j, t_k)$ the measured temperature variation at the discrete time t_k.

All of these image processing steps have been included in a software called *Source2D* implemented in the Matlab software. It enables one to estimate heat sources either for plate or tube geometry.

2.5.5.3 Validation of the method on tubes and calibration of the filters

Overview

The benchmark construction is explained in Figure 2.33; such a method was proposed in (Louche, 1999) with analytical benchmark on plates. First, thermal boundary value problem is solved on a rectangular domain representing the surface of the tube with finite element simulation. The theoretical heat sources s_{th} are given by a fully controlled analytical model, described in the next paragraph. Artificial noisy temperature fields θ_n are then created by adding experimental noise (NETD = 8 mK) to the numerical temperature field θ_{th}. Afterwards, the noisy temperatures are used to determine the corresponding heat sources s_{cal} via *Source2D*. Finally, these estimated heat sources are compared with the theoretical ones s_{th} in order to check the validity of the image processing.

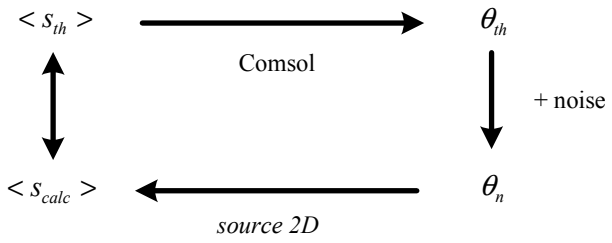

Figure 2.33: *Organisation of the benchmark used to calibrate and validate Source2D.*

The Numerically Simulated Temperature Fields (NSTF) construction.

Since the thickness of the tube was small compared to the other dimensions, a 2D thermal planar model was built in Comsol using a rectangular developed surface geometry, as shown in Figure 2.34:

1. Periodic boundary conditions were imposed between the left and right sides of the domain to all the variables involved in the problem (temperature, heat flow, heat sources). Adiabatic boundary conditions were imposed to the upper and lower part of the domain.

2. The position and shape of theoretical heat sources $\langle s_{th} \rangle$ have been modelled in order to be as close as possible to those observed during the experiments. The center P of a heat sources is moving at a constant velocity V_S along a direction $\overrightarrow{v}$ oriented with an angle β with respect to the direction $\overrightarrow{x}$ (Figure 2.35.a, eq. (2.61)).

$$P(t) = \left| \begin{array}{rcl} u_p(t) & = & 0 \\ v_p(t) & = & V_s(t - t_0). \end{array} \right. \tag{2.61}$$

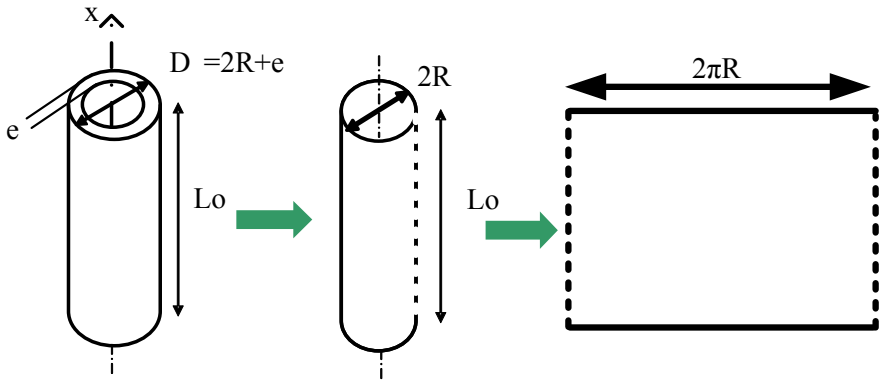

Figure 2.34: *2D thermal plate model of the tube.*

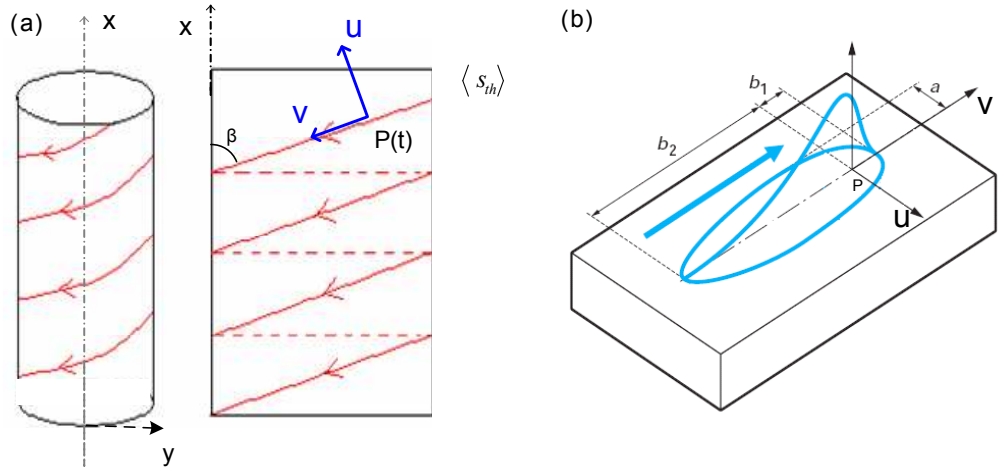

Figure 2.35: *(a) Heat sources propagation and periodicity. (b) Scheme of the theoretical heat sources distribution* $\langle s_{th} \rangle$.

This orientation is based on experimental temperature fields presented in typical tensile tests on NiTi thin tubes (cf Chapter 4, (Favier et al., 2007)). The shape of the heat sources $\langle s_{th} \rangle$ were modelled using non-symmetric exponential functions (Figure 2.35.b, eq. (2.62)):

$$\langle s_{th} \rangle = \begin{cases} Q_{max} \exp[-((\frac{u-u_p}{a})^2 + (\frac{v-v_p}{b_1})^2)] & \text{if } v > v_p \\ Q_{max} \exp[-((\frac{u-u_p}{a})^2 + (\frac{v-v_p}{b_2})^2)] & \text{if } v < v_p. \end{cases} \tag{2.62}$$

This function allows us to change the width $2a$ of the heat sources band, its length $b_1 + b_2$ and the velocity V_S of its centre P. Choosing high values for parameters a, b_1 and b_2 will induce diffuse heat sources distributions. Conversely, small values of a, b_1 and b_2, will create heat sources localisation in narrow bands. An example with propagation of heat sources bands is presented in Figure 2.35.a.

The heat balance equation that is solved is identical to eq. (2.53), in which the heat losses by convection and radiation (characteristic time τ_{th}) were neglected. The transient boundary value problem was solved with Comsol software. As shown in Figure 2.36.A, a fine 2D mapped mesh made of 150×100 quadrilateral elements with second-order polynomial interpolation functions was used to run the simulation. The numerical results were then projected onto a

Cartesian grid made of 77×51 points (Figure 2.36.B). Half the grid, i.e. a subset of 39×51 points (Figure 2.36.C), was extracted in order to select only the part of the tube observed by the infrared camera (view angle of 180°). Finally, as shown in Figure 2.36.D, the last grid was projected in the (x, y) plane of Figure 2.32, using eq. (2.59). It was also re-sampled with an equally spaced grid, to obtain virtual thermal images with 25×51 square pixels similar to those recorded by the infrared camera. These numerical thermal images were used, as input data, to check the validity of the software *Source2D*.

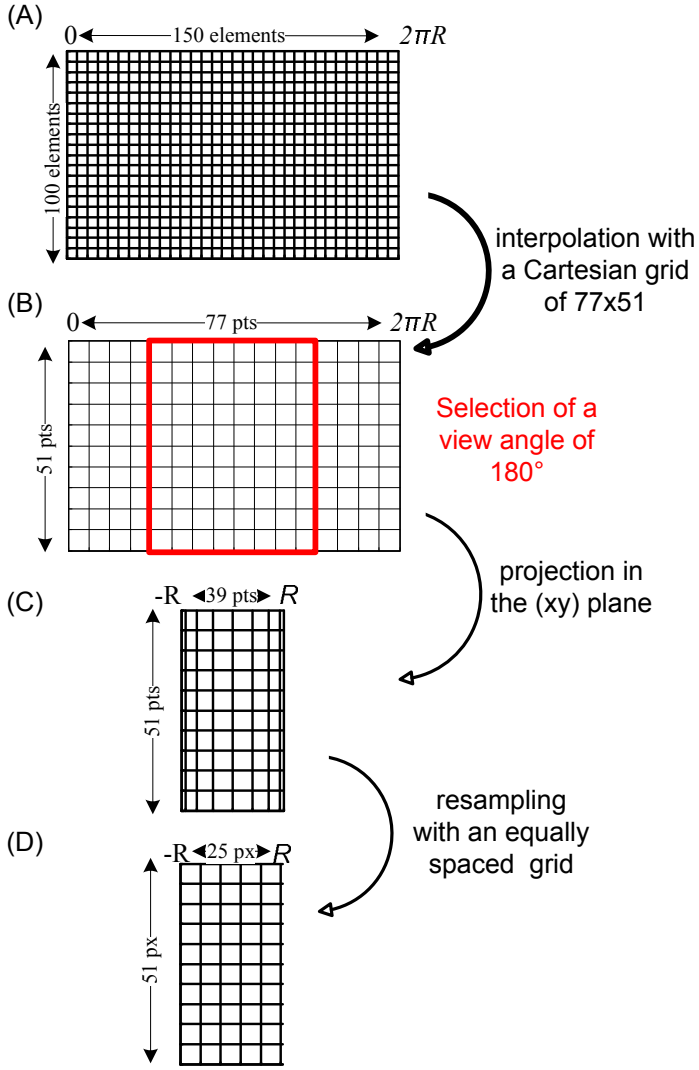

Figure 2.36: *Schematic view of the successive steps proposed to build a numerical thermal image. (A) 2D finite element mesh of the plate used to compute the thermal field. (B) Cropping operation in the transverse direction in order to select only a view angle of 180°. (C) Projection of the grid in the (xy) plane of Figure 2.32, using eq. (2.59). (D) Resampling of the grid, with an equally spaced mesh, in order to have a regular thermal image, with* 25×51 *square pixels, as for IR observations.*

Benchmark results

As the filter parameters are very sensitive to the spatial sampling frequency and to the heat sources characteristics, the NSTF's parameters have been selected close to the experimental data (Table 2.1).

V_s (m s^{-1})	a (m)	$b1$ (m)	$b2$ (m)	Q_{max} (W m^{-3})	Angle (°)
0.0110	0.0011	0.0033	0.0033	2e7	59
$\Delta x = \Delta y$ (mm)	Δt (s)	T_0 (K)	C (J kg^{-1}K^{-1})	ρ (kg m^3)	k (W m^{-1}K^{-1})
0.2477	0.1	297	490	6400	15

Table 2.1: *Heat source distribution parameters and other NSFT parameters.*

An example of results obtained at a given time (1.5 s), of the different fields described in Figure 2.33 is presented in Figure 2.37. This Figure confirms that the image processing software *Source2D* can achieve heat source estimation from temperature fields. Spatio-temporal representations of the benchmark results are also plotted in Figure 2.38. These representations show the time evolution of an axial profile of the previous fields. Because of thermal conduction, the axial heat sources and temperature distributions are very different and confirm the difficulty to interpret the observed temperature fields. Estimated heat source profiles are very similar to theoretical heat sources.

In order to check the validity and to adjust the parameters of the filtering process provided by *Source2D*, temporal evolutions or axial profiles (sections of the previous spatiotemporal images) have been plotted in Figures 2.39. Comparison between estimated $\langle s_{calc} \rangle$ and theoretical $\langle s_{th} \rangle$ heat sources profiles in Figures 2.39.A,E show that heat sources were 20% underestimated in the centre of the band. Moreover along the sample height (Figures 2.39.E), some edge effects were observed on the estimated heat sources. Outside the band, the estimation was better. Underestimations are due to the lowpass spatial filtering described before. Figures 2.39.B,D,F show that the estimation error is mainly induced during the Laplacian estimation, and not from the time-partial derivative which is rather well calculated. These figures also show the different filtering steps, for the Laplacian and for the time derivative. The edge effects were due to the extension of the data the FFT filtering process. Increasing the spatial resolution can reduce them.

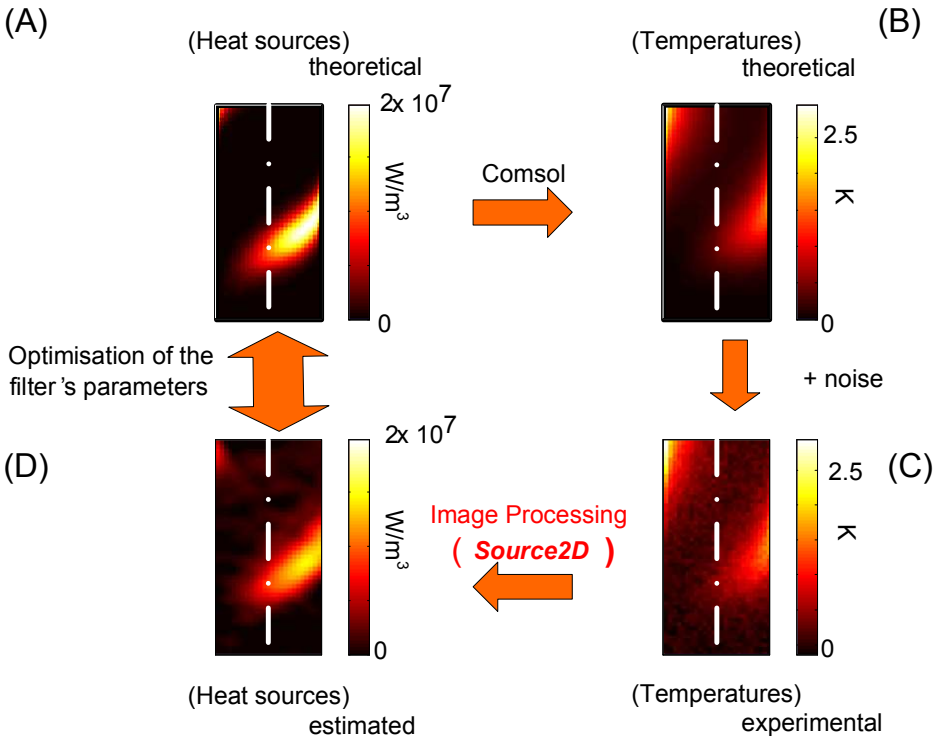

Figure 2.37: *Benchmark results at a current time (1.5 s). All the fields are projected on the tube surface as they are observed by the infrared camera: (A) theoretical (analytical) heat sources field; (B) associated temperature variation field estimated by the finite element model; (C) noisy temperature field; (D) heat sources field estimated by the image-processing software Source2D.*

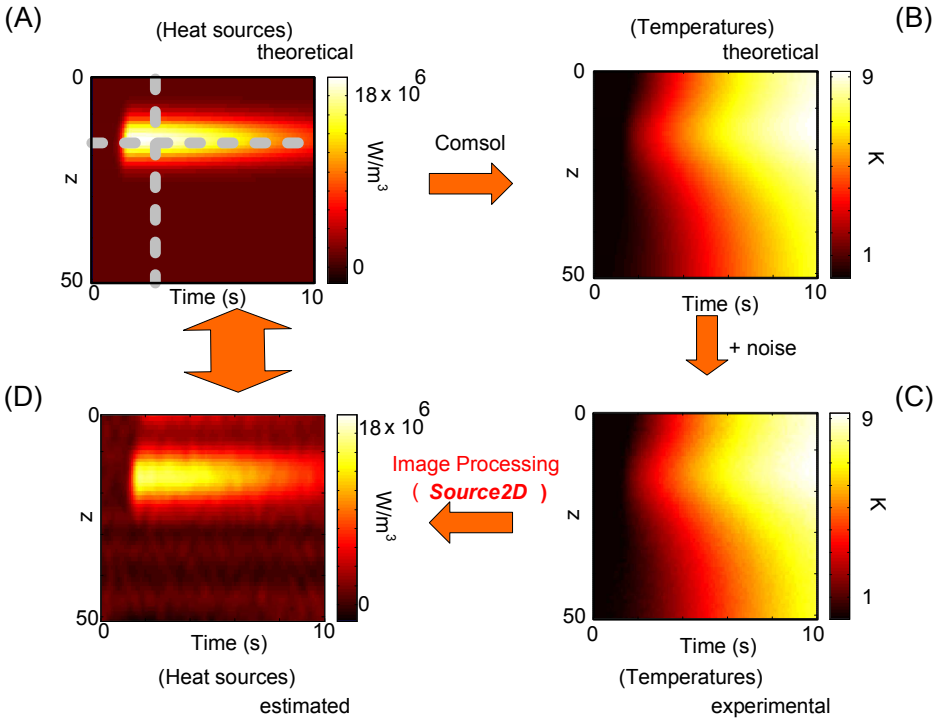

Figure 2.38: *Spatiotemporal representation of the benchmark results. Time evolution of an axial profile of: (A) theoretical heat sources; (B) associated temperature variation field estimated by the finite element model; (C) noisy temperature field; (D) heat sources field estimated by the image-processing software Source2D.*

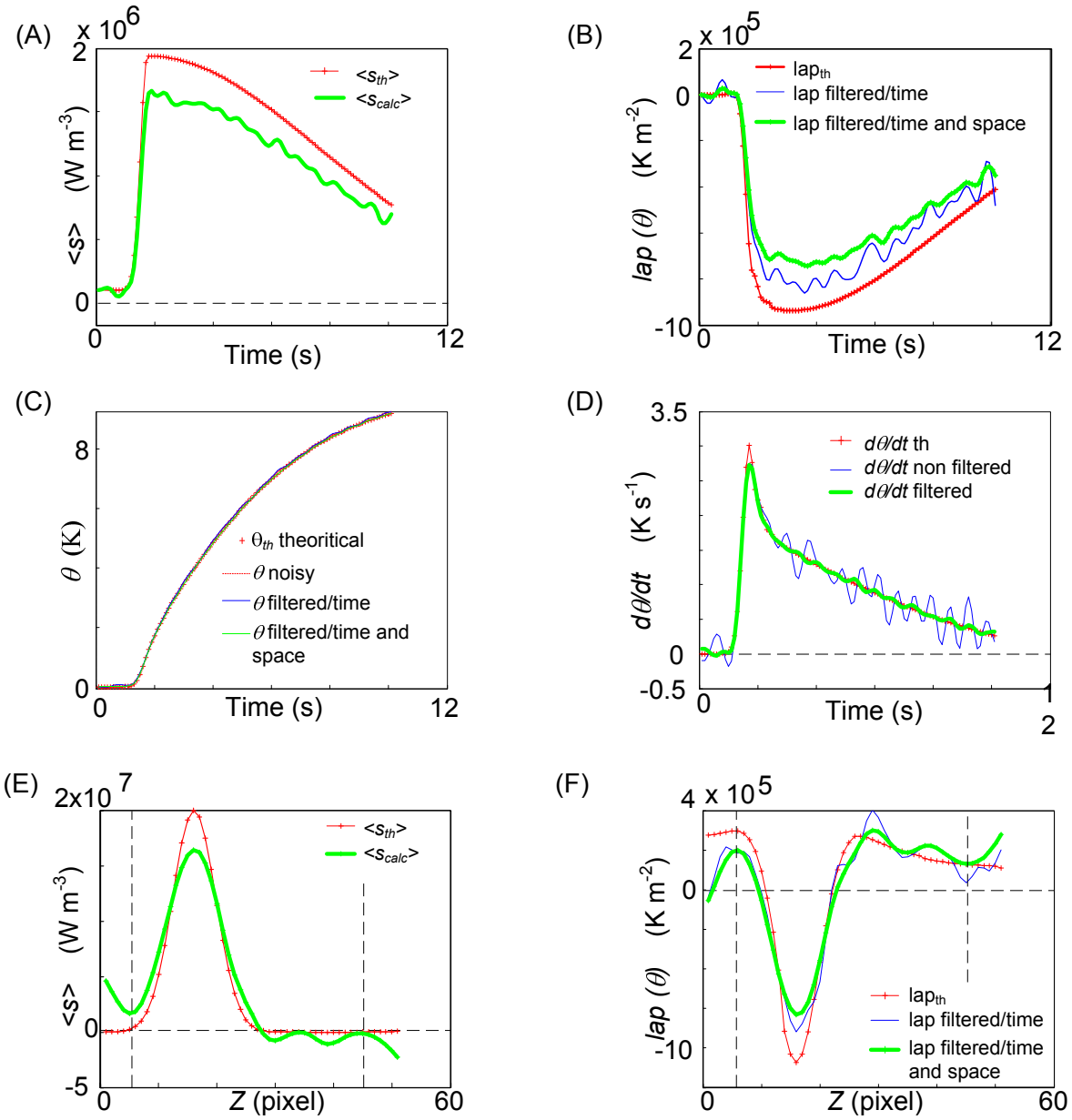

Figure 2.39: *Time evolution, at pixel 17 (see horizontal white dot line in Figure 2.38.A), of: (A) theoretical and estimated heat sources; (B) theoretical and estimated Laplacian operators with the two filtering steps; (C) theoretical and estimated temperature variations with the two filtering steps; (D) theoretical and estimated time derivative filtered and not filtered. Axial profiles, at time $t = 30s$ (see vertical white dot line in Figure 2.37), of: (E) theoretical and estimated heat sources, (F) theoretical and estimated Laplacian operators with the two filtering steps. The vertical lines in (E) and (F) shows the errors due to the edge effect.*

Figure 2.40 underlines the influence of cutoff frequencies on the filtering process. For that purpose, five different increasing values for the filter's cutoff frequencies have been tested, ranging between filter 0 and filter 4 respectively. Increasing the cutoff frequency reduces the heat sources noise but strongly reduce the amplitude of the band. Conversely, reducing the filtering allows one to better observe the heat source peak but with more noise outside of the bands. There is no universal filtering for heat source estimation and so far the filtering choice remains mainly manual. Depending on the spatial resolution (55 points in the axial direction) and on the heat source width, an optimal value has been fixed and corresponds to

filter 2. In this situation, the cutoff frequency equals 15% of Nyquist frequency and tends to minimise ripples in the Laplacian image (see filter 0 and 1 for example).

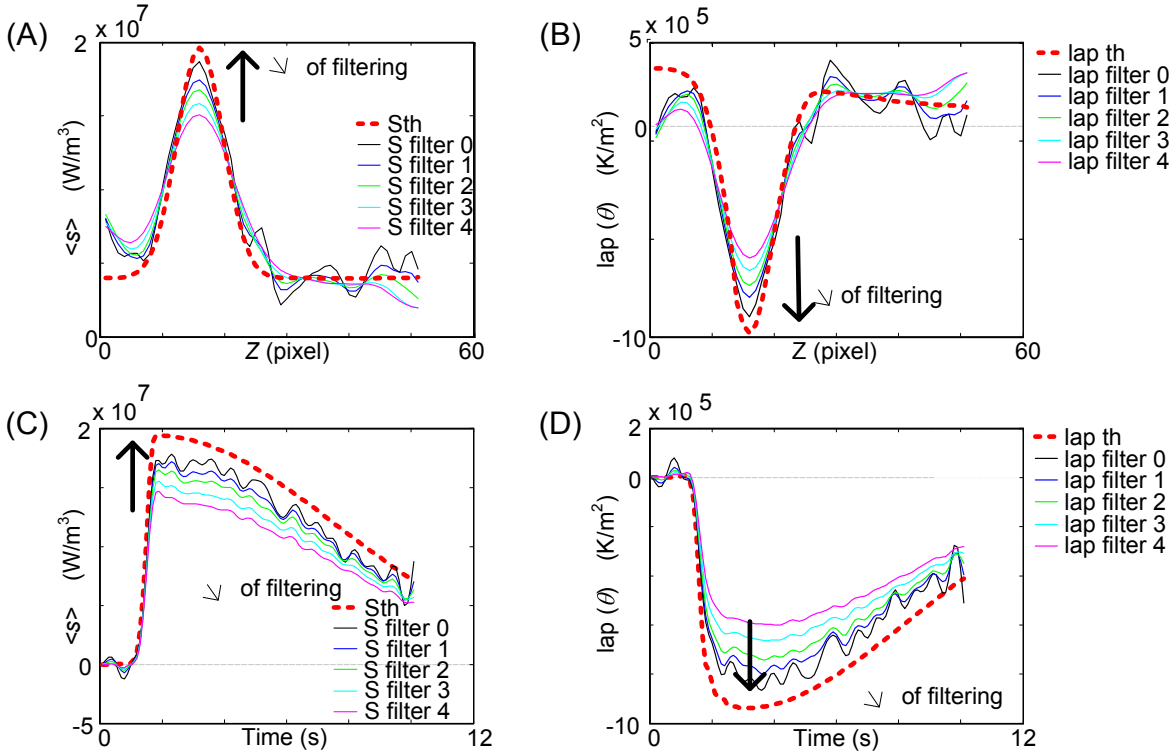

Figure 2.40: *Influence of filtering for: (A) a heat sources profile; (B) a Laplacian profile; (C) a temporal evolution of the heat source; (D) a temporal evolution of the Laplacian operator.*

2.5.6 Conclusions on the method accuracy

The previous sections have shown, using a benchmark, that it was possible to estimate heat sources from noisy temperature fields using the thin shell model. Several assumptions are made in this modeling and will be discussed hereafter.

Hypothesis on the temperature and heat sources within the sample thickness

As the temperature is only measured on the sample surface whereas heat sources are 3D, first assumptions on the distribution of the heat sources and temperature fields in the thickness are necessary to obtain a 2D formulation. Such assumptions require a small thickness and identical ambient temperature on each side of the sample. This may not be the case for tubular geometries, namely, air inside the tube may be at a different condition than outside. Verifications using thermocouple welded inside and outside the tube could confirm or unvalidated this hypothesis.

Heat source estimation in spatial coordinates

Although spatial synchronisation has been presented in Section 2.4, heat sources were estimated in spatial representation since spatial synchronisation on the DIC grid reduces the spatial resolution. However, during the heat source estimation in spatial representation, the time derivative of the temperature $\dot{T}$ is approximated with the temperature time derivative $T_{,t}$ in eq. (2.16). Such approximation is valid if the term **v.grad** T is negligible. In our case, it is more likely that this term will be negligible when the martensite phase transformation is uniform (NiTi shear tests and uniform stages of tensile tests). In case of strongly localised phase transformation (stress plateau during NiTi tensile tests), the term **v.grad** T should not be negligible. An estimation of the error made is possible with the information of the spatial synchronisation and should be investigated in further work.

Influence of filtering

Comparison of estimated to theoretical heat sources have shown that this method is very sensitive to filtering process. The chosen filters mainly depend on the observed phenomena. So far they still need to be adjusted almost manually, depending on the temperature field gradients. One method to verify the consistency of the filtering is to plot steps for different filtering parameter represented in Figures 2.39. When the thermal gradients are large, heat sources are underestimated. When the temperature variations are weak, heat source estimation is affected by temperature noise. Ideally, the filtering parameters should be different when the temperature field is uniform and when the temperature field has strong gradients.

Another drawback of the low-pass filtering method by FFT is the edge effect appearing on heat source estimations. In spite of the periodic extension, Laplacian estimation is inaccurate in all the edges of the fields. The length of such perturbations is fixed (absolute value) and is linked to the order (i.e. number of points) of the spatial filters. Typically, for the filters used, lengths of the edge effects were about six pixels, along each border, as can be seen for example by the two vertical dashed lines in Figures 2.39.E and 2.39.F.

Influence of material coefficients

Thin shell model of heat balance eq. (2.53) is strongly dependent on the material coefficients (ρ, C, k) and only valid if they are constant in the material during the test. Depending on the test conditions, all terms in the left side of eq. (2.53) are important.

- Figure 2.41.a shows the time evolution of the heat sources and its different terms during a NiTi tensile test, in uniform stage in almost adiabatic conditions[1]. The heat sources (in red) estimation depends mainly on term $\rho C\dot{\theta}$ (plotted in blue). In this case, error on the specific heat coefficient will have a strong influence on the estimated heat sources; other coefficients such as thermal conductivity have a weak influence.

- In some cases, for example tests involving localised phase transformations, the Laplacian is no longer negligible. Figure 2.41.b presents another tensile test on the same sample,

[1] this test will be presented in detail in Section 5.2.1

but stopping the test in the middle of the stress plateau[2]. In that case, Laplacian coefficient has a strong influence on the estimated heat sources.

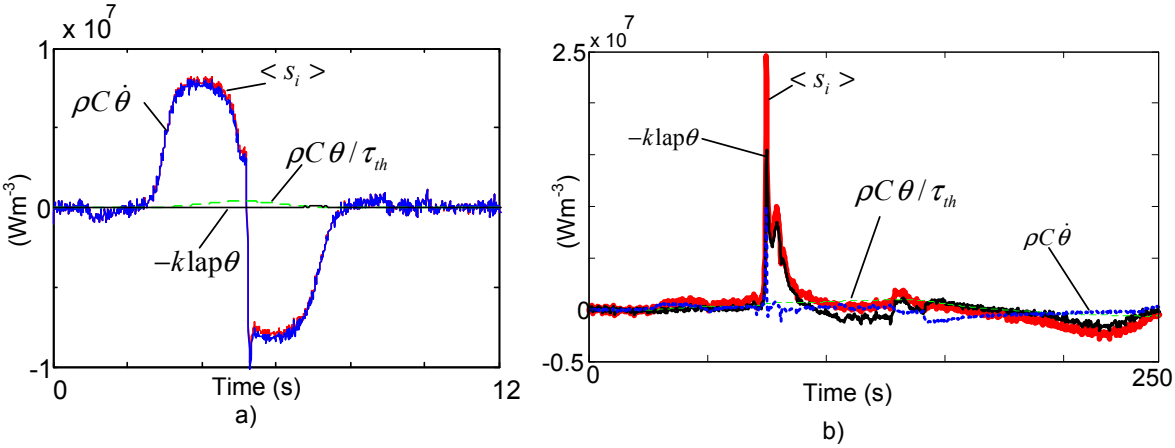

Figure 2.41: *Example of heat source estimation for two tensile tests performed on the same NiTi sample. For each figure, the different terms of the heat balance equation are plotted. a) uniform test at fast velocity. b) Tensile test presenting strongly localised exothermic martensite phase transformations.*

In NiTi materials, ρ and C are identical for martensite and austenite but it is not the case of thermal conductivity that strongly depends on the microstructure. Faulkner et al. (2000) have shown that the thermal conductivity of austenite $k = k_A = 18$ W.m^{-1}.K^{-1} is nearly two times higher than that of martensite $k = k_M = 8$ W.m^{-1}.K^{-1}. Figure 2.42 presents the heat sources of Figure 2.41 near their maximum between time 72 to 82 s (Figure 2.41.b) for different values of k. The thin black curve gives an upper bound associated with a value of $k = k_A = 18$ W.m^{-1}.K^{-1} and the thick red curve a lower bound associated with $k = k_M = 8$ W.m^{-1}.K^{-1}, respectively the austenite and martensite thermal conductivity. The blue curve is for an intermediate value of k. It is more likely that the heat sources are somewhere in between these upper and lower bounds.

Moreover, if along the sample and during the mechanical test, there is a phase transformation (e.g. martensite transformation), then the thermal conductivity $k(f_m)$ that depends on the microstructure will change during the test. In this case, thermal conductivity can be approximated with a linear rule of mixtures taking into account the martensite volume fraction f_m:

$$k(f_m) = f_m k_M + (1 - f_m) k_A \tag{2.63}$$

Depending on the phase transformation behaviour, two test configurations are possible:

1. **If the phase transformation is uniform ($f_m(M,t) = f_m(t)$)**, the thermal conductivity through the sample is uniform but changes during the test $k = k(f_m(t))$ depending on the martensite volume fraction (example of uniform A→M phase transformation). Therefore, eq. (2.64) can be simplified:

$$\begin{aligned} \text{div } \mathbf{q}(M,t) &= -k(f_m(t))\text{lap } T(M,t) && (2.64)\\ &= -\left(f_m(t)\ k_M + (1 - f_m(t))\ k_A\right)\text{lap } T(M,t), && (2.65) \end{aligned}$$

where k_A and k_M are the thermal conductivity of phases A and M respectively, $f_m(t)$ $(0 < f_m(t) < 1)$ represents the martensite fraction at time t. Heat source estimation is

[2]this test will be presented in detail in Section 5.2.2

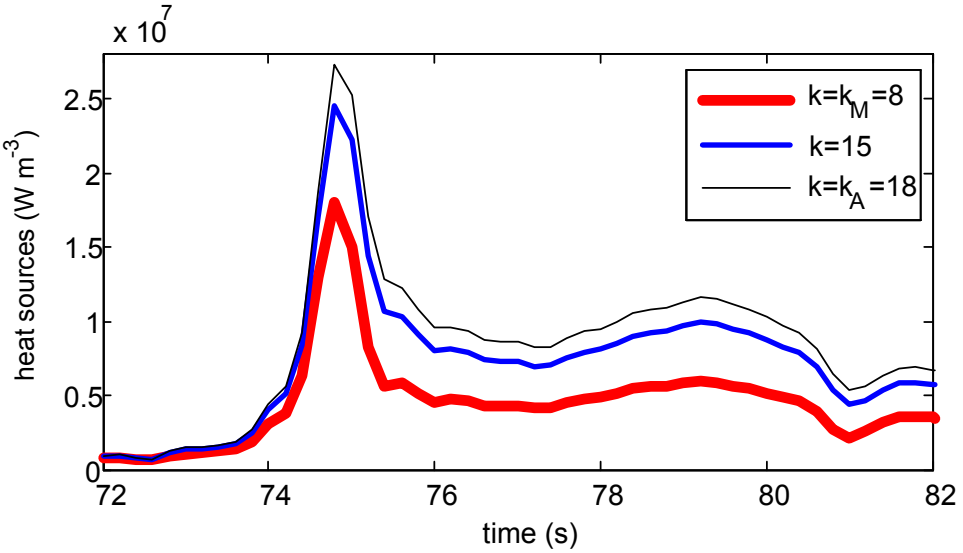

Figure 2.42: *Influence of the value of the thermal conductivity k on the heat source estimation; when the Laplacian operator plays a predominant role.*

therefore possible with an iterative process by estimating the martensite fraction. This method will be used in Section 5.3.

2. **If the phase transformation is localised**, the thermal conductivity is not homogeneous along the sample and eq. (2.64) cannot be simplified:

$$\begin{aligned} \text{div } \mathbf{q}(M,t) &= -\text{div } \big(k(f_m)\ \mathbf{grad}\ T(M,t)\big) \\ &= -k(f_m)\ \text{lap}\ T(M,t) - \mathbf{grad}\ k(f_m)\ \mathbf{grad}\ T(M,t) \\ &\neq -k(f_m)\ \text{lap}\ T(M,t). \\ &\neq -k\ \text{lap}\ T(M,t). \end{aligned} \tag{2.66}$$

Therefore, errors are made in the thin shell model when assuming this parameter constant especially during localised martensite phase transformation of NiTi. In Chapters 5 and 6 a first approximation of $-k(f_m)\ \text{lap}\ T(M,t)$ will be proposed.

2.6 Conclusions of chapter 2

This chapter has presented strain and temperature measurement techniques using DIC and infrared camera. In order to be able to compare and analyse the data given by the DIC software and the infrared camera, two post-processing softwares have been developed and validated using benchmark tests.

1. The first software performs spatial and temporal synchronisation of the data in order to observe, for every particle on the sample surface, both strain and temperature fields. The accuracy of the software will depend on the accuracy of the position of the characteristic points used to build the transformation matrix, the position of the cameras and the DIC accuracy.

2. The thin shell thermal model was extended to thin tubular geometries. For this second software, a numerical benchmark using finite element model has been developed to calibrate and validate the software. However, heat source estimation is very sensitive to filtering that needs to be adjusted almost manually. Moreover, estimation of the heat sources are difficult near the edge of the observation area and when the spatial resolution is low. Finally, some errors will be made if during the test, the thermal conductivity changes due to phase transformation.

Without spatial synchronisation, the heat sources are estimated on the spatial configuration. The energy estimation during a mechanical test, using a time integration of those heat sources will therefore induce some errors since they are estimated from spatial points. When those spatial synchronisation and heat source estimation are used together, it is possible to estimate the heat sources of every material points, and therefore the energy by time integration.

Experimental tests using simultaneous temperature and strain fields measurement will presented and analysed using both spatial synchronisation and heat source estimations on tubes and plates in Chapters 4, 5 and 6.

CHAPTER 3

Experimental set-up and material

Table of contents

3.1 Materials

Several samples of nearly equiatomic NiTi Shape Memory Alloys have been studied. These samples have different geometries, namely, plates and tubes, different thermomechanical histories and they display different phase transformations sequences.

3.1.1 Phase transformation characterisation

In order to characterise these materials, phase transformations of the samples was analysed using Differential Scanning Calorimetry (DSC) with a Diamond Perkin Elmer testing apparatus. For that purpose, specimens of weight ≈ 15 mg were cut from samples using a low speed diamond cut-off wheel in order to minimise the microstructure change. Prior to the tests, samples were also ground to remove the oxide layer.

During DSC measurements the specimen was rapidly heated up to 373 K, then the temperature was cooled down to 193 K at -10 K min^{-1}. Finally, the temperature was heated up to 373 K at 10 K min^{-1}. The DSC spectrum in Figure 3.1.a shows a typical temperature change of the specific heat released and absorbed by a specimen during the two last steps of the above procedure. The endothermic (up) and exothermic (down) peaks reveal phase transformations. Their start (subscript s) and finish (subscript f) temperatures have been estimated with the tangent method as depicted in Figure 3.1.a. Moreover, the latent heats released or absorbed during the phase changes have been determined by integrating areas between the peaks and their baselines, as shown by the colored areas sketched in Figure 3.1.a.

3.1.2 Plate P

Mechanical tests shown in Chapter 5 have been performed with the first type of samples cut from a Ti-50.6 at.% Ni plate of thickness $e = 0.5$ mm. This plate was processed in China by the company PeierTech. After being cold-rolled, the plate was solution treatment for 1 h at 1023 K and then age hardened at 773 K for 30 min.

DSC measurements of the thin plate are shown in Figure 3.1.a. Standard Austenite to Martensite and M$\rightarrow$A phase transformations occur upon cooling and heating, respectively. Transformation temperatures and enthalpies are summarised in Table 3.2.

3.1.3 Tubes T

As shown in Chapter 4, tensile tests were also performed on tubes with thin thicknesses. All these tubes were produced by Minitubes SA (Grenoble, France) by the following common processing route. Tubes were drilled from a 25 mm diameter NiTi cylindrical bar. The drawing consisted of a series of hot and cold drawings with intermediate annealings at 1023 K. Then, four cold drawings were performed without heat treatment. Finally, ageing heat treatments were performed. The heat treatments depended on the tube and will be specified

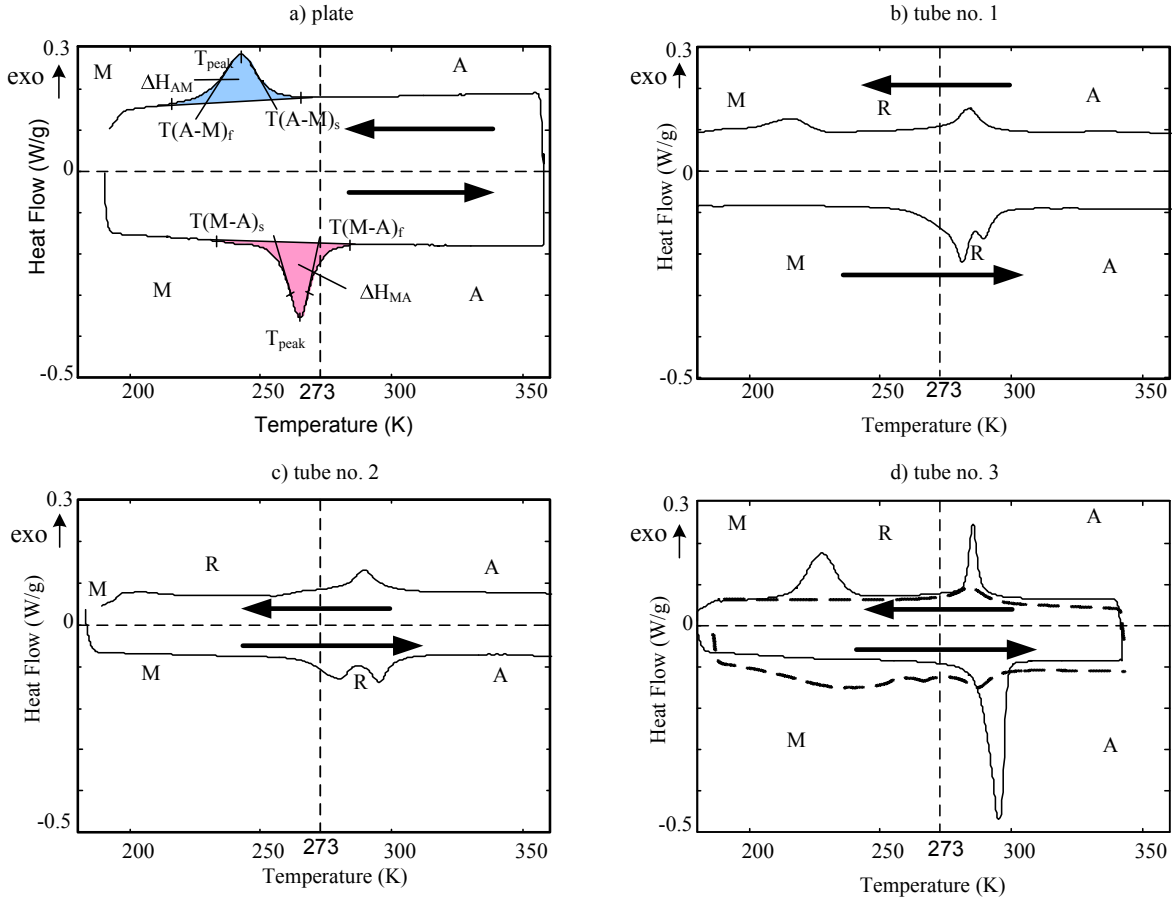

Figure 3.1: *DSC measurements for the plate, and tubular samples. For tube no. 3 the DSC before and after the ageing of 2 h at 775 K are plotted with dashed and solid lines, respectively.*

later.

3.1.3.1 Tube no. 1

Tube no. 1 has an external diameter of 6 mm, and a thickness of 0.12 mm. A final ageing heat treatment was performed at approximately 773 K for 15 min. Corresponding DSC measurements are shown in Figure 3.1.b. The tube exhibits a two-stage transformation upon both cooling and heating. Upon cooling, the first peak is associated with Austenite A→R-phase (labelled R) transformation, the second to R→M transformation. Upon heating, the two peaks correspond to M→R and R→A transformations, but the transformations overlap. Transformation temperatures and enthalpies are summarised in Table 3.2.

3.1.3.2 Tube no. 2

This tube has an external diameter of 10 mm and a wall thickness of 0.5 mm. The manufacturing route was the same as tube no. 1 except fewer hot drawings were performed since the outer diameter was higher. As for tube no. 1, an ageing treatment for 15 min at 773 K was performed after the cold drawing. Tubes 1 and 2 should therefore have nearly similar

microstructures and thermomechanical properties. As for the first tube, this tube exhibits a two stages A→R →M and M→R→A upon cooling and heating, respectively (see Figure 3.1.c). On cooling, the transformation R→M is not complete at the end of cooling. Upon heating, the two peaks overlap but their overlap were less pronounced than for tube no. 1 (see Table 3.2).

3.1.3.3 Tube no. 3

The third tube has an external diameter and thickness of 6.2 mm and 0.15 mm, respectively. After the common processing route, the tube was aged for 2 h at 775 K. The DSC measurements after are represented with solid line in Figure 3.1 and summarised in Table 3.2.d. After ageing, a single transformation M→A is observed upon heating. As for the other tubes, the tube exhibited a two-stage transformation A→R →M, upon cooling. Upon heating, the two-stages transformation M→R→A can hardly been observed from DSC, since the heating DSC curve only exhibits one peak (see Figure 3.1). Notice that DSC before the ageing has also been plotted in Figure 3.1 (dashed lines), showing the strong effect of ageing on phase transformations, that are hardly detected without it.

			Plate	tube no. 1	tube no. 2	tube no. 3
heating	M	$T(M\text{-}A)_s$	256 K			288 K
	↓	T_{peak} (A)	265 K			295 K
	A	$T(M\text{-}A)_f$	272 K			298 K
		$\Delta H(M\text{-}A)$	14 Jg^{-1}			21 Jg^{-1}
	M	$T(M\text{-}R)_s$		259 K	226 K	
	↓	T_{peak} (R)		280 K	280 K	
	R	$T(M\text{-}R)_f$		-	-	
		$\Delta H(M\text{-}R)$		-	-	
	R	$T(R\text{-}A)_s$		-	-	
	↓	T_{peak} (A)		286 K	296 K	
	A	$T(R\text{-}A)_f$		299 K	301 K	
		$\Delta H(R\text{-}A)$		-	-	
cooling	A	$T(M\text{-}A)_s$	253 K			
	↓	T_{peak} (M)	243 K			
	M	$T(M\text{-}A)_f$	229 K			
		$\Delta H(A\text{-}M)$	12 Jg^{-1}			
	A	$T(A\text{-}R)_s$		291 K	301 K	288 K
	↓	T_{peak} (R)		285 K	289 K	285 K
	R	$T(A\text{-}R)_f$		275 K	278 K	282 K
		$\Delta H(A\text{-}R)$		-	5.6 Jg^{-1}	4.7 Jg^{-1}
	R	$T(R\text{-}M)_s$		233 K	226 K	238 K
	↓	T_{peak} (M)		220 K	-	227 K
	M	$T(R\text{-}M)_f$		-	-	216 K
		$\Delta H(R\text{-}M)$		-	-	9.3 Jg^{-1}

Figure 3.2: *Summary of the DSC measurements*

3.2 Experimental set-ups

3.2.1 Overall "background"

To study the behaviour of NiTi under different thermomechanical loading conditions, several experimental set-ups have been used during this study. All tests were performed on conventional tensile testing machines. Two mechanical tensile testing machines were used, namely, a MTS 4M with a 20 kN load cell, and an Instron 5569 with a load cell of 50 kN. Various testing devices were mounted on the testing machines in order to subject SMA samples to tensile loading (see Figure 3.3, cf. Section 3.2.2) or to simple shear loading (see Figure 3.11, cf. Section 3.2.3).

As presented in Figure 3.3, infrared and visible cameras were used to obtain local temperature and displacement fields respectively. The infrared camera was a CEDIP Jade III MW with a maximum frequency of 145 Hz and a spatial resolution of 320×240 pixels. Two visible cameras were used, namely, a Hamamatsu with a spatial resolution 1280×1024 pixels and maximum frequency of 9 Hz, and a JAI with a spatial resolution 2000×2000 pixels and maximum frequency of 15 Hz.

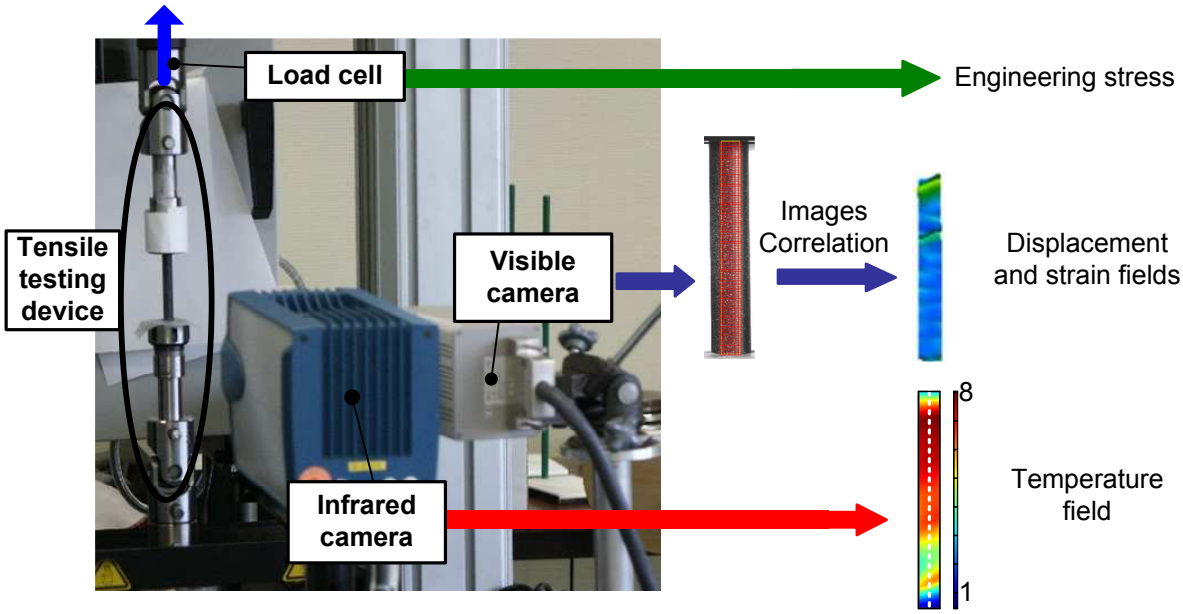

Figure 3.3: *Typical experimental set-up with its different acquisition systems. Example of tensile test performed on a tube.*

3.2.2 Tensile tests

As represented in Figure 3.4, a tensile sample (1) of initial length L_0 and section s_0 is mounted in grips. The bottom one (2) is fixed, whereas the upper one (3) can move. During the mechanical test, the sample is pulled up by the upper grip (3) at constant velocity $\dot{U}$. The cross-head displacement U as well as the axial load F are recorded during the test. The axial engineering stress ($\sigma_0 = F/s_0$) and engineering strain $\varepsilon_0 = U/L_0$ can then be estimated.

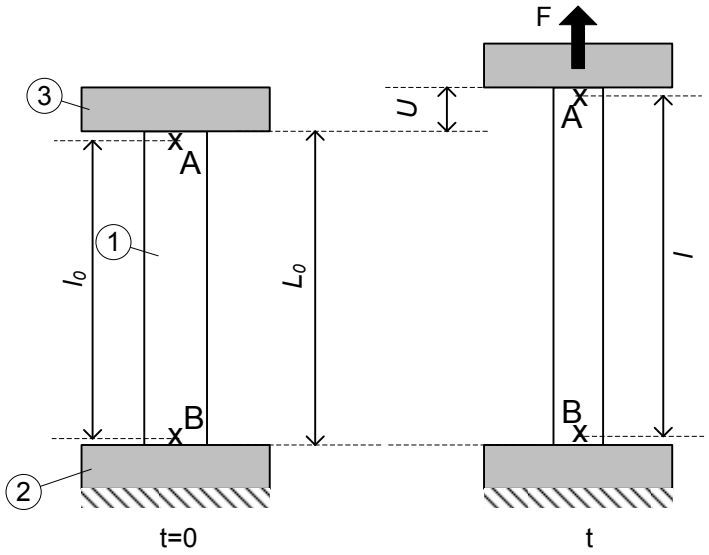

Figure 3.4: *Simplified schematic of a tensile test.*

Furthermore, due to our acquisition set-up (see Figure 3.3), thermal and kinematical fields were measured in an observation zone of length l_0 shorter than L_0. The current length l of this zone is deduced from optical measurements of the displacements of the material points A and B, allowing one to estimate a "global strain" $\varepsilon = \Delta l/l_0$ in a way similar to what could have been carried out with an usual extensometer.

The comparison of the engineering strain $\varepsilon_0 = U/L_0$ and the local axial strain $\varepsilon = \Delta l/l_0$ for a typical NiTi tensile test is shown in Figure 3.5. The last method allows one to avoid rigidbody displacements at the beginning of a test, deformation of the tensile machine or the gripping system and possible sample sliding within the grips.

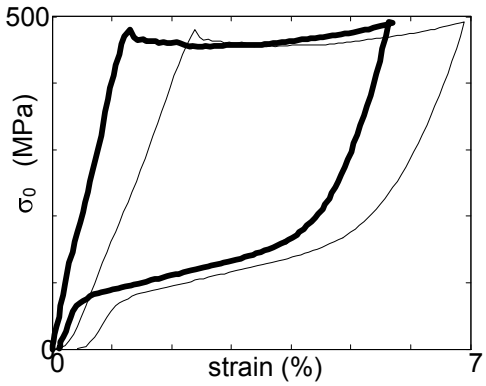

Figure 3.5: *Typical stress-strain curve obtained during a tensile test performed on a NiTi tube. Comparison of the engineering strain $\varepsilon_0 = U/L_0$ (thin line) obtained from the cross-head displacement U and the local axial strain $\varepsilon = \Delta l/l_0$ (thick line) obtained from the length change Δl measured by the DIC method.*

Plate samples were mounted on standard self tightening tensile grips. Due to their peculiar cylindrical shape, tube samples can unfortunately not be mounted on standard tensile grips. Therefore, two special gripping systems have been used to perform tensile tests on tubes. The first gripping system designed by Sandel (Sandel, 2000) is presented in Subsection 3.2.2.1. This gripping system was designed to minimise bending and torsion moments that might be

induced in the tube during its deformation. Unfortunately, only one size of tube can fit into it. In order to be easily able to change the tube size and thickness, a new universal gripping system has been designed. It will be presented in Subsection 3.2.2.2. Another advantage of this gripping system is the possibility of having a heat transfer fluid circulating inside the tube to perform tensile tests at controled temperature.

3.2.2.1 First gripping system for tubes

The first gripping system that minimised bending and torsion moments during a tensile test is schematised in Figure 3.6. The clamping blocks, at each extremity of the tube (1) are constituted of two half-cylinders (2), one pin (3) inserted inside the tube to avoid crushing the tube and two last parts (4). Each clamping block (2), (3), (4) is fixed to each of the two extremities of the tube by tightening the two half-cylinders (2) using two screws. Each clamping block is also connected to one of the two loading grips of the testing machine through two connectors (6) and (7) that are linked to the parts (4) via two sets of self-aligning washers (5). Such design has the advantage of being very easy and simple to set-up on the tensile machine.

The main disadvantages of this gripping system are that:

1. this gripping system prohibited observation of upper and lower parts of the tubes, as illustrated in Figure 3.6.a. Therefore, thermal and kinematic fields measurements are performed in a observation section of length l_0 much shorter than L_0;
2. the parts (2), (3) and (4) correspond to a given and fixed tube size, namely, they would have to be manufactured again when changing the tube dimension.

3.2.2.2 Second gripping system for tubes

Description of the gripping system and its temperature control device

In order to enable tensile tests on different tube diameters and thicknesses, a second gripping system has been designed and is shown in Figure 3.7.a. The tube is held by a pair of standardised FAHRION collets and collet holders with a very low taper (b, c, f). A pin (d) which was placed inside the tube (a), avoids crushing the tube. Both collets holders are linked to the universal testing machine via two driving shafts (h). However, this method does not avoid possible torsional moments that could be induced during the tests.

As presented in Chapter 1, NiTi presents a strongly exothermic or endothermic martensite phase transformation during tensile tests that can induce strong temperature variations and influence the mechanical response (Stalmans et al., 1992; Liu et al., 2006). Performing quasi-isothermal mechanical tests enables one to limit this thermomechanical coupling. So far, most of isothermal tensile tests on NiTi have been performed in either water or oil bath (Shaw and Kyriakides, 1997; Manach and Favier, 1997; Orgéas and Favier, 1998). In this case, the observation using infrared or visible cameras is not possible since water is opaque to infrared radiation and since DIC is very difficult to carry out with the flowing heat transfer fluid. To circumvent these difficulties and to acquire temperature and displacement fields during the

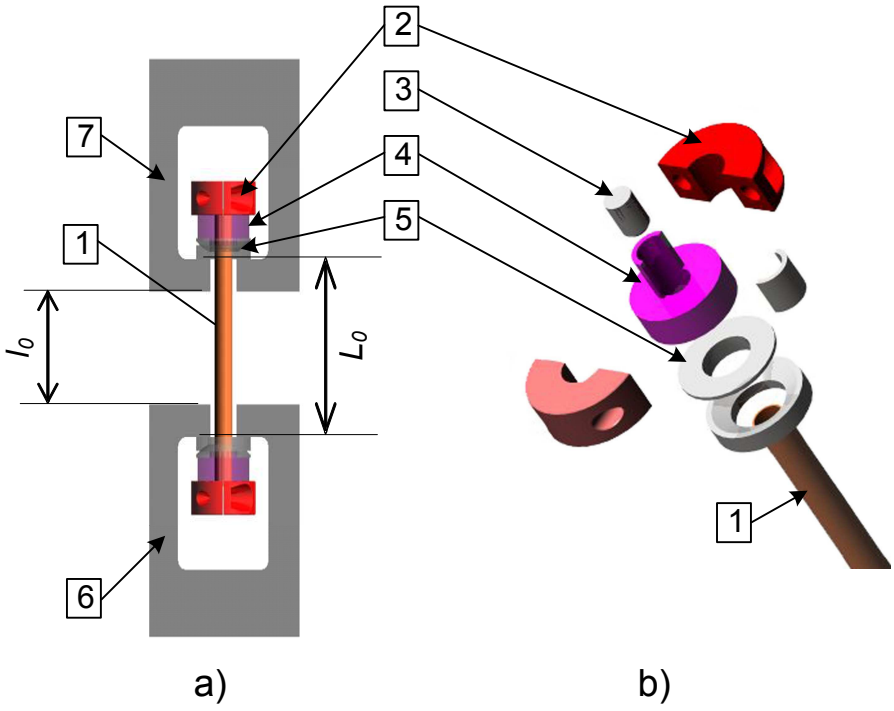

Figure 3.6: *Schematic of first gripping system for tubes: a) Tube specimen with the gripping system. b) Detail lf-aligning washers (5).*

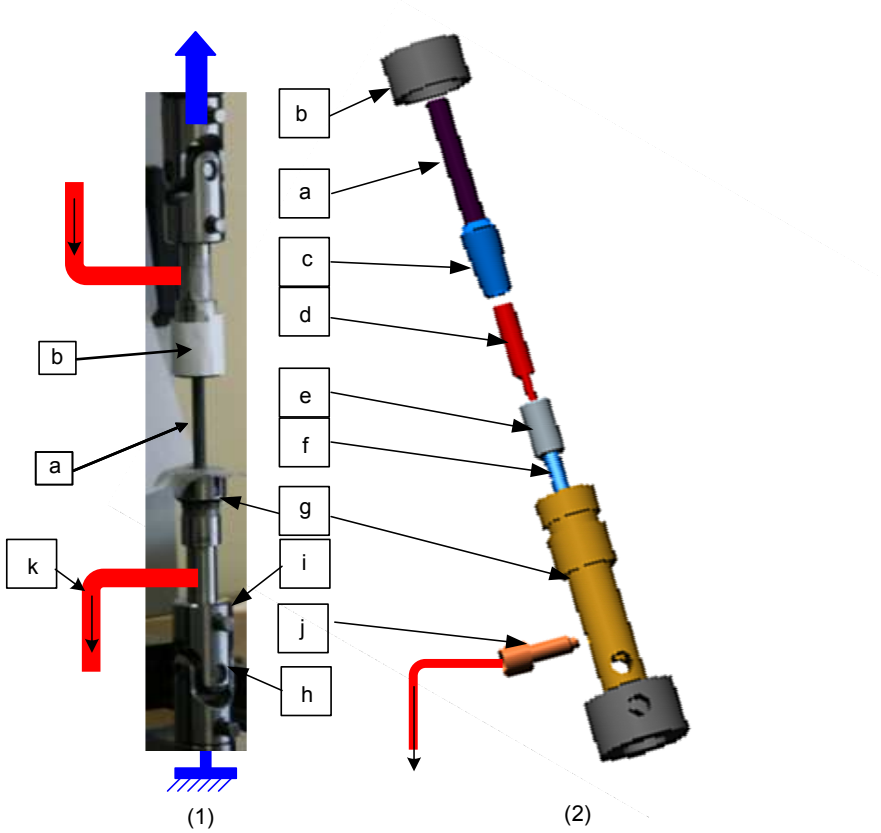

Figure 3.7: *Photograph (1) and schematic (2) of the universal gripping system together with the fluid circulation system.*

tests, Iadicola and Shaw (2002a) have controlled the temperature of thin wires (0.76 mm in diameter) by contact with a thermal conduction block behind it.

In order to make such measurements on tubes, the last gripping system was modified to allow the circulation of a heat transfer fluid (here water) inside the tube (Ramello, 2005), Figure 3.7. The temperature of the fluid was controlled using a thermocryostat (Julabo FP 50) with an accuracy of ±0.03 K. It was injected into the tube from the cryostat via two insulated pipes (k). Both insulated pipes are connected to the tube using the same mechanism. As represented in the bottom grip scheme in Figure 3.7.b, the pipe (k) is connected with two adaptors (f & j) to the free extremity of the pin (d) that was drilled in order to allow the fluid circulation. A Macor ceramic tube (e) was placed around (f) to limit heat losses.

Validation of the temperature control

To check the relevance of this system, two tensile tests have been performed on two identical Ti 50.8 at.% Ni thin tubes of external diameter 7.25 mm and thickness 0.19 mm. Both tubes were in an initial austenite state. The macroscopic strain rate was $\dot{U}/L_0 = 2\ 10^{-3}s^{-1}$. The ambiant temperature T_a was 293 K. The first test was performed with temperature control $T_{fluid} = T_a$. The second test was achieved at the same strain rate but without temperature control.

The mechanical responses of these two tests are represented in Figures 3.8.a and 3.8.b respectively. The graphs in Figures 3.8.c and d show the temperature variation (θ) along the vertical axis line at selected times on the stress plateau for each tensile test (see Figures 3.8.a and b).

- Despite a "rather high" macroscopic strain rate, the stress-strain curve recorded during the first test (with temperature control), exhibited two nice stress plateaux, both during loading and unloading. This behavior is typical of superelastic polycrystalline Ni-Ti SMAs for tensile test performed in air at a very low strain rate ($\approx 10^{-4}$ s^{-1}, Shaw and Kyriakides (1995); Ng and Sun (2006)) or performed in a thermally regulated fluid bath at higher strain rate ($\approx 10^{-3}$ s^{-1}, Shaw and Kyriakides (1995); Orgéas and Favier (1998)). As shown in Figure 3.8.c, the temperature variation along the length profile of the tube and for various deformation states is very weak ($\theta < 1$ K), so that the test can be considered as practically isothermal.
- On the contrary, when the fluid circulation was stopped (Figure 3.8.c), the horizontal stress plateau became inclined during loading and the tube was not superelastic anymore, namely, a significant residual strain of $\approx 2.5\%$ was observed after the test. Such behaviour is usually ascribed to thermomechanical couplings occurring during the deformation of the samples (Shaw and Kyriakides, 1995). This is confirmed from Figure 3.8.d. Upon loading, a significant increase of temperature along the length of the sample was recorded, so that at point c, $\theta = 12$ K. Such a temperature variation induces an increase of transformation stress (cf. Chapter 1, Clausius Clapeyron relationship).

The temperature control of the tube can therefore be considered as efficient with the cooling system.

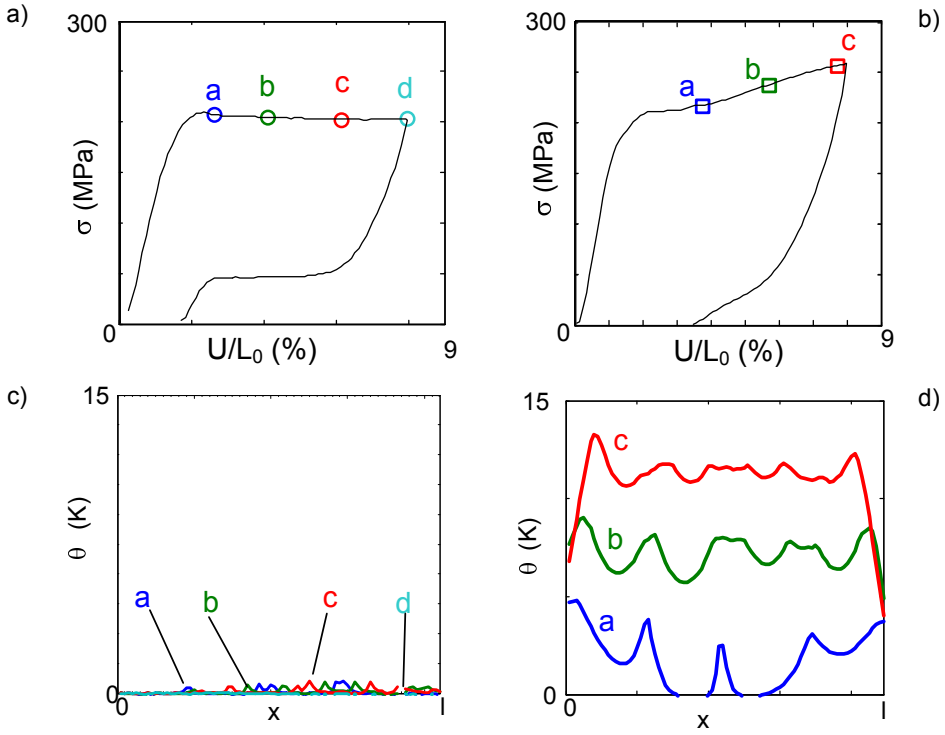

Figure 3.8: *Thermo-mechanical response of tensile tests performed at* $\dot{\varepsilon}_0 = 2\ 10^{-3} s^{-1}$ *with (left) and without (right) the temperature control system. a,b) Stress-strain curves. c,d) Temperature variation along the length of the sample.*

3.2.3 Simple shear tests

Performing shear tests on plates has many advantages to study the thermomechanical behaviour of NiTi. First, both shear and tensile samples can be machined from the same plate. It is then possible to compare for a same material the influence of loading. Second, shear tests enable cyclic or reversed deformation to be carried out. This type of test has already been successfully used to evaluate the mechanical properties of NiTi flat samples (Manach, 1993; Manach et al., 1995; Manach and Favier, 1997; Orgéas, 1997; Orgéas and Favier, 1998).

A brief description of the simple shear test and presentation of the shear test device are given in Sections 3.2.3.1 and 3.2.3.2. Then, the methods of estimation of the global shear strain will be briefly discussed in Section 3.2.3.3, through feasibility tests on a reference material (steel). The shear test device will then be quantitatively investigated using Digital Image Correlation measurements. First to check if the shear device was able to achieve correctly cyclic loadings (Section 3.2.3.5). Second to characterise the heterogeneity of the shear strain within the sample (Section 3.2.3.4). Then, to characterise the impact of sample height in Section 3.2.3.6. Finally, finite element simulation was carried out to identify the origin of the strain heterogeneities and to estimate the stress state (Section 3.2.3.7).

3.2.3.1 Description of a simple shear test

As shown in Figure 3.9, a simple shear test consists in deforming a volume of dimension $l_0 \times h \times e$ of a plate sample of initial dimension $L_0 \times h \times e$, by applying a vertical displacement

U_y on one edge of the sample whereas the opposite one remains fixed. Hence, the sample is subjected to a global shear strain $\overline{\gamma}_{xy} = U_y/l_0$ at a strain rate $\dot{\overline{\gamma}}_{xy} = \dot{U}_y/l_0$. During the test, the vertical load F_y is also measured by a load cell. This allows to estimate the mean shear stress $\overline{\tau}_{xy} = F_y/(eh)$.

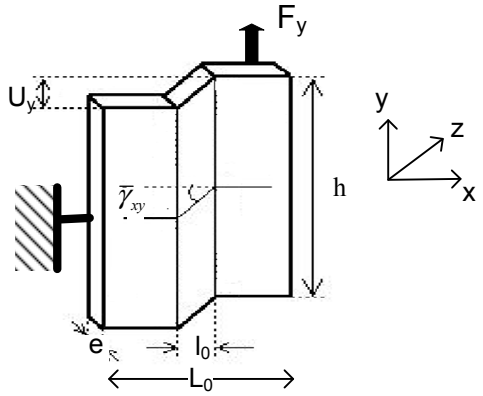

Figure 3.9: *Oversimplified scheme of a simple shear test.*

Due to free stress boundary conditions applied on the upper and lower gauge edges of the plates, the shear stress τ_{xy} is equal to zero in the horizontal edges of the plate. The shear stress is therefore not homogeneous as proved by Manach using finite element simulations with elastoplastic laws ((Manach, 1993, 1989) and presented in Figure 3.10.a). Similarly, the strain field is not homogeneous in these areas. G'Sell et al. (1983) have exhibited this phenomenon by painting small dot paints (Figure 3.10.b) on high density polyethylene HDPE samples. At large deformation ($\overline{\gamma}_{xy} = 2$ in Figure 3.10.b), the sample may be pulled out of the grips.

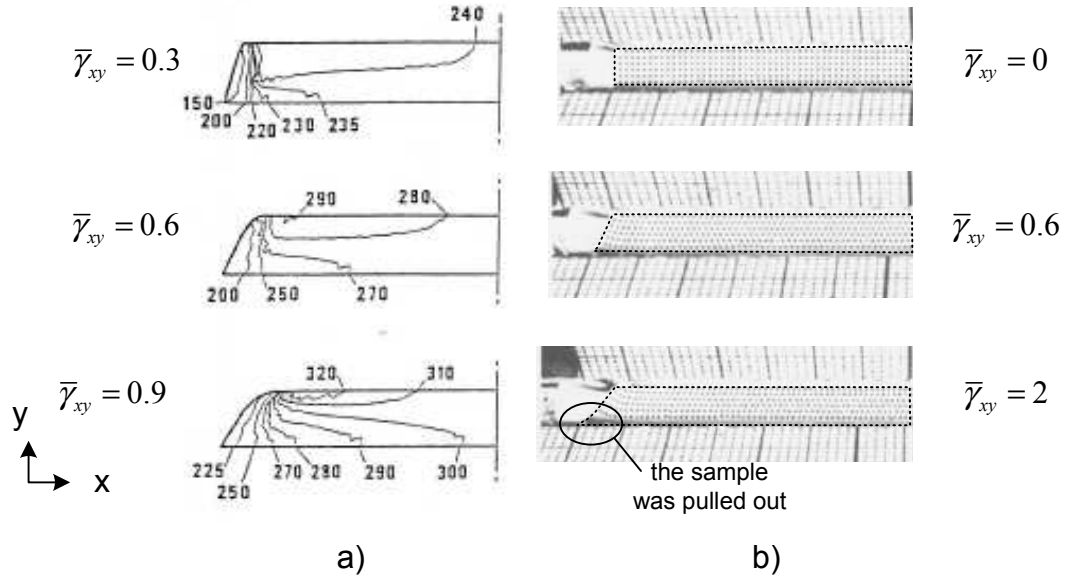

Figure 3.10: *a) Contours of the shear stress τ_{xy} in half of the shear sample estimated from finite element simulations (Manach, 1993). b) Qualitative observation of the displacement fields of a shear HDPE sample (G'Sell et al., 1983). The position of the sample has been emphasised using dotted lines.*

In order to reduce the influence of free edges effects it is recommended to use a sample height at least ten times bigger than its shear width, i.e. $h/l_0 \geq 10$ (G'Sell et al., 1983; Manach, 1993). Moreover, during a simple shear test, the sample experiences compressive stress along a direction inclined at 45° to the shearing direction: G'Sell et al. (1983) have shown that to avoid plastic buckling along such a direction, the ratio e/h should not be too small. In our case we did not observe such a buckling on our samples.

3.2.3.2 Description of the shear device

The testing device previously designed by Manach (1993) has been used. Its oversimplified schematic and photography are presented in Figure 3.11. Mounted on a conventional tensile testing machine, this device imposes parallel and vertical relative displacements of two lateral grips (1) and (2). The sample (3) is clamped between the two grips (1) and (2), both attached to the moving part (4) and the fixed part (6) of the apparatus respectively. The relative motion between (4) and (6) is obtained by pairs of linear guides symmetrically positioned with respect to the sample. The applied load is measured by a 20 kN load cell (7) and the relative displacement of the grips by the cross head displacement or a LVDT extensometer (5). This displacement can also be captured after a proper preparation of the sample by DIC and by using a visible camera (Figure 3.11.b). The temperature field was also recorded during the shear test using an infrared camera (Figure 3.11.b). Since the shear width l_0 is very narrow (l_0=3 mm), the IR and visible cameras were placed on top of each other. The heights of samples ranged between h=20 and 50 mm. The sample width was L_0 = 18 mm, and the gauge length l_0 = 3 mm was fixed by the device geometry.

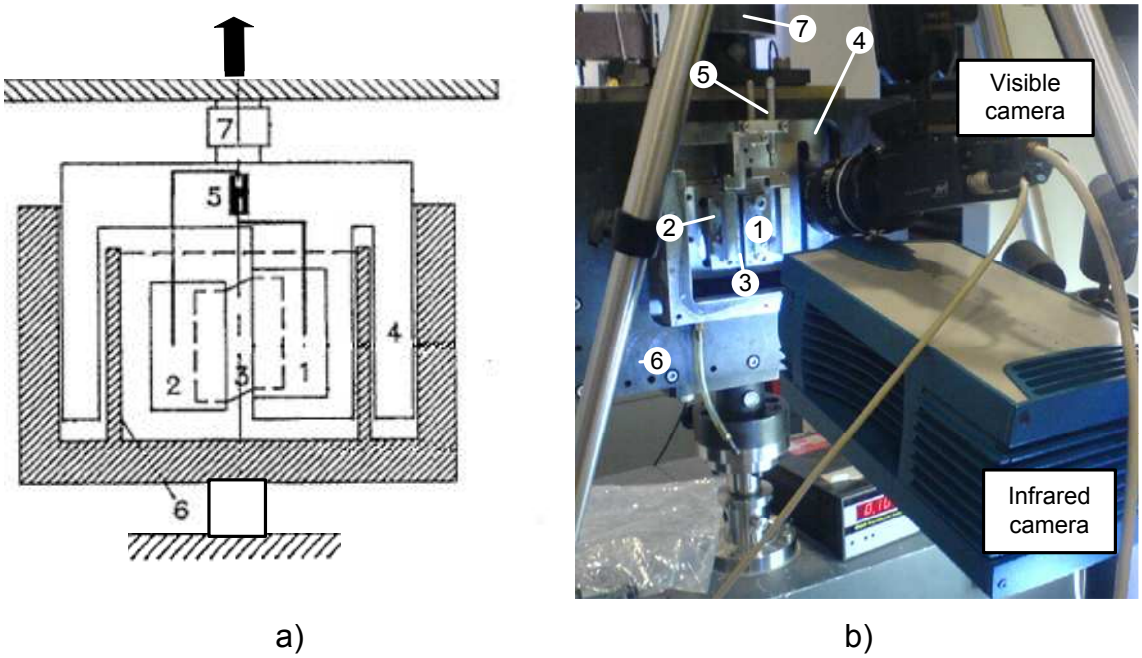

Figure 3.11: *a) Schematic view of the simple shear testing apparatus. 1, moving grip; 2, fixed grip; 3, sample; 4, upper frame part moving; 5, LVDT; 6, lower frame part fixed; 7, load cell. b) Photography of the device with the visible and IR cameras.*

3.2.3.3 Estimation of $\overline{\gamma}_{xy}$

The measurement of the shear strain $\overline{\gamma}_{xy}$ is quite complex (Wack and Tourabi, 1993). Several methods are possible (Manach and Favier, 1997). We have compared them during feasibility tests performed at a cross head velocity $\dot{U} = 0.03$ mm s^{-1} on a 301LN stainless steel plate sample (hereafter referred to as sample 1) produced by ArcelorMittal. The sample height was 30 mm, its total width 18 mm, its gauge width 3 mm and its thickness 1 mm. The sample surface was coated with black and white paints to obtain a random texture (Figure 3.12.a) in order to estimate displacement field using DIC during the test.

- The simplest method is to use the cross head displacement U ($\overline{\gamma}_c = U/l_0$) as plotted with thin line in Figure 3.12.b.
- Another method consists in using a LVDT to measure more precisely the relative motion of the grips. $\overline{\gamma}_{LVDT}$ is represented using dashed line in Figure 3.12.b.
- Manach and Favier (1997) have also tried to obtain directly the shear strain on the material by drawing one horizontal and one vertical line in the middle of the sample surface. The variation of the angle between these two lines was then estimated after recording images of the sample during the deformation. This technique was not tested in our samples since their surfaces were covered by black and white texture paint to perform DIC.
- Using DIC method enables to obtain the displacement field of every points of the correlation grid. As already done during tensile test, it is therefore possible to obtain $\overline{\gamma}_{AB} = (dy_A - dy_B)/l_{AB}$ (red thick dash lines in Figure 3.12.b) by comparing the displacement of two points AB located near the grips (see labels A and B in Figure 3.12.a).
- By noting s the area of correlation zone, a mean shear strain $\overline{\gamma}_{xy} = \frac{1}{s}\int_s \gamma_{xy}\, ds$ can also be estimated over a large area using the shear strain field γ_{xy} measured by DIC. The thick continuous line in Figure 3.12.b was estimated from the average of γ_{xy} over the area selected in Figure 3.12.a.

Comparison of curves in Figure 3.12.b shows that estimation of $\overline{\gamma}_{xy}$ using the displacement recorded by a LVDT extensometer is more accurate than using the cross head displacement since it avoids uncertainties induced by rigid body displacements at the beginning of the shear test. However, in case of rotation or miss orientation of the LVDT, some error can still be induced. Moreover, as already mentioned by Manach and Favier (1997), estimating $\overline{\gamma}_{xy}$ directly on the surface of the sample using DIC is even more accurate than using LVDT sensor with respect to the grips. For this material, the two methods used with DIC to estimated $\overline{\gamma}_{xy}$ are more accurate and give similar results. As a matter of simplicity, in the next analysis $\overline{\gamma}_{xy}$ will be estimated using DIC from the displacements of two points A and B.

3.2.3.4 Analysis of the local strain field γ_{xy}

DIC was used to quantitatively characterise the heterogeneity of the strain field within the deformed samples. Figure 3.13.b represents, for sample 1 that has been presented in the previous section, γ_{xy} strain fields maps plotted on the sample at the selected time marked

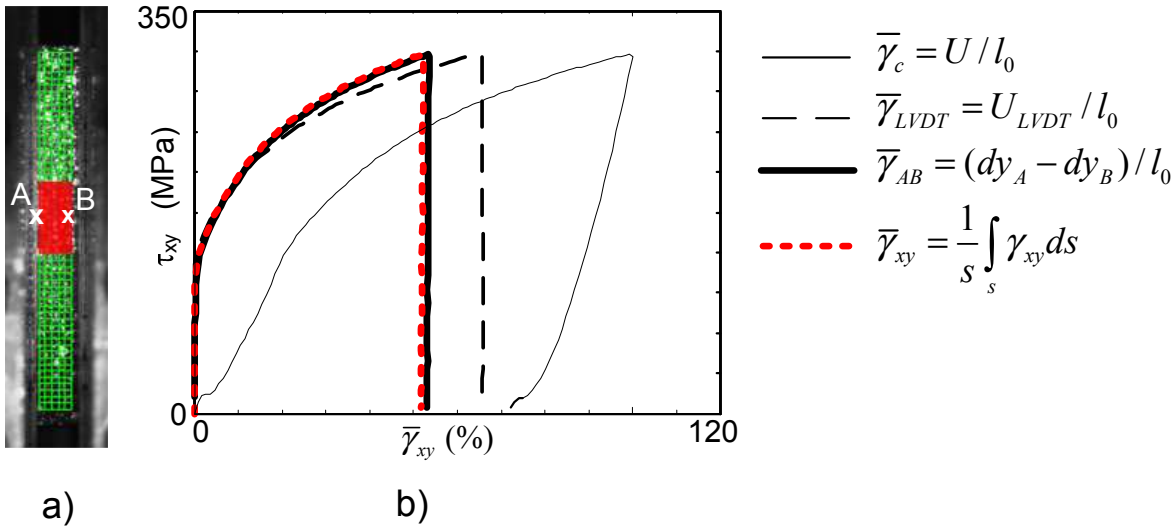

Figure 3.12: *Comparison of the method of estimation of $\overline{\gamma}_{xy}$ during shear test on a 301LN stainless steel plate. a) Shear sample image with the correlation grid in green. A and B are two selected points in the middle of the sample. The red area corresponds to a selected area. b) Stress strain curve ($\overline{\tau}_{xy} = f(\overline{\gamma})$ with different methods of estimation of $\overline{\gamma}$: estimation of $\overline{\gamma}$ using the cross-head displacement $\overline{\gamma}_c = U/l_0$; using the LVDT measurement $\overline{\gamma}_{LVDT} = U_{LVDT}/l_0$; using the vertical displacement of the two extremes particles labelled A and B in a) $\overline{\gamma}_{AB} = (dy_A - dy_B)/l_0$; or using the mean shear strain in a selected area (red area highlighted in in a) $\overline{\gamma}_{xy} = \frac{1}{s}\int_s \gamma_{xy}\, ds$.*

in Figure 3.13.a. The shear strain was not homogenous within the sample, this trend being amplified as the strain is increased. At time e, $0.4 < \gamma_{xy} < 0.66$.

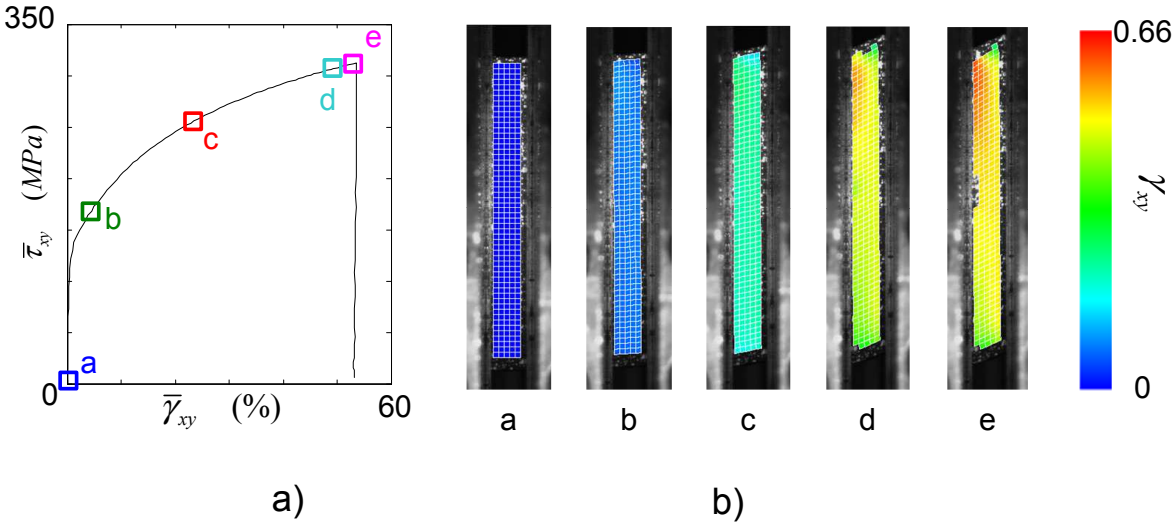

Figure 3.13: *a) Stress strain curve of the steel sample 1. b) γ_{xy} strain field on the sample at the times marked in a).*

To analyse more closely the homogeneity of the shear strain, γ_{xy} profiles represented in Figure 3.14.c up to 12 % of strain along two horizontal lines sketched in Figure 3.14.b. Due to the low spatial resolution of DIC, the strain fields along the horizontal lines are only described with 5 virtual subsets.

Along the horizontal lines (Figure 3.14), γ_{xy} strain field exhibited three distinct zones.

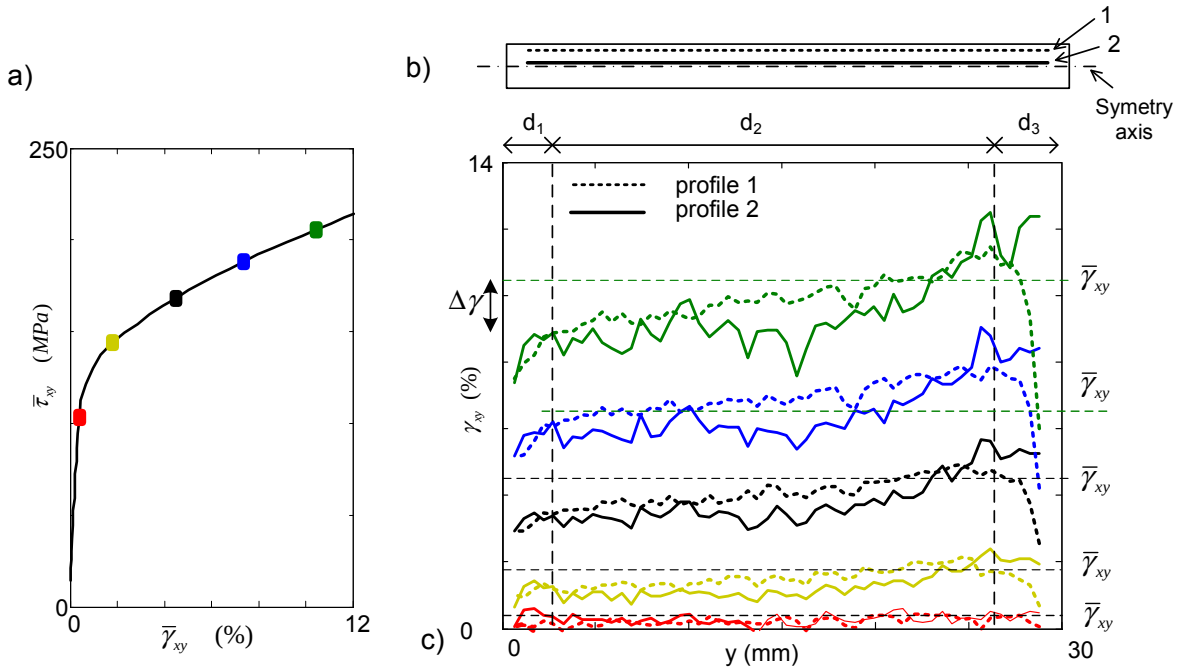

Figure 3.14: *a) Stress strain curve of the steel sample 1. b) Schematic of the sample (turned by -90°) with the position of the vertical profiles selected. c) γ_{xy} strain field along the vertical lines at the selected times marked in a).*

- d_1 and d_3: near the free ends of the sample, boundary effects disturbed the strain homogeneity $d_1 \approx d_3 \approx 3$ mm.
- d_2: in the middle of the sample height (zone d_2), the strain field γ_{xy} was almost homogeneous. However, some differences with the mean shear strain $\overline{\gamma}$ can be noticed in the x direction (i.e. differences between profiles 1 and 2) and in the y one. In this direction, a small gradient could thus be observed for profiles 1 and 2 (Figure 3.14). Such evolution (noted γ_{mean} in Figure 3.15) of the shear strain along the y axis was also obtained in the finite element simulation described in Section 3.2.3.7. As suggested by the simulation results, this evolution in the y direction is linear.

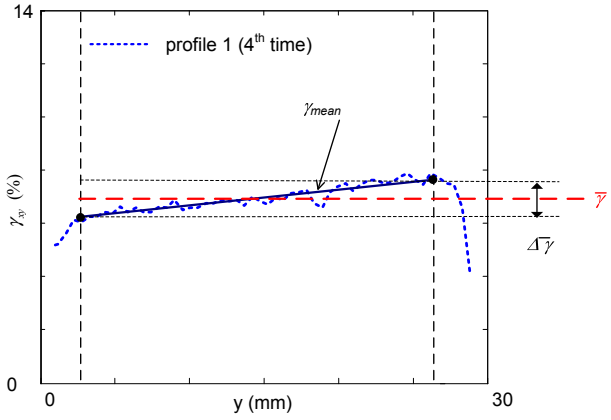

Figure 3.15: *Schematic showing a linear evolution along the y direction of the shear strain (γ_{mean}), the maximum difference ($\Delta\overline{\gamma}$) between the extreme values of γ_{mean} and the mean shear value $\overline{\gamma}$.*

In order to quantify (i) the accuracy of the shear strain field measurements and (ii) the dispersion of the shear strain γ_{xy} around the mean value $\overline{\gamma}$, we have computed for

profile 2 data:

- the scatter of γ_{xy} with the relation: $\Delta\gamma = 6\, std(\gamma_{xy} - \gamma_{mean})$, where γ_{mean} is a linear evolution obtained by least squares optimisation;
- the maximum difference, noted $\Delta\overline{\gamma}$, between the extreme values.

The evolution with the mean shear strain $\overline{\gamma}$ of these two quantities are plotted in Figure 3.16.a and shows that :

- the evolution with $\overline{\gamma}$ of the scatter $\Delta\gamma$ (noise of the DIC measurement technique) is week, the amplitude of $\Delta\gamma$ is limited to 2 % for $\overline{\gamma}$ up to 20 %,
- amplitude ($\Delta\overline{\gamma}$) of the shear strain heterogeneity increases linearly with $\overline{\gamma}$. The ratio $\Delta\overline{\gamma}/\overline{\gamma}$, plotted in Figure 3.16.b, indicates that after 5 % the heterogeneity of the strain field is less than 20 % of the mean value $\overline{\gamma}$ and after 8 % it stabilises at 16 %.

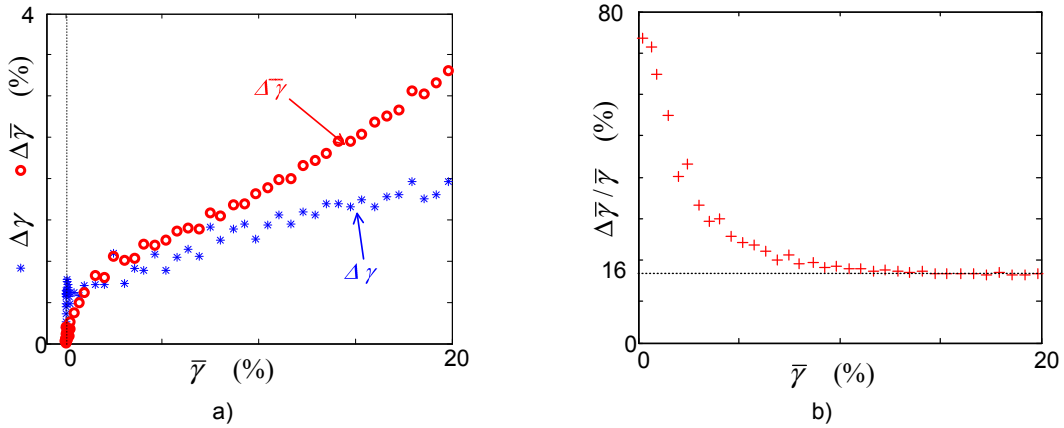

Figure 3.16: *a) Evolution, with the mean shear value $\overline{\gamma}$, of the maximum difference ($\Delta\overline{\gamma}$) and the dispersion $\Delta\gamma$. b) Evolution of the ratio $\Delta\overline{\gamma}/\overline{\gamma}$ with $\overline{\gamma}$, showing the "relatively weak" (less than 20 % after $\overline{\gamma}$=5 %) heterogeneity of the shear field in the y direction*

3.2.3.5 Symmetry of the shear device

In order to better understand the origin of the strain gradient observed previously and to check if the shear device was able to achieve correctly cyclic loadings, a second test was performed on another sample (sample 2). The loading path was τ_{xy}=0 MPa→+300 MPa →0 MPa for sample 1, and τ_{xy}=0 MPa→ -300 MPa → 0 MPa for sample 2. The cross head velocity was $\dot{U} = 0.03$ mm s^{-1}. The stress strain curves $|\overline{\tau}_{xy}| = f(|\overline{\gamma}_{xy}|)$ for the two tests are superimposed in Figure 3.17.a. In Figures b and c, the $|\overline{\gamma}_{xy}|$ profiles along the red line have been plotted at mechanical state marked in Figure 3.17.a for samples 1 and 2. For both tests, the strain fields exhibited a small gradient. However, the direction of this gradient depended on the loading direction. With regards to both mechanical responses and strain fields in the two loading conditions, this shear device can achieve correctly cyclic loadings at least for strain levels below 30 % (d) and it is more likely that the strain gradient observed is imposed by the loading conditions.

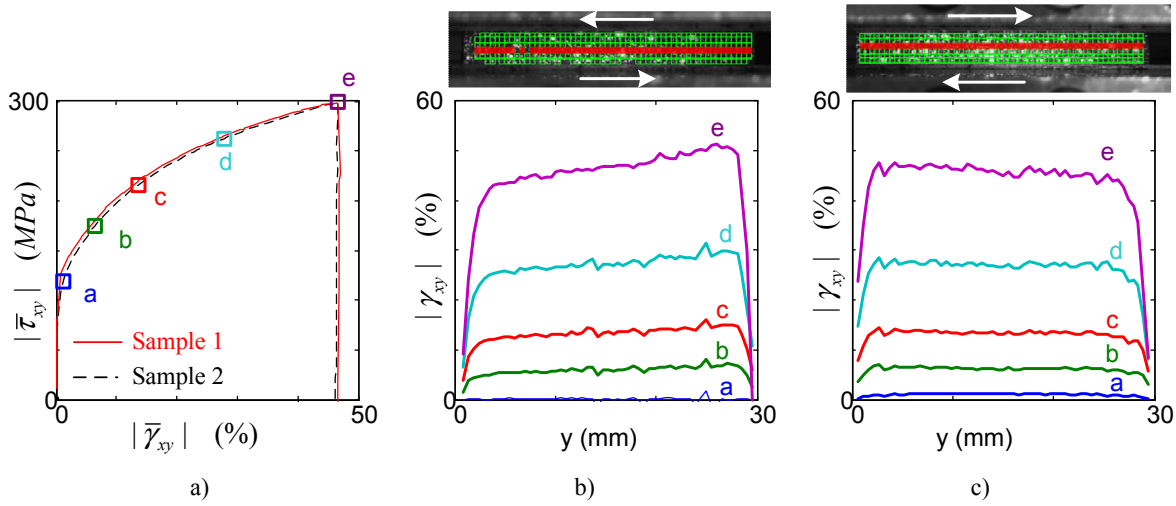

Figure 3.17: *Analysis of the symmetry of the gripping system. a) Comparison of* $|\tau_{xy}| = f(|\overline{\gamma}_{xy}|)$ *for the two tests.* $|\gamma_{xy}|$ *strain field along the selected profile marked in red during the first loading for sample 1 (b) and sample 2 (c).*

3.2.3.6 Influence of the sample height

Sample height influence on the homogeneity of γ_{xy} was tested using two other shear samples of the same plate of height 50 mm and 20 mm respectively. For these two shear tests, the loading paths and crosshead velocity were identical to the first 30 mm high plate sample: $\tau_{xy} = 0$ MPa $\rightarrow +300$ MPa $\rightarrow$ 0 MPa. Figure 3.18 shows the profiles of the three tests during loadings.

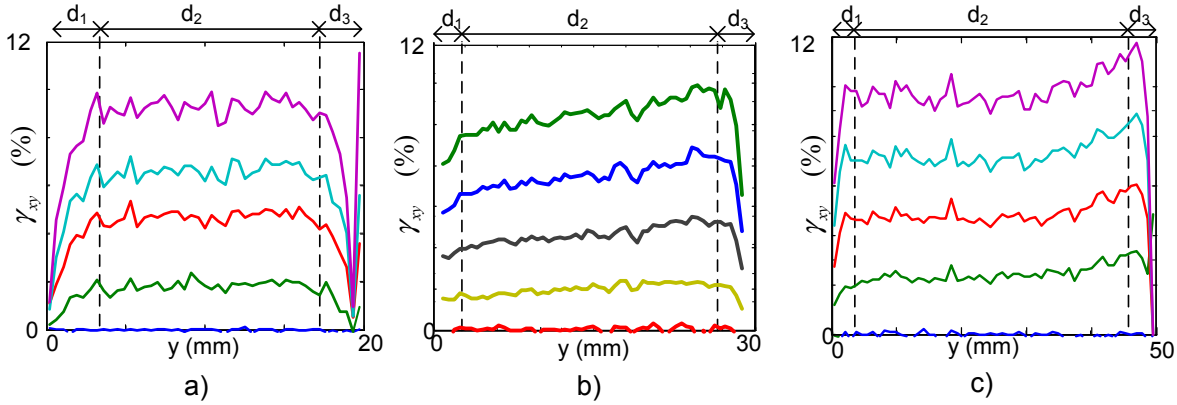

Figure 3.18: *Vertical profiles of* γ_{xy} *during loading for a) sample of 20 mm height , b) sample of 30 mm height, and c) sample of 50 mm height.*

The size of the edge effects (d_1) and the homogeneous zone (d_2) were estimated. The length of the non homogeneous zones (d_1 and d_3) were almost constant ($\approx$ 3 mm). This result confirms what G'Sell et al. (1983) said and will allow us to use plates with 20 mm height after removing 3 mm height of each edges during the analysis.

3.2.3.7 Comparison and validation using finite element simulations

Finite element simulations, similar to those performed by Manach (1993), have been carried out by Latil (2008) in order to better understand stress-strain states during the simple shear deformation of the steel sample. We have tried to compare simulation results to experimental ones, obtained previously for the local shear strain. In case of satisfactory comparison, this will allow us to obtain an estimation of the local stress distribution within the sample.

For the sake of simplicity, plane stress conditions were assumed. The geometry and the boundary conditions of the simulated simple shear test are represented in Figure 3.19.a and were chosen as close as possible to the experiment. The displacements along the direction x and y are denoted by U and V. The top and bottom edges are free. The left boundary is fixed ($U = V = 0$) and the right one is moving vertically at constant velocity ($U = 0$, $V = 0.03\,t$, where t represents the time) which corresponds to a shear strain rate of 0.01 s^{-1}.

This model was implemented in Comsol 3.2 by using regular quadrangle mesh with quadratic polynomial interpolation and large transformation elastoplastic with isotropic hardening constitutive law. The parameters of the law (shear modulus G_1, strain hardening G_2, τ_A) were manually estimated from the feasibility stress-strain curve in order to minimise the difference with the experimental results.They are summarised in Table 3.1. Comparison between the experimental feasibility test stress-strain curves and the constitutive law chosen is plotted with blue solid line and red dotted line respectively in Figure 3.19.b. This figure shows that the constitutive law fits well the experiment.

G_1 (MPa)	G_2 (MPa)	τ_A (MPa)
25770	812	129

Table 3.1: *Comsol constitutive law coefficients*

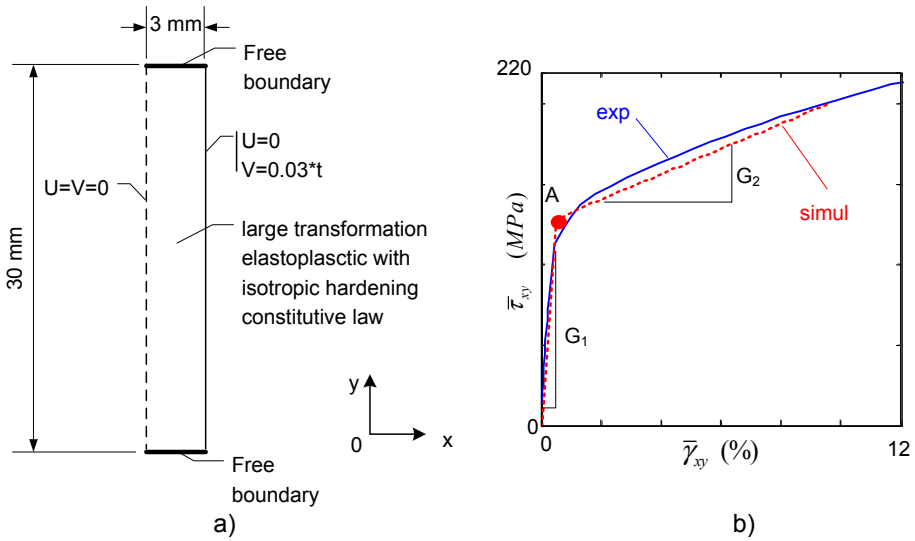

Figure 3.19: *Simulation of the simple shear test. a) Geometry and boundary conditions. b) Mechanical response of the feasibility test obtained in the experiment (continuous blue line) and numerical model (dotted line), with its coefficients.*

Experimental and simulated strain fields for two selected profiles are presented in Figure 3.20, at different loadings. Comparison of the profile near the edge (Figure 3.20.b) shows

that the simulated shear field is not homogeneous but present a gradient. This gradient was also observed experimentally (Figure 3.20.c thick line) when the profile was chosen in the middle of the sample. On the contrary, the simulation in the mid-profile did not present any gradient.

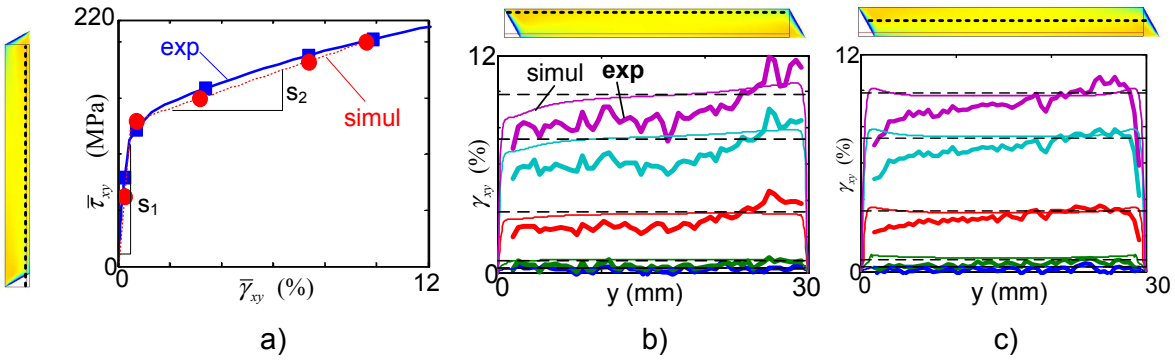

Figure 3.20: *a) Comparison of the mechanical response between the experiment (continuous line) and simulation (dashed line). b-c) Comparison of γ_{xy} shear strain field at selected times marked in a) the result from the simulation are plotted with thin line and the results from the experiment with thick line. b) comparison for a profile near the edge of the sample. c) Comparison for a profile in the middle of the sample. The images, plotted in the to, represent γ_{xy} shear strain field map given by the simulation at the end of loading, the dotted line show the position of the selected profiles.*

The comparison between the simulated and experimental shear strains, we conclude that the strain gradient experimentally observed along the vertical axis has several origins: first it is induced by boundary conditions of the simple shear test; second, the sample can be pulled out of the grips near the top and bottom extremities; finally, at the beginning of the shear test a small rotation of the grips is experimentally observed. Such small rotation may induce non pure simple shear loading and therefore non homogeneous shear stress.

Since the comparison between simulated and experimental shear strain fields is good, it is possible to estimate local shear stress (τ_{xy}) and mean shear stress ($\overline{\tau}_{xy}$) by simulation. Shear stress τ_{xy} profiles are shown in Figure 3.21. Due to the free extremities, τ_{xy} became equal to zero near the upper and lower edges ($y = 0$ and y=30 mm). In the middle, τ_{xy} was almost homogeneous. The vertical dotted lines represent the limit of the mean stress ($\overline{\tau}_{xy} = \frac{1}{s}\int_0^l \tau_{xy}(x_0, y)\, dy$) estimated on the edge of the sample $x_0 = 3$ mm. This mean stress corresponds to the nominal shear stress $F_y/(eh)$ measured during the experiments.

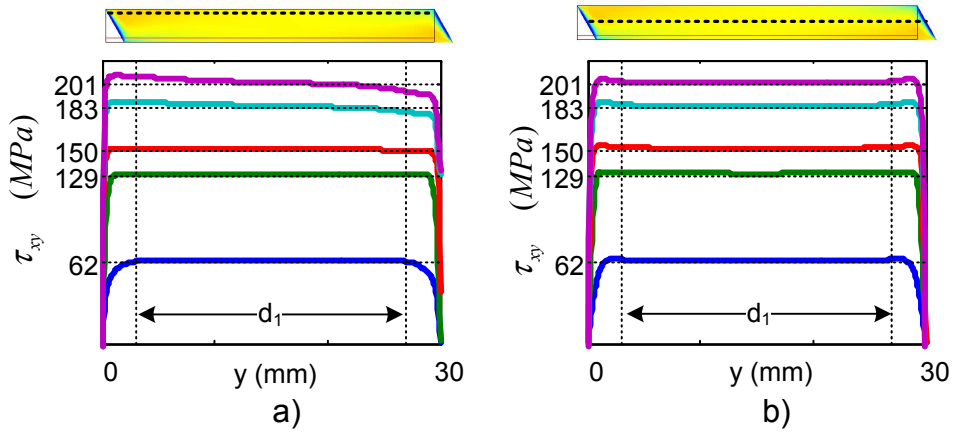

Figure 3.21: *Simulated shear stress τ_{xy} profiles along the line on the edge of the sample (a) in the middle of the sample (b) at several mechanical loadings (selected in Figure 3.20.b with red dot). The vertical dotted line indicates the limit of the mean stress along the line in zone d_2. The horizontal dotted lines represent the mean stress ($\overline{\tau}_{xy} = \frac{1}{s}\int_0^l \tau_{xy}(x_0, y)\, dy$) estimated on the edge of the sample $x_0 = 3$ mm*

Finite element simulations have shown that the mean stress $\overline{\tau}_{xy}$ (corresponding to the measured stress $F_y/(eh)$) is close to τ_{xy} shear stress field in the area d_2 ($|\tau_{xy} - \overline{\tau}_{xy}| < 3$ MPa for $\overline{\tau}_{xy} = 201$ MPa). Outside this area d_2, τ_{xy} field decreases due to the boundary conditions. In the following analysis we will therefore assume that the shear stress field τ_{xy} is homogeneous inside the area d_2 and that the nominal shear stress $F_y/(eh)$ is a good approximation of the global and local shear stress:

$$\frac{F}{s_0} \approx \overline{\tau}_{xy} \approx \tau_{xy}. \tag{3.1}$$

3.3 Conclusion

The different polycrystalline NiTi SMAs used during this work have been presented in this chapter. Then, the experimental set-up that allows both temperature and strain field measurement and the different gripping systems were presented. The gripping systems to perform tensile tests on tubes were of two types, namely, the first one had the advantage of being very easy and simple to set-up but it prohibited observations of upper and lower parts of the tubes and it was designed for only one size of tube (tube no. 1), the second was designed to hold tubes of different diameters and thicknesses. Moreover, this gripping system was designed to enable temperature control via circulation of a fluid inside the tube. The efficiency of the temperature control was checked by comparing temperature field of two tensile tests at the same temperature on a NiTi tube, namely, the first one without temperature control and the second one with temperature control. However, this gripping system does not avoid possible torsional moments that could be induced during the tests.

Finally, the gripping system to perform shear tests on plate was presented. Comparison of different methods to estimate the mean shear strain $\overline{\gamma}_{xy}$ have shown that measuring $\overline{\gamma}_{xy}$ using DIC gives a better estimation than using standard LDVT and will be used in the following. Experimental and simulated results have shown that, in the middle zone of length d_2, both strain γ_{xy} and stress τ_{xy} fields were almost homogeneous. However, the shear strain field is not exactly constant in the middle zone d_2, a small gradient was observed. The direction

of this gradient depends on the loading direction and represents less than 20 % of the mean shear and was mostly intrinsic to simple shear tests. Outside the zone d_2, both strain γ_{xy} and stress τ_{xy} fields decrease due to boundary conditions. The length of the non-homogeneous zone represents 3 mm of the sample height. Therefore, in the further shear tests, samples with height ranging from 20 to 30 mm height will be tested and only the zone d_2 will be kept for analysis. In this zone, the stress field τ_{xy} can be approximated with $\tau_{xy} \approx \overline{\tau}_{xy} \approx F_y/(eh)$ and the shear strain field γ_{xy} by the mean strain estimated from the displacement of two extreme points $\gamma_{xy} \approx \overline{\gamma}_{xy} \approx (y_B - y_A)/l_0$.

CHAPTER 4

Tensile tests on NiTi tubes exhibiting A-R-M phase transformations

Table of contents

4.1 Introduction

As presented in Chapter 1, most models and constitutive equations of the superelastic behaviour of NiTi are based on the conventional understanding of superelastic tensile test. However, the mechanical response (conventionnal stress-strain curve, see Figure 1.4.b) does not give any information on localization phenomena and call into question the validity of using simple tensile tests for determining the parameters of shape memory alloys. Despite the knowledge that have been brought by the many previous cited studies on NiTi behaviour, some questions still remain opened, during the homogeneous stages:

1. What are the mechanisms of deformation during stages 1, 4 and 6 ?
2. What are the parameters that influence these homogeneous deformation stages?

And during the localized stages:

1. Which parameters affect the initiation, propagation and growth of the localization bands ?
2. How are the thermomechanical (strain, stress, temperature, heat sources) and the metallurgical (phase type and fraction) data within the interior and exterior of the bands and in the narrow region between them ?

3. What is the link between the localization and conventional macroscopic strain and stress values that are measured during a tensile test?

With the development of full field measurement techniques presented in Chapter 2, this chapter focuses on providing some possible answers to the above questions for tensile tests on NiTi polycrystalline thin walled tubes.

4.2 First observations and analysis

4.2.1 Material and experimental procedure

Tensile tests have been performed on a piece of the tube no. 1[1] (100 mm in length). To ensure a fully austenitic initial microstructure, before being clamped, the tube was heated up to 373 K, i.e. 75 K above $T(R-A)_f$, and cooled down to room temperature $T_0 = 297$ K. Tensile tests were conducted in air at constant cross head velocity $\dot{U}$. The thermal and kinematics fields were measured in an observation section of length l_0 shorter than the gauge length L_0, as illustrated in Figure 4.1. Spatial resolution (pixel size) of the temperature

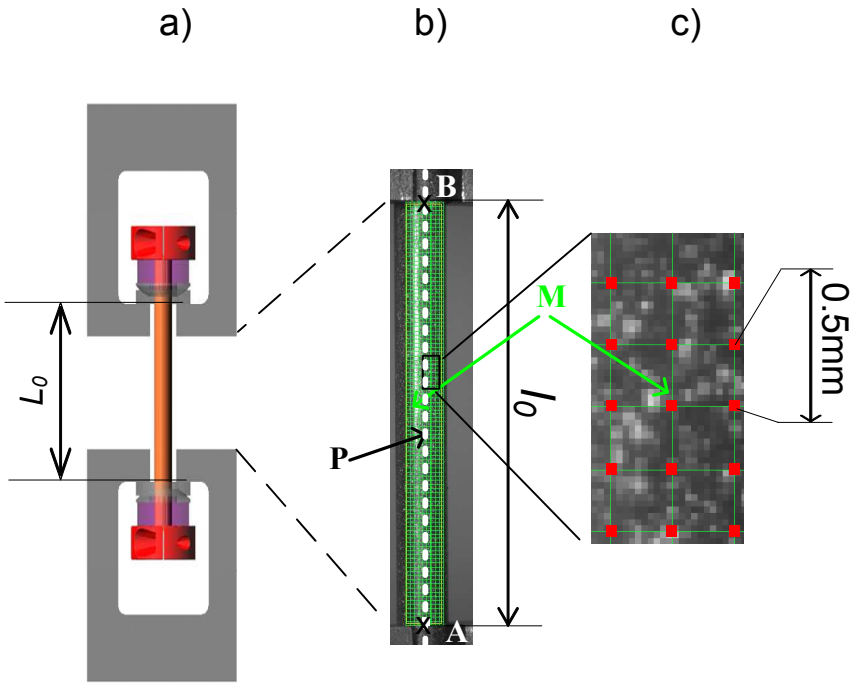

Figure 4.1: *Scheme of the experimental set-up. a) Tube specimen with the gripping system. b) Image of the observation section with the virtual grid used to compute the kinematics field. c) Close-up showing the virtual grid and the surface of the tube coated with a random pattern of white painted speckles superimposed on black paint.*

and displacement fields were estimated to be close to 0.25×0.25 mm^2 and 0.5×0.5 mm^2 respectively (see Figure 4.1.c).

[1]The tube characteristic and gripping system have been presented in Sections 3.1.3.1 and 3.2.2.1.

Figures 4.2-4.7 present results obtained for a tube deformed under tension in air at a cross head velocity $\dot{U} = 0.08$ mm·s^{-1}, i.e. at a global nominal axial strain rate $\dot{U}/L_0 \approx 10^{-3}$s^{-1}. In this section, the strain is characterized by one axial scalar strain defined by $\varepsilon_{X_0} = ln(X/X_0)$, where X_0 is the initial length of one segment initially aligned with the tension axis whereas X is its length after deformation. Taking $X_0 = L_0$ leads to a global strain ε_{L_0} obtained by approximating the current gauge length L by $L_0 + U$. Taking $X_0 = l_0$ leads to an average strain ε_{l_0} in the observation section. The current length l is deduced from measurements of the visible camera that allows to calculate the displacements of the two ends A and B of the dashed line plotted in Figure 4.1.b. Lastly, kinematics field measurements allow us to determine local axial strains $\varepsilon(M)$ from the displacement differences of two vertically aligned points initially distant of dl_0 and located around the point M of the observation section (Figures 4.1.b and 4.1.c). A gauge length dl_0 of 10 pixels corresponding approximately to 0.5 mm will be used in the following.

4.2.2 Results

Figure 4.2 shows the nominal axial stress $\sigma_0 = F/S_0$ (S_0 being the initial cross section of the tube) as a function of the global strain ε_{L_0} (thick curve) and of the average axial strain ε_{l_0} (thin curve). The observed engineering stress-strain behaviour (thick curve) is typical of polycrystalline Ni-Ti SMA with initial austenitic phase microstructures. Such engineering stress-strain curves are usually divided into several regions (Ng and Sun, 2006):

- **Stage 1 (O-a-b):** this initial almost linear part of the stress-strain curve is conventionally attributed to the elastic deformation of the austenitic phase.
- **stage 2 (b-g):** this stage starts with a slight overshoot followed by a small horizontal stress plateau (b-c) visible until a strain ε_{L_0} of approximately 2.5%. Then, the nominal stress increases smoothly (c-g) and after more abruptly in stage 3 (g-h). It is conventionally postulated that at point (b), the stress reaches a critical value at which the stress-induced martensitic transformation starts (Shaw and Kyriakides, 1995). Stage 2 is conventionally considered to be associated with initiation and propagation of heterogeneous macroscopic transformation-deformation bands, the increasing slope being due to thermal effects (Shaw and Kyriakides, 1997; Gadaj et al., 2002). Transformation is assumed to be complete at point (g).
- **Stage 3 (g-h):** this stage is conventionally seen as the elastic deformation and further detwinning of M phase.
- **Stage 4 (h-j):** the begining of unloading is conventionally seen as the elastic deformation of M phase.
- **Stage 5 (j-k):** reverse transformations are postulated to start only at point (j). As testing temperature was of the order of $T(R-A)_f$, notice that the reverse transformation was not complete at the end of unloading.

Almost the same stages are observed in the $\sigma_0 - \varepsilon_{l_0}$ thin curve of Figure 4.2. The differences between $\sigma_0 - \varepsilon_{L_0}$ and $\sigma_0 - \varepsilon_{l_0}$ curves are clearly dependent on the deformation range. In the sub-stage (0-a) of stage 1, ε_{L_0} and ε_{l_0} vary almost proportionally. In (a) ($\sigma_0 = 200MPa$, ε_{L_0} and ε_{l_0} are equal to 0.9 % and 0.53%, respectively. During the sub-stage (a-b), the difference

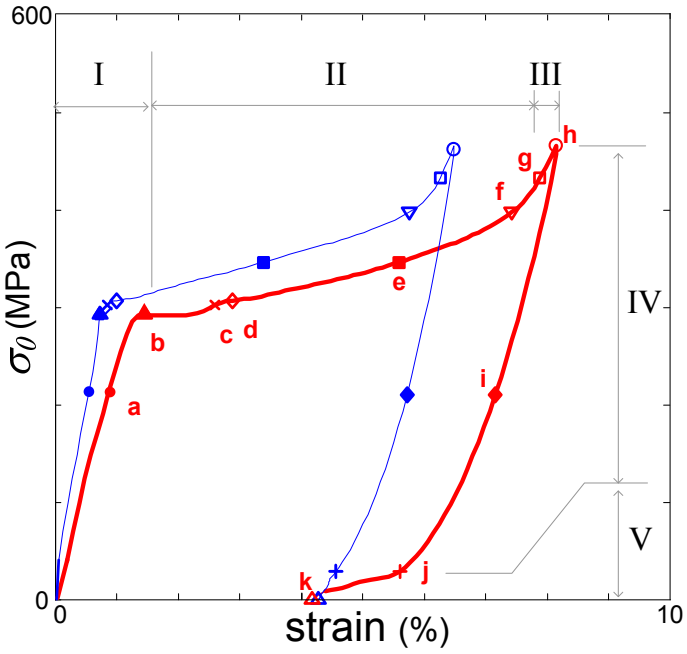

Figure 4.2: *Nominal stress σ_0 vs. global axial strain ε_{L_0} (thick curve) and average axial strain ε_{l_0} (thin curve). ε_{L_0} is determined from the cross-head displacement U and the sample gauge length L_0. ε_{l_0} is determined from the optical measurements of the displacements of the two points A and B in Figure 4.1.c. Markers and letters a to k indicate selected times in Figures 4.3 to 4.7.*

between ε_{L_0} and ε_{l_0} keeps on growing, ε_{L_0} and ε_{l_0} increasing of 0.63% and 0.22%, respectively. This difference increases drastically during the horizontal plateau (b-c) of stage 2, leading to respective values for ε_{L_0} and ε_{l_0} of 2.85% and 0.85% in (c). During the part (d-g) of stage 2, ε_{L_0} and ε_{l_0} increase both of 5.5%. During stages 3 and 4, ε_{L_0} and ε_{l_0} evolve almost linearly, whereas decrease of ε_{L_0} is higher than that of ε_{l_0} during the last stage 5.

Figure 4.3 shows coloured maps of the local temperature variation $\theta(M)$ and local strain $\varepsilon(M)$ fields on the surface of the tube at four selected times (a), (d), (e) and (f) marked in Figure 4.2. Coloured spatiotemporal maps displayed in Figures 4.4.a and 4.4.b correspond to time evolutions of $\theta(P)$ and $\varepsilon(P)$ for points P located on the vertical dashed line sketched in Figure 4.1.b. The superimposed curve plotted in Figure 4.4.a presents the time evolution of the nominal stress σ_0. The superimposed curve displayed in Figure 4.4.b represents the time evolution of the average strain ε_{l_0}.

Time histories of σ_0, $\theta(C)$ and $\theta(D)$ are shown in Figure 4.5.a, and time histories of ε_{l_0}, $\varepsilon(C)$ and $\varepsilon(D)$ are plotted in Figure 4.5.b. C and D are two spatial points[2] sketched in Figure 4.3.(e). They are located near the tube ends that did not move during the test so that $\theta(C)$, $\theta(D)$, $\varepsilon(C)$ and $\varepsilon(D)$ can be considered as temperature variations and local strains for almost motionless material points.

Figure 4.6.a and 4.6.b show axial profiles of $\theta(P)$ and $\varepsilon(P)$ for selected times (a) to (g) defined in Figure 4.2. Figure 4.7 shows similar temperature variations $\theta(P)$ and strain $\varepsilon(P)$ profiles for selected times (g) to (k), defined in Figure 4.2.

[2]Notice that during this first analysis, only a soft temporal synchronisation (cf Section 2.4) have been achieved and not the spatial one.

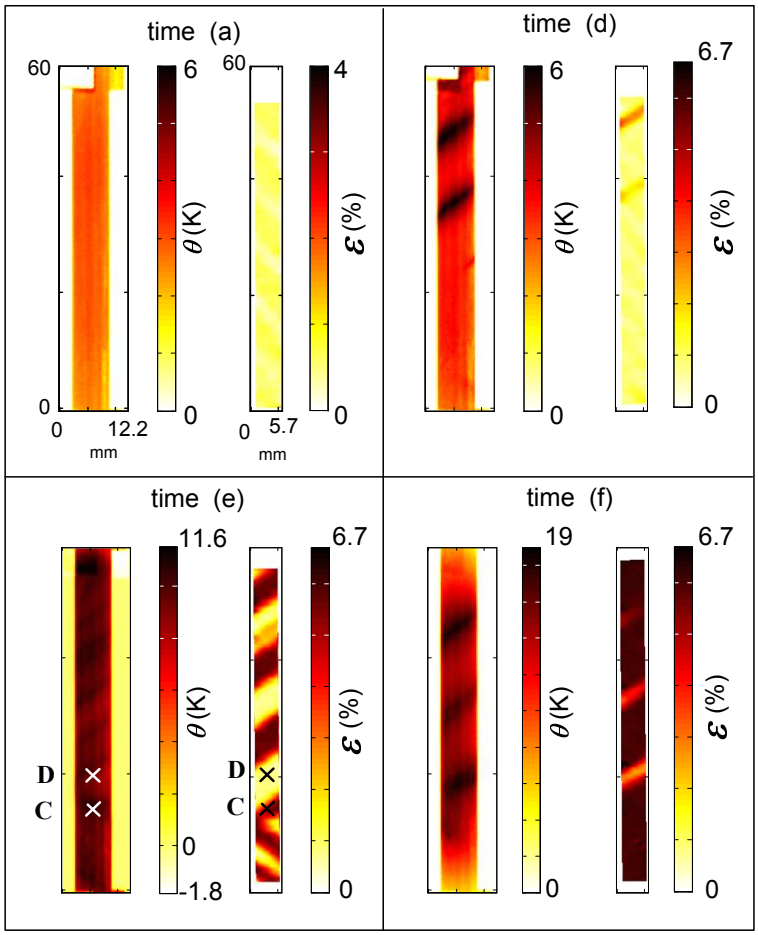

Figure 4.3: *Coloured maps showing the temperature variation $\theta(M)$ (left) and the local strain $\varepsilon(M)$ (right) fields on the surface of the deformed tube at four selected times marked in Figure 4.2.*

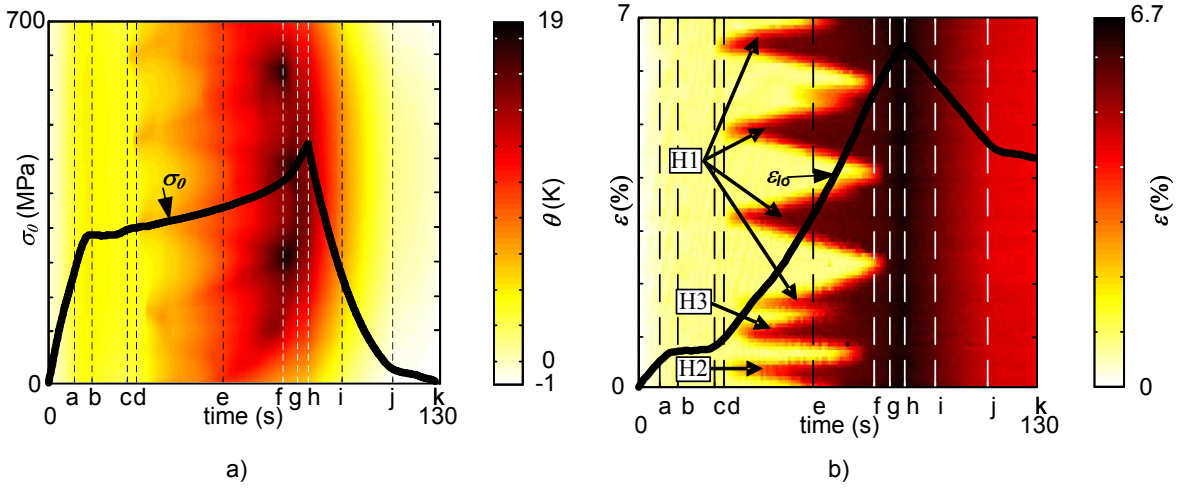

Figure 4.4: *a) Coloured map showing the time evolution of $\theta(P)$ at the spatial points M located on the vertical dashed line plotted in Figure 4.1.c. Superimposed curve: time evolution of the engineering stress σ_0. b) Coloured map showing the time evolution of $\varepsilon(P)$, at the spatial points P located on the vertical dashed line plotted in Figure 4.1.c. Superimposed curve: time evolution of the average axial strain ε_{l_0}.*

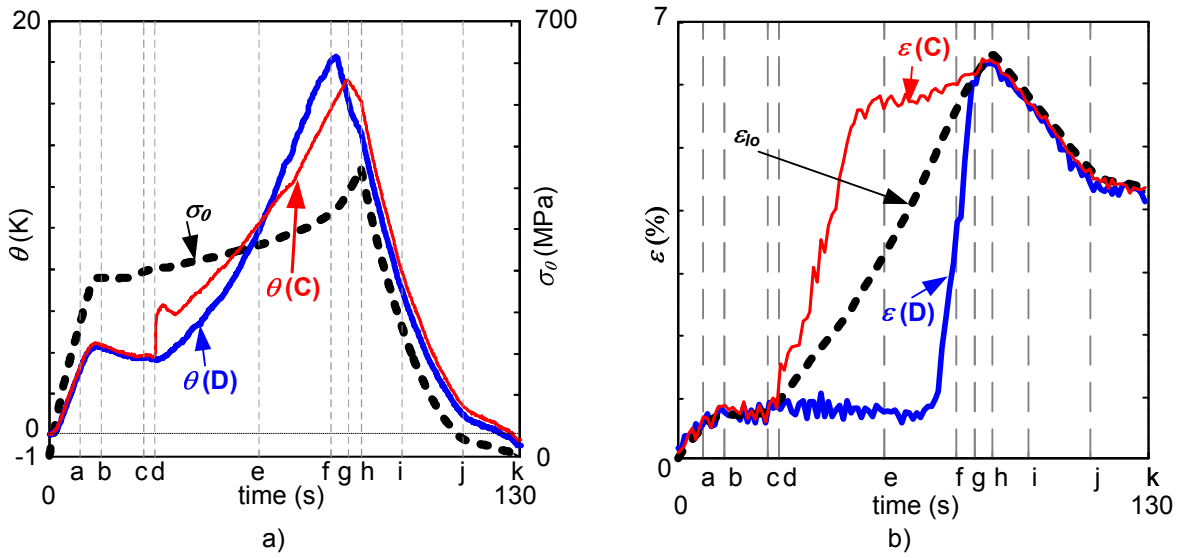

Figure 4.5: *a) Time histories of the engineering stress σ_0 and of the temperature variations θ at two spatial points C and D shown in Figure 4.3 for the time (e). b) Time histories of the average axial strain ε_{l_0} and local strains (C) and (D) at two spatial points C and D shown in Figure 4.3 for time (e).*

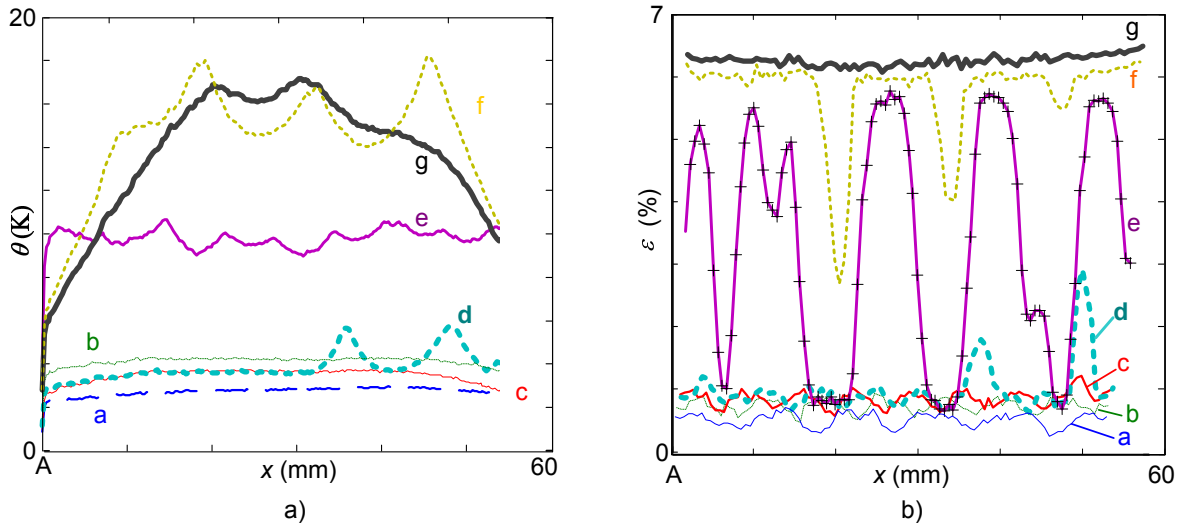

Figure 4.6: *a) Axial profiles (P) showing the temperature variations for the spatial points P located on the vertical dashed line plotted in Figure 4.1.c at selected times (a) to (g) marked in Figure 4.2. b) Axial profiles (P) showing the strains for the spatial points P located on the vertical dashed line plotted in Figure 4.1.c, at selected times (b) to (g) marked in Figure 4.2.*

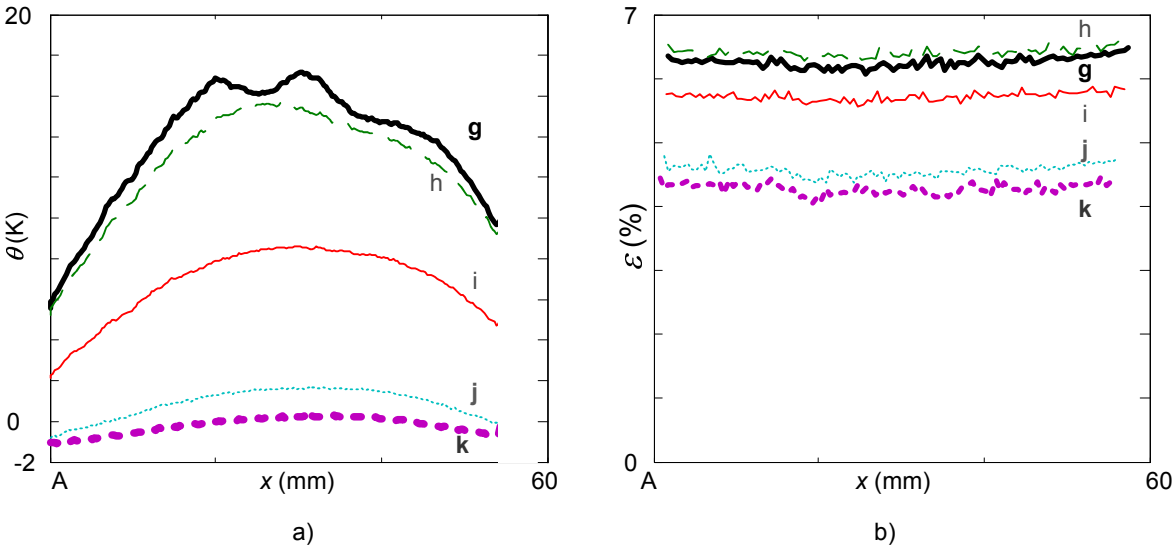

Figure 4.7: *Axial profiles (P) (left) and (P) (right) of the temperature variations and strains, respectively, for the spatial points P located on the vertical dashed line plotted in Figure 4.1.c, at selected times (g) to (k) marked in Figure 4.2.*

Figures 4.2-4.7 conjure up the following comments:

- **stage 1 (O-b):** during this stage, the deformation of the tube occurs homogeneously in the observed region, as demonstrated in the snapshot (a) of Figure 4.3 and in Figures 4.4.b, 4.5.b and 4.6.b. An almost homogeneous temperature increase is observed (Figures 4.4.a, 4.5.a and 4.6.a), starting as soon as the tensile deformation proceeds. It is also observed that during the sub-stage (0-a), both stress and strain but also temperature variation increase almost linearly with time (see Figures 4.5 for points C and D). At time (a), for any point of the observed region $\theta \approx 3K$ (Figures 4.4.a, 4.5.a and 4.6.a), $\sigma_0 \approx 200$ MPa and $\varepsilon \approx 0.53\% \approx \varepsilon_{l_0}$ (Figures 4.4.b, 4.5.b and 4.6.b). During the sub-stage (a-b), the time evolutions of σ_0, θ and ε are less and less linear. A temperature decrease is even measured just before time (b). However, at time (b), the temperature variations θ (profile (b) of Figure 4.6.a) and strains ε (profile (b) of Figure 4.6.b) still remain uniform throughout the observed tube length.

- **stage 2 (b-g):** during the sub-stage (b-c) of stage 2, θ decreases almost homogeneously in the observed region (Figure 4.4.a, 4.5.a and 4.6.a) whereas the local strain ε remains homogeneous and almost constant (Figure 4.4.b, 4.5.b and 4.6.b). During the sub-stage (c-g), temperature $\theta(M)$ and strain $\varepsilon(M)$ maps (d), (e) and (f) of Figure 4.3 reveal a highly heterogeneous deformation of the tube. The time evolutions of θ (Figure 4.5.a) and ε (Figure 4.5.b) for the two points C and D are different and the profiles sketched in Figures 4.6.a and 4.6.b for selected times (d) to (f) exhibit very strong gradients. Analysing more precisely both thermal and strain maps (d) of Figure 4.3, it is observed that a thin helical band (denoted by H1 in Figure 4.4) with higher strains ε and temperature variations θ appears from the upper gripping zone and propagates along the observation zone using a helical trajectory inclined at about 58° to the loading axis. Increased tensile deformation (map (e) of Figure 4.3) induces propagation and width enlargement of the first band and simultaneously appearance of two intertwinned helical bands (denoted by H2 and H3 in Figure 4.4.b) originated from the lower gripping zone, with an opposite angle of -58°. The profiles (d) of Figures 4.6.a and 4.6.b show

that, at selected time (d), the temperature variation and maximum strain in the band are respectively 6 K and 3%, whereas they only approach $\varepsilon \approx 1\%$ and $\theta \approx 3.5$ K in the reminder of the sample. Strain profiles (e), (f) and (g) of Figure 4.6.b demonstrate that the deformation is not homogeneous until the selected time (g) of Figure 4.2 even if the slope of the stress-strain curves in Figure 4.2 starts to increase between times (f) and (g).

- **stage 3 (g-h):** the θ and ε axial profiles of Figure 4.7 show that the temperature is not homogeneous at time (g) in spite of an homogeneous deformation of the tube. This is due to the temperature history during loading. It is worth observing that the almost homogeneous strain increase between times (g) and (h) is accompanied in every point of the tube by temperature decreases (see also part (g-h) of the curves $\theta(C)$ and $\theta(D)$ of Figure 4.5.a).

- **stage 4 (h-j):** the homogeneous strain decreases (Figures 4.4.b, 4.5.b and 4.7) is accompanied by a temperature decrease (Figures 4.4.a, 4.5.a and 4.7), with smooth bell-shaped temperature profiles (Figures 4.7). Note that at a given spatial point, the rate of this temperature decrease at the beginning of unloading stage 4 is higher than at the end of loading stage 3 (g-h) of loading as shown from comparison of parts (g-h) and (h-i) of the curves (C) and (D) of Figure 4.5.b.

- **stage 5 (j-k):** the deformation remains homogeneous in the observation region (Figures 4.4.b, 4.5.b and strain profiles (h) and (j) of Figure 4.7) and the temperature decrease rate is lower than during stage 4, as demonstrated by comparing parts (i-j) and (j-k) of the curves $\theta(C)$ and $\theta(D)$ of Figure 4.5.a.

4.2.3 Discussion

Although experimental observations of tensile tests on NiTi specimens and of localization phenomena occurring during these tests can be found in the references cited earlier (Miyazaki et al., 1981; Shaw and Kyriakides, 1995, 1997; Orgéas and Favier, 1998; Favier et al., 2001; Sun and Li, 2002; Brinson et al., 2004; Ng and Sun, 2006; Gadaj et al., 2002), simultaneous measurements of temperature and strain fields are original. They provide new results enabling us to revisit the conventional understanding of homogeneous and heterogeneous phenomena occurring during tensile tests on NiTi involving phase transformations. To take advantage of the simultaneous measurements of the strain and temperature fields, a simplified analysis is first developed. It will allow us to analyse the deformation mechanisms during these homogeneous stages by estimating heat sources from temperature field measurements during stages 1 and 4. For stages 2, 3 and 5, we will focus our analysis on the link between the recorded macroscopic nominal strain-stress tensile curve, the localization topology and the local strain field.

4.2.3.1 Hypotheses and basic equations for the analysis of homogeneous stages 1 and 4

During stages 1 and 4, the strains are homogeneous. We will assume that the heat sources are also homogeneously distributed. The “0D” formulation presented in Section 2.5.4 is then

satisfied during these two stages. Therefore, at any point on the outer surface of the tube, the heat sources rate ($\dot{q} = s_i/\rho$) is written as:

$$C(\frac{\partial\ \theta}{\partial t} + \frac{\theta}{\tau_{eq}}) = \dot{q}, \tag{4.1}$$

where $\theta = T - T_0$ is the temperature variation. The parameter τ_{eq} denotes a characteristic time reflecting heat losses both by convection through inner and outer surfaces of the tube and by conduction towards the grips.

It is well known that deformation mechanisms for NiTi include elastic distortion of the atomic lattice associated with martensitic and R phase transformations and variants detwinning (Sittner et al., 2006a). Local plastic accommodation of the transformation(s) may also be involved but is effective only for large local strains (Brinson et al., 2004). The heat source involved in eq. (4.1) are thus divided into $\dot{q}_{tr}$ due to phase transformations, $\dot{q}_{thel}$ due to usual thermoelastic coupling, and intrinsic dissipation $\dot{q}_{plast}$ due to plasticity:

$$\dot{q} = \dot{q}_{thel} + \dot{q}_{tr} + \dot{q}_{plast} \qquad \text{with} \qquad \dot{q}_{thel} = -\frac{\alpha T \dot{\sigma}}{\rho}, \tag{4.2}$$

where α is the coefficient of thermal expansion.

As presented in Chapter 1 in eq. (1.11), the heat source due to phase transformation $\dot{q}_{tr}$ is divided into chemical heat source $\dot{q}_{tr\ chem}$ and dissipated heat source $\dot{q}_{tr\ diss}$:

$$\dot{q}_{tr} \quad = \quad \dot{q}_{tr\ chem} + \dot{q}_{tr\ diss} \tag{4.3}$$

When expressed as function of the transformation fraction rate $\dot{f}_m = df_m/dt$, $\dot{q}_{tr\ diss} = E'_{iq}\,\dot{f}_m$ and $\dot{q}_{tr\ chem} = -(T_0+\theta)\Delta S_c\,\dot{f}_m = -(T_0+\theta)(S_c^M - S_c^A)\,\dot{f}_m$ for an A→M phase transformation with $\Delta S_c < 0$. Therefore,

$$\dot{q}_{tr} \quad = -(T_0+\theta)\Delta S_c \dot{f}_m + E'_{iq}\dot{f}_m \tag{4.4}$$

The classical additive decomposition of the strain rate $\dot{\varepsilon}$ is assumed:

$$\dot{\varepsilon} = \dot{\varepsilon}_{el} + \dot{\varepsilon}_{in}, \tag{4.5}$$

where $\dot{\varepsilon}_{el} = \dot{\sigma}/E$ and $\dot{\varepsilon}_{in}$ are the elastic and inelastic strain rates, respectively. The inelastic strain rate includes the rate due to transformation $\dot{\varepsilon}_{tr}$ and the rate due to variant detwinning $\dot{\varepsilon}_{de}$. In the present analysis, the rate due to plasticity is neglected ($\dot{\varepsilon}_{plast} \approx 0$).

Lastly, for any phase transformation, under tensile loading, both strain rate $\dot{\varepsilon}_{tr}$ and heat sources rate $\dot{q}_{tr}$ will be assumed proportional to the transformation fraction rate $\dot{f}_m$ (McCormick et al., 1993; Lexcellent and Vacher, 1993):

$$\dot{\varepsilon}_{tr} = \dot{f}_m \Delta\varepsilon_{tr} \ \text{ and } \ \dot{q}_{tr} = \dot{f}_m \Delta H_{tr}^{tensile}, \tag{4.6}$$

where $\Delta\varepsilon_{tr}$ and $\Delta H_{tr}^{tensile}$ stand for the transformation strain and the latent heat for a complete transformation ($f_m = 1$) under tensile loading. The latent heat for a complete phase transformation is often approximated by the enthalpy change ($\Delta H_{tr}^{tensile} \approx \Delta H_c$). However, it is worth noting that from eq. (1.13), ΔH_{tr} under tensile loading is also dependent on the elastic energy (E'_{el}), the non heat component of the irreversible energy (E'_{iw}) and the mechanical work presented in Chapter 1:

$$\Delta H_{tr}^{tensile} = -\Delta H_c - E'_{el} - E'_{iw} + \frac{1}{\rho}\sigma\Delta\varepsilon_{tr} \tag{4.7}$$

4.2.3.2 Deformation mechanisms in each deformation stages

Stage 1: this stage is conventionally attributed to the elastic distortion of the austenite lattice (Shaw and Kyriakides, 1995) or of the R-phase lattice (Ng and Sun, 2006). From the thick and thin curves plotted in Figure 4.5, two values of the apparent modulus of elasticity may be determined, to be 25 GPa and 40 GPa. The first (lower) value is calculated from the nominal strain ε_{L_0}. It is deduced from the cross-head displacement that includes the overall tube length variation, but also the elastic deformation of the gripping system and possible sliding of the tube in the gripping system. The second value excludes these experimental biases since the average strain ε_{l_0} is calculated from optical measurement of displacements in the observation zone l_0.

There are a lot of references in the literature concerning the values of the apparent modulus of elasticity of NiTi alloys determined from tensile stress-strain tests, both in austenitic and martensitic state (Liu and Xiang, 1998). The reported values range from to 20 to 50 GPa for martensite and from 40 to 90 GPa for austenite. The determined value of 40 GPa appears in the lower range of the values reported in the literature for austenite.

By having recourse to in situ neutron diffraction during loading, Rajagopalan et al. (2005) obtained a modulus as high as 110 GPa which is solely representative of elastic deformation. As already underlined by Liu and Xiang (1998) and by Sittner et al. (2006b), weak values of apparent modulus of elasticity determined from mechanical stress-strain as measured in this work, either in austenitic or martensitic state, are indications of occurrence of deformation mechanisms other than pure elastic distortion of crystalline lattice.

Indeed, the observed homogeneous temperature increase starting for very low stress levels during the sub-stage (0-a) suggests an additional deformation mechanism involving an exothermic phase transformation. A pure elastic deformation would have led to a homogeneous temperature decrease associated with the well-known thermo-elastic coupling (Chrysochoos and Louche, 2000), as shown by eq (4.2) that leads to $\dot{q}_{thel} < 0$ when $\dot{\sigma} > 0$

Equations developed in Section 4.2.3.1 are now used in order to analyse further the sub-stage (0-a) of stage 1. With regards to DSC measurements shown in Figure 3.1.c, the material is initially in an austenitic state. Hence, it will be assumed that during the sub-stage (0-a), the only inelastic mechanism is phase transformation (i.e. variants detwinning and plasticity are neglected, so that $\dot{q}_{plast} \approx 0$):

$$\dot{q}_{tr} = \dot{q} - \dot{q}_{thel} = \dot{q} + \frac{\alpha T}{\rho}\dot{\sigma}, \tag{4.8}$$

$$\dot{\varepsilon}_{tr} = \dot{\varepsilon} - \frac{\dot{\sigma}}{E}, \tag{4.9}$$

eq. (4.5) results in:

$$\frac{\Delta H_{tr}^{tensile}}{\Delta \varepsilon_{tr}} = \frac{\dot{q} + \frac{\alpha T}{\rho}\dot{\sigma}}{\dot{\varepsilon} - \frac{\dot{\sigma}}{E}} \tag{4.10}$$

With regards to the homogeneity of strains and temperature variations during sub-stage (O-a), heat source is assumed to be homogeneously distributed throughout the specimen; the heat source rate $\dot{q}$ can thus be estimated from eq. (4.1). In this equation, the term θ/τ_{eq} vanishes at the beginning of sub-stage (O-a), and is likely to remain weak during all the sub-stage (O-a). In order to ascertain this second hypothesis, a second tensile test has been

performed at a cross-head velocity 10 times faster than the first test. Temporal evolutions of average strain ε_{l_0} are plotted in Figure 4.8.a, the one for the first test being plotted using thin lines and a time range of 8 s, whereas that of the second test is plotted using thick lines and a time range of 0.8 s. The stress σ_0 and temperature variation θ evolutions are plotted as a functions of average strain ε_{l_0} during the sub-stages (0-a) for the first (thin curves) and second (thick curves) tests in Figure 4.8.b and 4.8.c, respectively. The similarities of the strain-stress (Figure 4.8.b) and strain-temperature (Figure 4.8.c) curves between the two tests lead us to conclude that testing conditions were very close from adiabatic conditions during sub-stage (0-a) in both cases. These near adiabatic conditions together with homogeneity of the heat source rate explain the flat shapes of the θ profiles for selected times (a) and (b) of Figure 4.6.a.

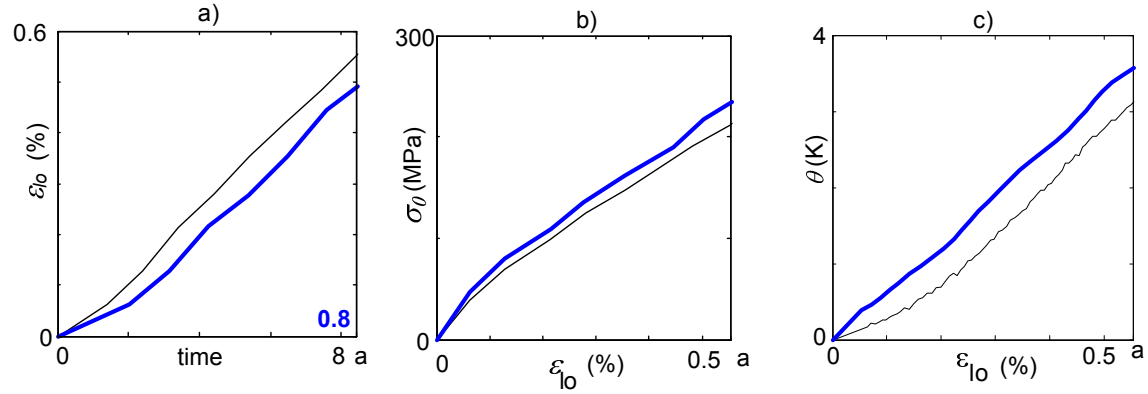

Figure 4.8: *a) Average strain ε_{l_0} as a function of time during sub-stage 0-a for the test shown in Figure 4.2 (Thin curve, time range 0-8 s) and for a second test performed with a crosshead velocity 10 times faster (Thick curve, time range 0-0.8 s). b) Stress σ_0 as a function of average strain ε_{l_0} for these two tests. c) Temperature increase θ as a function of average strain ε_{l_0} for these two tests.*

Consequently, with the previous assumption, eq. (4.1) and (4.10) show that the transformations involved during the sub-stage (O-a) of the two tests satisfy at any time:

$$\frac{\Delta H_{tr}^{tensile}}{\Delta \varepsilon_{tr}} = \frac{C\dot{T} + \frac{\alpha T}{\rho}\dot{\sigma}}{\dot{\varepsilon} - \frac{\dot{\sigma}}{E}} \tag{4.11}$$

Two different transformation are possible starting from an austenitic phase, namely, either A-R or A-M transformation. A third transformation R-M can occur from the R phase. Transformation strain $\Delta\varepsilon_{tr}$ for a complete A-R transformation is of the order of 1% (Sittner et al., 2006a), that for a complete A-M transformation is of the order of 8%, and that for a complete R-M transformation is of the order of 7% (Orgéas and Favier, 1995). The value of the latent heat ΔH^{AR}, ΔH^{AM} and ΔH^{RM} associated with these three transformations are of the order of 6 Jg^{-1}, 20 Jg^{-1} and 14 Jg^{-1}, respectively (Liu and McCormick, 1992) when estimated by temperature induced phase transformation. This leads to:

$$\begin{aligned}
\frac{\Delta H_{tr}^{tensile}}{\Delta \varepsilon_{tr}} &\approx \frac{\Delta H^{AR}}{\Delta \varepsilon_{tr}^{AR}} = 600 \text{ J/g for A-R;} \\
\frac{\Delta H_{tr}^{tensile}}{\Delta \varepsilon_{tr}} &\approx \frac{\Delta H^{AM}}{\Delta \varepsilon_{tr}^{AM}} = 250 \text{ J/g for A-M;} \\
\frac{\Delta H_{tr}^{tensile}}{\Delta \varepsilon_{tr}} &\approx \frac{\Delta H^{RM}}{\Delta \varepsilon_{tr}^{RM}} = 200 \text{ J/g for R-M.}
\end{aligned} \tag{4.12}$$

Comparison of the experimentally determined values $\Delta H_{tr}^{tensile}/\Delta\varepsilon_{tr}$ using eq. (4.11) with the three above values for the A-R, A-M and R-M transformations will allow to deduce which transformations occur during the sub-stage (0-a). In the following, the value $E = 110$ GPa determined by neutron diffraction (Rajagopalan et al., 2005) will be considered as the true elastic modulus for the austenite, martensite and the R phase. The specific heat will be considered as a constant, uniform and equal to $C = 0.49$ J.K^{-1}g^{-1} (Faulkner et al., 2000).

The measured ratios of $\Delta H_{tr}^{tensile}/\Delta\varepsilon_{tr}$ along the sub-stage (O-a) are plotted as a function of the strain in Figure 4.9, for the two tests performed at moderate and high strain rates using thin and thick lines, respectively. The dashed horizontal lines are the three values calculated for the A-R, A-M and R-M transformations.

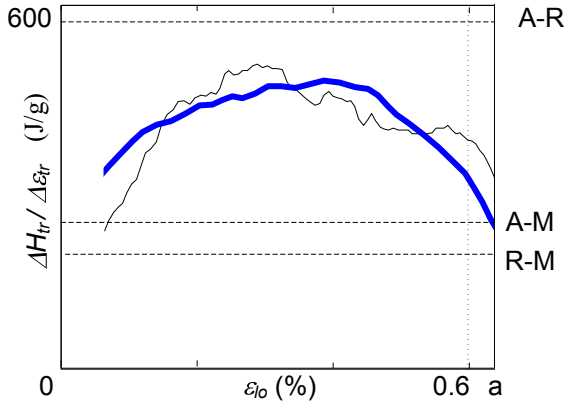

Figure 4.9: *Ratio of the latent heat of transformation to the transformation strain, $\Delta H_{tr}^{tensile}/\Delta\varepsilon_{tr}$, as a function of average strain ε_{l_0} during the sub-stage 0-a. The two solid curves are calculated from eq. (4.11) and from the experimental results shown in Figure 4.8, for the test of Figure.4.2 (thin curve) and for a second test 10 times faster (thick curve). The three horizontal dashed lines represent the value of ($\Delta H_{tr}^{tensile}/\Delta\varepsilon_{tr}$) for complete A-R, A-M and R-M transformations.*

These two curves demonstrate that deformation during the sub-stage (O-a) is never purely elastic. It involves at very low stress and strain levels additional deformation mechanisms associated with a mixture of the three types of transformation (A-R, A-M and R-M). This result agrees with two observations already reported in the literature. First, A-R transformation is known to proceed for specific NiTi throughout the whole part of the tensile stress-strain curve preceding the stress peak (Sittner et al., 2006b,a); the stress-strain curves associated with this transformation are reported to be linear or non linear and can present very short stress plateau. Second, macroscopically homogeneous and stable A-M transformation referred to "pre-burst transformation" or "incubation" (Brinson et al., 2004; Feng and Sun, 2006) can be involved in this stage. Our result is not surprising but is still qualitative. It is based on strong assumptions, as evident in eqs. (4.1) and (4.3) and on values of physical parameters (E, $\Delta\varepsilon_{tr}^{A-R}$, $\Delta\varepsilon_{tr}^{A-M}$, $\Delta\varepsilon_{tr}^{RM}$, ΔH^{AR}, ΔH^{AM} and ΔH^{RM}) which are difficult to determine. Qualitatively, the proportion of each transformation is not constant throughout homogeneous loading stage and it is not possible to distinguish during this stage a period during which only A-R transformation occurs.

stage 2: In quasi isothermal conditions, this stage is associated with a localized Lüders-like deformation over a stress plateau through the motion of localised bands. The measured engineering stress vs average strain ($\sigma_0 - \varepsilon_{l_0}$) curve shown in Figure 4.2 does not exhibit a stress plateau; however, it has been shown that despite the positive slope of the stress-strain curve, deformation proceeds heterogeneously. It is conventionally regarded that the

beginning and the end of this plateau are associated with the beginning and the end of the stress-induced transformation (Shaw and Kyriakides, 1995). The analysis of the thermal, kinematic and mechanical measurement during stage 1 has proved that the A-R, A-M or R-M transformations start before the onset of localization.

The positive slope can be tentatively analysed from our thermal measurements. The well-known Clausius-Clapeyron relationship (Wollants et al., 1979) expresses the fact that the transformation stress is a linear function of the temperature; it is worth recalling that this Clausius-Clapeyron relationship is valid locally where the transformation occurs and that the linear coefficient depends on the stress state, e.g. it is different in tension, compression and shear for a given alloy (Orgéas and Favier, 1998). When the temperature of the specimen is heterogeneous, the application of the Clausius-Clapeyron relationship would require to determine at which spatial point of the tube the transformation occurs and to know the local stress state at this point. It is thus difficult to analyse, in details, engineering stress-strain slope at each position of the heterogeneous stage 2. Nonetheless, times (c) and (e) are simpler to analyse since the temperature is almost homogeneous for these two times, as shown by profiles (c) and (e) of Figure 4.6.a. The temperature increase from (c) to (e) is equal to 7 K, whereas the stress increase is of the order of 40 MPa; if we assume that the positive slope is only due to temperature increase, a coefficient of $40/7 = 5.7$ MPa/K is obtained for the Clausius-Clapeyron relationship, which is in the range of the values reported in the literature for R→M tensile experiments (Liu and McCormick, 1994).

The macroscopic deformation patterns that have been observed in this test are helical bands initiating in the grips. It is known that band formation, morphology and propagation depend on a number of factors, including specimen shape, loading rate, heat transfer conditions, gripping system, heat treatment conditions (Miyazaki et al., 1981; Shaw and Kyriakides, 1995, 1997; Orgéas and Favier, 1998; Favier et al., 2001). In these first tests, the helical bands propagate (domain lengthening) and widen (domain lateral thickening) with deformation, keeping their helical shape throughout the whole test.

Experiments on NiTi tubes are less common than on wires or strips (Miyazaki et al., 1981; Shaw and Kyriakides, 1995, 1997; Orgéas and Favier, 1998; Favier et al., 2001). The few published papers on tubes (Sun and Li, 2002; Ng and Sun, 2006; Feng and Sun, 2006) have reported experimental results on macroscopic deformation instability and domain morphology in superelastic and ferroelastic NiTi microtubes. In Ng and Sun's experiments, the band shape has been observed changing from an inclined cylinder to a helical shape with increasing testing temperatures (Ng and Sun, 2006), the transition temperature being a few degrees above $T(M-A)_f$. For a testing temperature well above this transition temperature, Feng and Sun (2006) have observed initiation of localization through helical bands that afterward evolve in a complex way between various domain morphologies during loading and unloading. They explain these domain pattern evolutions in terms of competition between macroscopic domain wall energy (interfacial or front energy) and bulk strain energy of the overall tube. The differences in total energy (bulk strain energy and interfacial domain energy) among all the possible states of domains in the tubular system lead to morphology transitions. The interfacial energy is dependent on the forms of the domains, for instance helical domain or ring-like domain. The bulk strain energy is highly influenced by the interaction between material and structure geometry.

The present test temperature is of the order of $T(R-A)_f$. The initiation of the localization through helical bands agrees thus with Ng and Sun's results (2006). However, we did not

observe any evolution of the domain morphology during the heterogeneous deformation stage. This effect is apparently in contradiction with Feng and Sun's experiments (2006). Two factors influencing the bulk energy of the overall tube have to be pointed out. The first factor is the smaller thickness/mean radius ratio (here of the order of 0.04) compared to the cases of microtubes tested by Sun *et al.* (2002,2006) ranging from 0.2 to 0.5. This factor reduces the strain, stress and temperature heterogeneities in the tube thickness, diminishing thus the shell effects of the tube wall that behaves rather like a membrane. The second factor is the design of our gripping system and especially the use of self-aligning washers that allows the two ends of the specimen to rotate with weak resistive torques; the specimen is submitted only to tensile load and is free to deform asymmetrically through the development of helical bands. This is not the case of gripping systems used by Feng and Sun (2006) that transmits bending moment and torque to the tubular specimen as soon as the deformation of the tube is not axisymmetric anymore, strongly influencing the observed phenomena of morphology evolution. It is worth concluding that comparisons of our experimental results with those of Sun *et al.* (Sun and Li, 2002; Ng and Sun, 2006; Feng and Sun, 2006) highlight the strong influence of the structure-material coupling on the domain morphology evolution.

Results obtained also give some valuable information on the evolution of heterogeneous strain field during the stress "plateau". For instance, the initiation of the bands at the extremities of the gauge section L_0 explains the significative difference between increases of ε_{L_0} and ε_{l_0} during the sub-stage (b-c) of stage 2. During this sub-stage, local strains $\varepsilon(M)$ inside the observation region remain constant (a small decrease is even measured) and the temperature decrease is due to heat exchange with the surrounding. This heat exchange occurs both through the outer and inner surfaces of the tube by convection and by conduction mainly along the axis of tube. The temperature decrease between profiles (b) and (c) in Figure 4.6.a is mainly due to heat loss by convection and by conduction toward the grips which are cold.

Furthermore, during the sub-stage (c-f) of stage 2, the deformation proceeds through Localised Deformation Bands (LDB), here helical bands, separated from the less deformed regions by narrow regions, called in the following Band Boundaries (BB), across which strains and temperatures change very rapidly. Analysing temperature fields in order to extract meaningful local heat sources occurring during this heterogeneous stage is not straightforward ; it requires to develop a temperature data processing presented in Section 2.5. In this first study, we will consequently restrict our analysis of the sub-stage (d-g) to the observation of the strain fields.

A first result concerns the strain evolution between the different regions of the heterogeneously deformed tube. It is worth recalling that in the present experiments, the "local" strain $\varepsilon(M)$ was calculated with a gauge length of 0.5 mm, as indicated by the crosses plotted in the profile (e) of Figure 4.6.b. Temporal evolutions of $\varepsilon(C)$ and $\varepsilon(D)$ in Figure 4.5.b show that when the Band Boundary (BB) of a Localised Deformation Band (LDB) passes a certain point, there is a sudden increase of the local strain rate. This local strain rate remains finite and the local strain at one point (for example $\varepsilon(C)$) continues to increase after the BB has passed. The continuous time evolution of the local strain around one material point is illustrated in Figure 4.10 for the first band initiating in the upper grip. In this figure, the strain is plotted as a function of the initial coordinates x_0 (whereas spatial coordinates were used in Figures 4.6.a, 4.6.b and 4.7 for θ and ε) for all points P in Figure 4.1.b of initial coordinate greater than 44 mm. These profiles are plotted for the selected times (c), (d), (e), (f), (g) and (h) and for 4 times between (d) and (e) taken every 5 seconds.

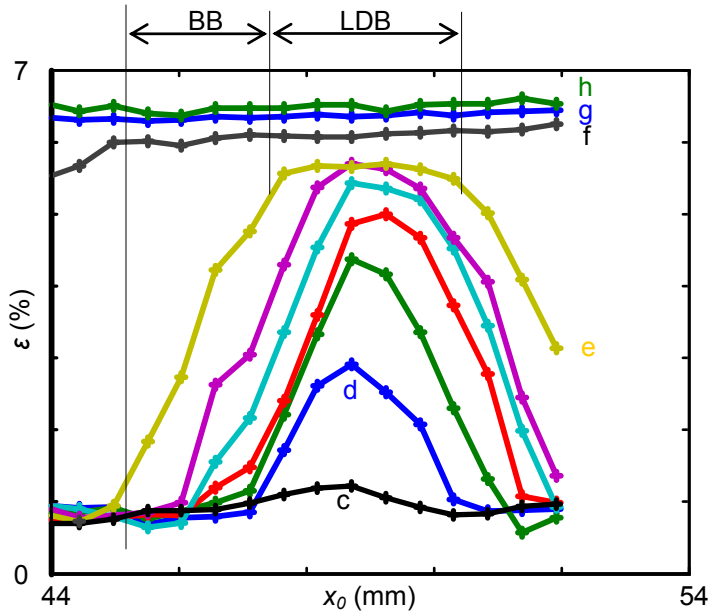

Figure 4.10: *Axial profiles of the local strain (P) as a function of the initial coordinates for the band initiating in the upper grip region. The profiles are plotted at selected times shown in Figure 4.2 and every 5 seconds between times (d) and (e). LDB and BB are notations for the Localised Deformation Band and the Band Boundaries, respectively; they are plotted for time (e).*

Strain profiles along a LDB shown in Figure 4.10 demonstrates that the bands nucleate neither with their final width nor with a strain level equal to the peak strain. In fact a narrow band (profile (d)) is nucleated that expands in its width direction with increasing peak strain level (evolution (d), (e)). Once the BB has passed a point (evolution between (e) and (f)), the strain continues to increase. As already shown by Brinson et al. (2004), Tan et al. (2004) and Schmahl et al. (2004) using optical microscopy, DSC and X-ray diffraction, respectively, this strain increase may be due either to an incomplete transformation inside the LDB, or elastic deformation or martensite detwinning. Further studies using heat sources estimation would allow to better understand the nature of the deformation.

For all profiles between (d) and (e) of Figure 4.10, the strain gradients in the two BB on both sides of the LDB are almost independent of the coordinate x_0 and equal to $d\varepsilon/dx_0 = 2.5\%\text{mm}^{-1}$. The resulting BB widths at time (e) are of the order of 2mm, giving a BB width / tube thickness ratio of the order of $2/0.12 = 15$. Such a ratio has to be compared with a ratio of only 1 in Feng and Sun's experiments (2006) and also with similar ratios measured for Portevin-Le Châtelier deformation bands that range from 1 to 2 independently of the tensile strain rates (Tong et al., 2005; Zhang et al., 2004). The higher value of the present ratio is likely to be induced by strong local thermomechanical coupling at the vicinity of the transforming region, as evidenced by the temperature profiles for snapshots (d) to (f) in Figure 4.6.a. This stronger coupling is in turn induced by higher nominal strain rate in our tensile experiment compared to those achieved in (Feng and Sun, 2006) (10^{-3}s^{-1} versus 10^{-5}s^{-1}) with similar heat exchange conditions. The influence of this coupling has to be further studied in order to come up with essential elements in the theoretical modelling of localization superelastic behaviour of NiTi (see Section 6.1).

Stage 3 This stage is seen conventionally as the elastic deformation and further detwinning of the oriented M-phase. During this stage, the temperature profiles shown in Figure 4.7

evolve from a wavy bell-shaped curve (profile g) to a smoother bell-shaped one (profile h) whereas strain profile evolution demonstrates homogeneous strain increases. This evolution may be due to homogenous or zero heat source throughout the tube and to conduction along the length of the tube toward the grips. However, it is not possible to estimate simply heat source values from the evolution of profiles during this stage, due to the complexity of the thermal process leading from wavy profiles like (g) to smoother ones like (h). No conclusions can be drawn from the full-field measurements during this stage as long as local heat sources are not determined. Example of local heat source estimation using method presented in Section 2.5.5 will be presented later on (in Section 6.1).

Stage 4 This stage is conventionally attributed to elastic deformation and detwinning of the oriented M variants formed during loading. However, observation of the time histories of $\theta(C)$ or $\theta(D)$ in Figure 4.5.a from (g) to (i) indicates that the temperature decrease rate is higher during the sub-stage h-i than during stage 3 (g-h). This proves a difference of heat source rate between (g-h) and (h-i), being due to exothermic heat source during stage 3 and/or endothermic heat sources starting at the beginning of unloading. The aim of the next paragraph is to check the existence of this hypothetical endothermic heat source and to analyse in more detail the physical mechanisms involved during unloading stage 4.

For that purpose, a third test has been performed to estimate τ_{eq} using the method presented in Section 2.5.4. The tube has been first heated to 373 K and cooled down to room temperature; it was then deformed in tension loading under the same conditions as those of the first test, but the deformation was stopped at the end of loading by holding the specimen at constant displacement for 35 s. It is assumed that negligible transformation occurred during the rest of time denoted by clock ($h^- h^+$). The natural temperature decrease θ was then recorded (part $h^- h^+$ of Figure 4.11.a). The two solid thick and thin curves in Figure 4.11.a represent time evolutions of temperature variations for two points of the tube sketched in Figure 4.11.b. The two dashed curves plotted in Figure 4.11.a show that the natural decrease is well modelled using eq. (4.1) with $\dot{q} = 0$ and $\tau_{eq} = 22 \pm 1s$. After a rest of 35 seconds (point h^+), the unloading was started leading immediately to a faster temperature decrease. This faster temperature decrease cannot be explained only by thermoelastic coupling ($\dot{q}_{thel} > 0$ when $\dot{\sigma} < 0$ in eq. (4.2)). It is thus obvious that endothermic heat sources occurs as soon as the specimen is unloaded and that three main mechanisms are involved during unloading, i.e. elasticity, detwinning and reverse transformation, plasticity being neglected.

Taking into account eq. (4.5), the additive decomposition of the strain rate is thus expressed as:

$$\begin{aligned} \dot{\varepsilon} &= \dot{\varepsilon}_{el} + \dot{\varepsilon}_{tr} + \dot{\varepsilon}_{de} \\ &= \frac{\dot{\sigma}}{E} + \frac{\dot{q}_{tr}}{\Delta H_{tr}^{tensile}} \Delta\varepsilon_{tr} + \dot{\varepsilon}_{de} \end{aligned} \tag{4.13}$$

where $\dot{\varepsilon}_{de}$ is the detwinning strain rate. During unloading, the value of the endothermic heat sources rate can be estimated from eq. (4.1) with $\tau_{eq} = 22$ s since the homogeneity of the strain field, as demonstrated by the evolution of profiles (h), (i) and (j) in Figure 4.7, suggests an homogeneous transformation strain rate during this stage, associated with homogeneously distributed heat source inside the tube.

The transformation strain rate $\dot{\varepsilon}_{tr}$ can therefore be deduced from eq. (4.13), if the two values ΔH_{tr} and $\Delta\varepsilon_{tr}$ involved during unloading stage 4 are known. At the end of loading, the material is at least 70% martensitic (Brinson et al., 2004). The endothermic phase

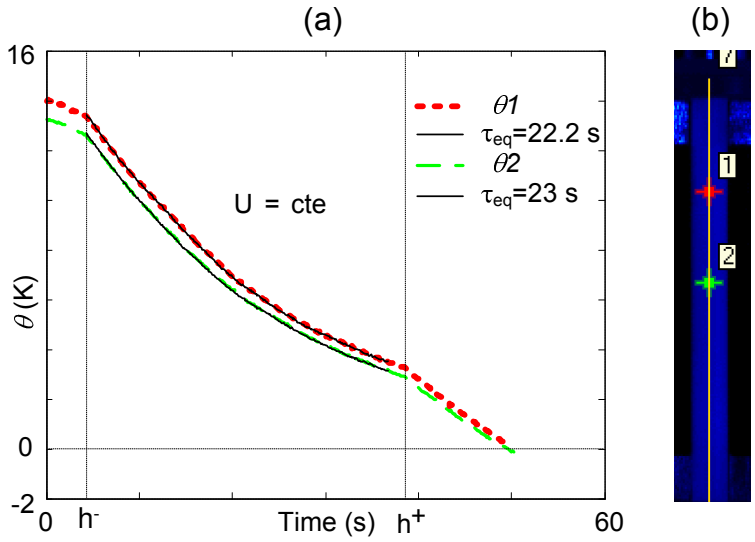

Figure 4.11: *For a test similar to that shown in Figure 4.2 but stopped at time (h) for 35 s ($h^- - h^+$) before unloading. The dashed curves represent the time evolutions of the temperature variations 1and 2 of the two points 1 and 2 shown in Figure 4.11.b. The solid curves show the modelling of these temporal evolutions using eq (4.1), assuming zero heat source during the rest $h^- - h^+$.*

transformation is thus likely to be mainly a M-A transformation, which leads to adopting $\Delta H_{tr}^{tensile} \approx \Delta H^{AM} = 20$ J/g and $\Delta\varepsilon_{tr} \approx \Delta\varepsilon_{tr}^{MA} = 8\%$.

Figure 4.12.a shows the stress σ, strain ε and temperature variations θ as a functions of time during the unloading stage 4. Thus, from these measurements and eq. (4.11), the absolute values of the elastic $\dot{\varepsilon}_{el}$, reverse transformation $\dot{\varepsilon}_{tr}$ and detwinning $\dot{\varepsilon}_{de}$ strain rates are plotted in Figure 4.12.b as a functions of the strain ε_{l_0} between times (h) and (j). As shown in Figure 4.12.b, deformation mechanisms other than pure elastic distortion of crystalline lattice occur as soon as the stress starts to decrease. From the above rough analysis, it is suggested that reverse phase transformation has a dominant effect during the whole unloading. Its contribution to the overall strain rate is almost constant and equal to half the total strain rate. Decreasing the strain ε_{l_0} leads to reducing the elasticity contribution and to increasing the detwinning phenomena. It is worth concluding that these results disagree with the usual assumption of elastic unloading that is commonly made in thermomechanical modelling for stage 4.

Stage V This stage appears very similar to the sub-stage (b-c) of loading stage 2. Reverse localised bands are likely to form at the ends of the tube, outside the observation region. This hypothesis would explain the high decrease of the nominal strain ε_{L_0} and the almost constant average strain ε_{l_0}. As the local strains $\varepsilon(M)$ keep constant in the observation zone, the temperature decreases slower, being only due to natural heat losses.

4.2.4 Conclusions

The tensile behaviour of an initially austenitic Ti-50.8at% Ni thin walled tube was investigated using synchronised measurements of the temperature and strain fields. The following points are the main results of this study:

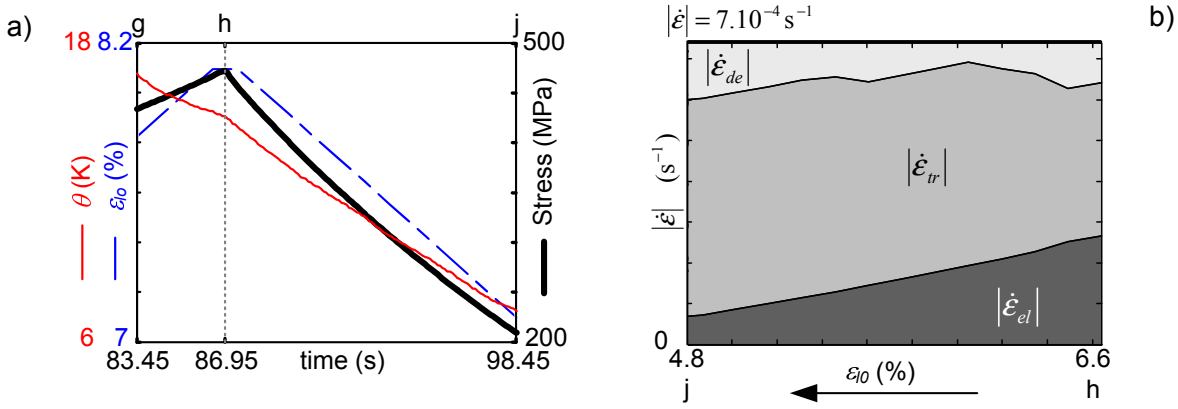

Figure 4.12: *a) Stress σ_0 (thick curve), strains (dashed curve) and temperature variations (thin curve) as a functions of time during the sub-stage h-j for the test shown in Figure 4.2. b) Estimation of the elastic, transformation and detwinning strain rates as a function of the strain ε_{l_0} during the unloading sub-stage h-j.*

1. The apparent initial linear elastic stage during loading is a homogeneous deformation stage, but does not correspond to pure elastic deformation of austenitic phase, as often assumed in the literature. As revealed by immediate temperature increases, it also involve phase transformations start as soon as the deformation proceeds. So far the nature of these phase transformation could not be determined precisely but is more likely to be a mixture of partial A→R, A→M and R→M transformations.

2. The previous observation disqualifies the stress peak on the stress-strain curves being regarded as due to the initiation of the product phase of the corresponding transformations.

3. Stress plateau is only a manifestation of strain localization. The transformations start before this plateau and are incomplete at the end of the plateau. The experimentally measured plateau stress and plateau strain do not correspond to the martensitic transformation stress and strain of NiTi as often assumed but to the beginning of localised phase transformation.

4. Localization can occur even if tensile stress-strain curves do not exhibit clear peak and plateau. The positive slope is due to thermal effects.

5. Localization is associated with macroscopic deformation instabilities leading to deformation bands throughout the specimen. The type and evolution of the morphology of these bands are dependent on a number of factors including specimen gripping. In our tests, the gripping system applies negligible bending and rotating torques to the tube ends and localization occurs through helical bands inclined at about 58° to the loading axis.

6. The localised deformation bands are separated from the low deformation regions by the band boundaries. The strain gradient inside these band boundaries is constant, equal to 2.5 % mm^{-1} for the investigated experimental conditions. This value is expected to be dependent on thermal effects.

7. The localised deformation bands do not nucleate with their final width and peak strain level, revealing that the transformation is not complete inside these localised deformation bands.

8. During the early stages of unloading, the apparent linear elastic stage is a homogeneous deformation stage, involving detwinning and M→A reverse transformation as soon as the unloading proceeds. Reverse transformation is the main deformation mechanism during unloading leading to a transformation strain rate approximately equal to half the total strain rate. The de-twinning strain rate is of the same order than the elastic strain rate. This unloading stage does not correspond to pure elastic deformation of oriented martensite as often assumed.

The synchronised measurements of both temperature variation and strain fields have thus brought valued information for analysing coupling effects and deformation mechanisms associated with stress-induced transformations in SMAs.

4.3 Influence of macroscopic strain rates

During the tensile test presented in the previous section, analysis of the homogeneous and localization stages (stage 1 and 2 respectively), have shown that (i) stage 1 exhibited a mixture of homogeneous A→R and A→M phase transformations and (ii) stage 2 exhibited strong localization phenomenon taking the shape of an helical band. In order to see the influence of the macroscopic strain rate ($\dot{U}/L_0$) on (i) stage 1 and (ii) the localization phenomena, four additional tensile tests have been performed in air at the same room temperature and various macroscopic strain rates (from $\dot{U}/L_0 = 2.3\ 10^{-4}\ s^{-1}$ to $2.3\ 10^{-2}\ s^{-1}$). These tests have been achieved on another tube T_2 presenting the same composition and similar DSC results as tube 1 (see material properties in Section 3.1.3).

4.3.1 Experimental procedure

Four tensile tests ($T2_1$ to $T2_4$) have been performed on tube T_2 on the second gripping system presented in Section 3.2.2.2. The characteristics of this tube are discussed in Section 3.1.3.2. The tube was deformed up to 7 % of global nominal axial strain $\varepsilon_0 = U/L_0$ at different macroscopic strain rates, namely, $\dot{U}/L_0 = 2.3\ 10^{-4}\ s^{-1}$, $2.3\ 10^{-3}\ s^{-1}$, $1.1\ 10^{-2}\ s^{-1}$ and $2.3\ 10^{-2}\ s^{-1}$. The spatial resolution (pixel size) of the infrared images was estimated to be close to 0.4 mm and the DIC resolution 0.5 mm, which also corresponds to the tube thickness. Depending on the macroscopic strain rate, different frame rates were used and are summarised in Table 4.1.

$\dot{U}/L_0$ (s^{-1})	f_{IR} (Hz)	f_v (Hz)
$2.3\ 10^{-4}$	3	1/3
$2.3\ 10^{-3}$	30	2.25
$1.1\ 10^{-2}$	145	9
$2.3\ 10^{-2}$	145	9

Table 4.1: *Values of the frame rates.*

4.3.2 Results

The nominal stress-strain curves of the four tests are superimposed in Figure 4.13. Unlike the first tube, those tests were nearly superelastic at room temperature. Moreover, the loading was stopped before the end of the stress plateau so that stage 3 could not be observed.

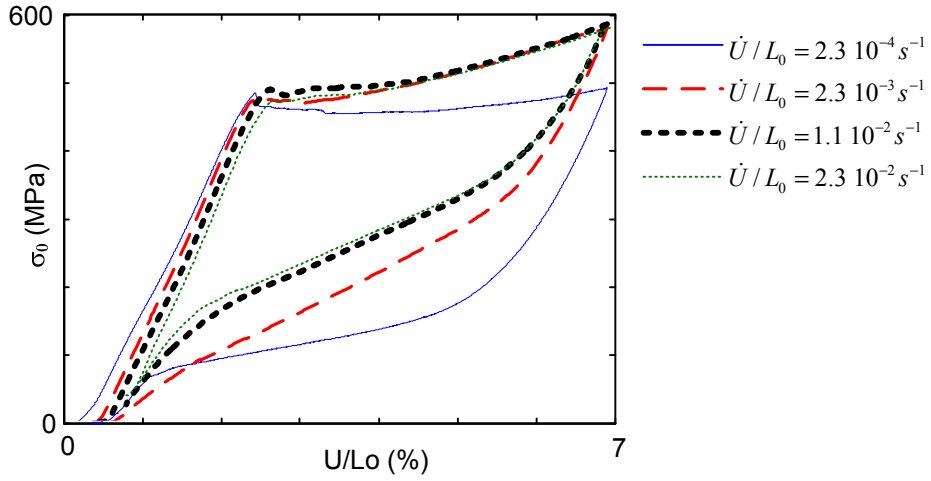

Figure 4.13: *Influence of the macroscopic strain rate on the nominal stress-strain curves on sample T_2.*

Temperature variations and strain maps on the tube surface are presented for each test in Figure 4.14. DIC strain fields were estimated in the yellow areas presented in Figure 4.14.1. Due to both strong and narrow localised phenomena that have been observed at macroscopic strain rate $\dot{U}/L_0 = 2.3\ 10^{-2}\mathrm{s}^{-1}$ and the poor spatial resolution of the visible images, DIC was not successful for this test, except during the homogeneous loading.

Axial temperature profiles along the central vertical axis of the four tests are shown in Figure 4.15. For each test, the stress-strain curve is represented in column a, temperature profiles during loading in column b and temperature profiles during unloading in column c. The times of the selected profiles are marked respectively in black and red dots in the stress-strain curves. These four tests exhibit several stages that will be described bellow.

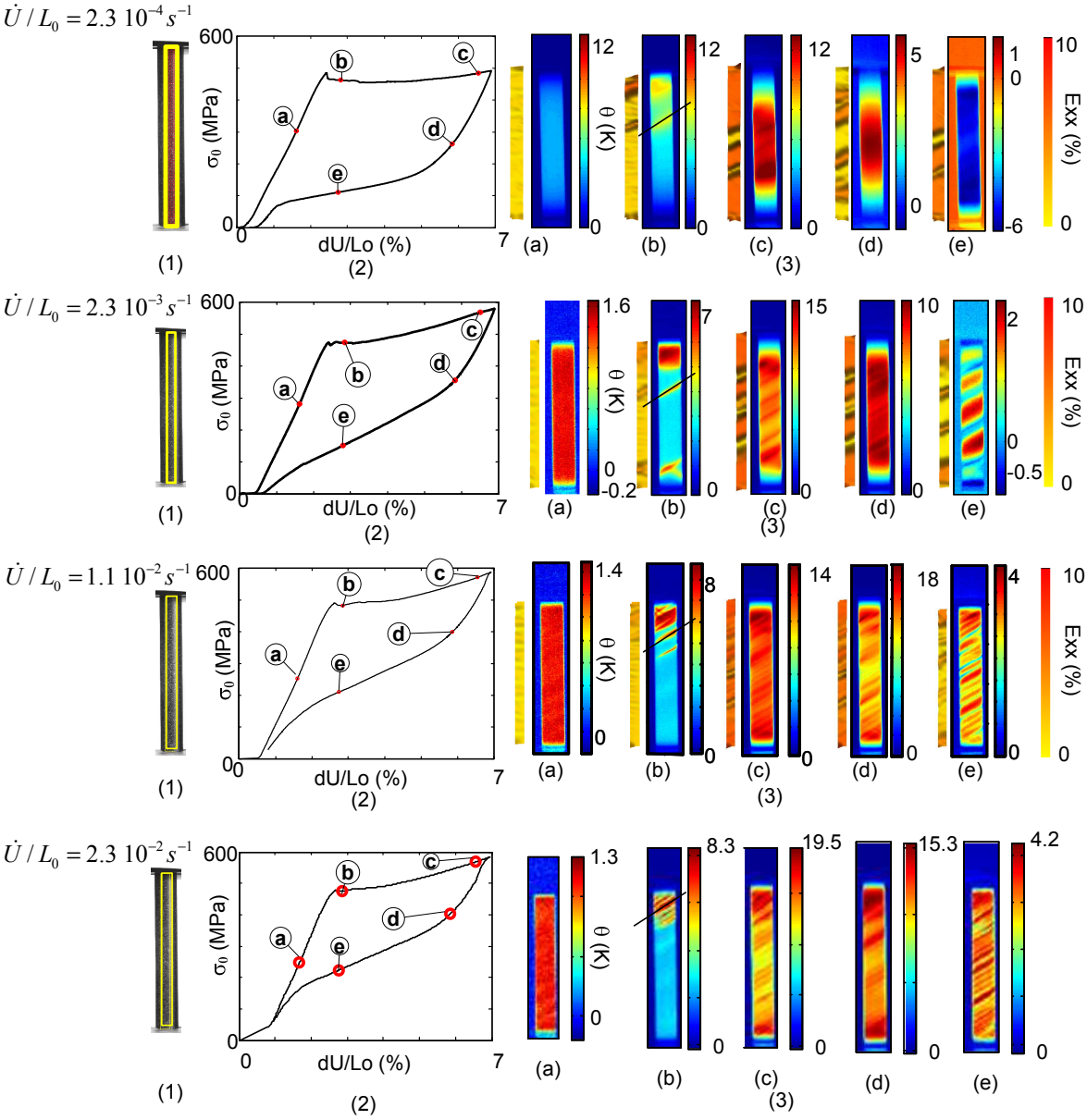

Figure 4.14: *Influence of the macroscopic strain rate on the Green Lagrange strain E_{xx} and the temperature variation θ. For each test, (1) position of the image correlation area (yellow) on the sample, (2) stress-strain curves, (3) coloured maps showing the local strain $E_{xx}(M)$ (left) and the temperature variation $\theta(M)$ (right) fields on the surface of the deformed tube, at four selected times marked in (2).*

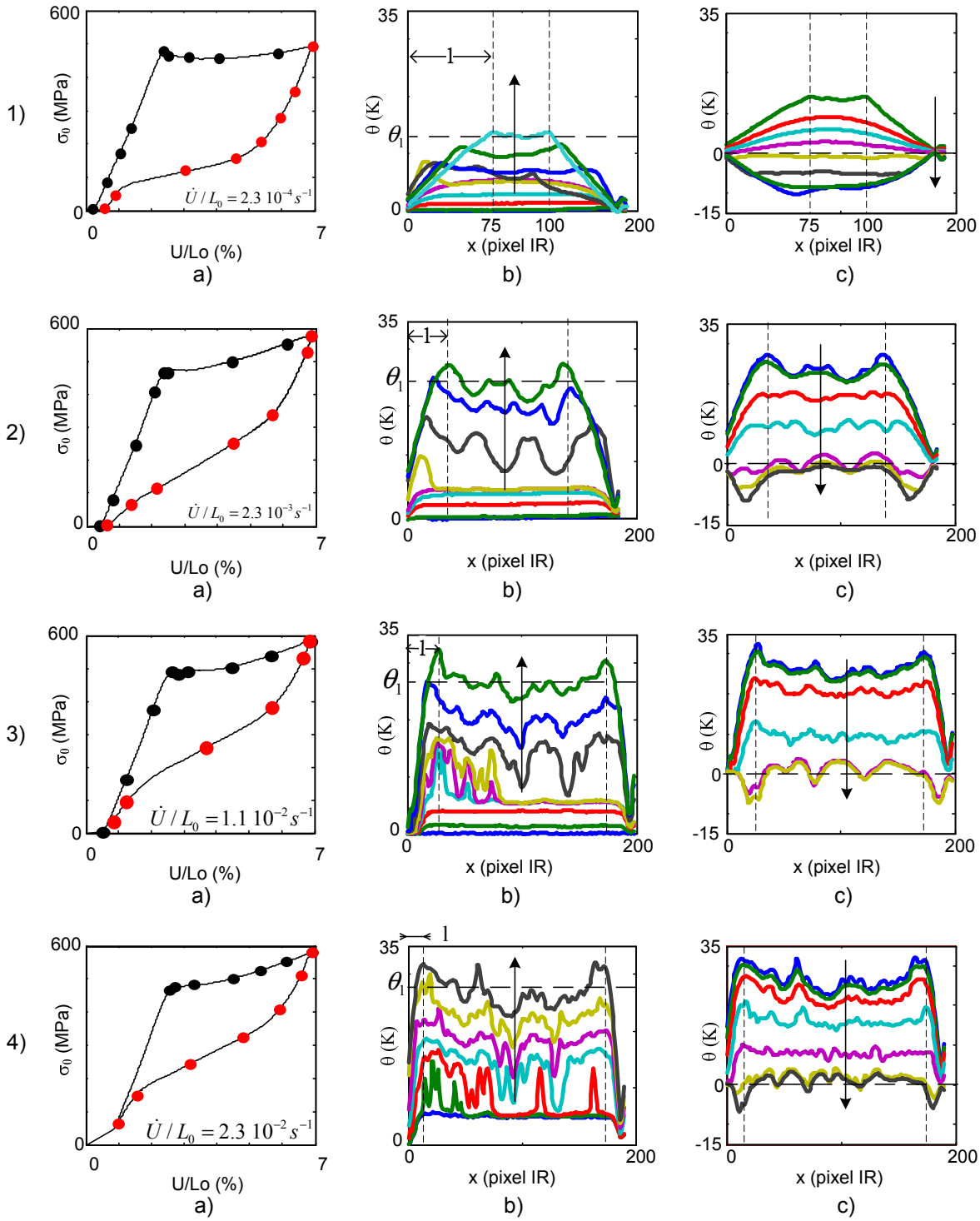

Figure 4.15: *a) Selection of time (black bullet during loading and red bullet during unloading) on the nominal stress-strain curve. b) Axial temperature profiles at the selected times during loading, c) during unloading.*

4.3.2.1 Stage 1

As for the first tube, the stress-strain curves (Figure 4.16.a) at the beginning of loading, were almost linear and identical for the four macroscopic strain rates. The apparent Young modulus during this stage is equal to 42 GPa irrespective of the macroscopic strain rate. In this Figure, the macroscopic strain $\varepsilon = \Delta l/l_0$ was calculated with the displacement Δl of two extreme points of initial length l_0 obtained by DIC.

Meanwhile, as observed in the temperature and strain maps at time (a) plotted in Figure 4.14, strain fields were homogeneous, regardless of the macroscopic strain rate. The temperature profiles plotted in Figure 4.15.b show that the temperature increased homogeneously in the central area of the tube. Near the edges, the tube was cooled down by the grips that were at room temperature. The mean temperature increase $\overline{\theta}$ in the centre of the tube versus the axial strain ε are plotted in Figure 4.16.b, for the four tests. As for the stress, the temperature variation $\overline{\theta}$ was insensitive to the macroscopic strain rate. At the end of the homogeneous loading, the nominal stress and temperature increase were identical for the four tests, namely, $\sigma_0 = 480$ MPa and $\overline{\theta}= 5$ K.

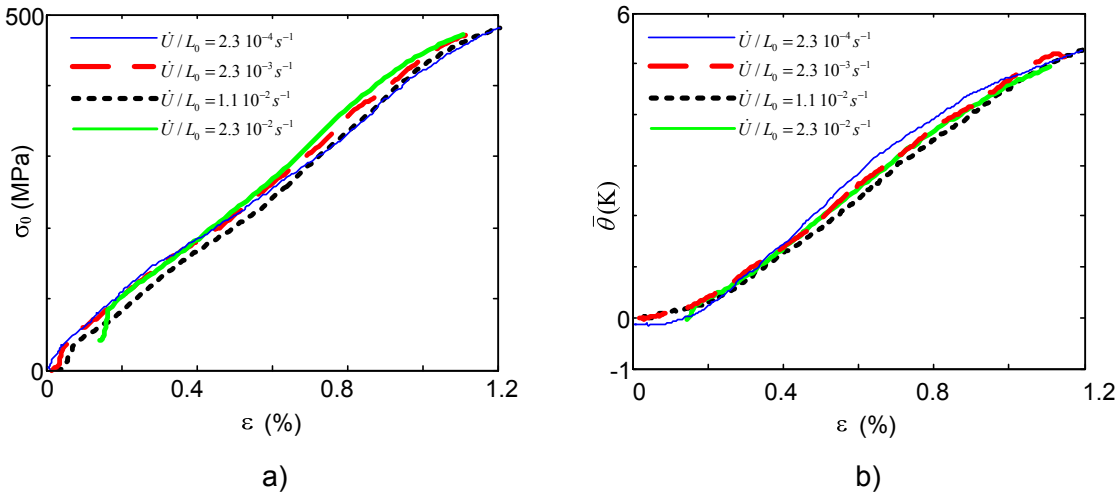

Figure 4.16: *a) Stress-strain curve response in stage 1. b) Evolution of the mean temperature variation $\overline{\theta}$=f(ϵ), during the homogeneous stage, for various macroscopic strain rates. The mean value was taken in a zone where the temperature was homogeneous i.e. in the centre of the tube.*

4.3.2.2 Stage 2

Stage 2 corresponds to the stress plateau defined between the initiation and propagation of the localization phenomenon.

Macroscopic behaviour

Two distinct phenomena were observed on the stress-strain curves plotted in Figure 4.13. For the first tensile test performed at the lowest strain rate ($\dot{U}/L_0 = 2.3\ 10^{-4}\text{s}^{-1}$), the stress-strain curve exhibited a nearly horizontal stress plateau. On the contrary, no horizontal stress plateaux were observed during the other tensile tests performed at higher strain rates.

Localization morphology

As observed at time (b) and (c) shown in Figure 4.14, all four tests exhibited strong localization phenomena both in temperature and strain fields. The localization phenomena took the shape of one or several helical bands turning around the tubes and widening. For each test, the localization appeared in the strain field in the same place as in the temperature field.

Regardless of the strain rate, all bands were turning with an identical angle of 58° with respect to the vertical axis, as presented with the thin line in Figure 4.14.3.(b). The majority of the bands were parallel and few were symmetric (-58°), like the band starting from the bottom right endside of test $T2_2$ in Figure 4.14.3 time (b).

The number of helical bands and their width strongly depended on the imposed macroscopic strain rate. The sample tested at the lowest macroscopic strain rate had only one large helical band. As the macroscopic strain rate increased, the number of bands increased but their width reduced (3 bands at $\dot{U}/L_0 = 2.3\ 10^{-3}\text{s}^{-1}$, 13 at $\dot{U}/L_0 = 1.1\ 10^{-}2\text{s}^{-1}$ and 16 at $\dot{U}/L_0 = 2.3\ 10^{-2}\text{s}^{-1}$) and the image correlation was less successful.

The tensile test at $\dot{U}/L_0 = 2.3\ 10^{-3}\text{s}^{-1}$ was similar to the tensile test performed on the first tube T_1 presented in Section 4.2 and performed at $\dot{U}/L_0(T_1) \approx 10^{-3}\text{s}^{-1}$. In both tests, 3 helical bands were observed. The temperature profiles for tube T_2 in Figures 4.15.2.b were higher than for tube T_1 (see Figure 4.6) since the strain rate was two times faster. The localization behaviours of the first two tests were mostly propagating the already formed bands whereas initiations of new localizations were preponderant in the two faster tests.

Table 4.2 summarises the influence of the macroscopic strain rate on the number of bands that initiated, the preponderant localization mode, the temperature variation at the end of loading in the middle area (θ_1), the maximum temperature variation (θ_{max}) and the length of the tube affected by the conduction with the grips. The evolution of the number of bands and θ_1 are plotted in Figure 4.17.

$\dot{U}/L_0$ (s^{-1})	nb bands	Preponderant localization behaviour	θ_1 (K)	θ_{max} (K)	l (pixels)
$2.3\ 10^{-4}$	1	propagation	13.5	14.1	75
$2.3\ 10^{-3}$	3	propagation	23.8	28.8	30
$1.1\ 10^{-2}$	13	initiation	26	33.8	20
$2.3\ 10^{-2}$	16	initiation	27	33.8	13

Table 4.2: *Influence of the macroscopic strain rate on the number of helical bands observed, temperature variation and size of the edge effect.*

Temperature fields

Figure 4.18 shows, for each test, several temperature profiles near the top grip just before and just after the stress peak. For the four tests, the temperature was homogeneous along the vertical axis before the stress peak in the central area. Then, several behaviours were observed depending on the macroscopic strain rate:

- **At $\dot{\mathbf{U}}/\mathbf{L_0} = \mathbf{2.3\ 10^{-4}}\text{s}^{-1}$**: the localization started at time $t_4 = 104.7$ s although the

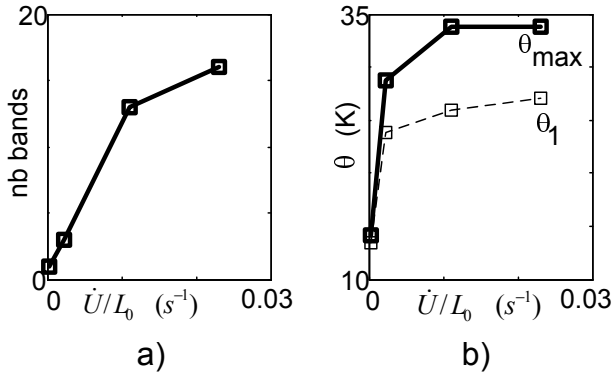

Figure 4.17: *Influence of the macroscopic strain rate ($\dot{U}/L_0$) on: a) the number of band observed, b) the temperature variation θ_1 and θ_{max}.*

stress peak was at time $t_2 = 104.1$ s (see Figure 4.18). The band was then propagating by widening (time $t_5 = 111$ s). At time $t_6 = 117.7$ s, the band had turned around the tube. After the stress peak (time 2, $\sigma_0 = 485$ MPa) the stress decreased and reached the stress plateau value at time 6 ($\sigma_0 = 464$ MPa). Outside the temperature peak, the temperature profile remained constant and even decreased slightly at time 5 and 6. As the test went on (Figure 4.15.1), the stress remained almost constant while the band continued turning and widening but the temperature peaks were less visible due to conduction phenomena. At the end of loading, even through the strain field (image time e in Figure 4.14.3) was still localised, the temperature profile in the middle of the sample (noted θ_1 in Figure 4.15) was almost homogeneous and equal to 13.5 K. During all the test, temperature decreased near the edge of the sample due to conduction phenomena with the grips. The length $l = 75$ pixels of tube affected by this conduction at the end of loading is represented in Figure 4.15 and in Table 4.2.

- **At $\dot{\mathbf{U}}/\mathbf{L_0} = \mathbf{2.3\ 10^{-3}}\mathrm{s}^{-1}$**: Figure 4.18 shows that localization started at time 3 ($t_3 =$ 10.26 s, $\sigma_0 = 474$ MPa). Then, while the band was widening, the stress decreased down to $\sigma_0 = 465$ MPa at time $t_6 = 10.53$ s and then started increasing again σ_0 reached 476 MPa at time $t_8 = 11.22$ s. Up to time 8, outside of the temperature peak, the temperature remained constant. As the test went on (see Figures 4.14 time b and 4.15.2), the stress was increasing almost linearly. The first band kept propagating by turning and widening and two other bands appeared near the bottom grip (time b in Figures 4.14). One of them had the same angle as the first one, the second was symmetric about the vertical axis. Like the first test, at the end of loading, the temperature profile was nearly homogeneous although the strain field was still strongly localised. θ_1 was equal to 23.8 K and the area affected by the conduction with the grips decreased to $l = 30$ pixels.

- **At $\dot{\mathbf{U}}/\mathbf{L_0} = \mathbf{1.1\ 10^{-2}}\mathrm{s}^{-1}$**: localization started at time 3 (t_3=1.8 s, $\sigma_0 = 487$ MPa, $\theta = 8$ K). Very quickly (time $t_4 = 1.814$ s) the temperature increased up to $\theta_{max} = 14.8$ K while the stress remained constant. The bands were very narrow: about 5 pixels wide. At time $t_5 = 1.834$ s, a second band of same width was initiated very close to the first one. Finally, the first band had turned around the tube and reappeared at time $t_6 = 1.903$ s. As the test went on, the stress increased following the same path as the previous test (see Figure 4.13). During stage 2, up to 13 helical bands initiated, all in same direction (see Figures 4.14 and 4.15.3). The bands were very narrow and close to each other and hardly detected on the strain field maps due to poor DIC resolution. Another set of optic would have allow to better describe the temperature

and strain fields. At the end of the test, the area affected by the conduction with the grips decreased to $l = 20$ pixels.

- **At $\dot{\mathbf{U}}/\mathbf{L_0} = \mathbf{2.3\ 10^{-2}s^{-1}}$**: localization started in three different areas very close to each other (see Figure 4.18), at the same time 3 ($t_3 = 0.7931$ s, σ_0= 477 MPa). Like the test at $\dot{U}/L_0 = 1.1\ 10^{-2}\text{s}^{-1}$, the band widths were near 5 pixels. Then, instead of propagating, other very narrow bands (same width) initiated near the first ones at time $t_4 = 0.8207$ s, meanwhile the stress decreased to 475 MPa. The temperature variation was 6 to 8 K within the bands. Since the test was very fast, the temperature remained constant outside the bands. At time $t_5 = 0.9586$ s, one of the band had turned around the tube and the stress was increasing again. 16 bands were observed in the temperature maps in Figure 4.14. Temperature variation reached up to $\theta_{max} = 33.8$ K above room temperature. Once again, DIC was not successful for this test since the bands were too small compared to the DIC resolution and were very close to each other. At the end of loading, due to the proximity of the bands, the temperature profile was almost homogeneous ($\theta_1 = 27$ K). The area affected by conduction with the grips was only $l = 13$ pixels.

Band Boundary

Observation of the macroscopic strain rate effect on the initiation and growth during the stress plateau of a Localised Deformation Band (LDB) is shown in Figure 4.19, for the first two tests ($\dot{U}/L_0 = 2.3\ 10^{-4}\text{s}^{-1}$ and $2.3\ 10^{-3}\text{s}^{-1}$). Like in Section 4.2, regardless of the macroscopic strain rate, the LDB was separated from the less deformed regions by narrow regions (Band Boundaries (BB)) across which strain and temperature change very quickly. At the end of loading the strain field inside the LDB was 0.066 at $\dot{U}/L_0 = 2.3\ 10^{-4}\text{s}^{-1}$ and 0.07 at $2.3\ 10^{-3}\text{s}^{-1}$.

The strain gradient dE_{xx}/dX was estimated for each strain profile on the left and right sides of the band of Figure 4.19 and is plotted in Figure 4.20. In this figure we observed two distinct phenomena.

- **Before time e**, Depending on the macroscopic strain rate, different behaviours were observed. At low strain rate dE_{xx}/dX decreased quickly from 3.4 to 1.7 % mm^{-1} whereas at faster strain rates, the strain gradient inside BB increased from 1 to 1.7 $\%\text{mm}^{-1}$. These variations may be explained by the simultaneous evolution of the band at these times, namely, initiation and widening.
- **After time e**, the strain gradients in the BB were almost constant for the two tests on both sides of the LDB. Its value was $dE_{xx}/dX \approx 1.7\%\text{mm}^{-1}$. At these times the band was widening in a reduced zone of limited length (BB).

4.3.2.3 Unloading

Localization was also observed during unloading, both in temperature and strain fields. Like loading, temperature fields strongly depended on the strain rate. At low macroscopic strain rate (Figure 4.15), the temperature decreased by 8 K below the initial temperature, in the middle of the sample. The temperature variation during unloading was up to 23 K. As

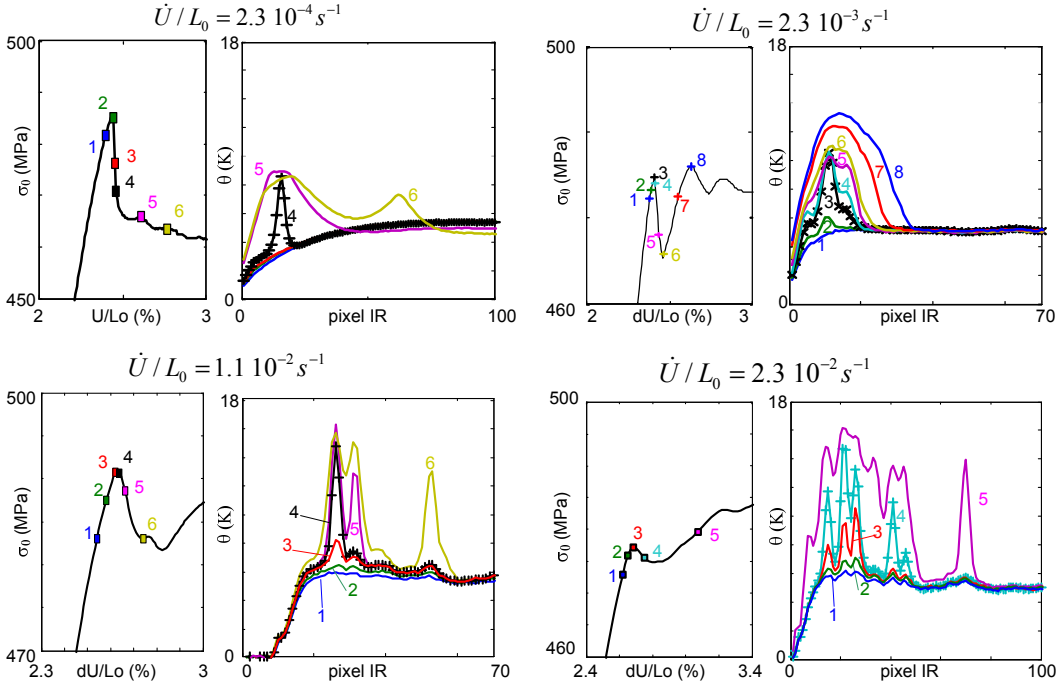

Figure 4.18: *Observation of the temperature profile near the stress peak during each test performed on tube T_2.*

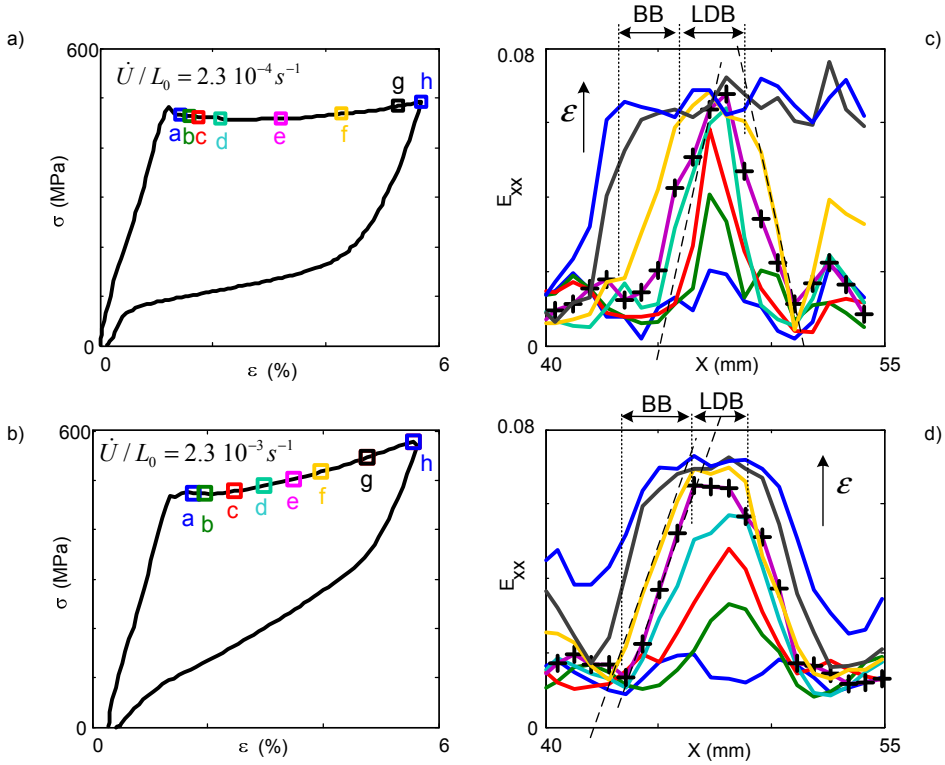

Figure 4.19: *Influence of the macroscopic strain rate on the local axial strain profiles. For each selected time, represented on the stress-strain curve in a) and b), the profiles of the local strain along a central vertical profile are plotted as a functions of the initial coordinates (X) for the band initiating at time b in Figure 4.14. LDB and BB designate the Localised Deformation Band and the Band Boundaries, respectively. The markers represent the position of the DIC subsets.*

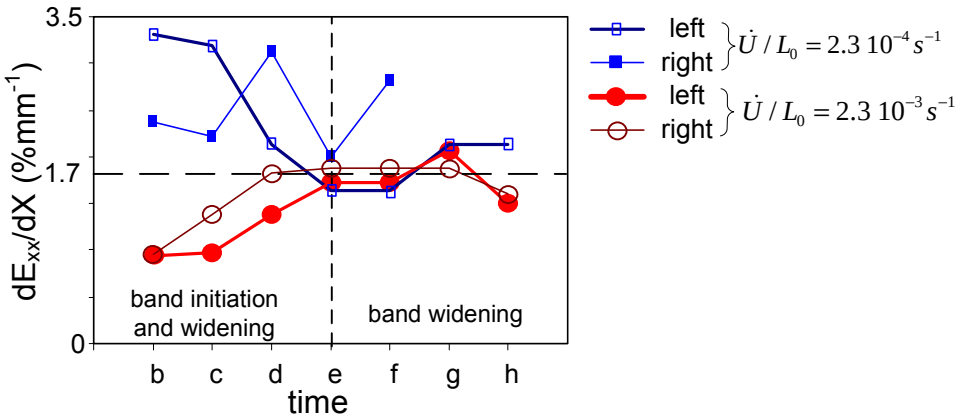

Figure 4.20: *Influence of the macroscopic strain rate on the evolution of the strain gradient in the Band Boundary. $d\varepsilon/dX$ is plotted on the right side (thick line) and left side (thin line) of the bands at the different times selected in Figures 4.19.a and b respectively for the velocities $\dot{U}/L_0 = 2.3\ 10^{-4} s^{-1}$ and $\dot{U}/L_0 = 2.3\ 10^{-3} s^{-1}$. After the vertical dashed line the band is only widening.*

the macroscopic strain rate increased, temperature variations at the end of unloading in the middle of the sample returned to their initial values. This final thermal state, at the end of loading confirms that the tests at the high strain rates were almost adiabatic. For the low strain rates, heat losses (conduction with the grips) are important during loading. The temperature variations are weak (13.5 K). During unloading, the temperature decreased ($\theta = -10$ K, Figure 4.15.c).

4.3.3 Discussion

4.3.3.1 Influence of strain rate on the initial stage of deformation

As observed on the first sample in Section 4.2, both stress and temperature in Figure 4.16 increased almost linearly with strain. By adopting the same hypotheses as that made in Section 4.2.3.1, it is possible to estimate

$$\frac{\Delta H_{tr}^{tensile}}{\Delta \varepsilon_{tr}} = \frac{\dot{q} + \frac{\alpha T}{\rho}\dot{\sigma}}{\dot{\varepsilon} - \frac{\dot{\sigma}}{E}}. \tag{4.14}$$

The local heat sources $\dot{q}$ can be estimated by using the simplified thermal conduction model presented in Section 2.5.4 from the temperature field $\overline{\theta}$. The strain rate $\dot{\varepsilon}$ involved in eq. (4.14) was estimated with the axial strain $\varepsilon = \Delta l/l_0$ obtained from the displacement of two extreme points of the sample. $\alpha = 1.1 \times 10^{-5}$ K^{-1} is the coefficient of thermal expansion, and $E = 110$ GPa is the Young modulus.

The influence of this macroscopic strain rate on the evolution of $\Delta H_{tr}^{tensile}/\Delta\varepsilon_{tr}$ is presented in Figure 4.21. When no phase transformation is present both $\Delta H_{tr}^{tensile}$ and $\Delta\varepsilon_{tr}$ should be equal to zero. If only one phase tansformation is present The ratio is constant. Three

horizontal lines show the values of $\Delta H_{tr}^{tensile}/\Delta\varepsilon_{tr}$ of the three possible phase transformations:

$$\begin{aligned}
\frac{\Delta H_{tr}^{tensile}}{\Delta\varepsilon_{tr}} &\approx \frac{\Delta H^{AR}}{\Delta\varepsilon_{tr}^{AR}} = 600 \text{ J/g for A-R;} \\
\frac{\Delta H_{tr}^{tensile}}{\Delta\varepsilon_{tr}} &\approx \frac{\Delta H^{AM}}{\Delta\varepsilon_{tr}^{AM}} = 250 \text{ J/g for A-M;} \\
\frac{\Delta H_{tr}^{tensile}}{\Delta\varepsilon_{tr}} &\approx \frac{\Delta H^{RM}}{\Delta\varepsilon_{tr}^{RM}} = 200 \text{ J/g for R-M.}
\end{aligned} \tag{4.15}$$

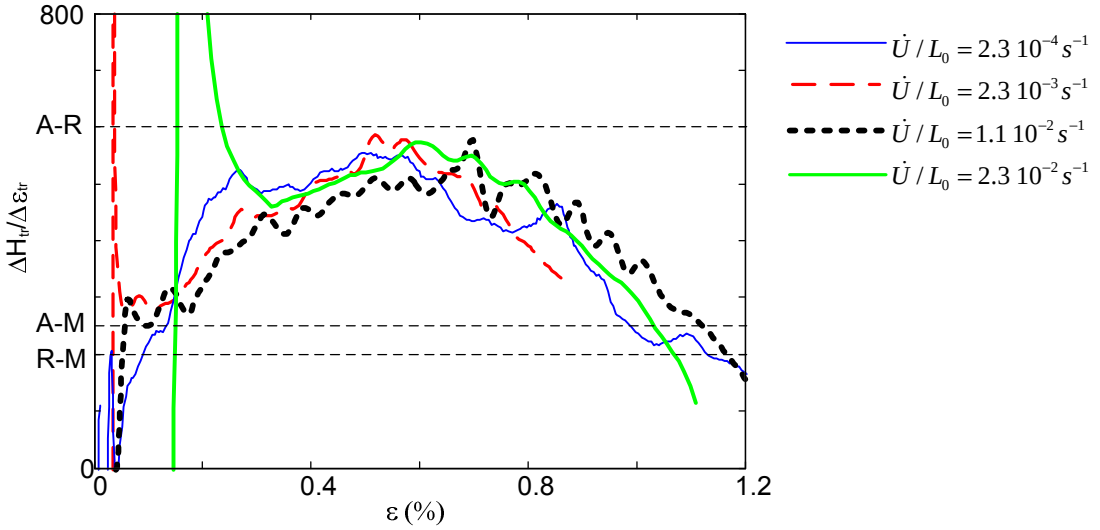

Figure 4.21: *Influence of the macroscopic strain rate on the evolution of $\Delta H_{tr}/\Delta\varepsilon_{tr}$ vs. ϵ during the homogeneous loading. The horizontal dashed lines represent the value of $\Delta H_{tr}/\Delta\varepsilon_{tr}$ for A-M, A-R and R-M phase transformation.*

As already observed on the first sample in Figure 4.9, these four curves confirm that the deformation during stage 1 is never purely elastic and involves, even at very low stress and strain levels, additional deformation mechanisms associated with a mixture of the three transformations (A-R, A-M and R-M). Moreover, the behaviours are very similar for all tests which means that stage 1 is not influenced by the macroscopic strain rate. It is worth notice that this behaviour is strain rate insensitive because the tess were almost adiabatic in this deformation stage (see Figure 4.17.b 4.16).

4.3.3.2 Influence of strain rate on deformation localization

Stress peak

Unlike the first test presented in Section 4.2, all the tube gauge length was visible when using the second gripping system (see presentation of the gripping system in Section 3.2.2.2). It allows therefore to observe the initiation of the localization phenomena. Regardless of the velocity, strain fields were homogeneous during stage 1. As already discussed by Feng and Sun (2006), the localization started at the stress peak (Figure 4.18) for the three fast tests. At strain rate $\dot{U}/L_0 = 2.3\ 10^{-4}\text{s}^{-1}$, localization was observed 0.6 s after the stress peak and at 15 pixels = 6 mm from the sample end. It is likely that for this test, localization started on the back side of the tube (not visible).

As shown in the analysis of the homogeneous stage, the phase transformation had already started before the stress peak. Therefore the stress peak does not correspond to the beginning of the phase transformation but only to a change of deformation mode from homogeneous to localised.

Mechanical response after the stress peak

It is known that the transformation stress increases with the temperature, therefore, as expressed by the Clausius-Clapeyron relationship:

- at low macroscopic strain rate, thermal conduction cools down the sample and the temperature remains almost uniform. The sample is not subjected to thermomechanical coupling and the transformation stress remains constant as well. A horizontal stress plateau is observed on the stress-strain curve;
- at high strain rates, the sample does not have the time to cool down by conduction and its mean temperature increases. Thermomechanical coupling is important and temperature increase induces a transformation stress increase.

In our experiment, a horizontal stress plateau was only observed at low macroscopic strain rate. In the centre of the tube the temperature increase θ_1 was 13.5 K at the end of loading. At this rate, the thermomechanical coupling are not very important. During the three faster tests, the temperature increases θ_1 were much higher and similar (see Figure 4.17). From the comparison of temperature profiles at the end of loading with those at the end of unloading those tests were nearly in adiabatic conditions. Meanwhile, mechanical response of the three tests were identical. No horizontal stress plateau was observed and the mechanical response exhibited a second stress slope of 3.3 GPa imposed by the temperature increase. For those tests the thermomechanical coupling were important and induced the transformation stress increase.

Influence of the macroscopic strain rate on the localization morphology and evolution

Depending on the macroscopic strain rate, two phenomena were observed, namely, initiation and propagation of highly deformed domain morphologies. As already observed by Feng and Sun (2006), we observed propagation in two principal directions, namely, (a) in the tip direction along the helical bands, (b) perpendicular to the band, widening the band (Figure 4.22).

Estimation of the velocities of propagation V_t and V_m are possible from a spatiotemporal representation of E_{xx}. From this representation, velocity V of widening of the bands represents the projection of V_m along the vertical axis. Velocity V_m is then estimated with $V_m = cos(90 - 58)V$. Estimation of V_t is more complicated. It is possible to estimate the time Δt for the band to make a complete turn around the tube. Therefore, with the orientation of the band (58°) it is possible to obtain the distance $d = 2\pi R\, sin(58)$, with R being the radius of the tube. Finally the velocity is obtained with $V_t = d/\Delta t$. The velocity of propagation in the first direction (V_t) is higher than in the second one (V_m), giving a much

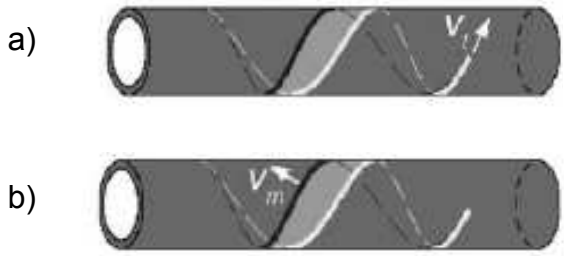

Figure 4.22: *Schematic of the helical band propagation with the two directions (a) the front velocity at the helical domain tip (V_t) and (b) the front normal velocity at the mid-point of the long front (V_m) (Feng and Sun, 2006).*

faster domain lengthening than its lateral thickening. For the test at $\dot{U}/L_0 = 2.3\ 10^{-4}\text{s}^{-1}$, $V_{t_{max}} \approx 3.3$ mm.s^{-1} and $V_{m_{max}} \approx 0.08$ mm.s^{-1}. For $\dot{U}/L_0 = 2.3\ 10^{-3}\text{s}^{-1}$, $V_{t_{max}} \approx 26$ mm.s^{-1} and $V_{m_{max}} \approx 0.55$ mm.s^{-1}. Both velocity ratios were similar $V_t/V_m \approx 41$ for the first test and $V_t/V_m \approx 47$ for the second test. Further test at different velocities and on different tubular geometries are necessary to confirm this first result.

At low strain rate ($\dot{U}/L_0 = 2.3\ 10^{-4}\text{s}^{-1}$ and $2.3\ 10^{-3}\text{s}^{-1}$), 1 and 3 helical bands were observed and propagating during the test. As the macroscopic strain rate increased, instead of propagating, new bands were created next to the previous ones (up to 16 bands were observed). Those bands were becoming narrower as narrower and closer to each other as the macroscopic strain rate increased. The temperature gradients were much higher. Outside the localised domain the temperature remained constant since the test was almost adiabatic.

Observation of the strain profiles confirms that the bands initiated neither with their final width nor with a strain level equal to their final amplitude (see Section 4.2).

When initiating (before time e in Figure 4.20), the bands were propagating along both the tip and the normal directions ($V_t > V_n$) and the ratio dE_{xx}/dX was decreasing as the band formed at low strain ratse and was increasing at higher strain rate. Such behaviour was not observed on the first tube that was much thinner. Further tests will be necessary to better understand this behaviour under different conditions (strain rate, tube thickness). For those tests spatial resolution should be increased. It is important to note that during these two tests, the spatial resolution of the strain field was equal to the tube thickness and only few data describe the band growth before time e.

When the band was only propagating along its normal direction (after time e in Figure 4.20). The band boundaries between those two domains were very narrow and were the same for the two tests $dE_{xx}/dX \approx 1.7\%\text{mm}^{-1}$. This value was different from the test performed on the first tube ($d\varepsilon/dX(\text{tube } 1) = 2.5\%\text{mm}^{-1}$). In fact, those two samples have different sizes, namely, their thickness are $e_1 = 0.12$ mm and $e_2 = 0.5$ mm for tube 1 and 2 respectively; their diameters are 6 mm and 10 mm respectively. It is more likely that the size of BB depends on the tube geometry. For this test, the BB width was nearly constant and equal to 3.9 mm. Therefore the BB width/tube thickness ratio was of the order of $3.9/0.5 = 7.8$. This value is higher than the ratio obtained for the thin tube P_1 and but smaller to the ratio obtained by Feng and Sun on microtube (Feng and Sun, 2006) and indicates strong local thermomechanical coupling (Iadicola and Shaw, 2004).

4.3.4 Conclusion

This study confirmed the following conclusions:

1. Regardless of the macroscopic strain rate,
   - the homogeneous deformation during stage 1 involves a mixture of partial A→R, A→M and R→M phase transformations. In this stage, macroscopic strain rate does not have an influence on the phase transformation behaviour;
   - the stress peak marks the beginning of localised deformation and not initiation of the phase transformation;
   - the propagation of the localized deformation bands is along two directions, namely, (i) helical rotation around the tube and (ii) band widening.
2. Other parameters were strongly influenced by the macroscopic strain rate:
   - stage 2 exhibits unpredictable and complex localization phenomenon, both propagation (then widening) and initiation in another area may occur. Propagation is predominant at lower macroscopic strain rates while initiation of new localizations are observed at high macroscopic strain rates,
   - during loading, high macroscopic strain rates tend to increase elevation of the temperature variation and the number of bands; meanwhile, the bands are narrower and temperature gradient is increased.

4.4 Quasi-isothermal loadings

4.4.1 Introduction

4.4.2 Experimental procedure and set-up

Several tensile tests on various imposed temperatures T_{fluid} ranging between 310 and 325 K have been performed on two specimens extracted from tube no. 3 (T3), respectively referred to as sample 1 and sample 2. The total length of the sample is 99 mm and gauge length is $L_0 = 65.5$ mm (see Figure 4.23). The samples were mounted using the second gripping that allows the circulation of a heat-transfer fluid (here water) inside the tube. The temperature T_{fluid} was controlled using a thermocryostat (Julabo FP 50, $T = \pm 0.03$ K).

All tests were performed at constant macroscopic strain rate, corresponding to a global nominal axial strain rate of $\dot{\varepsilon}_0 = \dot{U}/L_0 = 2.10^{-3}s^{-1}$ where U is the cross head displacement. The room temperature was $T_{room} = 298$ K. The mechanical loading was imposed up to $\varepsilon = 7\%$ and unloading was performed down to zero load ($F = 0$). The axial strain ε was estimated from the vertical displacement difference Δl between two extreme points A and B, initially separated by a length l_0 (see Figure 4.23.b). Point A was close to the lower fixed grip ($x = 0$) and B close to the upper moving grip ($x = l_0$). Between two consecutive tests, heating and cooling of the tube were performed at zero force and thermal equilibrium was reached before starting the test.

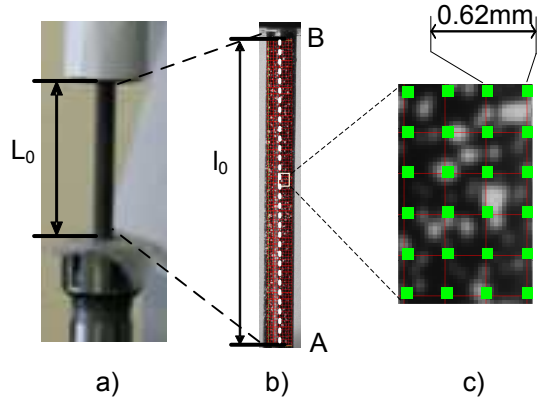

Figure 4.23: *a) Photography of the tube mounted in the two grips of the second gripping system. b-c) Observation area and virtual grid applied to calculate the kinematic fields.*

The spatial resolution was estimated to be close to 0.24 mm for the infrared camera and 0.062 mm for the visible images. The grid size of the DIC processing was 10×10 pixels so that the resolution (grid size) of the strain fields was 0.62 mm (Figure 4.23.c). In order to obtain, for every particles, at the same time, the mechanical data, the kinematic and temperature fields, the temporal synchronisation and spatial synchronisation presented in Section 2.4 was used. Hence, in the following all the figures will be plotted for material points using the spatial synchronisation.

Tests performed on sample 1

Sample 1 was subjected to ten cycling loadings, as represented in Figure 4.24, at constant temperature 315 K in order to observe the influence of cycling on its mechanical behaviour.

Tests performed on sample 2

Seven tensile tests have been chronologically performed on the second sample for various prescribed temperatures as summarised in Table 4.3.

	$T3_1$	$T3_2$	$T3_3$	$T3_4$	$T3_5$	$T3_6$	$T3_7$
T_{fluid}	310 K	315 K	320 K	325 K	325 K	320 K	315 K

Table 4.3: *Prescribed temperature (T_{fluid}) for each tensile tests.*

Time evolutions, during the seven tensile tests, of the prescribed temperature T_{fluid}, axial strain ε and the nominal stress $\sigma_0 = F/s_0$ are plotted in Figure 4.25.

Although the fluid temperature $T3_{fluid} = 310$ K applied during the first tensile test was higher than $T(R-A)_f = 301$ K, the first test $T3_{1A}$ was not superelastic. The remaining axial strain was $\varepsilon = 4\%$ at the end of the first unloading (see Figure 4.25.b). Therefore, the bottom pin that links the collet holder (f) to the driving shaft (h) (Figure 3.7) was removed. The sample was free of load ($\sigma = 0$) and allowed to deform. The tube was then heated up slowly from 310 K to 330 K and visible images were recorded during test $T3_{1B}$ in order to

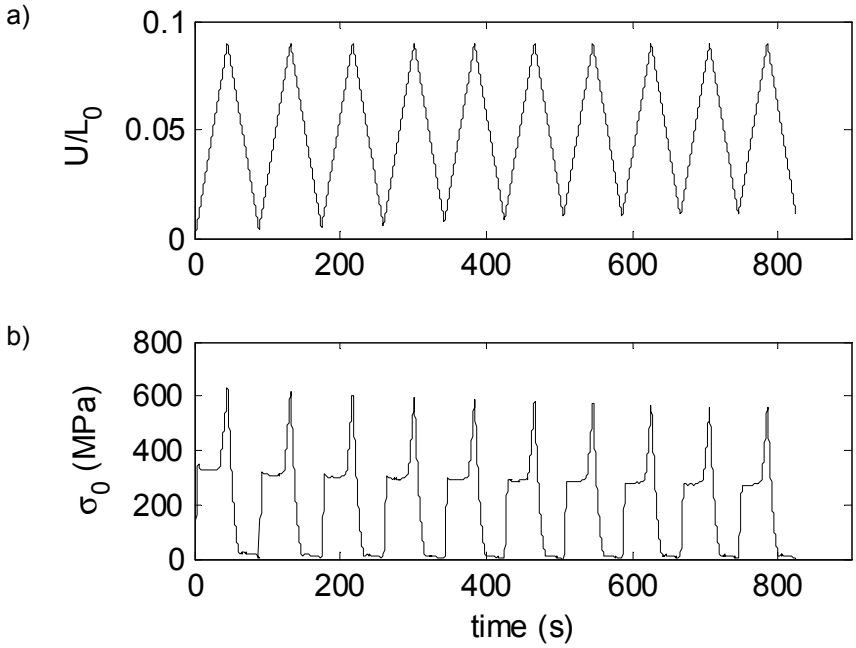

Figure 4.24: *Tests performed on sample 1 at temperature $T_{fluid} = 315$ K: chronographs showing the time evolution of a) the nominal strain $\varepsilon_0 = U/L_0$ and b) the nominal stress $\sigma_0 = F/s_0$ during the ten cycles.*

analyse the shape memory effect.

4.4.3 Results

4.4.3.1 Sample 1: influence of cyclic loading at constant temperature T_{fluid}

Macroscopic results

The nominal stress-strain curves recorded during the ten cyclic loadings are plotted in Figure 4.26. During these tests, evolution of the residual strain (ε_r) and the stress plateau during loading (σ_{tr}^{A-M}) and unloading (σ_{tr}^{M-A}) were measured and plotted in Figure 4.27.

As commonly observed during cyclic loadings (Iadicola and Shaw, 2002b; Liu et al., 2006), the stress plateau σ_{tr}^{A-M} decreased whereas σ_{tr}^{M-A} remained unchanged during cycling. Therefore, the stress hysteresis $\sigma_{hys} = \sigma_{tr}^{A-M} - \sigma_{tr}^{M-A}$ decreased as well. The stress plateau decrease during loading was especially important between the first and second cycle, its decrease was 20 MPa, then stabilised itself at about 5 MPa per cycle. Such behaviour is mostly attributed to dislocations generated during cycling (Siddons and Moon, 2001; Iadicola and Shaw, 2002b). Meanwhile, the residual strain ε_r plotted in Figure 4.27.b increased with cycling from 0.4 to 1.2 %. This may be attributed to martensite stabilisation.

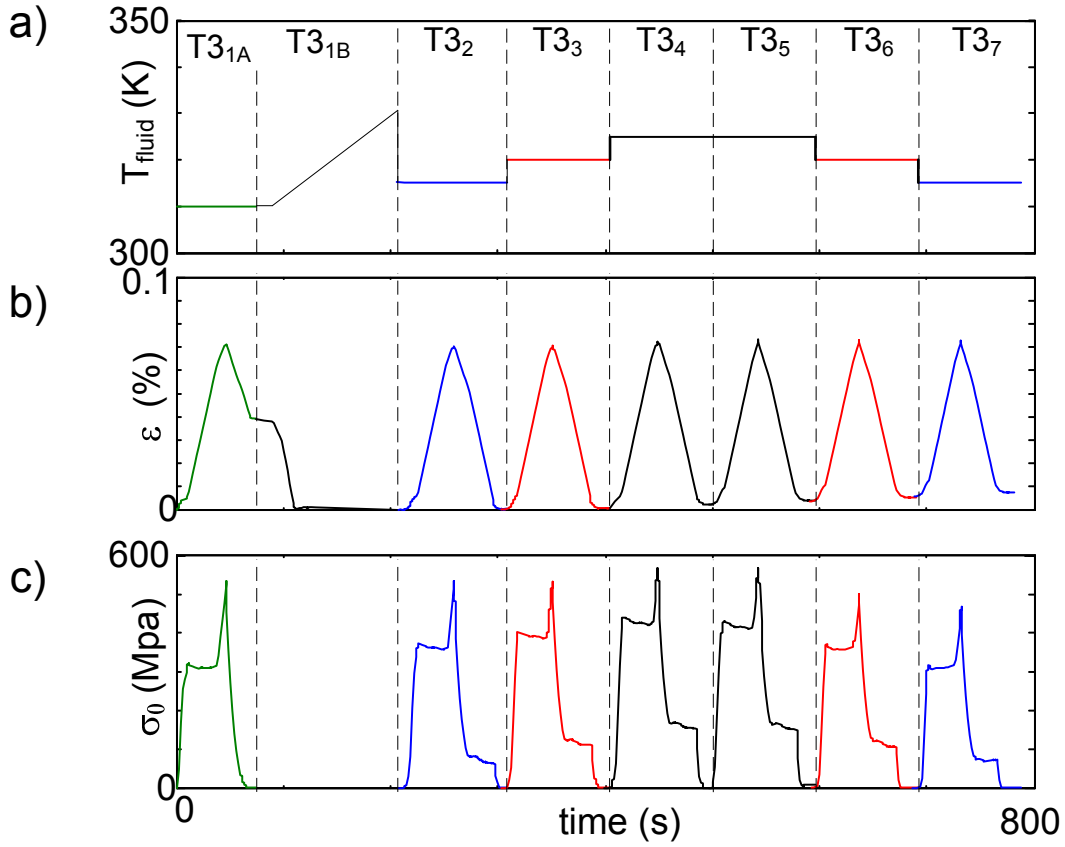

Figure 4.25: *Tests performed on sample 2: chronographs showing the time evolution of a) the prescribed fluid temperature T_{fluid} during the tests $T3_1$ to $T3_7$; b) the axial strain $\varepsilon = \Delta l/l_0$; c) the nominal stress $\sigma_0 = F/s_0$ during the seven tensile tests.*

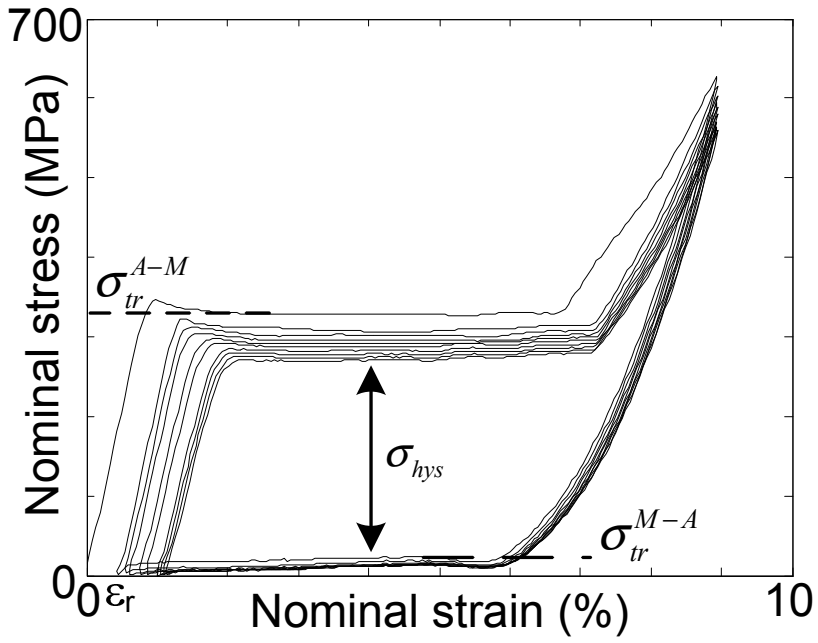

Figure 4.26: *Nominal stress-strain curve measured during the 10 cycles at a constant imposed circulating fluid $T_{fluid} = 315K$.*

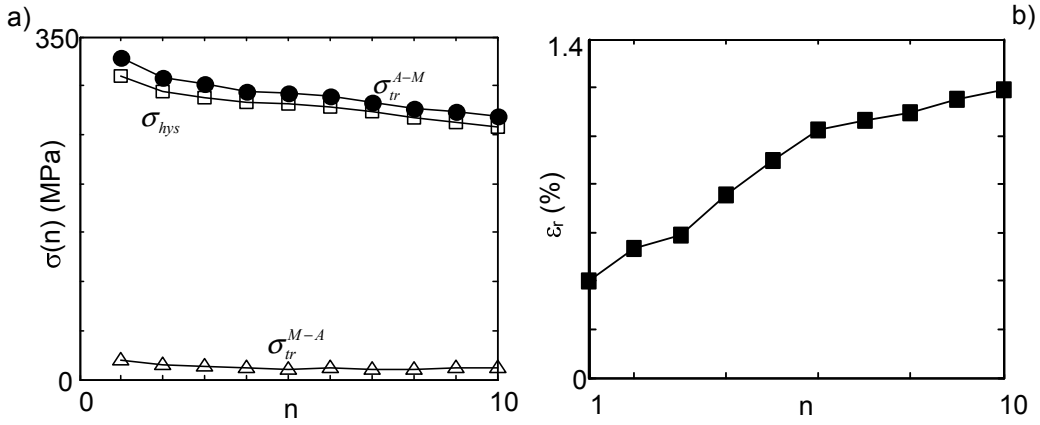

Figure 4.27: *a) Evolution with the number of cycle n, of the stress plateau measured during loading σ_{tr}^{A-M} and unloading σ_{tr}^{M-A} respectively at $\varepsilon_0 = 2\%$ and $\varepsilon_0 = 4\%$ and the stress hysteresis σ_{hys}. b) Evolution of the residual strain ε_r at the end of loading.*

Strain field measurements

The Green-Lagrange strain field E_{xx} measured on the tube at $U/L_0 = 4\%$ and $U/L_0 = 2\%$, respectively during loading and unloading, are presented in Figures 4.28 and 4.29.

The first loading exhibited a localization into two helical bands and one front starting from each extremities of the sample. At $U/L_0 = 4\%$, the bottom front had caught up the lower band whereas the unloading strain morphology was very different and exhibited two annular fronts, almost perpendicular to the sample axis.

Likewise, the mechanism of localization during loading changed, during the first cycles. After five cycles, the localization mode became stabilised into one front going upwards. In contrast, the localization mechanism during unloading did not vary with cycling. The reverse localization started from each grip and propagated to the centre of the sample (Figure 4.29).

4.4.3.2 Sample 2: influence of temperature

The nominal stress $\sigma_0 = F/S_0$ as function of the axial strain ε for each tensile tests $T3_{1A}$ to $T3_7$ are superimposed in Figure 4.30. Due to the high thermal exchange between the heat-transfer fluid and the tube, the observed stress-strain curves are typical of polycrystalline NiTi with initial austenitic phase structures in nearly isothermal conditions (Brinson et al., 2004) i.e. they exhibit horizontal stress plateaux during stage 2 and 4. For tensile tests performed in air, these conditions would be obtained at much lower strain rate, typically less than $10^{-4}s^{-1}$ (Shaw and Kyriakides, 1995; Ng and Sun, 2006).

4.4.3.2.1 Tensile test $T3_{1A}$ (310 K)

The temporal evolution of an axial profile of the Green-Lagrange strain E_{xx} field along the vertical axis of the tube is plotted in Figure 4.31.a. The grey dotted curve is the axial strain (ε) and the white thick curve is the nominal stress (σ_0). Figure 4.31.c represents the axial Green-Lagrange strain field $E_{xx}(x,t)$ on the tube sample at 2% and 4% of axial strain during

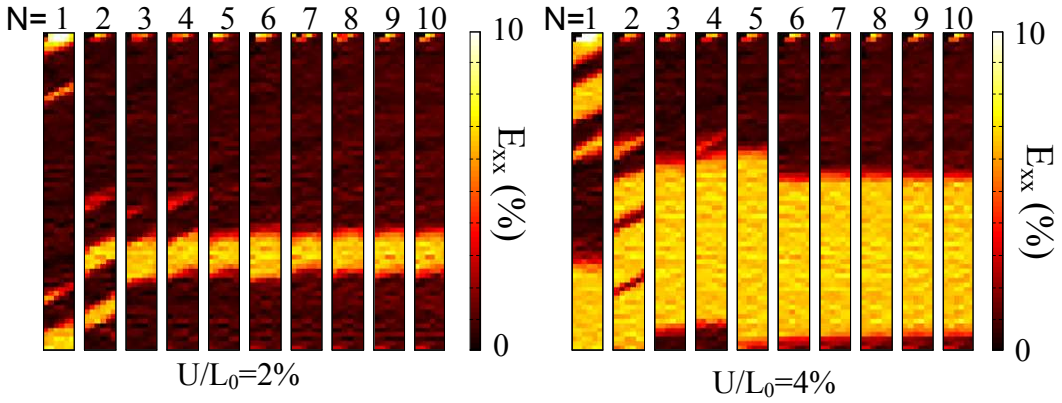

Figure 4.28: *Green-Lagrange axial strain field E_{xx} observed for each cycle during loading at $U/L_0 = 2\%$ (left) and $U/L_0 = 4\%$ (right).*

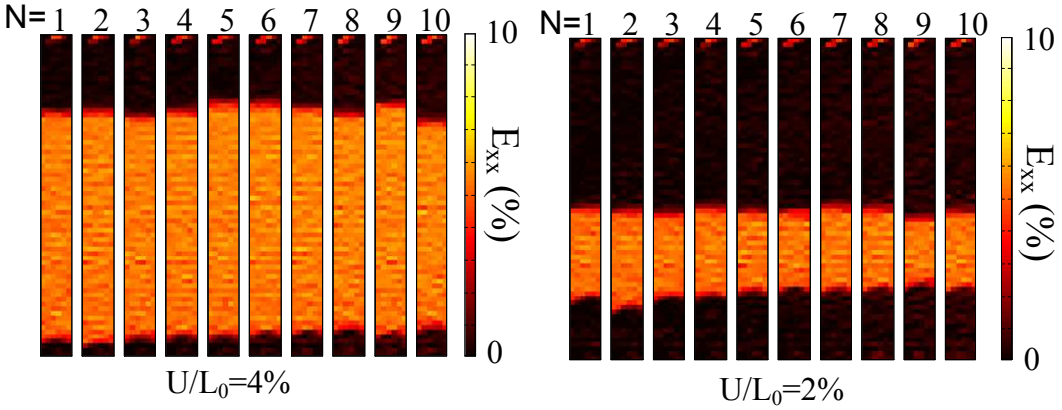

Figure 4.29: *Green-Lagrange axial strain field E_{xx} observed for each cycle during unloading at $U/L_0 = 2\%$ (left) and $U/L_0 = 4\%$ (right).*

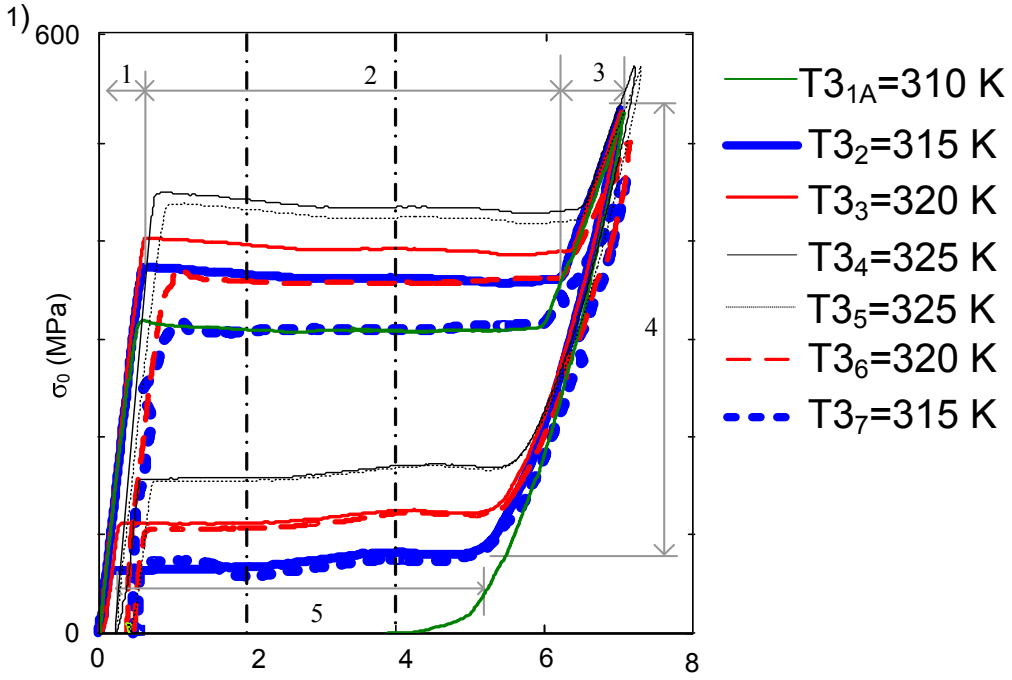

Figure 4.30: *1) Nominal stress-strain curve for the seven tensile tests performed in a row. Arrows and number represent the 5 characteristic zones of behaviour.*

loading (respectively after 19 and 28 s) and the strain field at the beginning and the end of unloading (50 and 70 s respectively). Figures 4.31.b and d show local strain measurements recorded during the shape memory effect ($T3_{1B}$) at the beginning of heating and will be presented in details in Section 4.4.3.3.

During stage 1 (up to 15 s), the strain field increased homogeneously up to $E_{xx} = 0.0056$. Then, the stress reached the stress plateau (stage 2). The localization initially started in two areas. First, close to the upper grip, an helical band appeared with an angle and propagated towards the bottom grip turning around the tube (Figure 4.31). Second, from the bottom grip, a strain localization front emerged with an orientation almost perpendicular to the tube axis. The first front started on the edge of the gripping system at the back side of the tube (not visible with our camera). Over stress plateau, the strain state along the sample was heterogeneous and was separated into two areas. In Figure 4.31.c, the area labelled 1 was less deformed ($E_{xx}(1) = 0.0056$) and the area labelled 2 was highly deformed with $E_{xx}(2) = 0.0633$. At the end of the stress plateau, the strain field was homogeneous again ($E_{xx} = 0.0633$) and increased homogeneously up to $E_{xx} = 0.0774$ at the end of loading (stage 3).

During unloading, the nominal stress reached practically zero at the very beginning of stage 5, when the stress plateau of the localised reverse M→A phase transformation was reached. At the end of unloading (Figure 4.31.c), the strain field along the tube was separated into two areas. In area 1, $E_{xx}(1) = 0.05$ and in area 2 $E_{xx}(2) = 0.0005$ The morphology during unloading was different than during loading and exhibited only one annular front (Figure 4.31.c).

4.4.3.2.2 Superelastic tests $T3_2$ to $T3_7$ at temperatures 315 K to 325 K

Test $T3_2$ (315 K): Strain and temperature fields measured during this test are plotted in Figures 4.32.1 and 4.32.3 at four times, namely, *a* (2% loading), *b* (4% loading), *c* (4% unloading) and *d* (2% unloading).

The profile of the Green-Lagrange axial strain $E_{xx}(M,t)$ and temperature variation θ at the four selected times are represented in Figures 4.32.2 and 4.32.4 for the dashed line sketched in Figure 4.23.2. The strain fields (Figure 4.32.1) exhibited strong strain localizations. They were very different during loading from those observed in the first tensile test $T3_{1A}$ (Figure 4.31). At each time, the tube was separated into two areas, namely, (1) a less area deformed and (2) an highly area deformed. These two areas were separated by a unique front of strain localization taking the shape of an almost horizontal front that propagated from bottom to top during loading and from top to bottom during unloading.

In the same position as the strain gradient, we observed a positive temperature peak during loading and negative one during unloading. The temperature peaks took the shape of an almost horizontal narrow annular band (Figure 4.32.3). The axial component of the Green-Lagrange strain measured during loading (Figure 4.32.2, profiles *a* and *b*) were $E_{xx}(1) = 0.0054$ and $E_{xx}(2) = 0.0654$ respectively inside the less (1) and highly (2) deformed areas. Same observations were made during unloading with the following values: $E_{xx}(2) = 0.0531$, $E_{xx}(1) = 0.0016$ (Figure 4.32.2, profiles *c* and *d*).

Comparison of the temperature variation and the strain profiles (Figure 4.32.2 and 4.32.4)

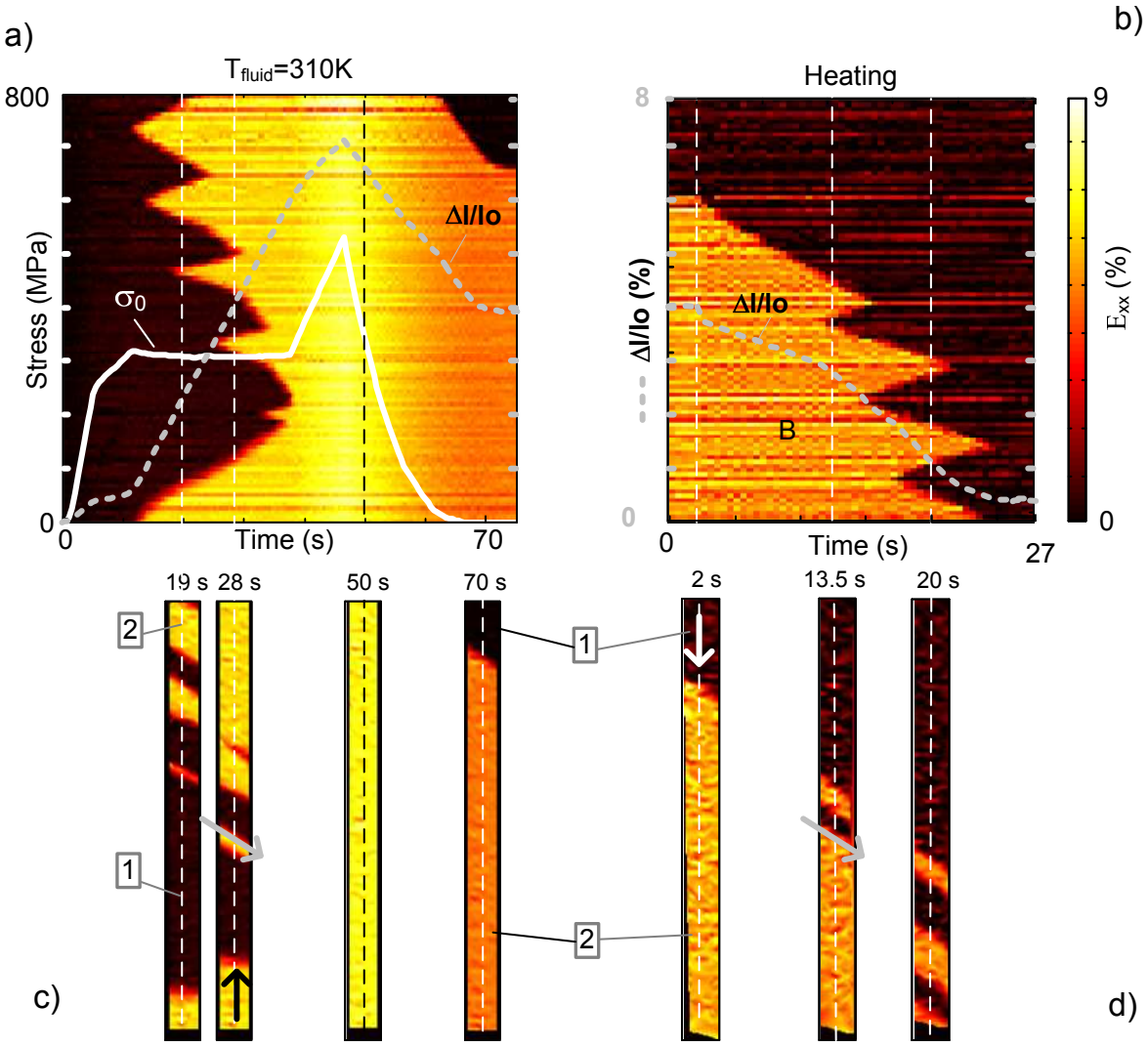

Figure 4.31: *Tensile test $T3_{1A}$ achieved at constant temperature T_{fluid} = 310 K (a and c) and consecutive shape memory effect $T3_{1B}$ recorded at zero force (b and d). a) Coloured map: temporal evolution of axial profile of Green-Lagrange strain E_{xx} along the longitudinal axis of the tube during the first tensile test $T3_{1A}$ at constant temperature T_{fluid} = 310 K. Nominal stress (white solid curve), strain (grey dotted curve) evolution. b) Time evolution of the strain field along the longitudinal axis of the tube during the heating showing the shape memory effect. During heating, the tube is not attached to the bottom grip. The temporal evolution of the strain is super-imposed (grey dotted curve). c) Green-Lagrange strain E_{xx} on the tube surface after respectively 19 s, 28 s, 50 s, and 70s during the tensile test a). d) Green-Lagrange strain E_{xx} on the tube surface after respectively 2 s, 13.5 s, and 20 s during heating. The arrows in c) and d) represent the direction of propagation of strain localization. The position of the selected times are plotted with vertical dashed line in a) and b).*

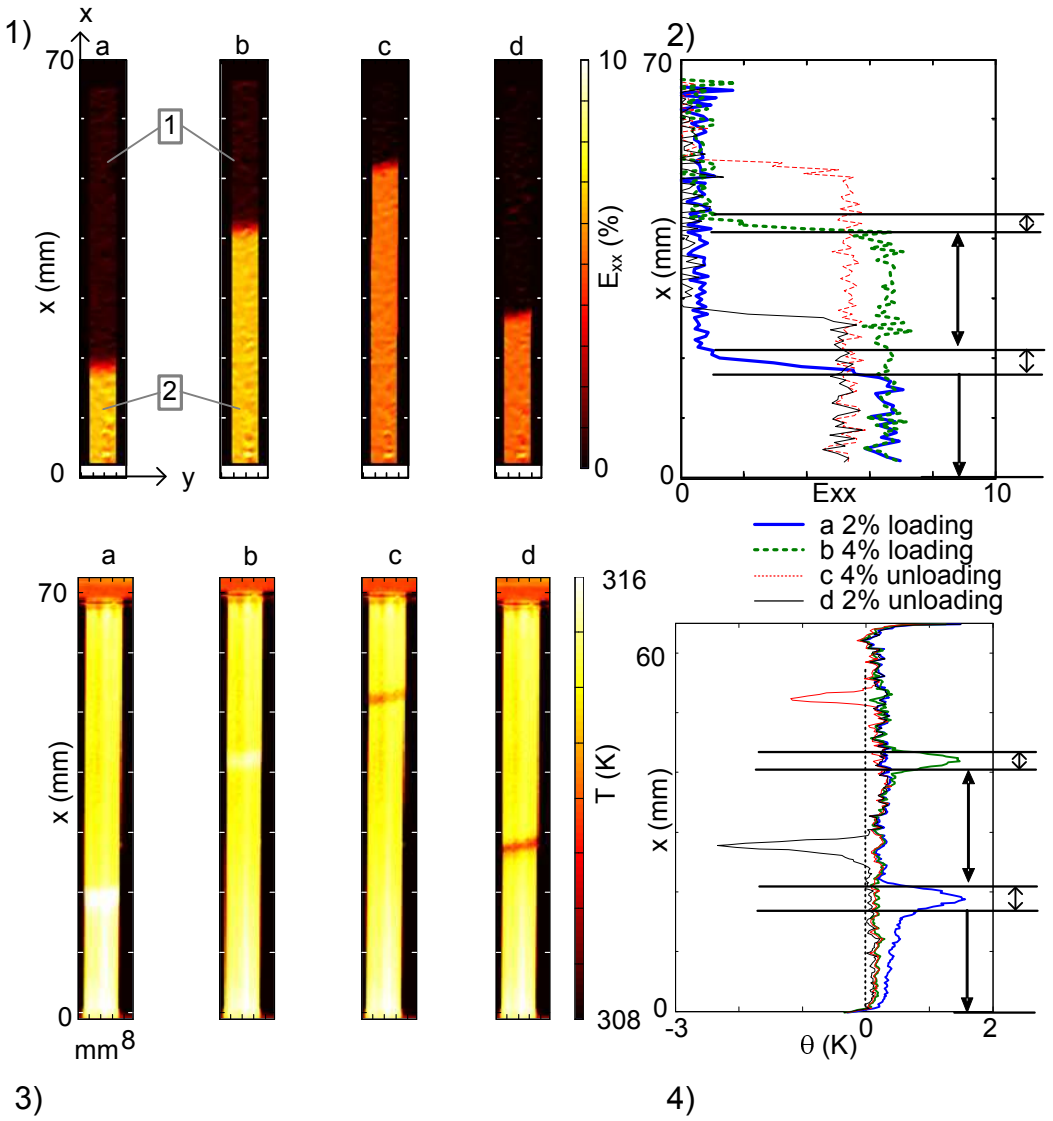

Figure 4.32: *Tensile test $T3_2$ ($\dot{U}/L_0 = 2.10^{-3}s^{-1}$, $T_{fluid} = 315$ K). Colored maps (1) and profiles (2) of the axial Green-Lagrange strain E_{xx} and the temperature at times a, b, c, d, (respectively $\varepsilon = 2\%$, 4% during loading and then 4% and 2% during unloading (see Figure 4.30)). 3) Temperature fields T on the outer surface at the same time. 4) Temperature variations profile θ along the same profile as E_{xx}.*

shows that during loading, at both $\varepsilon = 2\%$ and $\varepsilon = 4\%$, the strain localization fronts were in the same zone as the temperature peak.

Figure 4.33 shows the temporal evolution of the axial profile $E_{xx}(M,t)$ (Figure 4.33.1) and the temperature variation axial profile $\theta(M,t)$ (Figure 4.33.2). The intensity of both E_{xx} and θ are given by the colorbar on the right of the figure. The temporal evolution of the axial strain ε and the nominal stress σ_0 are superimposed in Figures 4.33.1 and 2.

These figures clearly show the strain and temperature localizations associated with the direct and reverse martensite phase transformations. At any time, the sharp strain jump and the temperature peak occurred at the same location. Figure 4.33.1 shows that as long as the localization front was within the gauge length (between A and B), the global elongation velocity $d(\Delta l)/dt$ was constant and respectively equal during loading and unloading:

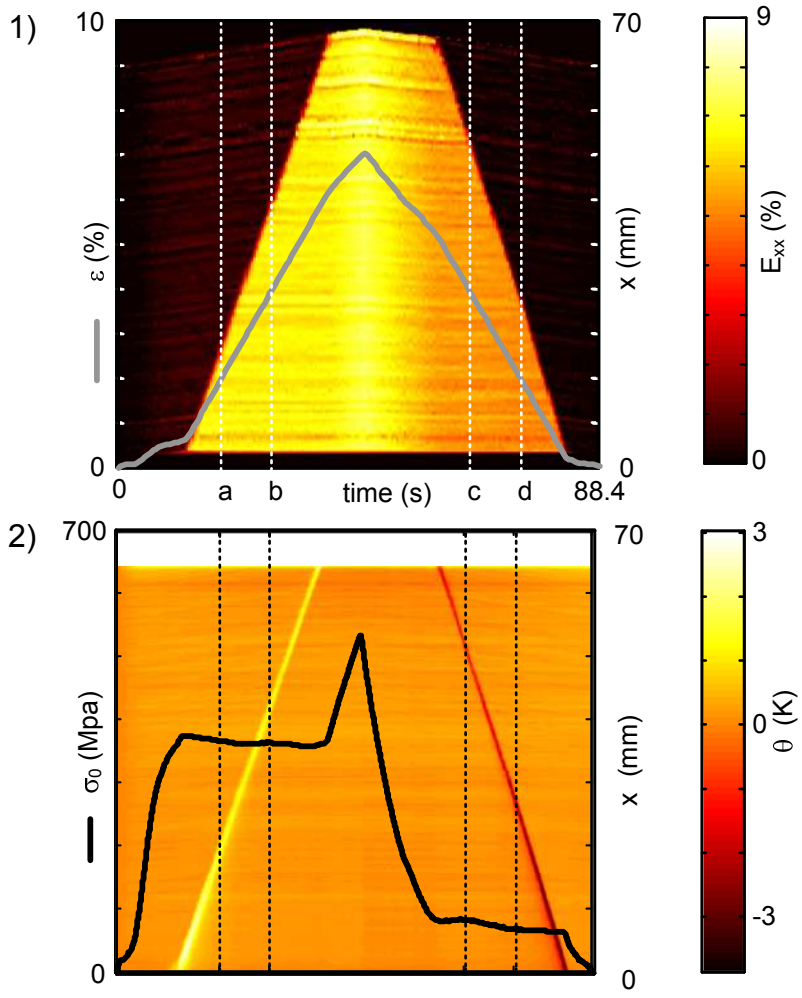

Figure 4.33: *Tensile test $T3_2$. 1) Temporal evolution of an axial profile of the Green-Lagrange strain $E_{xx}(M,t)$ (colored map) superimposed with the sample deformation ε (curve). 2) Temporal evolution representation of the axial temperature variation $\theta(M,t)$ (colored map) superimposed with the nominal stress curve.*

$d(\Delta l)/dt_{loading} = 0.13$ mm s$^{-1} = d(\Delta l)/dt_{unloading}$.

Besides, the front velocity c can be estimated using the slope of the strain jumps shown in Figures 4.33.1 or 4.33.2. For the tensile test $T3_2$, these velocities calculated from the spatial configuration, were $(c_{front}(loading))_{T3_2} = 2.41$ mm s^{-1} and $(c_{front}(unloading))_{T3_2} = 2.68$ mm s^{-1} respectively on loading and unloading, showing that the front velocity was faster during unloading.

Tests $T3_3$ (320 K), $T3_4$ (325 K) and $T3_5$ (325 K) In Figure 4.34, the same spatio-temporal evolutions were chosen for tests $T3_3$ and $T3_4$ to represent the Green-Lagrange axial strain and the temperature variation fields. Notice that test $T3_5$, which was performed at the same fluid temperature as $T3_4$ ($T_{fluid} = 325$ K) exhibited the same temperature, the same local strain profiles, and the same macroscopic strain ε. Only the nominal stress σ_0 was slightly different and therefore represented with white dotted line in Figure 4.34.d.

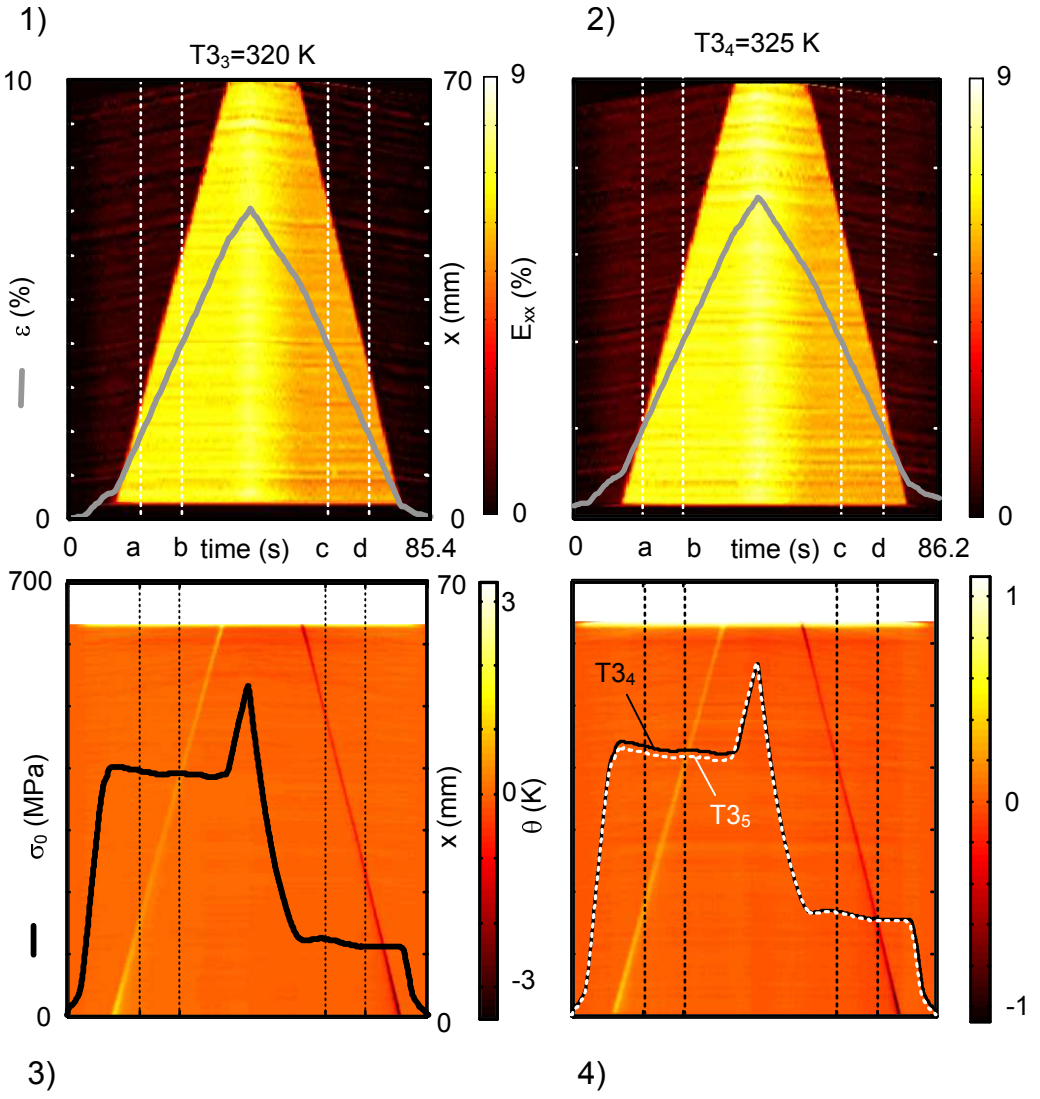

Figure 4.34: *Time evolution representation for the tensile tests $T3_3 = 320$ K and $T3_5 = 325$ K (same as those given in the Figure 4.33 in case of test $T3_2$).*

The three tests $T3_3$, $T3_4$ and $T3_5$ had the same localization morphology as $T3_2$. During both

loading and unloading, one front of strain localization and one annular temperature variation band were observed. The band and the front were almost perpendicular to the axis of the tube, and started from the lower grip during loading and the upper grip during unloading.

The results obtained for tests $T3_2$ to $T3_5$ during loading and unloading respectively are summarised in Tables 4.4 and 4.5, which show:

- the axial component of the Green-Lagrange strain tensor on each side of the localization front (i.e. $E_{xx}(1)$ in the less deformed and $E_{xx}(2)$ highly deformed areas);
- the propagation velocity of the front (c_{front}) estimated from the slopes appearing in the spatio-temporal representation of the strain and thermal fields;
- the gauge length elongation velocity $d(\Delta l_{AB})/dt$ of AB. The quantity $d(\Delta l_{AB})/dt$ was constant as long as the localization front was between A and B.

Loading				
	$E_{xx}(1)$ (%)	$E_{xx}(2)$ (%)	c_{front} $(mm.s^{-1})$	$d(\Delta l_{AB})/dt$ $(mm.s^{-1})$
$T3_2$	0.55 %	6.56 %	2.41	0.130
$T3_3$	0.63 %	6.72 %	2.46	0.130
$T3_4$	0.72 %	6.85 %	2.55	0.132
$T3_5$	0.72 %	6.85 %	2.55	0.132
mean			**2.49**	**0.131**

Table 4.4: *Tests $T3_2$ to $T3_5$, parameters during loading: the Green-Lagrange axial strain in area 1 and 2 respectively before and after the strain localization front, the propagation velocity of the front (c_{front}) and gauge length elongation velocity $d(\Delta l_{AB})/dt$.*

Unloading				
	$E_{xx}(1)$ (%)	$E_{xx}(2)$ (%)	c_{front} $(mm.s^{-1})$	$d(\Delta l_{AB})/dt$ $(mm.s^{-1})$
$T3_2$	5.34 %	0.16 %	2.68	0.130
$T3_3$	5.54 %	0.29 %	2.74	0.130
$T3_4$	5.75 %	0.56 %	2.89	0.129
$T3_5$	5.75 %	0.56 %	2.89	0.129
mean			**2.80**	**0.129**

Table 4.5: *Tests $T3_2$ to $T3_5$, parameters during unloading: the Green-Lagrange axial strain in area 1 and 2 respectively before and after the strain localization front and the front velocity propagation, the propagation velocity of the front (c_{front}) and gauge length elongation velocity $d(\Delta l_{AB})/dt$.*

The progressive increase of $E_{xx}(1)$ during loading and decrease during unloading is explained by the accumulation of residual local deformation with the number of cycles (see Figures 4.30 and 4.27.b). But so far there is no element to tell whether this residual strain was linked to usual plasticity or phase transformation. For all the tensile tests $T3_2$ to $T3_5$, the localization front had a velocity higher level during unloading than during loading.

Test $T3_6$ (320 K) and $T3_7$ (315 K)

Strain and temperature fields of tests $T3_6$ and $T3_7$ exhibited nearly the same morphology of localizations. For example, full field results for test $T3_7$ using the same maps and profiles as those used in Figure 4.32 for Test $T3_2$ (315 K) are plotted in Figure 4.35.

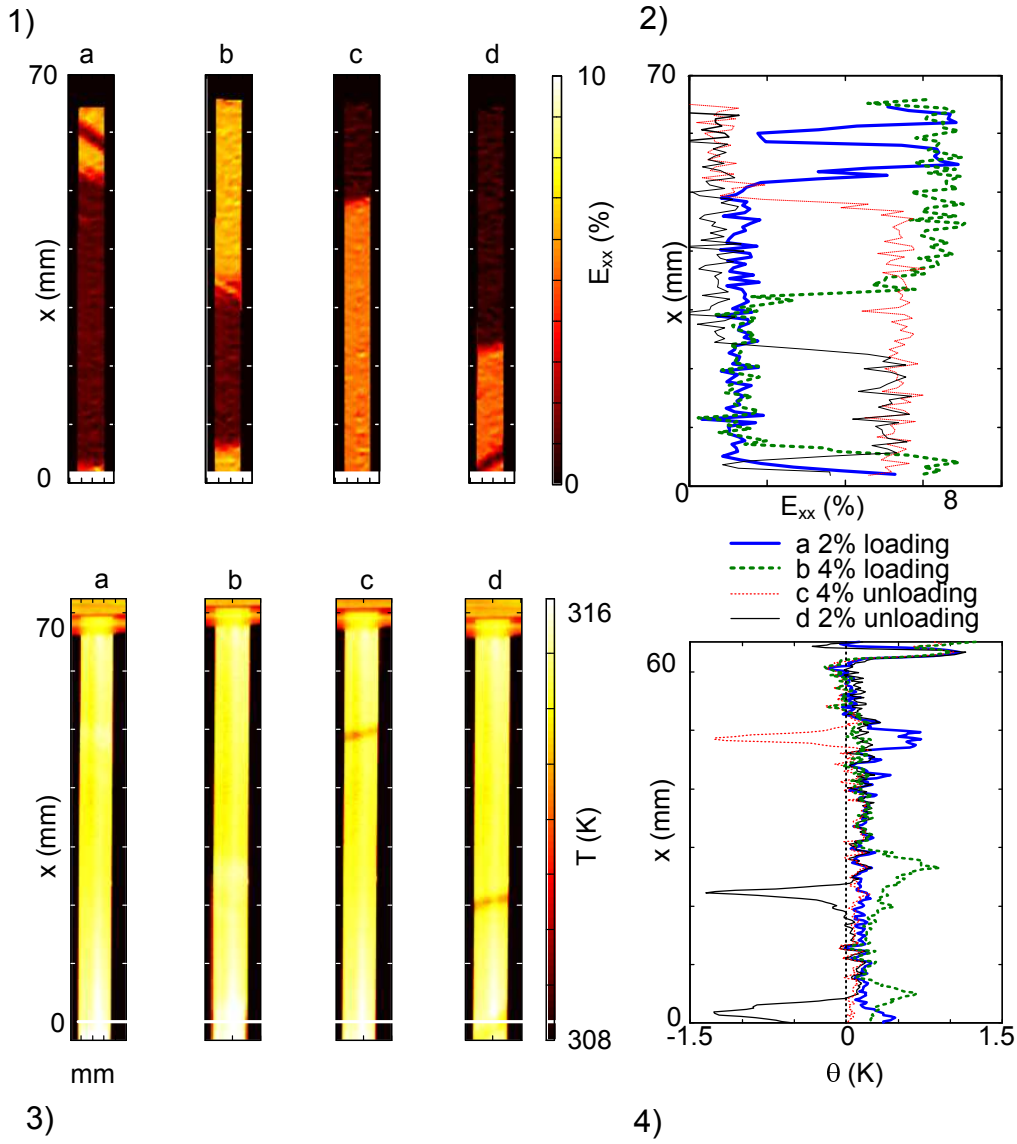

Figure 4.35: *Tensile test $T3_7$ ($2.10^{-3}s^{-1}$, T_{fluid} = 315 K). Colored maps and profiles of the local axial Green-Lagrange strain E_{xx} and the temperature at times a, b, c, d, (respectively ε = 2%, 4% during loading and then 4% and 2% during unloading (see Figure 4.30)). (1) Green-Lagrange axial strain fields E_{xx}, (2) Axial strain profiles, (3) temperature axial fields T on the outer surface and (4) temperature variations θ.*

As for test $T3_{1A}$, the localization initially took the shape of a helical band that was slightly inclined about the axis of the tube. Its initiation was in the upper grip (Figure 4.35.1.a). Then, a second localization was created on the upper grip and took the shape of an annular front, moving toward the lower grip as the first helical band turned around the tube. The annular band caught up by the helical band just after ε = 4% (Figure 4.35.1.b). Finally, a second front perpendicular to the tube axis started from the lower grip and propagated toward the upper grip (Figure 4.35.1.b).

The strain fields on the tube surface, every $5s$ during loading, are plotted in Figure 4.36 to emphasise the helical and front bands propagation during test $T3_7$. Their propagation along the tube axis had almost the same vertical velocity, 2.3 mms^{-1}.

Upon unloading, the behaviour was first similar to test $T3_2$, with a localization front going from the upper to the lower grip of the sample (see strain in Figure 4.35.1.c or temperature in Figure 4.35.3.c). At the end of unloading, the localization morphology changes and a helical band started from the lower grip (Figure 4.35.1.d or 4.35.3.d). Temporal evolution of the axial profiles of the Green-Lagrange axial strain $E_{xx}(M,t)$ and $T(M,t)$ for both tensile tests $T3_6$ and $T3_7$ are presented in Figure 4.37 in the same way as Figure 4.33 for test $T3_2$ and as Figure 4.34 for test $T3_3$ and $T3_4$. Those temporal evolutions confirm that the two tests were very similar, namely, each test exhibited both a helical band propagating and an annular front at the beginning of the stress plateau. The helical band in test $T3_6$ only started earlier.

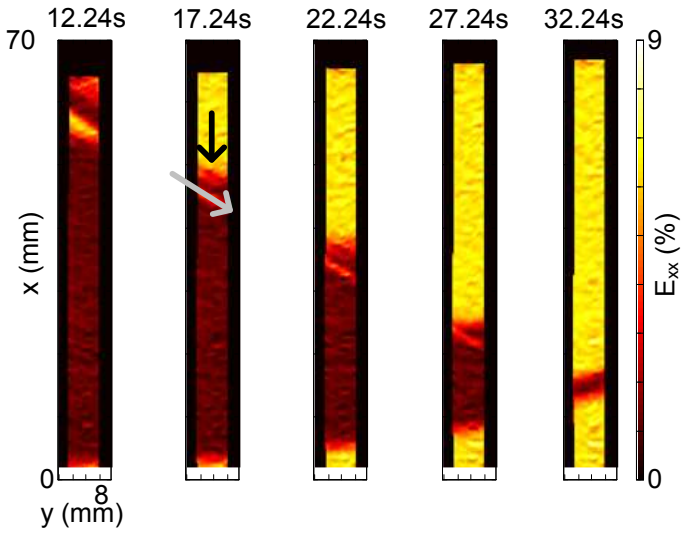

Figure 4.36: *Test $T3_7$ (315 K). Green-Lagrange axial strain field E_{xx} during stress plateau during loading, emphasising the helical band propagation that was then caught up by the front. The arrows show the direction of the propagation of both helical band and fronts.*

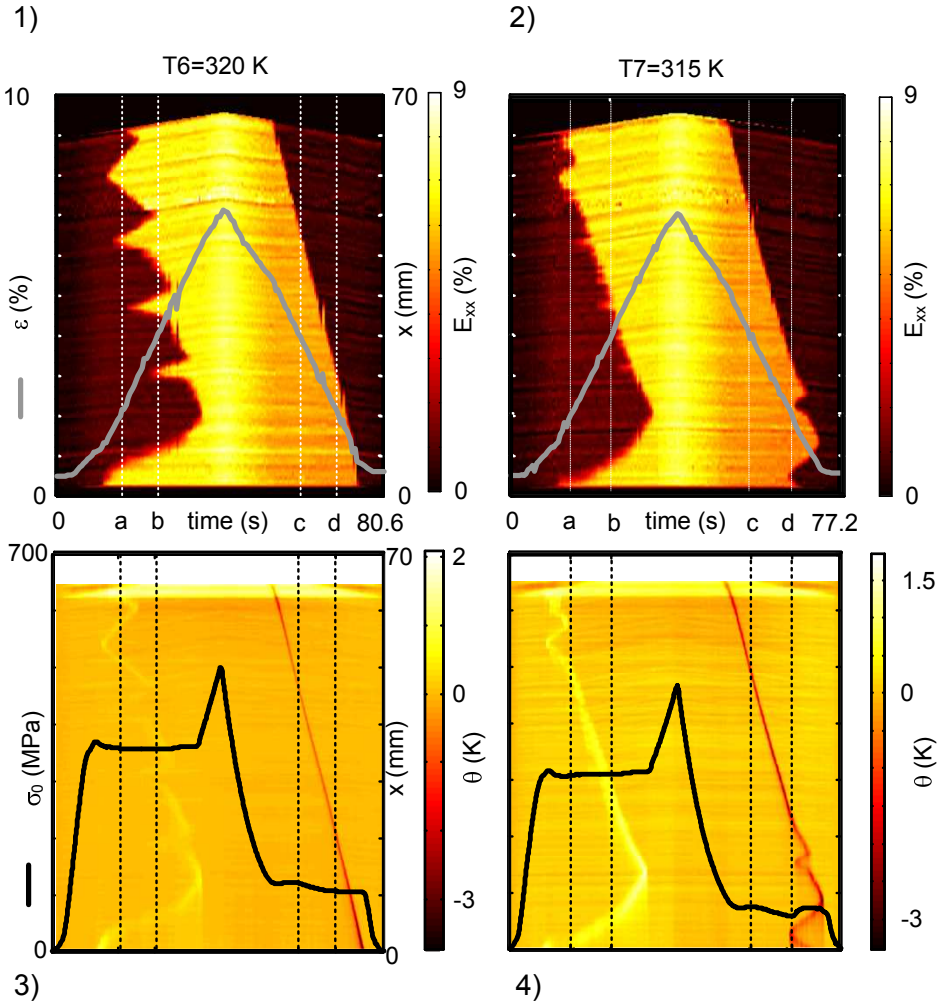

Figure 4.37: *Time evolution representations of strain and temperature variation fields during the tensile test $T3_6$ (320 K) and $T3_7$ (315 K).*

4.4.3.3 Sample 2: shape memory effect on tensile test $T3_{1B}$

After the first mechanical test at constant fluid temperature $T_{fluid} = 310K$ presented in Figures 4.31.a and c. The sample was heated up in order to recover its original length by shape memory effect.

Like in Figures 4.31.a and c, Figures 4.31.b and d show the results of the shape memory effect during heating. In b, the colored map shows the temporal evolution of an axial profile of E_{xx} and the grey dotted curve shows the global axial strain. The nominal stress was zero during all the heating and is not represented. The Green-Lagrange strain is plotted at three characteristic times in Figure 4.31.d, namely, the beginning of the transformation (2 s), and when a helical band was formed (13s and 20s). The same vertical and colorbar scale are used in both Figures 4.31.a for comparison purpose. The remaining global axial strain was $\varepsilon = 0.5\%$ at the end of the heating. This reverse transformation was also strongly localised, it started at the same position and with the same morphology as the end of unloading. However, after 13 s (Figure 4.31.c, time=13.5 s) an helical band was created and moved downward and faster than the annular front.

4.4.4 Discussion

4.4.4.1 Influence of cycling

The cycling effect on NiTi behaviour has already been studied in NiTi by Liu et al. (2006) on wires, Siddons and Moon (2001) on tubes, and Iadicola and Shaw (2002b) on thin wires using temperature field measurements. The test parameters of those studies are summarised in Table 4.6.

publication	composition	geometry	strain rate (s^{-1})	temperature (K)	other
Siddons	nearly equi atomic	tube	10^{-3}	310	$A_f = 264.5$ K
Liu	50.8 at.% Ni	wire	-	313	in water bath
Iadicola sample 1 sample 2	nearly equi atomic	wire	10^{-3}	 289.5 297.5	$A_f = 285$ K temperature controlled
$T3$	50.8 at.% Ni	tube	$2\ 10^{-3}$	315	water circulation

Table 4.6: *Parameters of the bibliographic review.*

The stress decrease ($\Delta\sigma_{tr}$) measured by these different authors during the first ten cycles are superimposed with the stress plateau decrease ($\Delta\sigma_{tr}^{T3}$) measured for our sample (represented with black "+" markers) in Figure 4.38. The comparison of the different stress plateau decreases, shows that the cycling effect is important but varies from one sample to another. The evolution of sample T3 performed at $T_{fliud} = 315$ K was close to Iadicola wire samples.

The stress plateau decrease ($\Delta\sigma_{tr}$) during cycling is dependent on many factors (Iadicola and Shaw, 2002b), namely, the sample composition, heat treatment, grain size, testing temperature and localization morphology. The two samples of Iadicola and Shaw (2002b), deformed

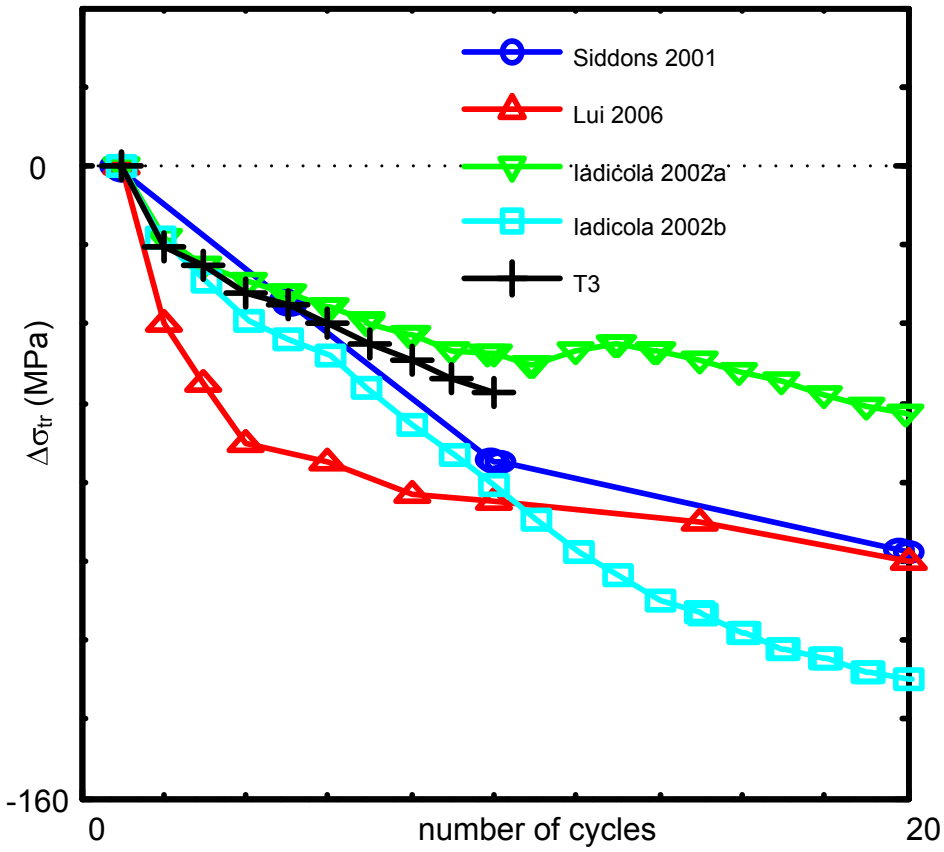

Figure 4.38: *Influence of cycling on the stress decrease of the stress plateau $\Delta\sigma_{plateau}$ during superelastic tensile test of nearly equiatomic NiTi. In black: our sample, in blue: Siddons at 310 K (Siddons and Moon, 2001), red: Liu at 313K (Liu et al., 2006), green and ceylan: Iadicola at 289.5 and 297.5 K (Iadicola and Shaw, 2002b)*

at 289.5 and 297.5 K show that the impact of cycling remained small during the first cycles.

Few studies have analysed the impact of cycling on the NiTi localization morphology. Iadicola and Shaw (2002b) have shown on wires using infrared measurements that the morphology can change during cycling. Similarly, the localization of our sample changed during cycling (see Figure 4.28), especially in the first four cycles of loading. Conversely, localization morphology was more stable during unloading (tests $T3_2$ to $T3_7$, Figure 4.29). It is worth noting that at the end of unloading, ε_r corresponded to localised deformation of the specimen.

4.4.4.2 Localization morphology

Compared to other tensile tests presented earlier without any temperature control (temperature variation up to 10 to 30 K), the temperature peaks observed in the localization area (Figure 4.32.4) had a low amplitude ($1K$ to $3K$) and were very narrow. Same observations have been made by Shaw and Kyriakides (1995) on wires, in water bath using thermocouples. Localization phenomena are emphasised using this set-up. In our tests, several localization morphologies were observed, their shapes and positions seemed unpredictable.

Localization morphology for tests $T3_2$, $T3_3$ and $T3_4$

These three tests exhibited the same localization morphologies. Only one annular band, perpendicular to the tube axis, propagated at a constant velocity, from the lower to the upper grip during loading and from the upper to the lower grip during unloading. The propagation velocity was always faster during unloading. Hahn (1962) on Lüders bands, thenShaw and Kyriakides (1995) on NiTi have shown that it is possible to use the following relationship for tensile test on wires, in the case of a unique propagating front:

$$C_{front}\Delta\epsilon_{xx} = \frac{d\Delta l_{AB}}{dt}, \tag{4.16}$$

where C_{front} is the propagation front velocity observed on the initial configuration of the sample ("Lagrange" velocity) and $\Delta\epsilon_{xx}$ is the strain step associated with the localization front using the small strain formalism. In our experiments, $\Delta\epsilon_{xx}$ was estimated using the local Green-Lagrange E_{xx} axial strain given by DIC:

$$\begin{aligned} \Delta\epsilon_{xx} &= \epsilon_{xx}(2) - \epsilon_{xx}(1) && (4.17)\\ &= \left(\sqrt{1+2E_{xx}(2)}-1\right) - \left(\sqrt{1+2E_{xx}(1)}-1\right) && (4.18) \end{aligned}$$

where $\epsilon_{xx}(1)$ and $\epsilon_{xx}(2)$ are the local axial strains outside and inside the transformation area as marked in Figure 4.32. The "Lagrange" propagation velocity C_{front} was estimated by plotting the temporal evolution of E_{xx} as a function of the initial position of points on the surface of the tube and not the spatial one as done in Figures 4.33 and 4.34. Finally, the strain increment rate $d(\Delta l_{AB})/dt$ was given by the numerical derivation of the displacement difference in the extreme points A and B of the gauge length.

Tables 4.7 and 4.8 illustrate the results respectively during loading and unloading for the tensile tests $T3_2$ to $T3_5$. Eq. (4.16) established for a wire was checked for our tube both

during loading and unloading as shown in the two last columns of Tables 4.7 and 4.8. This can be explained by the simple localization morphology observed for these tests.

	measured					
	$\epsilon_{xx}(1)$ (%)	$\epsilon_{xx}(2)$ (%)	$\Delta\epsilon_{xx}$ (%)	C_{front} (mm.s^{-1})	$C\Delta\epsilon_{xx}$ (mm.s^{-1})	$d(\Delta l_{AB})/dt$ (mm.s^{-1})
$T3_2$	0.55 %	6.36 %	5.81 %	2.28	0.132	0.130
$T3_3$	0.63 %	6.51 %	5.88 %	2.31	0.136	0.130
$T3_4$	0.72 %	6.63 %	5.91 %	2.40	0.139	0.132
$T3_5$	0.89 %	6.63 %	5.91 %	2.40	0.139	0.132
mean			5.87 %	2.35	**0.134**	**0.131**

Table 4.7: *Summary of the local axial strains in area 1 and 2 respectively before and after the strain front, the strain step ($\Delta\epsilon_{xx} = \epsilon_{xx}(2) - \epsilon_{xx}(1)$), the propagation velocity of the front (C_{front}) observed in the initial configuration and gauge length elongation velocity $d(\Delta l_{AB})/dt$ during loading for the tensile tests $T3_2$ to $T3_5$.*

	measured					
	$\epsilon_{xx}(1)$ (%)	$\epsilon_{xx}(2)$ (%)	$\Delta\epsilon_{xx}$ (%)	C_{front} (mm.s^{-1})	$C\Delta\epsilon_{xx}$ (mm.s^{-1})	$d(\Delta l_{AB})/dt$ (mm.s^{-1})
$T3_2$	0.16 %	5.20 %	5.04 %	2.53	0.127	0.130
$T3_3$	0.29 %	5.39 %	5.10 %	2.59	0.132	0.130
$T3_4$	0.56 %	5.59 %	5.04 %	2.68	0.135	0.129
$T3_5$	0.56 %	5.59 %	5.04 %	2.68	0.135	0.129
mean			5.06 %	2.6	**0.132**	**0.129**

Table 4.8: *Summary of the local axial strains in area 1 and 2 respectively before and after the strain front, the strain step ($\Delta\epsilon_{xx} = \epsilon_{xx}(2) - \epsilon_{xx}(1)$), the propagation velocity of the front (C_{front}) observed in the initial configuration and gauge length elongation velocity $d(l_{AB})/dt$, during unloading for the tensile tests $T3_2$ to $T3_5$.*

Localization morphology for the tests $T3_1$(loading), $T3_6$ and $T3_7$

Although tests $T3_7$ and $T3_2$ and tests $T3_6$ and $T3_3$ were performed on the same sample at the same temperature respectively 315 K and 310 K, the localization morphology during loading of $T3_7$ (Figures 4.35.2 and 4.35.6) and $T3_6$ (Figure 4.37.1 and 4.37.3) were very different from $T3_2$ (Figure 4.32) and $T3_3$ (Figure 4.34.3). However, both $T3_6$ and $T3_7$ were similar, in loading, to the first test $T3_{1A}$ (Figure 4.31). The behaviour during unloading, at least at the beginning, was very similar for all tests.

Localization morphologies, such as fronts and helical bands during tensile tests on tubes, have already been observed by Ng and Sun (2006) and in Section 4.2. Usually, the localization morphologies during loading and unloading are the same (see tests $T3_2$ to $T3_5$ for instance). Tests $T3_1$, $T3_6$ and $T3_7$ were unusual. First their morphologies were rather complex during loading, with both helical bands and annular front. Second, they were not symmetric during unloading. Localization in this case was simpler, taking the shape of a single annular front. Finally, unlike tests $T3_2$ to $T3_5$, the initiation of the localization was always on the bottom grip.

To conclude, there is nothing that allows us to estimate what type of localization morphology

will be involved during a tensile test. The parameters that could have an influence are as follows:

- Material defects already existing inside the sample before testing.
- The shape of the sample. Unlike the tests done by Ng and Sun (2006), our sample did not had a dog-bone shape. Therefore, localizations always started from the grips (stress concentrations due to the gripping system).
- The gripping system. As presented in Section 3.2.2.2, bending was avoided by our gripping system, but no rotation was possible around the tube axis. As noted by Sun and Li (2002), avoiding any rotation may not be favourable to helical bands morphology. Further studies need to be done to analyse more precisely the influence of the boundary conditions on the morphologies.
- The thermal and loading history of the material. Tests $T3_2$ and $T3_7$ have undergone several thermo-mechanical loadings that could have affect their behaviour.
- The loading conditions (test velocity, room conditions and heat exchanges).
- The cycling effect.

4.4.4.3 Influence of temperature on transformation stress

Clausius-Clapeyron approach

As presented in Chapter 1, the transformation stress under tensile loading (labelled in this chapter σ_{tr}^{AM}) is a function of the temperature T in eq. (1.17):

$$\frac{d\sigma_{tr}^{AM}}{dT} = -\rho\frac{\Delta S_c}{\Delta\varepsilon_{tr}^{AM}}. \tag{4.19}$$

If all the above parameters remain constant during a phase transformation, under a given loading state, the transformation stress is a linear function of the transformation temperature.

Many studies (Miyazaki et al., 1981; Stalmans et al., 1992; Zhang et al., 2004; Liu et al., 2006) have shown that the above relationship is well suited to predict transformation stress (σ_{tr}^{AM}) evolution as a function of the temperature T in fully austenitic SMAs that exhibit AM transformation, provided:

- the effect of cycling on the stress plateau level is weak by either taking new samples for every temperature (Miyazaki et al., 1981; Liu et al., 2006; Zhang et al., 2004) or stabilising the behaviour by performing many cycles prior to the test itself (Liu et al., 2006);
- thermomechanical couplings are low: since the martensitic phase transformation is exothermic, a temperature elevation is observed in the area of phase transformation. Therefore tests are performed under quasi-static conditions either in a water bath or at low strain rate (see Table 4.6);

Those studies have shown that, depending of the shape of the specimens, both level of the stress plateau and value of the slope $d\sigma_{tr}^{AM}/dT$ vary between 5 and 8 MPa/K. $d\sigma_{tr}^{AM}/dT \approx 5$ MPa/K is usually for R→M transformation and $d\sigma_{tr}^{AM}/dT \approx 8$ MPa/K is for A→M transformation. However, as presented in chapter 1:

- the Clausius-Clapeyron relationship is only true locally where the transformation takes place;
- eq. (1.15) and (1.16) show that the Clausius-Clapeyron relationship is highly dependent on the nature of the stress field (for example compression, shear, tension... (Orgéas and Favier, 1998)). Orgeas and Favier have shown that for Ni-Ti alloys, the transformation deformation $\Delta\varepsilon_{tr}^{AM}$ was lower in compression than in tension, which leads to a stress-temperature slope $\mathrm{d}\sigma_{tr}^{AM}/\mathrm{d}T$ higher in compression than tension (Orgéas and Favier, 1998);
- the heat component E'_{iq} of the irreversible energy (see eq. 1.5) changes with the temperature (Ortin and Planes, 1988, 1991).

We have tried to check with the quasi-isothermal tests given previously if the Clausius-Clapeyron relationship was valid for our tubes. For that purpose, the nominal stress plateau in tension σ_{tr} vs. temperature T_{fluid}, are plotted for tests $T3_1$ to $T3_7$ in Figure 4.39.1 during loading and in Figure 4.39.2 during unloading. During loading, the stress was measured at 2 % nominal strain. During unloading, the stress was collected at 4 %.

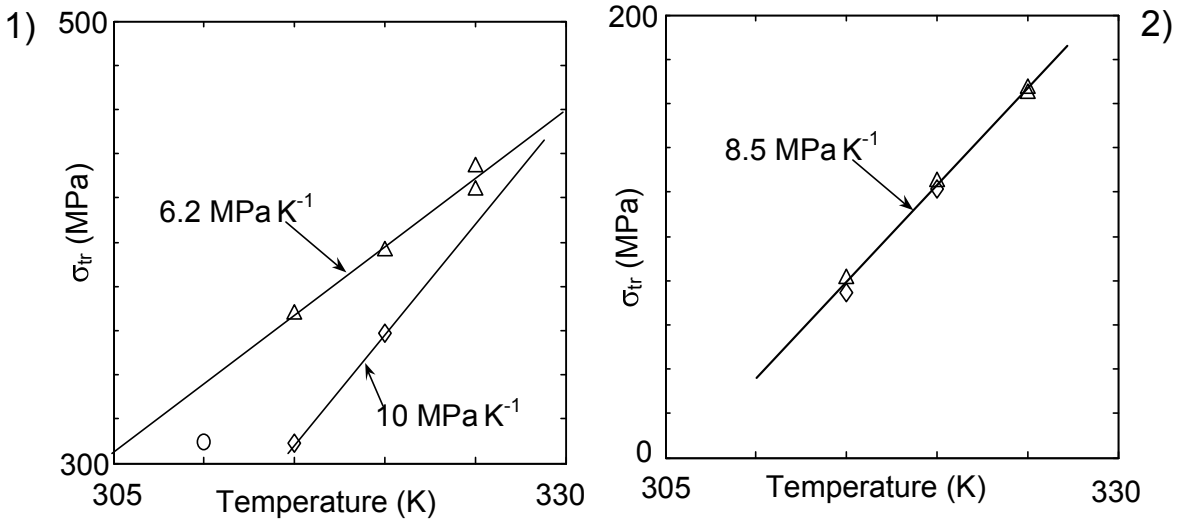

Figure 4.39: *Nominal tensile stress σ_{tr} as a function of the applied temperature T_{fluid} during loading (1) and unloading (2) for a nominal deformation of 2% and 4%, respectively. The markers are: circle for $T3_1$, triangles for $T3_2$ to $T3_5$ and diamonds for $T3_6$ and $T3_7$.*

During loading, the test points of $T3_2$ to $T3_5$ plotted in Figure 4.39.1, aligned themselves along a line of slope 6.2 MPa K^{-1}. A higher slope of 10 MPa K^{-1}, fits the results for $T3_6$ and $T3_7$. The first tensile test $T3_1$ does not align with any other test.

In contrary, all the tests were aligned during unloading with one single line of slope 8.5 MPa K^{-1}. Although tensile tests $T3_2$ and $T3_7$ have been performed at the same temperature

$T_{fluid} = 315$ K, the stress plateau σ_{tr} recorded during loading of tensile test $T3_7$ was 40 MPa less than for $T3_2$.

Conversely, during unloading, both mechanical responses are identical. The same observation can be done for $T3_3$ and $T3_6$, both performed at $T_{fluid} = 320$ K. It is important to notice that during unloading, the localization morphologies were identical and that unloading was not affected by a stress plateau decrease due to cycling (see Figure 4.27.a). Although stress plateau during loading was affected by cycling (see Figure 4.27.a) and we observed some modification of the localization morphologies within the different loadings.

Influence of cycling

As presented in Section 4.4.4.1, cycling induces an important decrease of the stress plateau during the first ten cycles. In our case, all the tests ($T3_1$ to $T3_7$) were performed one after another on the same sample. Stress plateau decrease $\Delta\sigma_{tr}$ due to cycling during loading should therefore be taken into account in the Clausius-Clapeyron approach.

Assuming the influence of cycling is independent of the temperature, it is possible to take into account the stress plateau decrease for sample 2 from the stress decrease obtained during cycling on the first sample (see Figure 4.40). Therefore for each test, the stress plateau σ_{tr}^{cor} is estimated with:

$$\sigma_{tr}^{cor}(n) = \sigma_{tr}(n) - \Delta\sigma_{tr}^{T3}(n) \tag{4.20}$$

The corrected stresses have been reported in Figure 4.40 for each tests. After the correction two slopes still exist, namely, one for tests $T3_2$ to $T3_5$ with 7.5 MPa K^{-1}; the second includes $T3_6$ and $T3_7$ but also $T3_1$ with a slope of 8.8 MPa K^{-1}. Moreover, tests $T3_4$ and $T3_6$ are now almost superimposed.

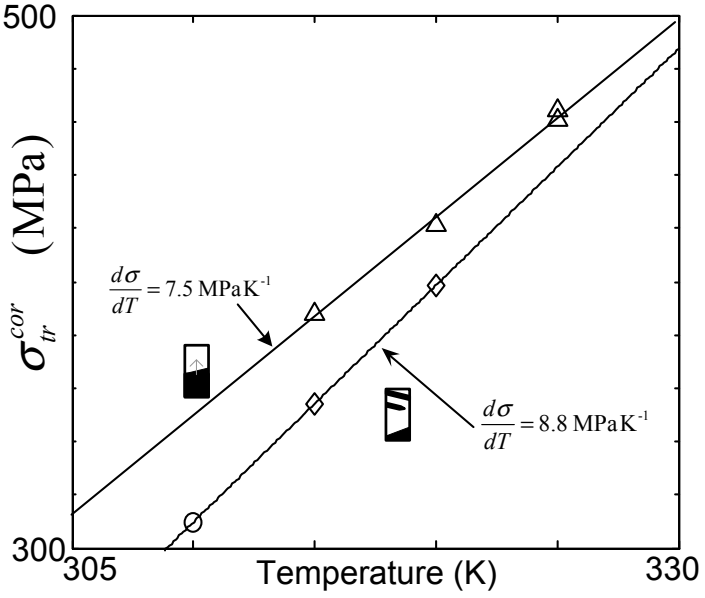

Figure 4.40: *Corrected stress plateau as a function of the applied temperature during loading at $\varepsilon = 2\%$. The markers are: circle for $T3_1$, triangle for $T3_2$ to $T3_5$ and diamond for $T3_6$ and $T3_7$.*

As depicted in Figure 4.40, all tests that follow the same line, have identical localization morphologies. These different morphologies may explain the difference of slopes.

Influence of localization morphology on Clausius-Clapeyron model

During loading, the localization morphologies of tests $T3_2$ to $T3_5$ were very similar (annular band perpendicular to the tube axis). We can therefore assume that the nature of the "local" stresses at the localization front were identical for tests $T3_2$ to $T3_5$. The Clausius-Clapeyron relationship was checked using global nominal tensile stress during loading. On the contrary, $T3_{1A}$, $T3_6$ and $T3_7$, which were not performed in a row but that had similar localization morphologies, aligned on a second slope. For those tests, since the morphology was different from an annular front, the nature of the local stress should be different. This would lead to a different Clausius-Clapeyron slope (8.8 MPa K^{-1} for these three tests after the correction of cycling, instead of 7.5 MPa K^{-1}) for $T3_2$ to $T3_5$. The line fitting tests $T3_2$ to $T3_5$ exhibiting only one annular front propagating vertically is above the line fitting the tests $T3_1$, $T3_6$ and $T3_7$ exhibiting an helical band followed by a vertical annular front. It is more likely that the stress needed to propagate one annular front is higher than helical bands since the tube is more constrained. Such influence of localization morphology on the stress plateau level have already been observed on wires by Iadicola and Shaw (2002b).

So far the localization phenomena that appear or not during the shape memory effect or two way memory effect (TWME) have not been studied. In this first test, strong localization were present during the shape memory effect. These localizations were very different from those observed during loading in $T3_{1A}$ and much more complex than every other superelastic tests ($T3_2$ to $T3_7$). The localization even changed in morphology after 13.5 s, as presented in the colored images of Figure 4.31.d.

From this first test, we conclude that Shape Memory Effect after stress induced martensitic transformation involves localised phenomena such as superelasticity. Further studies are necessary to confirm this first observation.

4.4.5 Conclusion

The conclusions of the present section are summarised as follows:

- The temperature fields increased (or decreased), suddenly, in the same areas as strain localizations.
- Localization morphologies seem unpredictable. They can be very simple, for example, having only one annular front almost perpendicular to the tube axis, or they can also be complex, such as those involving helical bands and annular fronts. At this stage of the study, it is not clear which parameter dominates and determines the type of localization morphology.
- When the morphology was only a single annular front, the global elongation rate of the sample was directly linked to the strain step across the localization front and the front velocity.

- The localization can vary during cycling but tends to stabilise after several cycles.
- The level of the stress plateau (σ_{tr}) depends on the temperature, the loading history (cycling effect) and the type of strain localization morphology which induces different local strain and stress.
- Strong and complex localizations have been observed during shape memory effect. Those localizations had different morphologies than those observed during loading.

This last result underlines the difficulties in understanding and analysing tests involving localization phenomena, especially when they are used to construct constitutive laws.

4.5 Conclusion of Chapter 4

The main results of the analysis presented in this chapter are:

- The homogeneous loading (stage 1) is not influenced by the macroscopic strain rate. Its nature is not a purely elastic, namely, a mixture of A→M, A→R and R→M phase transformation was observed during the homogeneous loading and started as soon as the test started.
- Analysis of the homogeneous unloading on tube T_1 has shown that this stage exhibited reverse transformation, contrary to the common assumption that it exhibit purely elasticity of martensite.
- Stage 2, corresponds to a change in deformation mode and is strongly influenced by the macroscopic strain rate. The deformation and phase transformation change from homogeneous to strongly localised in stage 2. The beginning of the localization corresponded to the stress peak.
- The level of the stress plateau is not only influenced by the Clausius-Clapeyron relationship but is also influenced by thermomechanical coupling, by the loading history and by localization morphology. The localization morphology is unpredictable and induced variations of the local strain and stress.

Still some behaviour remains unexplained and would need further investigations. These include:

- Since these alloys presented R-phase transformation, it was not possible to analyse precisely the proportion of A→M and A→R phase transformation during the homogenous stage. It was only possible to observe the presence of mixture of those two phases during this stage. Alloys presenting only A→M would allow for a better understanding of the behaviour in this stage.
- The localization morphology and the number and position of initiations strongly depend on the temperature and macroscopic strain rate but seem to be unpredictable and are probably due to a strongly heterogeneous stress field inside the sample.

- Due to conduction phenomena, temperature fields were difficult to analyse in the localised stages. Therefore, analysing coupling effects and deformation mechanisms associated with stress-induced transformations in these stages is difficult. Heat source fields estimation from the temperature fields should allow us to better analyse the phase transformation behaviour.

CHAPTER 5

Tensile and shear tests on NiTi plates exhibiting one reversible phase transformation A-M

Table of contents

Since the tubular samples exhibited an R-phase transformation, the nature of the phase transformation could not be estimated. For those tests only the presence of a mixture of A→R, A→M, and R→M could be concluded in Chapter 4.

Localization phenomena were also investigated in Chapter 4 on tubes. It has been demonstrated that localization is influenced by many parameters. The influence of the macroscopic strain rate, cycling, and temperature were analysed during tensile tests on tube geometry in the previous chapter. Another parameter that influences localization is the sample geometry and the type of loading. Li and Sun (2002) have shown using a smooth and transparent layer of rosin brittle coating on NiTi microtubes that the localization morphology of tubular samples are different from plate samples (Shaw and Kyriakides, 1997). Orgéas and Favier state that shear tests were homogeneous since during quasi-isothermal shear tests (performed in temperature controlled bath) the shear stress was increasing continuously and no stress plateau was observed. So far this has not been confirmed and can be carried out by using full field measurements techniques.

In this chapter we will investigate the thermomechanical behaviour of NiTi plates. These plates presented in Section 3.1.3 have the advantage, over tubular samples, to present only A→M phase transformations. The analysis of the thermomechanical behaviour is therefore simpler and the shape of the sample allows one to analyse the influence of the loading type by performing both tensile and shear tests.

The experimental procedures and mechanical results will be presented in Section 5.1. Then, the analysis of the tensile and shear tests will be presented in Sections 5.2 and 5.3. During the tensile tests, the analysis of the homogeneous stage will allow for a better understanding when the martensitic transformation starts and estimate martensite fraction at the end of the homogeneous loading. This first investigation will be developed, in Section 5.2.1, using the same method as the one used on tubes in Sections 4.2 and 4.3. Tensile tests performed at two distinct macroscopic strain rates will be analysed and compared. Then, the observation and analysis of localization phenomena will be presented in Section 5.2.2. During this analysis, 2D heat sources and energy fields were estimated and compared to the strain fields.

Concerning the shear tests presented in Section 5.3, homogeneity of the NiTi shear test will first be investigated on two tests in Section 5.3.1. Then, same investigations as during the homogeneous loading will be presented on the second shear test in Section 5.3.2.

5.1 Experimental procedure

5.1.1 Tensile tests

Three tensile tests have first been performed on one rectangular plate sample P of gauge length $L_0 = 59$ mm. The plate was 7.14 mm wide and 0.5 mm thick. The sample was mounted in a standard self tightening Instron grips. Before being clamped, the plate was heated up to 372 K, 100 K above $T(M-A)_f$, and cooled down slowly to room temperature. The initial microstructure of the sample was thus fully austenitic.

The tests were conducted without temperature control (room temperature 298 K) at constant cross-head velocity $\dot{U}$. The applied strain rates were $\dot{U}/L_0 = 4.9\ 10^{-3}s^{-1}$ for test P_1, $\dot{U}/L_0 = 4.9\ 10^{-4}s^{-1}$ for tests P_2 and P_3. During the tensile tests, the axial force F and cross-head displacement U were recorded. The sample was coated with a high emissivity black paint with a white texture on top of it as shown in Figure 5.1.a. As presented in Section 2.3.2, temperature, displacement and strain fields were simultaneously measured on the plate surface.

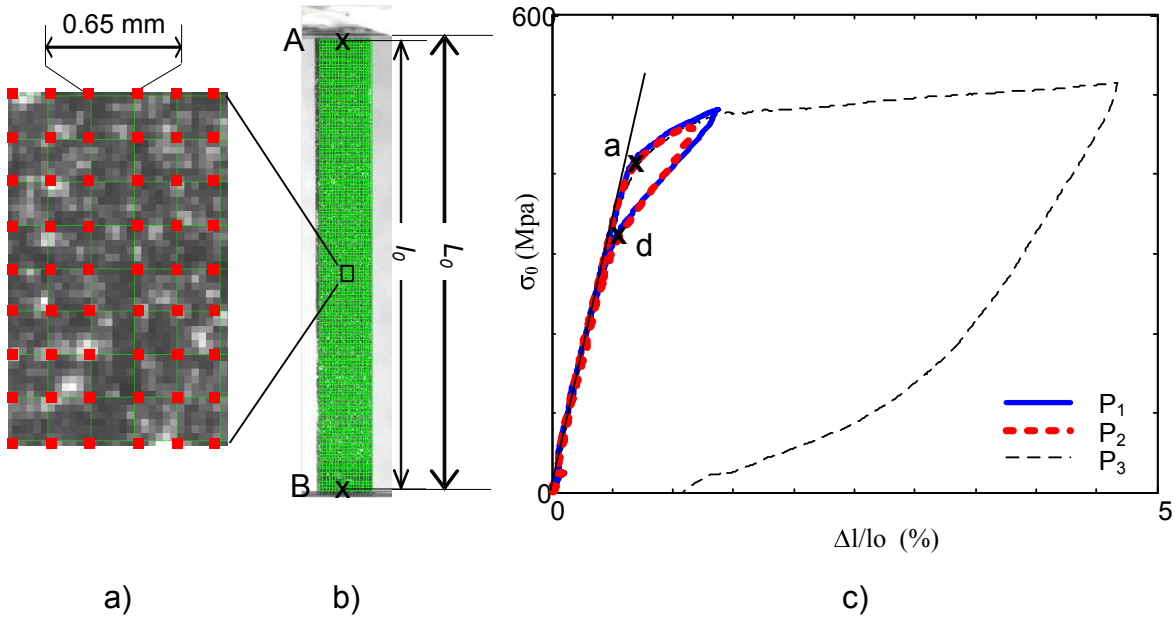

Figure 5.1: *(a-b) Observation area and virtual grid applied to calculate the kinematics fields. c) Stress strain curve of the three tensile tests conducted on the plate. Test P_1 (solid thick blue line) was performed at velocity $\dot{U}/L_0 = 4.9\ 10^{-3}s^{-1}$, test P_2 (thick dashed line) and test P_3 (thin dashed line) at velocity $\dot{U}/L_0 = 4.9\ 10^{-4}s^{-1}$.*

The infrared camera measured the temperature field $T(M,t)$ at an acquisition frequency of $f_{IR} = 5$ Hz. The spatial resolution (pixel size), was estimated to be close to 0.22 mm for the carried out tests. The displacement field $\overrightarrow{u}$ was obtained using a digital visible camera and a DIC processing presented in Section 2.2 at an acquisition frequency of $f_v = 0.5$ Hz. The grid size was 10×10 pixels and the spatial resolution (pixel size) was estimated to be 0.065 mm, the resolution of the local strain calculation (grid size) was then 0.65 mm (Figure 5.1.a). The Green-Lagrange strain fields are estimated from the displacement field $\overrightarrow{u}$. The thermal and kinematical fields were measured in an observation section of length $l_0 = AB = 58\ mm$ shorter than $L_0 = 59$ mm, as illustrated in Figure 5.1.b.

The nominal stress-strain curves ($\sigma - \Delta l/l_0$) of the three tests are plotted in Figure 5.1.c. Tests 1 and 2 were stopped at the beginning of the stress plateau (end of stage 1) and test 3 in the middle of the stress plateau (middle of stage 2, $\Delta l/l_0 = 4.6$ %). The three curves superimposed on top of each other in the homogeneous stage (stage 1).

Test P_3 (black dashed curve Figure 5.1.c) exhibited a typical behaviour of polycrystalline Ni-Ti. Although no overshoot was observed, a stress plateau (almost horizontal) started at $\Delta l/l_0$ of approximately 1.2%. This corresponded to stage 2, conventionally considered to be associated with nucleation and propagation of heterogeneous macroscopic transformation-deformation bands, the increasing slope being due to thermal effects (Shaw and Kyriakides, 1997; Gadaj et al., 2002). The loading finished at $\Delta l/l_0 = 4.6$ %. Only the beginning of the unloading plateau could be observed since at this temperature the material was not fully superelastic. At the end of the test, the permanent strain was $\Delta l/l_0 = 1.8$ %.

5.1.2 Shear tests

Two shear tests have been performed with the shear device presented in Section 3.2.3 using two virgin samples from the same plate.

The first shear test (cis_1) was performed at low strain rate in almost quasi static conditions (cross-head velocity $\dot{U}/L_0 = 2.6\ 10^{-5}\ s^{-1}$) up to 8% of strain. The sample height was $L_0 = 20$ mm. Due to the very low strain rate, no temperature variation was expected. Therefore only one visible camera was used. In order to increase the DIC resolution, the camera was observing only the top half of the sample. The spatial resolution of the visible image was 0.0084 mm. However, during this test the texture size was not perfectly adapted to this high resolution, therefore grid and subset sizes of 20 pixels were chosen, so that the DIC grid spatial resolution was only 0.168 mm (see Figure 5.2.a). The curve $(\overline{\tau}_{xy}, \overline{\gamma}_{xy})$ is plotted with thick solid line in Figure 5.2.c.

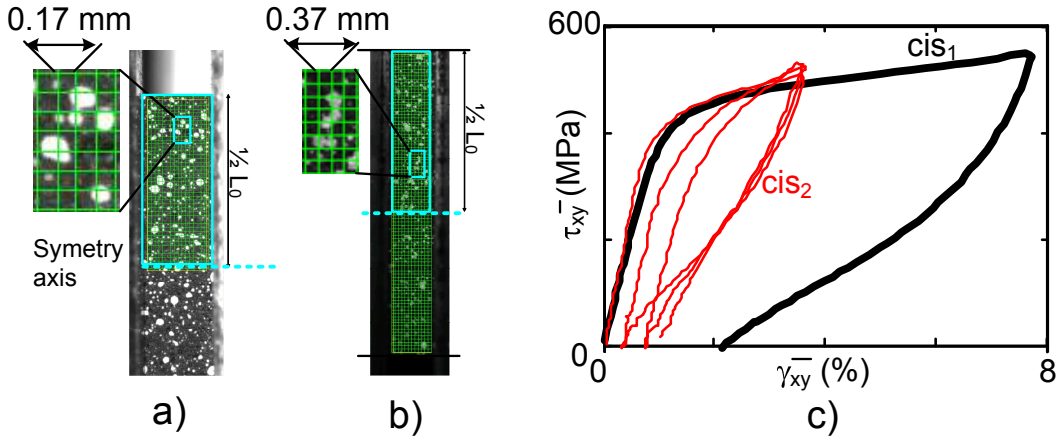

Figure 5.2: *a) Observation area and virtual grid applied to calculate the kinematic fields of test cis_1. b) Observation area and virtual grid applied to calculate the kinematic fields of test cis_2. c) Shear tests mechanical responses. cis_1, cis_2 are plotted respectively with solid thick line, solid thin line.*

Three loops have then been performed on the second shear test cis_2 at a faster strain rate $\dot{U}/L_0 = 10^{-2}\ s^{-1}$ from zero force to $\overline{\gamma}_{xy} = 4\%$, on a 30 mm high plate. Both temperature and strain fields were recorded during the test. The spatial resolution of the temperature

field was 0.12 mm. The spatial resolution of the visible image was 0.037 mm. The grid and subset size were 10 pixels, so that the DIC grid spatial resolution was estimated of the order of 0.37×0.37 mm^2 (see Figure 5.2.b). The curve $(\overline{\tau}_{xy}, \overline{\gamma}_{xy})$ is plotted with thin continuous line in Figure 5.2.c.

5.1.3 Comparison of Von Mises stress-strain curves

As presented by Manach and Favier (1997) it is possible to compare the mechanical response of tensile and shear tests using Von Mises stress (σ_{mises}) and strain (ε_{mises}). Von Mises stress and strain were estimated for the tensile test P_3 using:

$$\varepsilon_{mises} = \varepsilon, \tag{5.1}$$

$$\sigma_{mises} = \sigma_0, \tag{5.2}$$

and for the shear tests using:

$$\varepsilon_{mises} = \frac{\overline{\gamma}_{xy}}{\sqrt{3}}, \tag{5.3}$$

$$\sigma_{mises} = \overline{\tau}_{xy} \times \sqrt{3}. \tag{5.4}$$

The comparison of Von Mises stress-strain curves is presented in Figure 5.3. The level of the stress plateau is slightly higher in tension than in shear ($\sigma_{mises}(P_3) = 480$ MPa, $\sigma_{mises}(cis_1) = 416$ MPa at $\varepsilon_{mises} = 3\%$). Such results have already been observed (Manach and Favier, 1997; Orgéas and Favier, 1998). In fact, as shown by Manach and Favier (1997), the ratio $\sigma_0/\overline{\tau}_{xy}$ depends on the test temperature with respect to $T(M-A)_f$. Finally, the level of the stress plateau might have been influenced by the unknown anisotropy of the sample which we did not test.

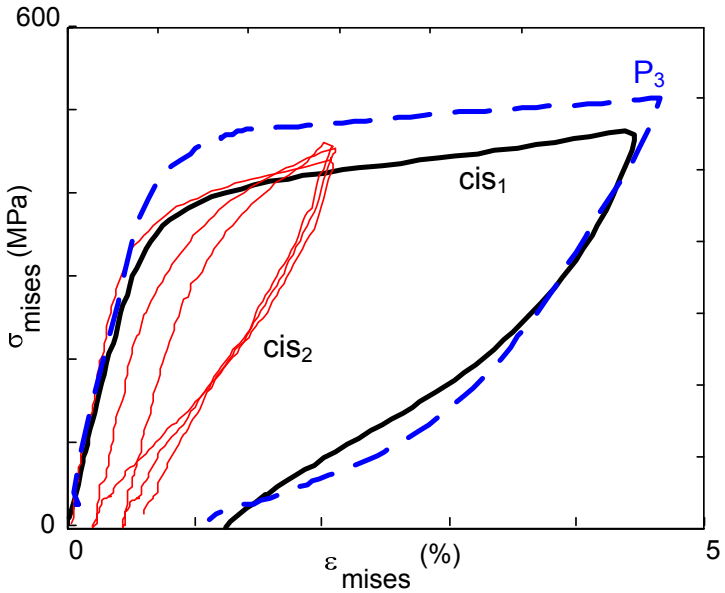

Figure 5.3: *Comparison of the Von Mises stress-strain curves. The tensile test P_3 is plotted with thick dashed line. The shear tests cis_1, cis_2 are represented respectively with solid thick line, solid thin line.*

5.2 Tensile tests on plates

5.2.1 Study of the homogeneous stages

5.2.1.1 Macroscopic results

Figure 5.4 shows the three stress strain curves superimposed during the homogeneous stages of deformation. During the homogeneous stages both strain and temperature variation fields were homogeneous for the three tests in the observation area (Figure 5.1.a-b). Time evolution of mean local strain ($\varepsilon = \Delta l/l_0$), stress ($\sigma$), mean temperature variation (θ) are superimposed in Figures 5.5 and 5.6 for tests P_1 and P_3 respectively.

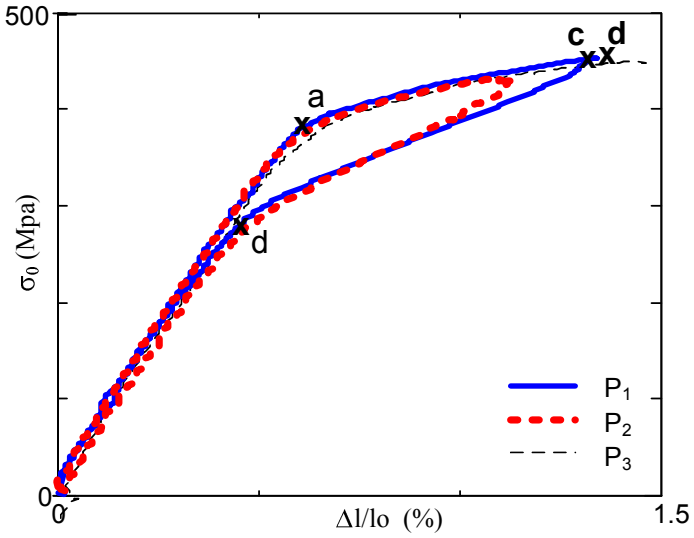

Figure 5.4: *Stress-strain curves of tests P_1, P_2 and P_3 superimposed during the homogeneous stage.*

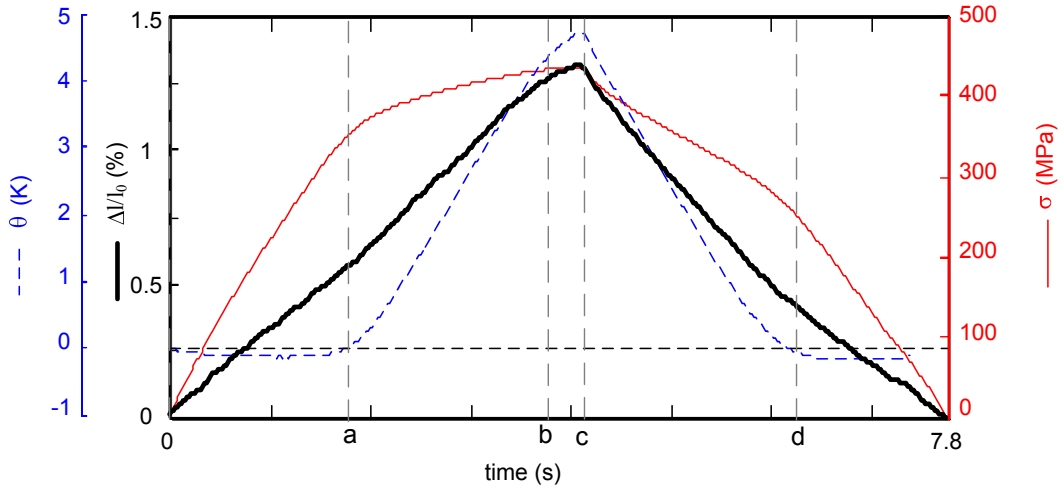

Figure 5.5: *Tensile test P_1 performed on the plate. Thick solid black line: time evolution of the local axial strain ($\varepsilon = \Delta l/l_0$) measured from the displacement of two extreme points A and B. Thin solid red line: time evolution of the nominal stress. Dashed thin blue line: time evolution of the mean temperature variation.*

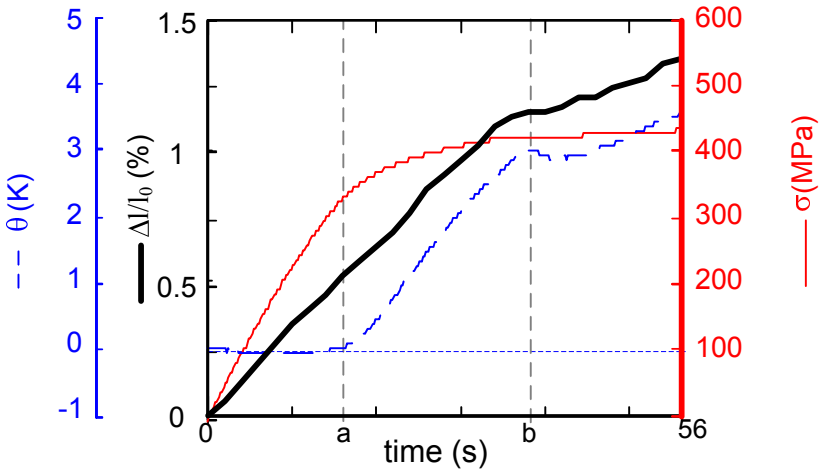

Figure 5.6: *Homogeneous stage of loading during tensile test P_3. Thick continuous black line: time evolution of the local axial strain $\varepsilon = \Delta l/l_0$. Thin continuous red line: time evolution of the nominal stress. Dash thin blue line: time evolution of the mean temperature variation.*

For every tests, several stages presenting an identical behaviour can be underlined:

- **time 0-a:** both strain and stress increased almost linearly. Meanwhile, the temperature decreased slightly ($\theta_{min} = -0.016$ K);
- **time a-b:** the stress increased less, whereas the temperature increased almost linearly up to 4.5 K for test P_1;
- **time b-c:** beginning of the stress plateau: the stress became constant, the temperature field was still homogeneous but its increase reduced slightly. The strain field was also homogeneous in the observation area but the macroscopic strain rate $\dot{\varepsilon}$ in the observation area was almost zero. Since the shape of the plate was rectangular (and not bone shape), the localization of the strain field started (certainly) near the grips, outside the observation area. Unloading started time (c) for tests P_1 and P_2.
- **time c-d:** (P_1) symmetric to the end of loading, the stress decreased slowly at the beginning of unloading. Meanwhile, the temperature decreased almost linearly.
- **time d-end:** after time (e), $|\dot{\sigma}|$ increased and the stress-strain curves were almost linear with the same rate as in the loading (see Figure 5.4). During this stage, the temperature went below the room temperature.

Estimation of Young's modulus E.

The value given to austenite Young's modulus is rather controversial. Its typical value is often reported to be near 60 GPa (Liu and Xiang, 1998), but Rajagopalan et al. (2005) have obtained 110 GPa using in situ neutron diffraction during loading. It is possible to obtain the Young's modulus by derivation of the stress strain curve using a local measurement of the axial strain:

$$E = \lim_{\varepsilon \to 0} \frac{d\sigma}{d\epsilon}. \tag{5.5}$$

In our case the mean local axial strain rate was estimated using DIC from relative displacement of the two extreme points of the correlation area A and B. The time evolution of the

estimation of $\frac{d\sigma}{d\epsilon}$ is represented in Figure 5.7 for tests P_1 in red and P_2 in blue. Loading and unloading are almost symmetric and the two curves for test P_1 and P_2 lie on top of each other well.

Both curves start at around $\frac{d\sigma}{d\epsilon} = 150$ GPa and decrease quickly. The markers in Figure 5.7 represent the estimation of $\frac{d\sigma}{d\epsilon}$ on each visible image. Clearly, the acquisition frequency of the visible camera was not fast enough to obtain enough data to be confident on the estimation of such parameter, but the order of magnitude was near 110 GPa, as obtained by Rajagopalan et al. (2005).

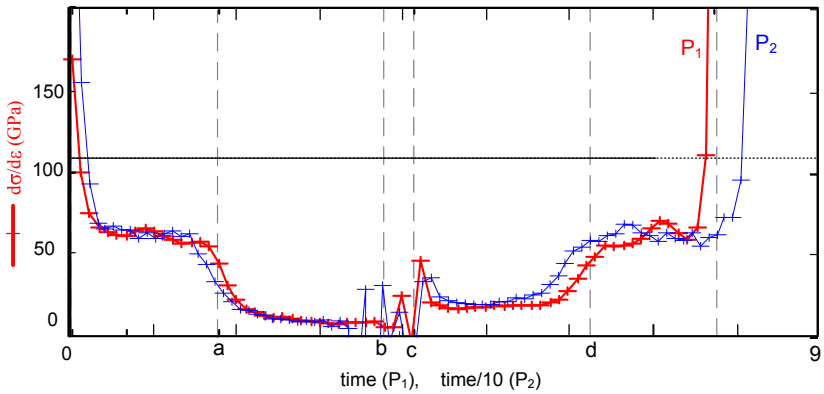

Figure 5.7: *Evolution of the ratio $d\sigma/d\varepsilon$. The term $d\varepsilon$ is the time derivative of the local axial strain $\varepsilon = \Delta l/l_0$ estimated from relative displacements of the two extreme points of the correlation area A and B. The markers represent the time of visible image acquisition. To be able to compare the two curves, the time has been normalised by the strain rate.*

After the quick decrease, both curves reach a first plateau at $\frac{d\sigma}{d\epsilon} = 60$ GPa until time (a) and a second at $\frac{d\sigma}{d\epsilon} = 8$ GPa from (a) to (b). However, the DSC measurement presented in Section 3.1.2 showed that this alloy has only one phase transformation A→M and no R-phase, as in the tubular specimens, these two distinct plateaux exhibit the presence of two other deformation phenomena than pure elastic one. It is likely that since the temperature fields were almost constant during times (0-a), the first plateau at 60 GPa refers to another mechanism of deformation such as the presence of precursor phenomena of the martensitic transformation (Otsuka and Ren, 2005) which induce lattice softening. From times a to b, the temperature increased indicated that the second plateau refer to martensitic transformation. In that interpretation, the true elastic modulus of the austenite is of the order of 150 GPa and the value of 60 GPa probably due to precursor phenomena and associated with elastic softening (Otsuka and Ren, 2005).

5.2.1.2 Heat source estimation

Specific heat sources $\dot{q} = s_i/\rho$ (in W kg^{-1}) were estimated with the heat diffusion equation (2.53) from the temperature variation θ. For the heat source estimations, the characteristic time τ_{th} reflecting heat losses both by convection through the specimen surface (back and front surfaces for plates, inner and outer surfaces for tubes) was estimated using the method presented in Section 2.5.5.1. As shown in Figure 5.8, $\tau_{th} = 55$ s.

Figure 5.9 represents the heat source estimation and the influence of each term during the

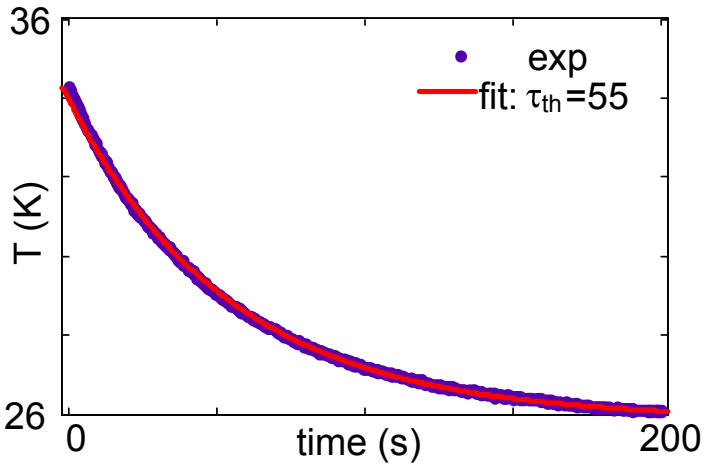

Figure 5.8: *Estimation of the characteristic time τ_{th} using a self cooling test.*

test. Since the temperature field was homogeneous, the heat sources depended mostly on the term "$C\ \theta_{,t}$" and were uniform and constant during the tensile test. The value chosen for k, the thermal conductivity did not affect the heat source values. We can therefore be very confident on this heat source estimation.

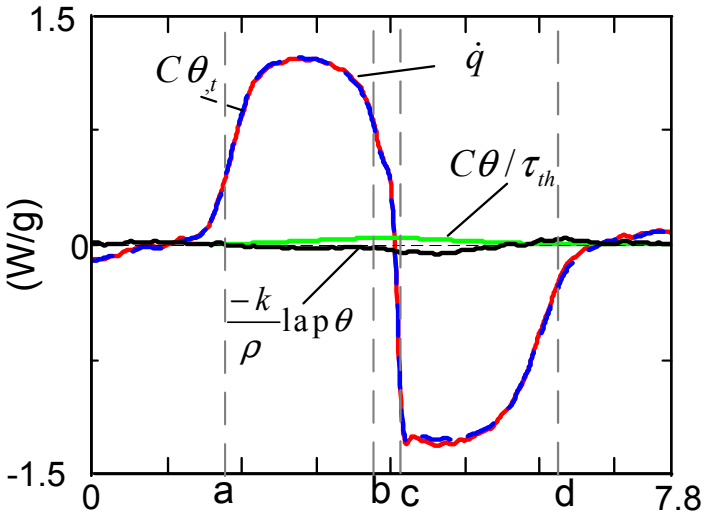

Figure 5.9: *Time evolution of the heat sources and its different terms during test P_1.*

As already presented in Section 4.2, heat sources $\dot{q}$ include $\dot{q}_{thel}$ the usual thermoelastic coupling:

$$\dot{q}_{thel} = -\frac{\alpha T_0 \dot{\sigma}}{\rho}, \tag{5.6}$$

where α is the coefficient of thermal expansion.

Figure 5.10 shows for test P_1 the comparison between those terms: estimated heat sources ($\dot{q}$) are plotted with thick solid grey line; the thermoelastic heat sources ($\dot{q}_{thel}$) estimated from the stress variation field are superimposed in thin solid red line. Finally, $\dot{q} - \dot{q}_{thel}$ is plotted in thick dash blue line. At the beginning of loading, heat sources of thermoelastic origin were preponderant, but there were some remaining exothermic heat sources of other origin that started as soon as the deformation process started. Those exothermic heat sources increased

up to time $t = 4$ s. They reached a maximum of 1.2 W/g and decreased down to the end of loading (c). Meanwhile, thermoelastic heat sources decreased and were almost equal to zero in (b). The unloading was almost symmetric to the loading, $\dot{q}$ was endothermic. Its minimum is -1.2 W/g at time $t = 6$ s. During unloading, the thermoelastic heat sources were exothermic.

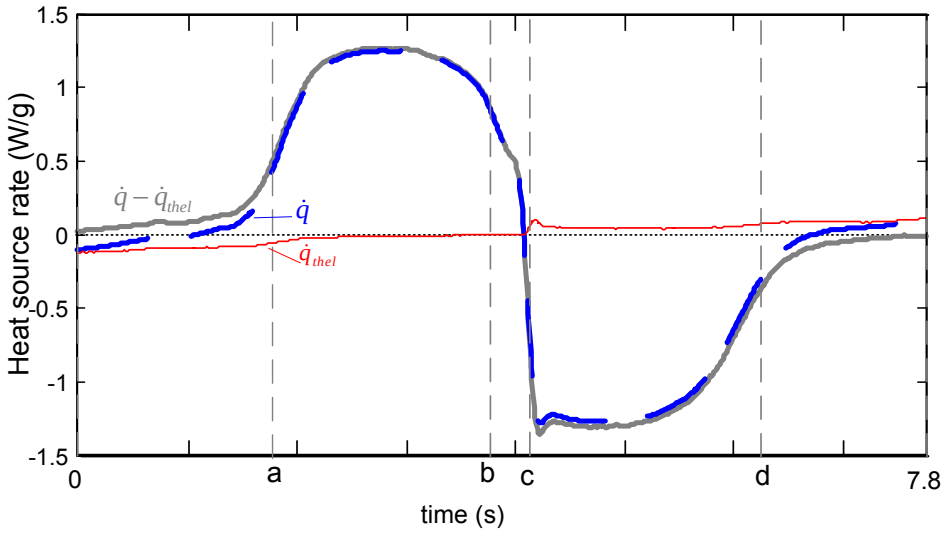

Figure 5.10: *Test P_1. Time evolution of the estimated heat source rate $\dot{q}$ (dashed thick line), $\dot{q}_{thel}$ the heat sources due to the thermoelastic coupling (red thin line), the remaining heat source rate ($\dot{q} - \dot{q}_{thel}$) (grey thick solid line).*

Figure 5.11 represents the heat sources (a) and energy (b) excluding the thermoelastic effect as functions of the strain. The energy was estimated by time integration of the heat sources:

$$q(t) = \int_0^t \dot{q}(u)du. \tag{5.7}$$

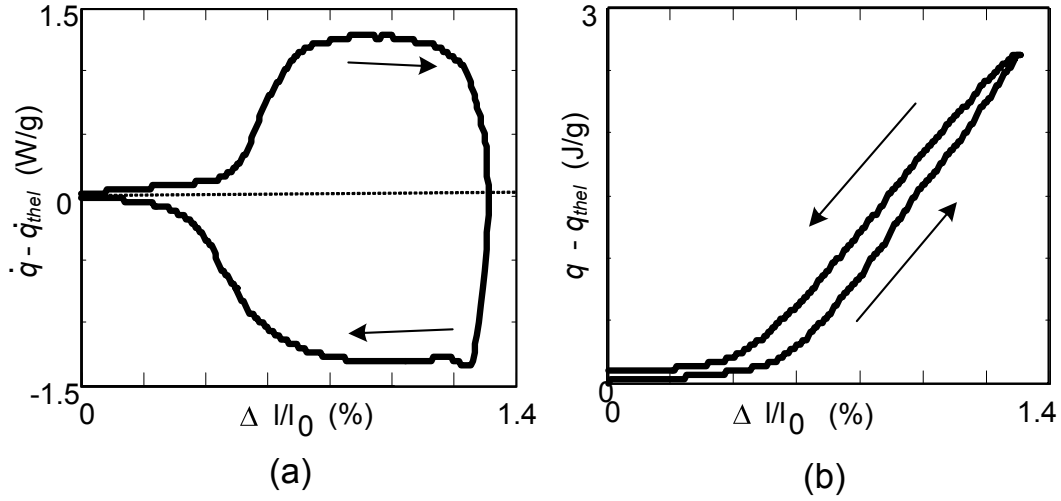

Figure 5.11: *Test P_1. a) Heat sources $\dot{q} - \dot{q}_{thel}$ as functions of the strain. b) Evolution of the energy ($q - q_{thel}$) as a function of the strain.*

As presented in Figure 5.11.a, heat source evolution during loading and unloading were not

totally symmetric. As expected, the evolution of the energy (Figure 5.11.b) was higher during unloading than loading. At the end of the test, $\dot{q} - \dot{q}_{thel} = 0.076$ J g^{-1}.

5.2.1.3 Estimation of the latent heat

In the following, we assume that each time, the deformation is due to elasticity of the lattice and an additional phenomenon associated with phase transformation; so that (McCormick et al., 1993; Lexcellent and Vacher, 1993):

$$\dot{\varepsilon} = \dot{\varepsilon}_{el} + \dot{\varepsilon}_{tr} \qquad \text{with} \quad \dot{\varepsilon}_{tr} = \dot{f}\ \Delta\varepsilon_{tr} \qquad \text{and} \quad \dot{\varepsilon}_{el} = \frac{\dot{\sigma}}{E} \quad (E = 110 \text{ GPa}). \tag{5.8}$$

Moreover, excluding the heat sources due to classical plasticity, we assume that each time, heat sources are due to thermoelastic and phase transformation heat sources (McCormick et al., 1993; Lexcellent and Vacher, 1993) so that:

$$\dot{q} = \dot{q}_{thel} + \dot{q}_{tr} \qquad \text{with} \quad \dot{q}_{tr} = \dot{f}\ \Delta H_{tr}^{tensile} \qquad \text{and} \quad \dot{q}_{thel} = -\frac{\alpha T_0 \dot{\sigma}}{\rho}. \tag{5.9}$$

Therefore,

$$\frac{\Delta H_{tr}^{tensile}}{\Delta\varepsilon_{tr}} = \frac{\dot{q}_{tr}}{\dot{\varepsilon}_{tr}} = \frac{\dot{q} + \frac{\alpha T_0 \dot{\sigma}}{\rho}}{\dot{\varepsilon} - \frac{\dot{\sigma}}{E}}. \tag{5.10}$$

The time evolution of $\Delta H_{tr}^{tensile}/\Delta\varepsilon_{tr}$ is plotted in Figure 5.12. In this figure, a first "plateau" is observed up on loading between time (0) to (a) when $\Delta H_{tr}^{tensile}/\Delta\varepsilon_{tr} = 60$ J g^{-1}. The second one is between (a) to (b) at about $\Delta H_{tr}^{tensile}/\Delta\varepsilon_{tr} = 375$ J g^{-1}. During unloading the plateaux are at 350 and 60 J g^{-1} during (c-d) and (d-7.8) stages respectively.

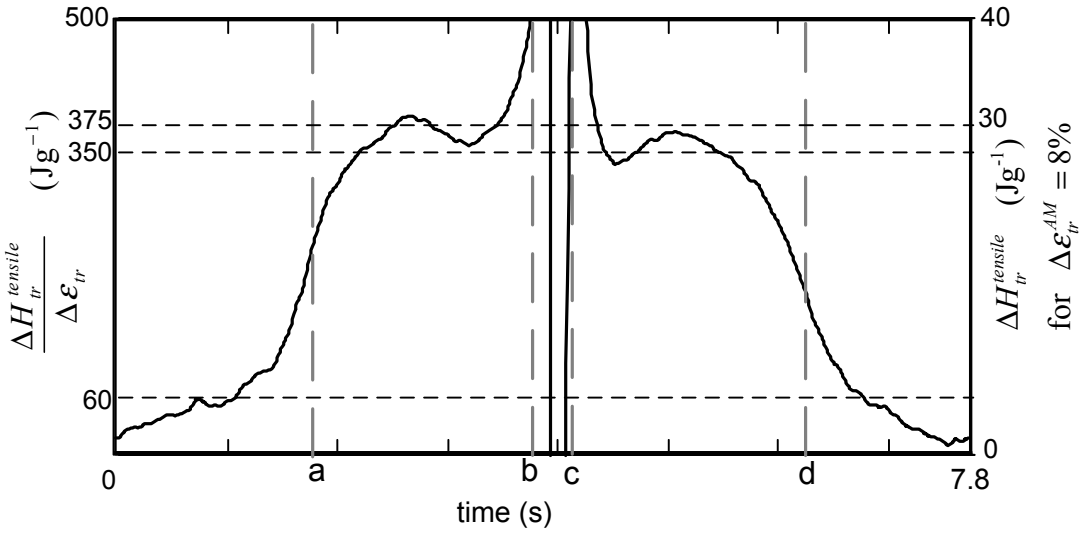

Figure 5.12: *Test P_1. Time evolution of $\Delta H_{tr}^{tensile}/\Delta\varepsilon_{tr}$ (left axis) and $\Delta H_{tr}^{tensile}$ (right axis) when taking $\Delta\varepsilon_{tr} = \Delta\varepsilon_{tr}^{AM} = 8\%$.*

As in Figure 5.7, this curve shows the presence of two transformations. It can be assumed that the two plateaux at $\Delta H_{tr}^{tensile}/\Delta\varepsilon_{tr} = 60$ J g^{-1} is associated with precursor phenomena.

The two other plateaux at 375 and 350 J g^{-1} can be associated with the martensitic transformation (A→M). For A→M transformation $\Delta H_{tr}^{tensile}$ was defined in Chapter 1 with eq.

(1.13):

$$\Delta H_{tr}^{tensile} = -\Delta H_c - E'_{el} - E'_{iw} + \frac{1}{\rho}\sigma\Delta.\varepsilon_{tr} \tag{5.11}$$

where $\Delta\varepsilon_{tr}$ and $\Delta H_{tr}^{tensile}$ stand for the transformation strain and the latent heat for a complete transformation ($f_m = 1$) under tensile loading. E'_{el} and E'_{iw} are the elastic energy and the non heat component of the dissipation and were defined in Chapter 1.

The difference of $\Delta H_{tr}^{tensile}/\Delta\varepsilon_{tr}$, is explained by the nature of the latent heat of transformation. In eq. (5.11), considering that the elastic energy E'_{el} has the same value during loading and unloading and that the non heat components of the dissipation E'_{iw} are negligible ($E'_{iw} \approx 0$), we obtain:

$$\Delta H_{tr}^{tensile}(loading) - \Delta H_{tr}^{tensile}(unloading) \approx \frac{\Delta\varepsilon_{tr}}{\rho}\big(\sigma(loading) - \sigma(unloading)\big), \tag{5.12}$$

where $\sigma(loading) - \sigma(unloading)$ is the stress hysteresis (see Figure 5.4). Therefore, since $\sigma(loading) > \sigma(unloading)$, $\Delta H_{tr}^{tensile}(loading) > \Delta H_{tr}^{tensile}(unloading)$, the plateau at 375 J g^{-1} corresponds to martensitic transformation $\Delta\varepsilon_{tr}^{AM} = 8\%$ (Orgéas and Favier, 1998) and latent heat $\Delta H_{tr} = 30$ J g^{-1}.

As expected from eq. (5.11), the latent heat value of stress induced martensitic transformation under tensile loading is higher than the temperature induced latent heat of phase transformation obtained by DSC. In our case we have found that $\Delta H_{tr}^{tension} \approx 30$ J.g^{-1}. Liu and Favier (2001) have found similar values for reverse transformation.

Figures 5.7 and 5.12 have shown that the precursor phenomena could not be neglected especially at the beginning of loading (time 0-a) and at the end of unloading (after time d). Therefore, the strain rates $\dot{\varepsilon}$ is expressed as:

$$\dot{\varepsilon} = \dot{\varepsilon}_{el} + \dot{\varepsilon}_{prec} + \dot{\varepsilon}_{AM} \tag{5.13}$$

where the elastic strain rate is $\dot{\varepsilon}_{el} = \frac{\dot{\sigma}}{E}$ by assuming negligible thermoelastic strain. And $\dot{\varepsilon}_{AM}$ and $\dot{\varepsilon}_{prec}$ are respectively the strain rate due to martensite phase transformation and precursor phenomena.

However, it is difficult to estimate $\dot{\varepsilon}_{prec}$. Since identical plateaux at 60 GPa were observed for the two macroscopic strain rate in Figures 5.7, we propose, as a first approximation, to express the precursor phenomena strain as function of the stress:

$$\dot{\varepsilon}_{prec} \approx \frac{\dot{\sigma}}{E_{prec}}. \tag{5.14}$$

Therefore, the martensitic transformation strain rate $\dot{\varepsilon}_{AM}$ reads:

$$\begin{aligned} \dot{\varepsilon}_{AM} &= \dot{\varepsilon} - \dot{\varepsilon}_{el} - \dot{\varepsilon}_{prec}, \\ &= \dot{\varepsilon} - \dot{\sigma}\left(\frac{1}{E} + \frac{1}{E_{prec}}\right) \end{aligned} \tag{5.15}$$

with

$$\frac{1}{E} + \frac{1}{E_{prec}} = \frac{1}{60}\ \text{GPa}^{-1}. \tag{5.16}$$

5.2.1.4 Estimation of the martensite fraction f_m

The martensite fraction can either be expressed as function of the transformation strain with eq. (5.8) or as function of the phase transformation heat sources with eq. (5.9). Figure 5.13 shows the estimation of $\dot{f}_m$ using the two methods (cf eq. (5.8) and (5.9)). To estimate $\dot{f}_m$, the latent heat associated with the martensitic transformation was assumed constant and equal to 30 J g^{-1}. The two curves are very similar and confirm our approximation of the strain rate due to the precursor phenomena. However this approximation seems to be not valid at the beginning of loading and induces estimations of negative martensite fraction. Estimation using heat sources is more accurate and will be used in the following.

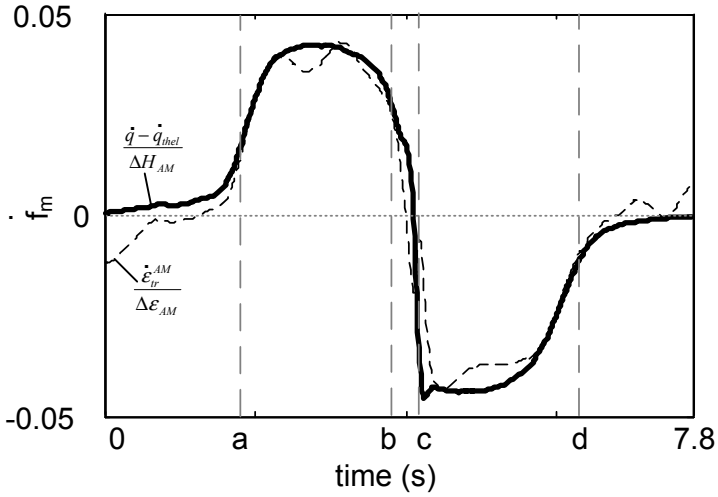

Figure 5.13: *Test P_1. Comparison of the martensite fraction estimated from the phase transformation strain rate ($\dot{f}_m = \dot{\varepsilon}_{tr}^{AM}/\Delta\varepsilon_{AM}$) and from the phase transformation heat sources ($\dot{f}_m = \dot{q}_{tr}/\Delta H_{AM}$) with $\Delta H_{AM} = 30\ J\,g^{-1}$.*

Figures 5.14 and 5.15 show the evolution of the martensite fraction as a function of the strain and stress, respectively. The martensitic transformation started as soon as the test started. At the end of loading the martensite fraction present was about $f_m = 8.7\%$. At the end of unloading the remaining martensite fraction was 0.25 %. Figure 5.15 shows that the forward and the reverse transformations were not at constant stress and did not have the same slope ($d\sigma/df_m$). The hysteresis between the beginning of the forward and reverse transformations was about 100 MPa.

5.2.1.5 Thermodynamic analysis

This paragraph will present a thermodynamic analysis (cf relationship defined in Chapter 1) and try to estimate the different components of eqs. (1.24) and (1.27) during a cyclic loading, with $f_{m1} = 0$:

$$q_{tr}^{1-2-3} = -f_{m3}\,\Delta H_c - \oint_{123} E'_{el}\,df_m - \oint_{123} E'_{iw}\,df_m + \oint_{123} W'_{mech}\,df_m, \qquad (5.17)$$

and:

$$\begin{aligned} q_{tr}^{1-2-3} &= \Big(-T_1\Delta S_c f_{m3} - \Delta S_c \oint_{123}\theta\,df_m \Big) + \oint_{123} E'_{iq}\,df_m, \qquad (5.18)\\ &= q_{tr\,chem}^{1-2-3} + q_{tr\,diss}^{1-2-3}, \end{aligned}$$

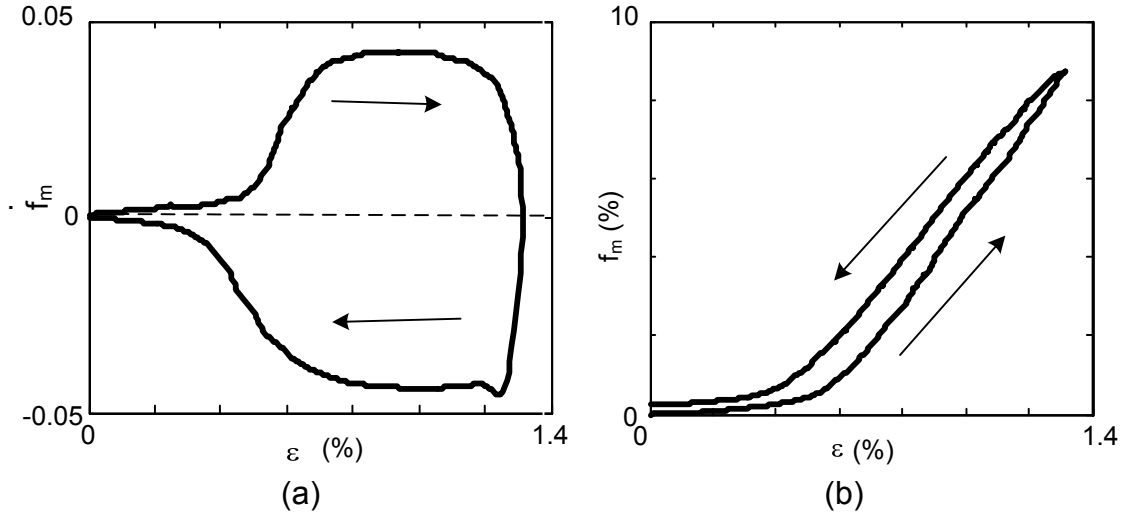

Figure 5.14: *Martensite fraction estimated during test P_1. a) $\dot{f_m}$ evolution as a function of strain. b) Martensite fraction f_m as a function of strain.*

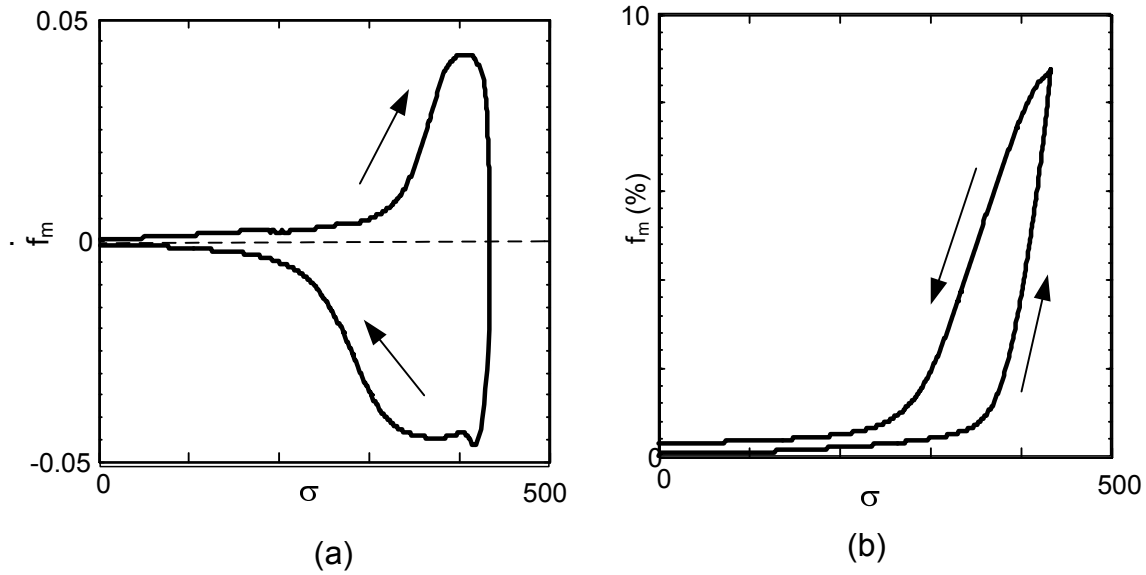

Figure 5.15: *Martensite fraction estimated during test P_1. a) $\dot{f}$ evolution as a function of nominal stress. b) Martensite fraction f as a function of nominal stress.*

with the notations:

$$q_{tr}^{1-2-3} = \int_{t_1}^{t_2} \dot{q}(u)du + \int_{t_2}^{t_3} \dot{q}(u)du \tag{5.19}$$

$$\oint_{123} \xi' \, df_m = \int_{f_{m1}}^{f_{m2}} \xi' \, df_m + \int_{f_{m2}}^{f_{m3}} \xi' \, df_m \tag{5.20}$$

In eq. (5.18), $\Delta H_c = H_c^M - H_c^A$, E'_{el} is the elastic energy and E'_{iw} is the non heat component of the irreversible energy. $\oint_{123} W'_{mech} \, df_m$ is the mechanical work during the test.

In eq (5.17), $\Delta S_c = S_c^M - S_c^A$ and E'_{iq} is the heat component of the irreversible energy dissipated during the cycle, namely, $\oint_{123} E'_{iq} \, df_m = q_{tr\,diss}^{1-2-3}$. The energy $q_{tr\,chem}^{1-2-3}$ is the sum of the chemical energy due to the phase transformation during the cycle.

In the initial state the sample was fully austenitic ($f_{m1} = 0$), $f_{m2} = 8.7\%$ and $f_{m3} = 0.25\%$ are the martensite fraction at the end of loading and at the end of unloading for test P_1 (see Figure 5.14). From Figure 5.11,

$$q_{tr}^{1-2-3} = 0.076 \text{ J g}^{-1}. \tag{5.21}$$

With $\Delta S_c = -0.045$ J g^{-1}K^{-1} (McCormick et al., 1993), we estimated the different terms of the chemical energy from eq. (5.18). The test temperature was $T_1 = 298$ K, therefore,

$$T_1 \Delta S_c f_{m3} = -0.067 \text{ J g}^{-1}. \tag{5.22}$$

Figure 5.16 shows the change of the temperature variation vs. the martensite fraction. We can then estimate the term $\oint_{123} \theta \, df_m = 0.07$ K and then:

$$\Delta S_c \oint_{123} \theta \, df_m = -0.003 \text{ J g}^{-1}. \tag{5.23}$$

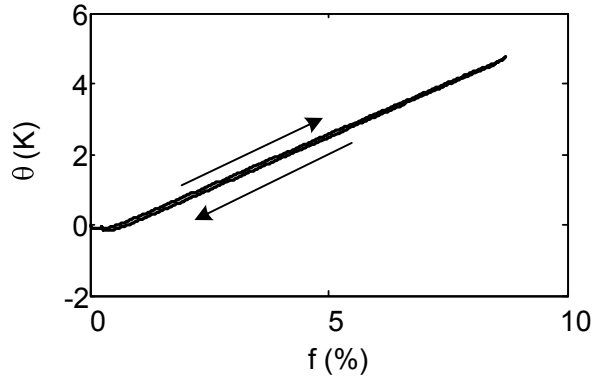

Figure 5.16: *Temperature variation vs. martensite fraction during test P_1.*

Therefore, the total irreversible energy dissipated during the cycling loading reads:

$$\begin{aligned} q_{tr\,diss}^{1-2-3} &= \oint_{123} E'_{iq} \, df_m \\ &= q^{1-2-3} + T_1 \Delta S_c f_{m3} + \Delta S_c \oint_{123} \theta \, df_m, \\ &= 0.006 \text{ J g}^{-1}. \end{aligned} \tag{5.24}$$

Such result shows that the dissipation was very small compared with the transformation heat. It is in good agreement with previous works obtained on polycrystalline NiTi and CuZnAl alloys and monocristal CuZnAl (McCormick et al., 1993; Lobel, 1995).

From the mechanical curve in Figure 5.1, the mechanical work during test P_1 was $\oint \delta W_{mech} = \frac{1}{\rho} \oint \sigma\varepsilon = 0.06$ J g^{-1} which is of the same order of magnitude as transformation heat q_{tr}.

5.2.1.6 Comparison of the martensite fraction transformed in the homogeneous stage

Martensite fractions of tests P_1 and P_3 were estimated using the same method as that used in the previous section. Figure 5.17 shows the comparison of the martensite fraction estimated

for the two tensile tests. Regardless of the test strain rate, the curves are identical during loading. They can be modelled, during loading, by two linear evolutions. Below time a ($\varepsilon = 0.6\%$ and $\sigma = 375$ MPa), the martensite fraction is almost zero but increases linearly very slowly. Thereafter and up to the end of the homogeneous stage, the phase transformation velocity increases much faster with a higher slope. To transform nearly 8 % of martensite fraction the stress increased by 100 MPa, the phase transformation in the homogenous stage was therefore not at constant stress. Moreover, contrary to localization phenomena that start instantaneously, homogenous martensitic transformation is a slow process.

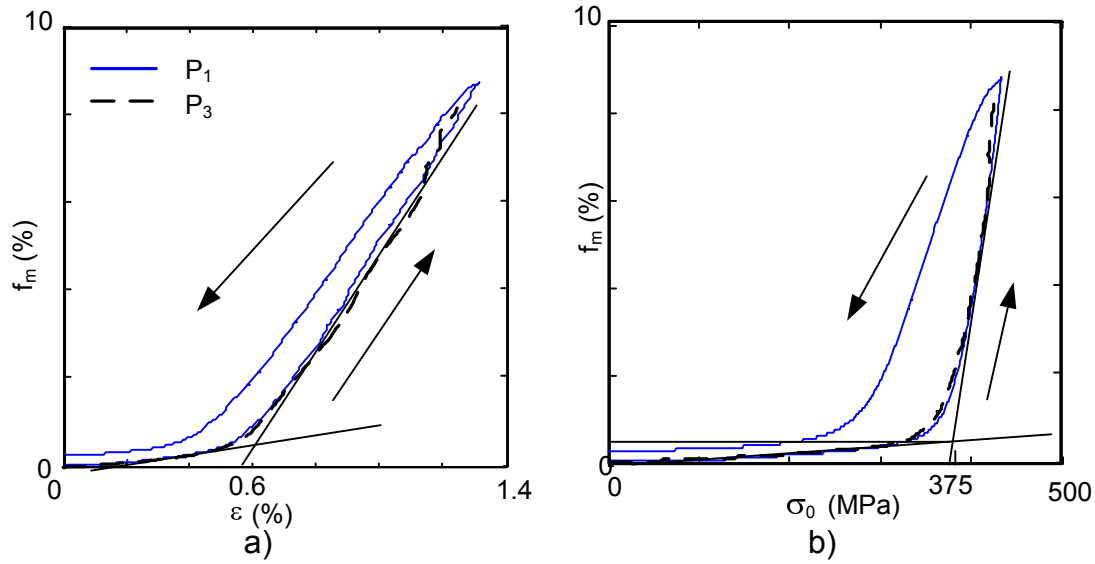

Figure 5.17: *Martensite fraction estimated during tests P_1 (thin continuous blue line) and P_3 (dash black line). a) Martensite fraction f_m evolution as function of the strain ε. b) Martensite fraction f_m evolution as function of the nominal stress σ.*

This confirms that the first part of loading (time 0-a, $\varepsilon < 0.6\%$), elastic strain was predominant and the precursor phenomena played an important role. From time a until the end of the homogeneous stage, the deformation was mostly due to martentite transformation. A complementary study by stopping in the middle of the homogeneous area or at time a for instance would be necessary to better analyse this homogenous loading.

5.2.2 Study of the localization phenomena during test P_3

In order to analyse the localization stage during test P_3, strain, temperature and heat source fields are first compared in Section 5.2.2.1. Then, heat source estimation will be presented in Section 5.2.2.2. Since the strain field was localised during the stress plateau, the martensite fraction was not homogeneous through the sample and taking a unique value of thermal conductivity induced many errors. Section 5.2.2.3 will present a first proposition to better estimate the heat sources. Finally, energy will be calculated in Section 5.2.2.4 and Section 5.2.2.5 will show the main difficulties and errors during this energy estimation.

5.2.2.1 Observation of the localization phenomena

Only test P_3 was performed beyond the homogenous stage. In order to analyse this test, thermal and kinematic fields were synchronised using the method presented in Section 2.4. Three characteristic points, visible on the two initial images were used to obtain the transformation matrix **v2ir**. The synchronisation was performed at the infrared frequency f_{IR} on the DIC grid (i.e. at a spatial resolution of 0.65 mm). Therefore, for each particle $P(x, y, t)$ of initial coordinate (X, Y) the temperature variation was estimated using:

$$\theta = T(x, y, t) - T(X, Y, 0). \tag{5.25}$$

Figure 5.18 presents the Green-Lagrange E_{xx} strain fields and temperature variation fields θ change at four different times of .

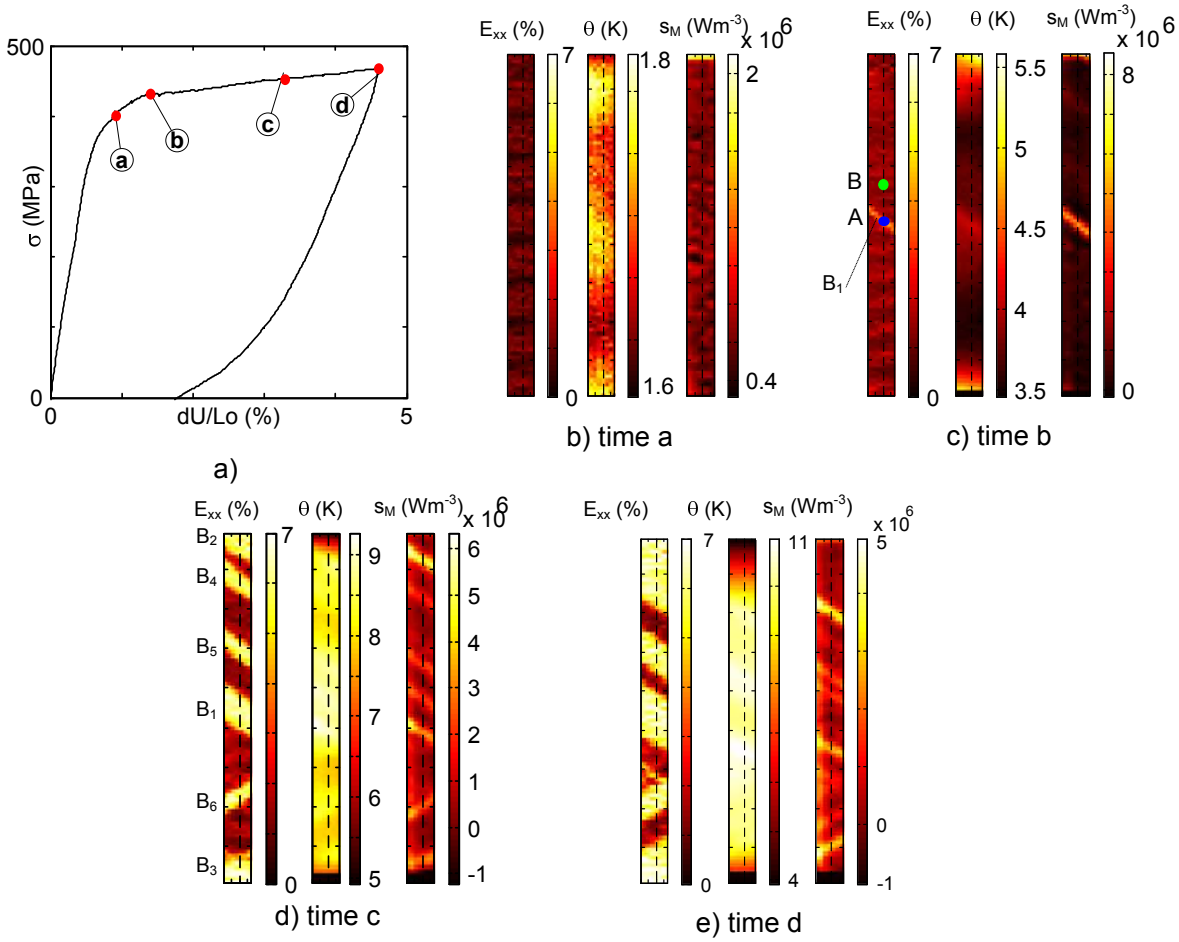

Figure 5.18: *Comparison of the thermal and kinematic fields at several times during test P_3. a) Nominal stress strain curve and position of the selected times during loading. Time a-d: at the selected time marked in a, colored map of the synchronised data of the Green-Lagrange E_{xx} strain field, the temperature variation field θ and the heat sources s_M estimated using $k = k_M$.*

Figure 5.19.a and b presents the spatiotemporal evolution of E_{xx} and θ along the vertical axis of the plate. As can be seen on the strain fields, at times a and b, in Figures 5.18 and 5.19.a, localization phenomena started only at time b in the observation area. The first observed localization band B_1 was in the middle of the sample; at the same time, the temperature

had also increased near the upper and lower grips. In fact, localization had started before time b but was hidden by the grips. After time b, the middle band B_1 became wider and the two bands B_2 and B_3 that initiated outside the observation area were also widening and therefore visible. Finally, three other bands appeared. The bands near the top grip B_1, B_2, B_4 and B_5 had same orientation ($\approx 59°$ to the vertical axis). The bottom band B_3 and B_6 were orientated in the other direction ($\approx$-59° to the vertical axis). Unlike tube, the bands were stopped on the left and right edges of the plate sample and could only grow wider along the vertical axis. The spatiotemporal representation in Figure 5.19.a allows us to detect the creation of six localization bands during the stress plateau. At the end of loading, time d, the plate strains were still strongly localised since the test was stopped before the end of the stress plateau.

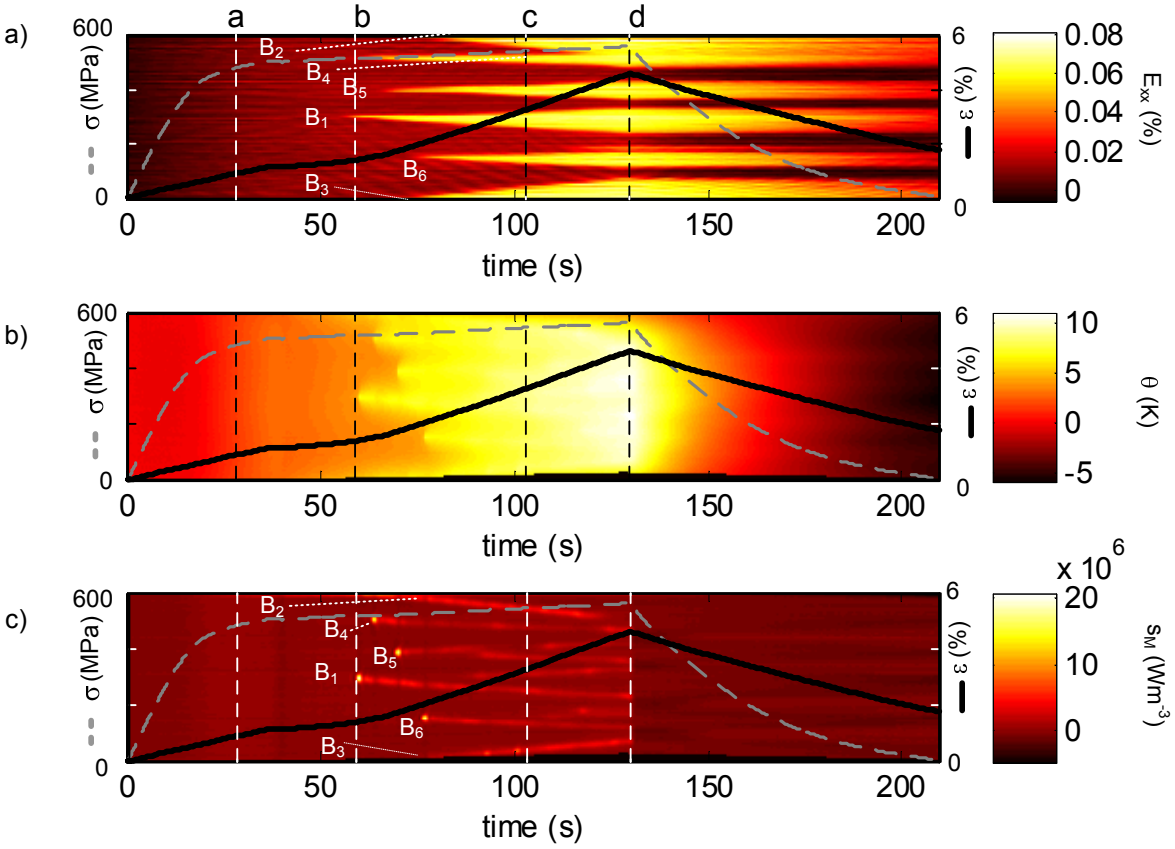

Figure 5.19: *Test P_3: spatiotemporal representation along the plate axis of a) the Green Lagrange E_{xx}, b) the temperature variation field θ and c) the heat sources s_M. The grey dotted line represents the nominal stress and the continuous line the local axial strain ε.*

As already observed on tubes in Chapter 4, localization can easily be detected using the temperature field at the very beginning of localization (e.g. temperature field at time b in Figures 5.18 and 5.19.b). But soon after, due to conduction phenomena, temperature fields are difficult to analyse (see temperature field at time c in Figures 5.18 and 5.19.b). Since the test was stopped before the end of the stress plateau, the strain field was localised at the end of loading. Upon unloading, the temperature decreased from +10 K to -5 K.

5.2.2.2 Observation of the localization phenomena using heat source estimation

Specific heat sources s_i^0 (in Wm^{-3}) were estimated using image processing presented in Section 2.5.5 from the temperature fields $\theta^0 = T(x,y,t) - T(x,y,0)$ using the diffusion equation expressed in spatial coordinate system[1]:

$$s_i^0 = \rho C(\ \theta^0_{,t} + \frac{\theta^0}{\tau_{th}}) - k\ \mathrm{lap}_{2Dcart}\ \theta^0, \tag{5.26}$$

with

$$\mathrm{lap}_{2cart}\ \theta^0 = \ \theta^0_{,xx} + \ \theta^0_{,yy}, \tag{5.27}$$

where k is the thermal conductivity. The terms C (490 J kg^{-1} K^{-1}) and ρ (6400 Kg m^{-3}) denote the specific heat and the mass density respectively; they are assumed to be homogeneous and constant. The characteristic time $\tau_{th} = 55$ s reflecting heat losses both by convection through the plate surface (front and back) was estimated using the method presented in Section 2.5.5.1. Heat sources $s_i(P,t) = \rho \dot{q}_i(P,t)$ were estimated for every particle P using the spatial synchronisation.

Since the thermal conductivity of martensite $k = k_M = 8.6$ $\mathrm{Wm}^{-1}\mathrm{K}^{-1}$ is different from that of austenite $k = k_A = 18$ $\mathrm{Wm}^{-1}\mathrm{K}^{-1}$ (Faulkner et al., 2000), heat sources were estimated for the two thermal conductivity values. They will be labeled s_M when $k = k_M$ and s_A when $k = k_A$.

Heat sources s_M are plotted in Figures 5.18 and 5.19.c and give some indication on the behaviour of the phase transformation. The position of the heat sources peaks corresponds to the position of the phase transformation fronts (initiation or propagation). They were concentrated at the same positions as the strain steps. When no strain variation was observed, the heat sources were weak. The position of the localised heat sources give an information on the kinematics of the phase transformations. The bands in Figure 5.19.c, with intense amplitude, show the propagation (at constant velocity) of the front of transformation. We recall that it was impossible to detect these local fronts when observing only the (diffuse) thermal fields (Figure 5.19.b).

5.2.2.3 To a better heat source estimation

Influence of thermal conductivity on the heat source estimation

In order to estimate the influence of the thermal conductivity on our heat source estimation, s_A and s_M were plotted in Figure 5.20 for two particles A and B. The heat sources s_A, obtained with higher values of $k = k_A$ give upper bound values and s_M are lower bound values. Particle A was chosen in the middle of the sample where the first band appeared whereas particle B was chosen in an area that remained outside the localisation bands (see position in Figure 5.18.c). Their strain evolutions are plotted in Figures 5.20.a and b and the heat sources in Figures 5.20.c-f.

[1]In all this section, temperature T, temperature variation θ, heat sources s, and energy q will be indicated with superscript "0" when expressed for spatial point and without superscript when expressed for a material point (after performing the spatial synchronisation).

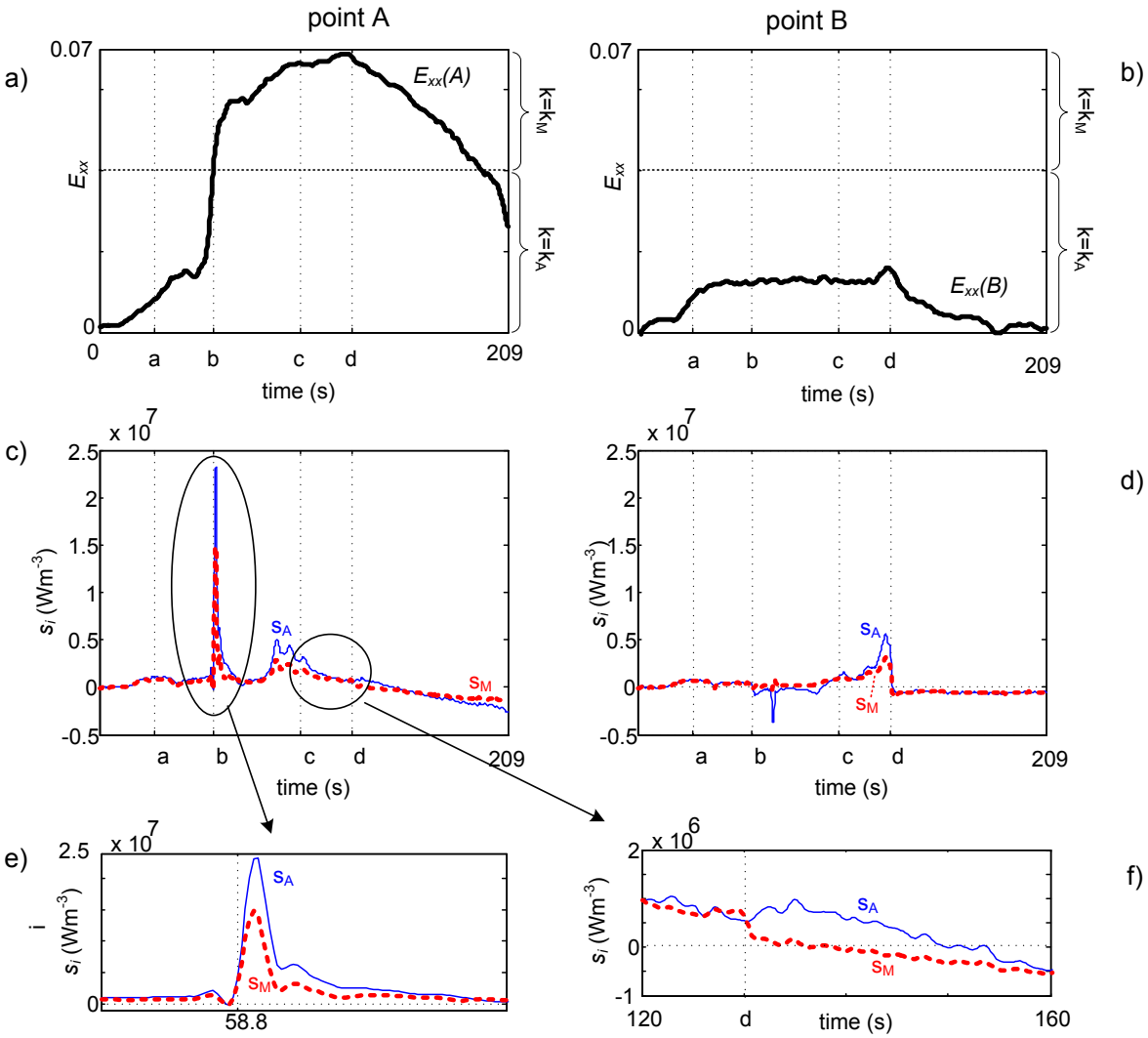

Figure 5.20: *Influence of the thermal conductivity coefficient k on the heat source estimation in two points A and B (see position in Figure 5.18.c). a-b) Temporal evolution of the Green Lagrange axial strain $E_{xx}(A)$ and $E_{xx}(B)$. c-f) Temporal evolution of the heat source estimation using $k = k_A$ (solid lines) and $k = k_M$ (dashed lines).*

These figures confirm that for particle A, the heat source peak correspond to the position of strain jump. Both strain jump and heat source peak were almost instantaneous. On the contrary, particle B whose strain remained bellow $E_{xx} < 0.02$ did not present any heat sources peak. Figures 5.20.e-f emphasise, near the heat source peak (time b) and at the beginning of unloading (time c to d) the differences:

- in Figure 5.18.c, around time b, the heat sources are strongly localized. Therefore the Laplacian term ($-klap_{2Dcart}\theta = -k(\theta_{,xx} + \theta_{,yy})$) had a strong influence on the heat source estimation, the value of k chosen will therefore strongly affect the heat sources (see for example Figure 5.20.c).
- At the beginning of unloading (Figure 5.20.f), the temperature field was heterogeneous and more than 10 K above the initial temperature (see Figure 5.19.b). Meanwhile, E_{xx} decreased slightly and was then constant. Heat sources calculated with $k = k_A$ appeared as exothermic whereas they are almost equal to zero with $k = k_M$.

- Only heat sources estimated at the beginning of loading (0-a) were not affected by the choice of k, since the Laplacian was negligible in the homogeneous stage (see also Figure 5.9.

To conclude, the thermal conductivity k has a strong impact on the heat source estimation, it is more likely that the thermal conductivity was not homogeneous during the test along the sample and that the real heat sources values are s_M and s_A.

First proposition of estimation

Since NiTi martensitic transformation is very localised during a tensile test, each time the strain field along the plate is divided between two states:

1. a less deformed region that is mostly austenitic, where we assume that the thermal conductivity is close to $k = k_A$,
2. a high deformed region that is mostly martensitic, where we assume that the thermal conductivity is close to $k = k_M$.

Figure 5.21.a shows that the boundary (denoted by D) between the less deformed and highly deformed areas is very narrow. The phase transformation strain (when A→M is completed) is 8 % (Orgéas and Favier, 1998). We have chosen to delimit these two regions by the mid-value of $E_{xx} = 0.04$. Figures 5.21.b and c present the position of the two regions on a spatiotemporal representation along the vertical axis of the plate and on the sample at time b (beginning of localization). Due to strong localization phenomena, the two areas were well defined.

Therefore, depending on the local strain state, the weighted heat sources s_w will be estimated with:

$$s_w = s_A \quad \text{if} \quad E_{xx} < 0.04 \quad \text{(white area in Figure 5.21.b)} \tag{5.28}$$

$$s_w = s_M \quad \text{if} \quad E_{xx} \geq 0.04 \quad \text{(grey area in Figure 5.21.b)} \tag{5.29}$$

Figure 5.22 shows the evolution of E_{xx} and s_w for two selected particles A and B (see Figure 5.18.c). The austenite thermal conductivity was used to estimate $s_w(B)$ since during the whole test $E_{xx}(B) < 0.04$. For particle A, the austenite thermal conductivity $k = k_A$ was used from 0 to b and that of martensite $k = k_M$ after time b.

From 0 to a, the strain and heat source fields were homogeneous therefore $E_{xx}(A) = E_{xx}(B)$ and $s_w(A) = s_w(B)$. Time b corresponded to the beginning of localization in A. Strain field increased quickly from $E_{xx}(A) = 0.017$ to 0.051, heat source amplitude peak was 1.5 10^7 Wm^{-3}. Meanwhile, $E_{xx}(B)$ was constant and $s_w(B)$ almost equal to zero. From b to d, the heat sources in A decreased as fast as they had appeared but they were still positive. At the same time, the strain $E_{xx}(A)$ increased slowly. Time d corresponded to the end of loading and band B_2, which was widening, was reaching particle B. A heat source peak of amplitude $s_w(B)$=5.6 10^6 Wm^{-3} was measured at time d and $E_{xx}(B)$ only increased from 0.013 to 0.015.

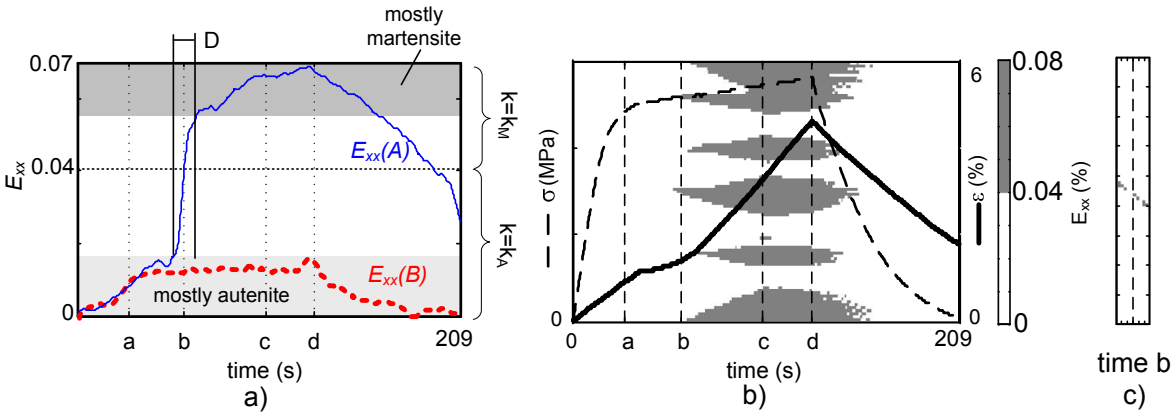

Figure 5.21: *Test P_3: a) time evolution of the strain E_{xx} for particles A and B. Strain areas where the material is mostly in martensite and austenite phase. Within the boundary D, the material is a mixture of both austenite and martensite. b) Spatiotemporal representation along the vertical axis of the plate of the position of the less deformed region ($E_{xx} < 0.04$, white) and the highly deformed region ($E_{xx} > 0.04$, grey). The stress σ and the strain ε are represented in dash and continuous lines, respectively. c) Position of the two region on the sample at the selected time b.*

Figure 5.23 shows the strain and heat source axial profiles at four selected times during loading. At time a, heat sources and strain fields are homogeneous and positive. When the strain localization started at time b, a heat source peak was observed in the same area. At times c and d the localization bands were propagating and widening. The position of the heat sources corresponded to a strain gradient. At the beginning of unloading, $E_{xx}(B)$ decreased quickly down to zero (time d in Figure 5.21) while heat sources where almost zero (time d in Figure 5.22). $E_{xx}(A)$ was decreasing as well but was still equal to 0.025 at the end of the test (Figure 5.21). The heat sources $s_w(B)$ were negative and decreased as well (Figure 5.22).

Figure 5.24 presents the strain and heat sources profile at two selected times during unloading. In this figure, between the beginning of unloading (time d) and time e, both strain field and heat sources decreased homogeneously. Soon after time e, the areas that were still mostly austenitic at the end of loading (like particule B) were back to $E_{xx} = 0$ and $s_w = 0$. The strain decreased almost homogeneously in other areas. Negative heat sources were measured in these areas where reverse transformations happened. At the end of unloading (f), the strain performed in those area was $E_{xx} = 0.025$.

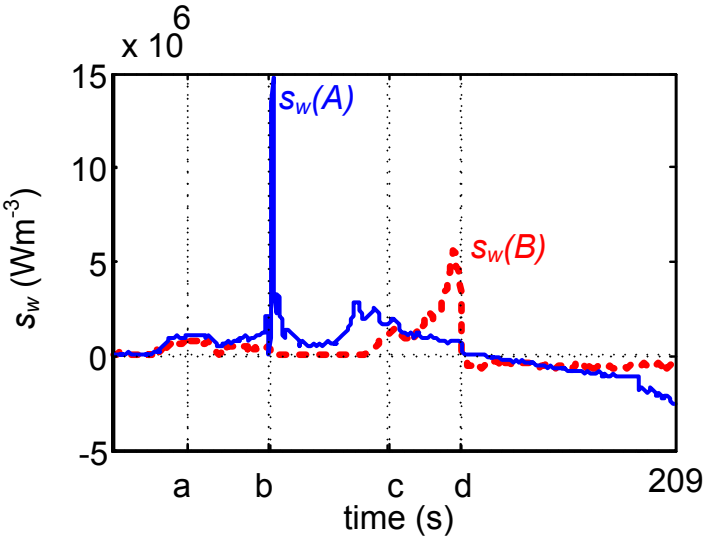

Figure 5.22: *Evolution of the weighted heat sources s_w for two selected particles A and B: particle A (plotted with thin solid line) was selected in the middle of the sample where the first band B_1 initiated. Particle B (plotted with thick dotted line) was close to A but in an area where no band passed during loading (see Figure 5.18.c).*

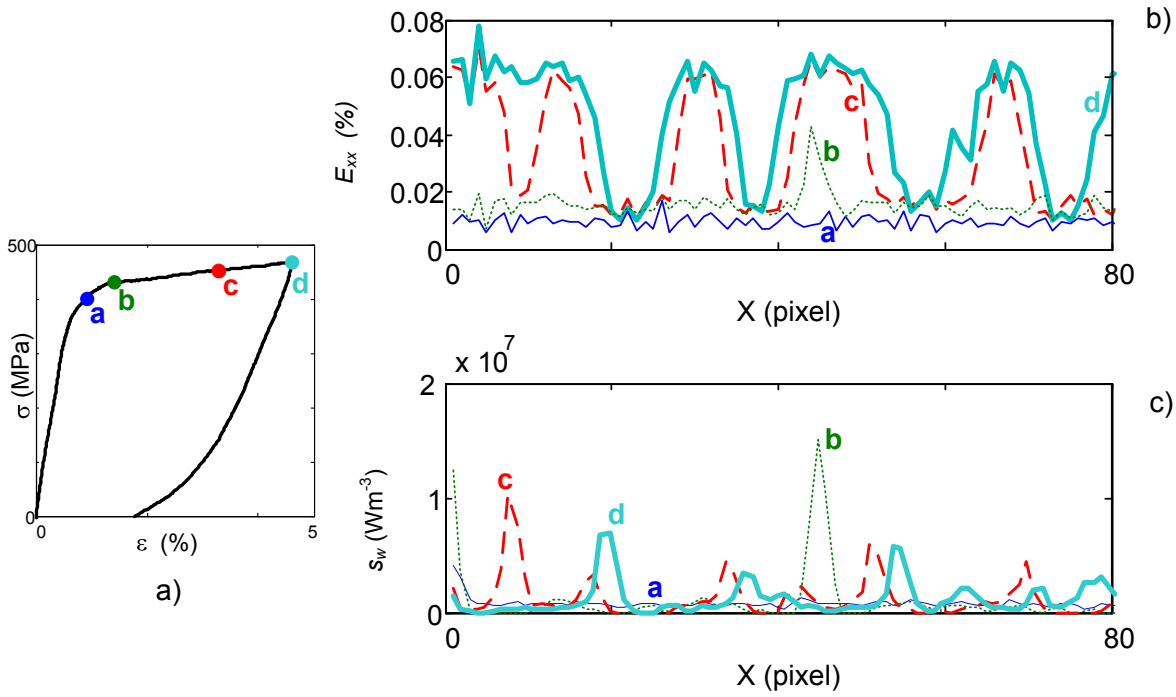

Figure 5.23: *Test P_3. a) Stress-strain curve with the position of four selected profiles during loading. b) E_{xx} strain axial profiles. c) Heat sources estimated on the same profiles.*

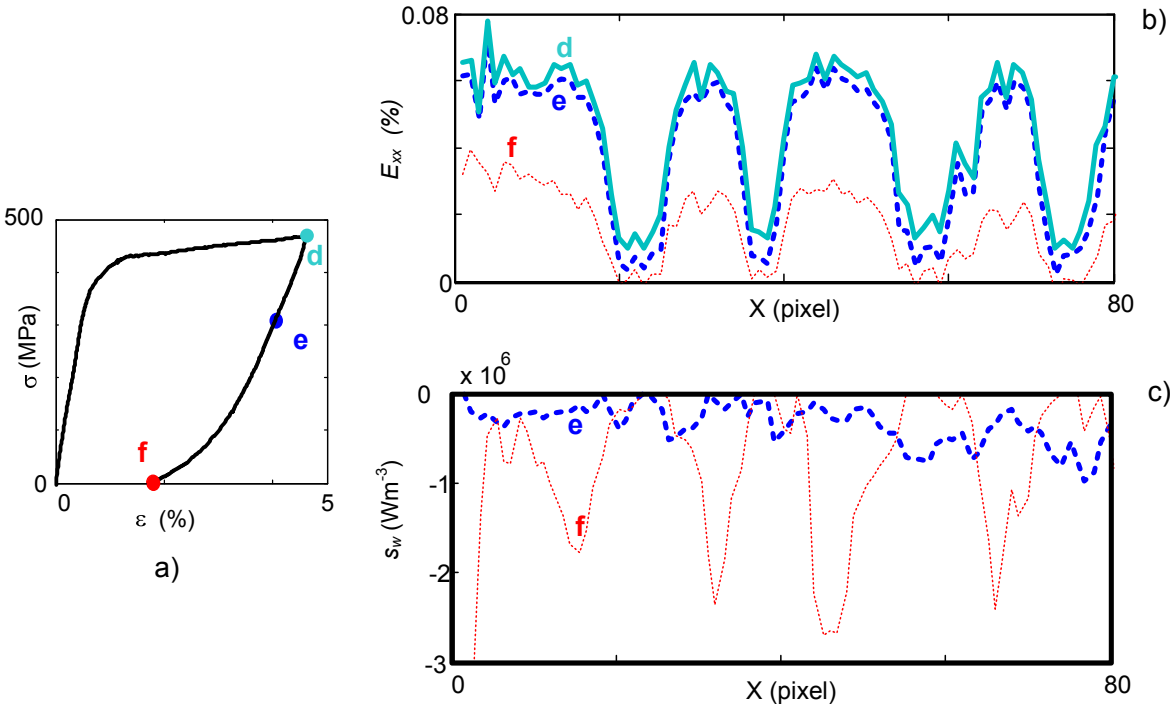

Figure 5.24: *Test P_3. a) Stress-strain curve with the position of two selected profiles during unloading. b) E_{xx} strain axial profiles. c) Heat sources estimated on the same profiles. In order to emphasise the heat source scale in c), heat source profile at time d, which were positive, have not been represented.*

5.2.2.4 First energy estimation

From $s_w(P,t)$ it is possible for each particle $P(x,y,t)$ of initial coordinate (X,Y) to estimate the energy $q_w(P,t)$ (in J g^{-1}) by a time integration for each particle:

$$q_w(P,t) = \frac{1}{\rho}\int_0^t s_w(P,u)\,du. \tag{5.30}$$

Figure 5.25 presents four strain and energy profiles q_w along the vertical axis during loading (time a, b, c and d). It is worth noting that these two fields (E_{xx} and q_w), obtained by two independent set-ups (visible and infrared cameras), are very similar. At the end of loading, the transformation was not completed and some areas were still austenitic at time d in Figure 5.25. In the localised areas, the deformation was the same and equal to 0.065. The martensitic transformation was not complete since $\Delta\varepsilon_{AM} = 8\%$ (Orgéas and Favier, 1998). Meanwhile the energy profiles are almost identical to the deformation ones and reach a maximum near 27 J g^{-1} in the deformed area.

Figure 5.26 presents the spatiotemporal evolution of E_{xx} and q_w along the vertical axis of the plate and allows for an overview of the test. This representation emphasises the similarity between E_{xx} obtained by DIC and q_w obtained by a time integration of the heat sources estimated from the temperature field. As presented in eq. (1.13) the energy between two states of martensite fraction (f_{m1} and f_{m2}) is a function of the latent heat $\Delta H_{tr}^{tensile}$:

$$\begin{aligned} q^{1-2} &= \int_{f_{m1}}^{f_{m2}} \left(-\Delta H - E'_{el} - E'_{iw} + W'_{mech}\right) df_m \\ &= \int_{f_{m1}}^{f_{m2}} \Delta H_{tr}^{tensile} df_m \end{aligned} \tag{5.31}$$

In our case the sample was assumed to be fully austenitic at the beginning of the test. $f_{m1} \approx 0$. Inside the localised area, the energy was $q^{1-2} \approx q_w^{1-2} = 27$ J g^{-1} although the phase transformation was not complete. As expected, this value is smaller than $\Delta H_{tr}^{tensile} = 30$ J g^{-1} estimated during the homogeneous stage ($\int_0^{f_{m2}} \Delta H_{tr}^{tensile} df_m < \Delta H_{tr}^{tensile}$), but still much higher than typical literature values for such alloy $\Delta H_{tr} = 20$ J g^{-1} (Liu and McCormick, 1992) obtained by temperature induced transformation (e.g. DSC). When the phase transformation is temperature induced, the term $\int_{f_{m1}}^{f_{m2}} W'_{mech}\, df_m = 0$, therefore the latent heat should be smaller. Finally, such results have already been observed by Favier and Liu (2000); Liu and Favier (2001) but during the reverse transformation (M→A).

5.2.2.5 Critical remarks on the energy estimation

Although both E_{xx} strain and q_w energy fields are similar, some errors are made during the estimation of s_w when assuming that there are two distinct regions having a constant thermal conductivity k. As presented in Figure 5.27, the bands do not nucleate with a strain level was equal to the peak strain. For the two bands B_1 and B_5 (see Figure 5.19), the slopes were the same, namely, $dE_{xx}/dX = 2.77\%\text{mm}^{-1}$. This value is different from that observed on tubular sample.

In the Band Boundary, the material is neither fully austenitic nor martensitic ($f_m = f_m(M,t)$) and the thermal conductivity is not homogeneously distributed within the sample ($k =$

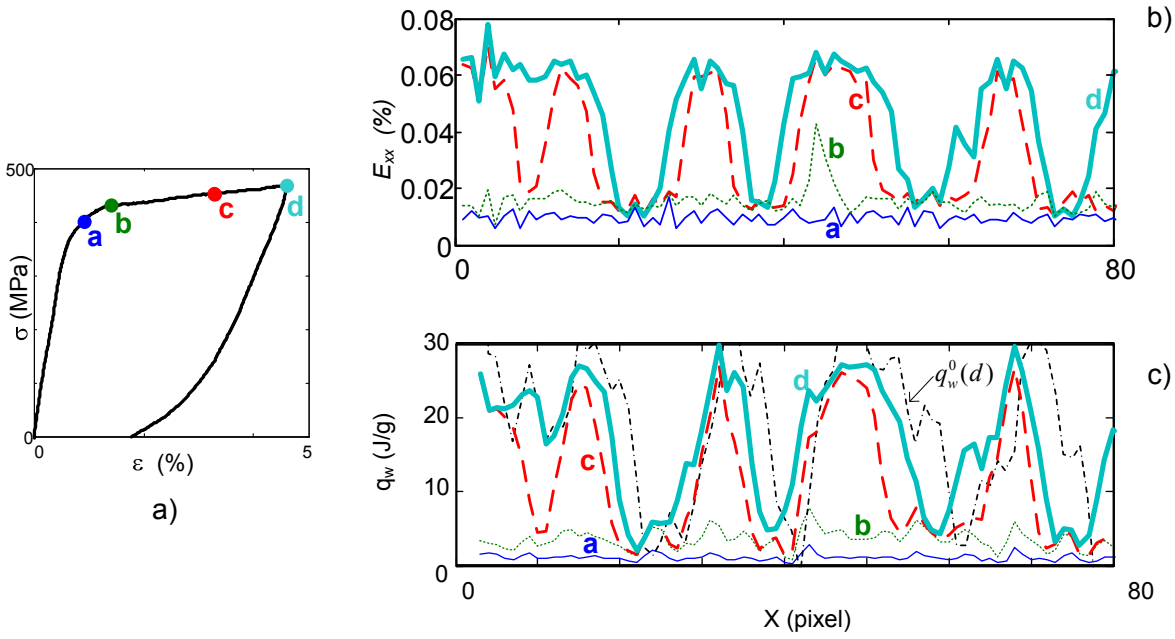

Figure 5.25: *Test P_3. a) Stress-strain curve with the position of four selected profiles during loading stress plateau. b) E_{xx} axial strain profiles. c) Heat energy estimated on the same profiles.*

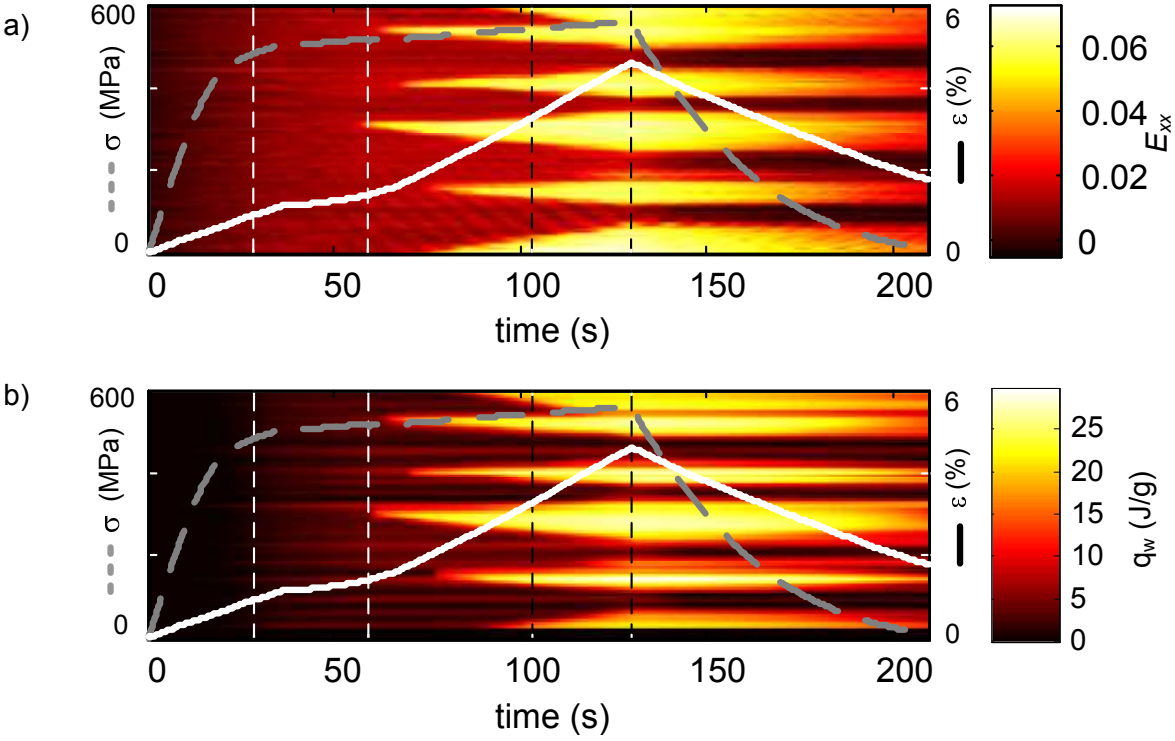

Figure 5.26: *Test P_3: Spatiotemporal representation along the plate profile a) the Green Lagrange $E_{xx}(P)$, b) the energy $q_w(P)$. The grey dotted line represents the nominal stress and the solid line the axial strain $\varepsilon = \Delta l/l_0$.*

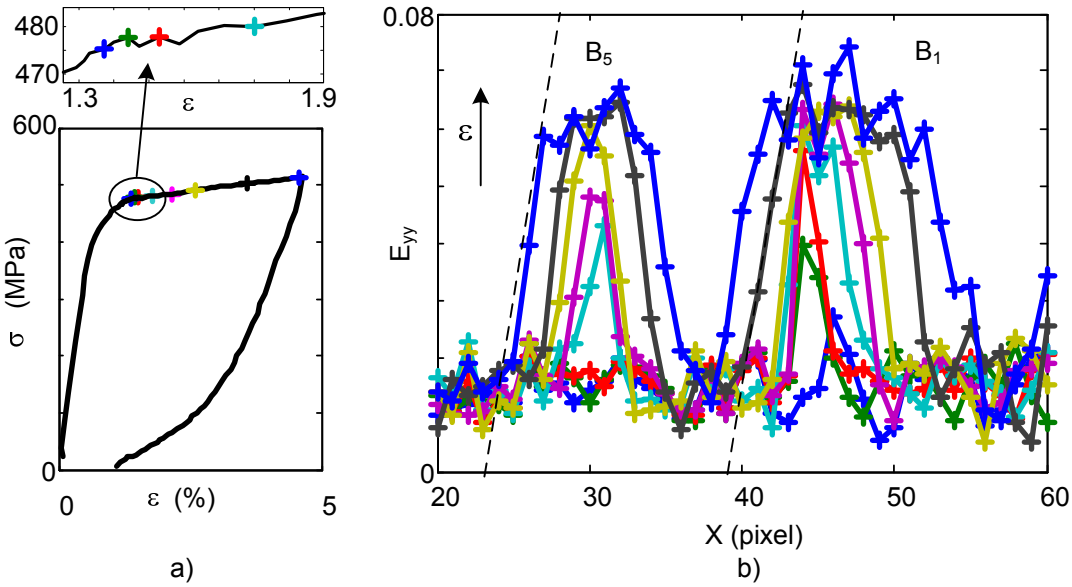

Figure 5.27: *For each selected time represented on the stress-strain curve in a), the profiles of the local strain along a central vertical profile are plotted as functions of the initial coordinates (X). The marker represents the position of the DIC subsets.*

$k(f_m) \neq$ cte) and equation (5.32) cannot be simplified:

$$\begin{aligned} \text{div } \mathbf{q}(M,t) &= -\text{div } \Big(k(f_m(M,t))\ \mathbf{grad}\ T(M,t)\Big) \\ &= -k(f_m(M,t))\ \text{lap}\ T(M,t) - \mathbf{grad}\ T(M,t)\mathbf{grad}\ k(f_m(M,t))), \\ &\neq -k(f_m(M,t))\ \text{lap}\ T(M,t), \end{aligned} \tag{5.32}$$

Due to localization, heat source estimation using a non constant thermal conductivity was not possible for this test but will be investigated in the following Section 5.3 for shear test.

Despite these strong approximations, the method allows one to obtain good qualitative results since strain and energy profiles were similar. Moreover, in Figure 5.25.c, the energy at the end of loading (time d), was almost constant within a localisation band. In this case the spatial synchronisation is particularly important during the time integration of the local heat sources. As an example, the energy q_w^0, estimated without spatial synchronisation, was superimposed with a dotted line at the end of loading (time d) in Figure 5.25.c. This figure shows that the energy q_w^0 was noisier than q_w, the energy peaks q_w^0 did not correspond to strain peaks. The deformed areas could have an energy close to 20 J g^{-1} whereas undeformed area an energy of the order of 5 J g^{-1}. Such observation confirms the importance of the spatial synchronisation to estimate energy when the heat source fields are localised and the position of the particles move during a test.

In order to better estimate the energy, the heat source estimation should be modified in order to take into account the possibility of non homogeneous martensite fraction on the surface of the sample ($k = k(f_m)$). Another possibility would be to create a numerical benchmark such as presented in Chapter 2 to estimate the errors made on the energy estimation.

5.3 Shear tests on plates

Two shear tests have been performed on a two different samples. The experimental procedure and mechanical curve were described in Section 5.1.2. The first test was performed at very low macroscopic strain rate up to $\overline{\gamma}_{xy} = 10\%$ in order to observe the NiTi behaviour under quasistatic shear loading and to check if A→M phase transformation is homogeneous. However, despite the good resolution of the visible images, inappropriate texture size has reduced the DIC resolution and probably induced noise during the DIC estimation. The second test was performed at a faster macroscopic strain rate ($\dot{U}/L_0 = 10^{-2}$ s^{-}1) up to $\overline{\gamma}_{xy} = 4\%$. During this second test, both temperature and strain fields were acquired but with a much smaller resolution.

5.3.1 Homogeneity of the shear test

In order to analyse if shear tests on NiTi are homogeneous or localized, horizontal and vertical profiles were plotted using the same procedure as in Section 3.2.3.4.

5.3.1.1 Test at low macroscopic strain rate: cis_1

Figure 5.28.c presents the shear strain profile γ_{xy} at four selected times during loading (red dot in Figure 5.28.b). The position of the profile selected is plotted in red in Figure 5.28. As represented with the vertical black dashed line, γ_{xy} is almost homogeneous at this strain rate except in a 3 mm large zone close to the edge of the sample.

Figure 5.29.c-f presents, for four selected profiles, the shear strain profiles γ_{xy} at four selected times during loading (red dot in Figure 5.29.b). The position of the selected profiles is plotted in white in Figure 5.29.b. In the middle of the sample, γ_{xy} was almost homogeneous. On the edge of the sample (profile c), the shear strain was heterogeneous and had a small level.

5.3.1.2 Test at high macroscopic strain rate: cis_2

The second shear test was performed at higher strain rate. In order to compare both temperature, heat sources and strain fields during this test, the temporal and spatial synchronisations presented in Section 2.4 have been performed. Heat sources were estimated using the method developed in Section 2.5 by taking a thermal conductivity coefficient of $k_A = 15$ W.m^{-1}.K^{-1}.

Shear strain γ_{xy}, temperature variation θ and heat source fields are presented at four selected times during first loadings of the test in Figure 5.30.

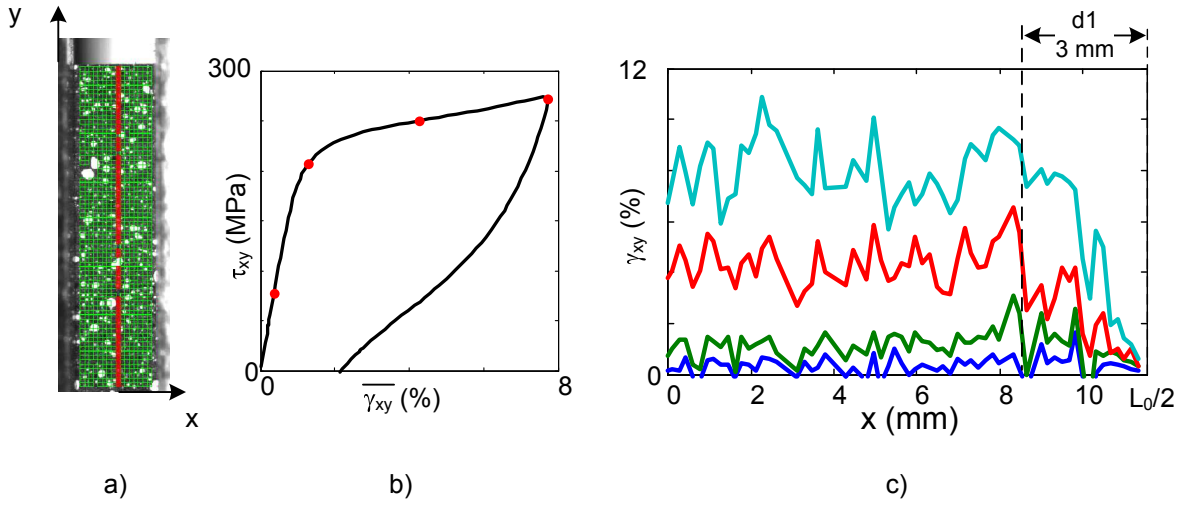

Figure 5.28: *Test cis_1 at $\dot{U}/L_0 = 2.6\ 10^{-5}\ s^{-1}$. Verification of the homogeneity of the shear test. a) Photography of half of the shear sample. b) Stress strain curve. c) γ_{xy} strain profile along the vertical axis plotted in red in a) at the four selected times marked with red bullet in b). The vertical dashed line marks the beginning of the non homogeneous area.*

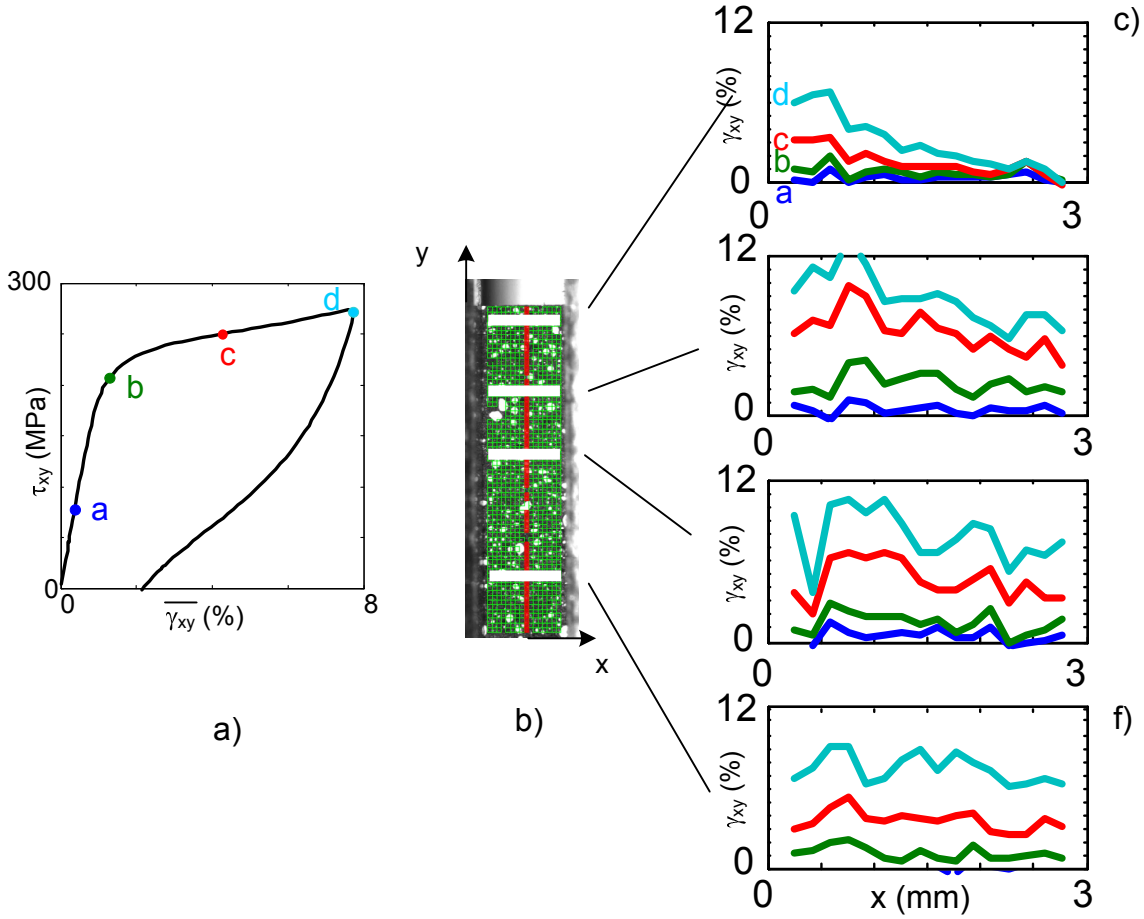

Figure 5.29: *Verification of the homogeneity of the shear test when performed on cis_1 at $\dot{U}/L_0 = 2.6\ 10^{-}5\ s^{-}1$. a) Stress strain curve. b) Photography of half of the shear sample. c-f) γ_{xy} strain profile along the horizontal profiles plotted in white in b) at the four selected times marked with red bullet in a).*

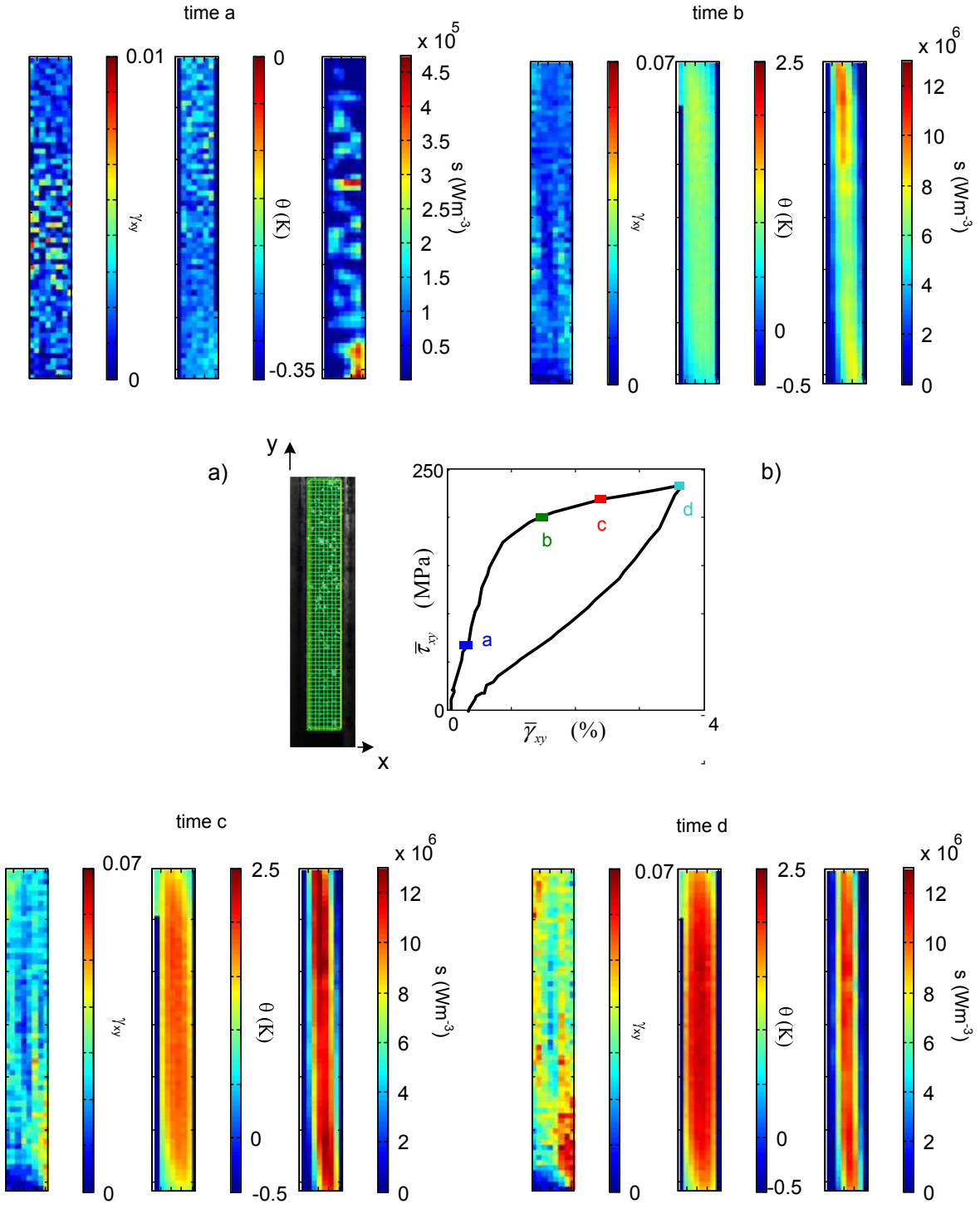

Figure 5.30: *Test cis$_2$: a) Photography of the shear sample with the image correlation grid. b) stress-strain curve ($\overline{\tau}_{xy} - \overline{\gamma}_{xy}$) with selection of four times a-d during loading. The maps represent for each time selected in b, shear strain field γ_{xy}, temperature variation field θ and heat sources fields.*

Figure 5.31 shows the comparison between three vertical profiles at the four times indicated in Figure 5.30.b. The evolution of the shear strain γ_{xy}, the temperature variation θ and the heat source s are respectively plotted in a), b) and c). Figure 5.32 shows the comparison between three horizontal profiles at the four times indicated in Figure 5.30.b. The evolution of the shear strain γ_{xy}, the temperature variation θ and the heat source s are respectively plotted in a), b) and c). At time a, all fields were homogeneous. The temperature decreased homogeneously to -0.3 K. From time b to c, strain, temperature and heat source fields were almost homogeneous in the central area. In the upper left and lower right ends, γ_{xy} and s increased whereas they decreased in the upper right and lower left (see Figures 5.30 and 5.31). The heat sources plotted along the vertical profiles are very similar to shear strain profiles. Along the horizontal direction, the heat sources were not constant and decreased on the side of the sample.

5.3.1.3 Analysis of the homogeneity of the shear test

Regardless of the strain rate, the shear tests results on NiTi were noisier than the feasibility test conducted on a steel material (cf Section 3.2.3). The amplitude $\Delta\gamma$ of the noise was about 2% for strain $\overline{\gamma}$ up to 6% (compared to 1% of noise at the same strain in steel material). Such variation of noise can be explained by texture size and/or the difference of lightning. Further tests would be necessary to analyse these experimental difficulties and find good condition for DIC measurements.

Observation of the shear profiles along the vertical and horizontal lines, showed that for both shear tests, the shear strain is noisy but almost homogeneous in the central area. The shear strain are noisier but very similar to those observed in Section 3.2.3.4 on steel material. Similar behaviour was also observed near the free ends.

From the observation of the temperature field and heat sources during tests cis_2, the sample exhibited exothermic phase transformation (temperature increase up to 2.5 K and the heat sources where positive) during loading. The estimated heat sources where homogeneous along the middle vertical profile in Figure 5.31.d. On the transverse direction in Figures 5.30 and 5.32, the heat sources did not correspond to the shear strain field. Along this direction, only few data were available due to the poor resolution and the rectangular shape of the sample. It is more likely that heat source estimation on the edge were altered by this low number of available data.

In conclusion to this homogeneity analysis, the strain fields were very similar to those observed in Section 3.2.3.4 on steel material but were noisier. No localization phenomena were observed for macroscopic strain below 4 %. The heat source fields were exothermic revealing the presence of martensite phase transformation. Those heat sources were homogeneous along the vertical direction (Figure 5.31) but not along the horizontal one (Figure 5.32).

In spite of the heterogeneity in the transverse direction, we will consider in the future analysis the shear test as homogeneous in strain, temperature and heat sources *in the middle of the sample*.

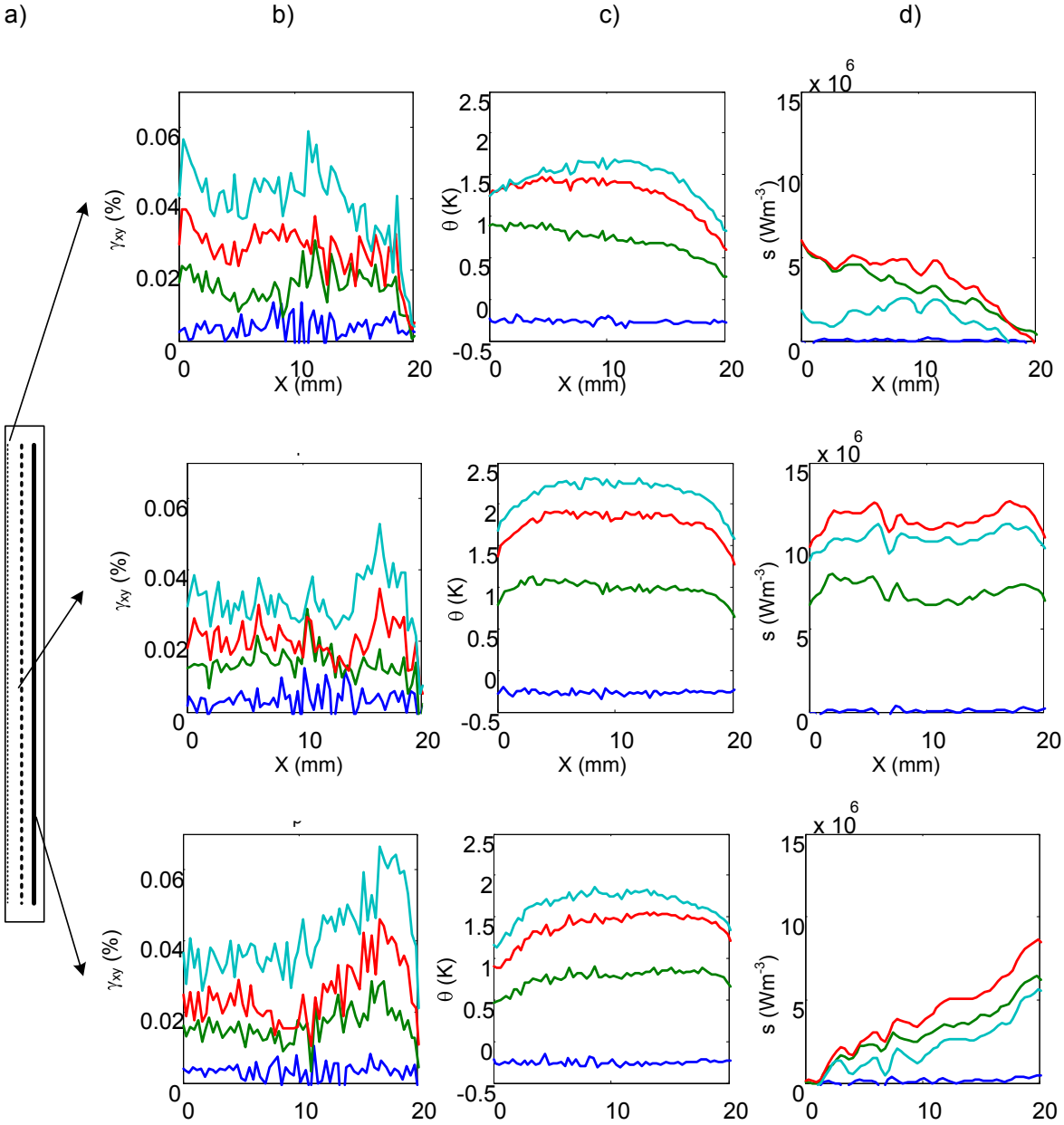

Figure 5.31: *Test cis$_2$: a) Shear sample with the position of the selected profiles. For each profile at the four selected times marked in Figure 5.30.b. b) γ_{xy} strain, c) temperature variation θ, d) heat source profiles.*

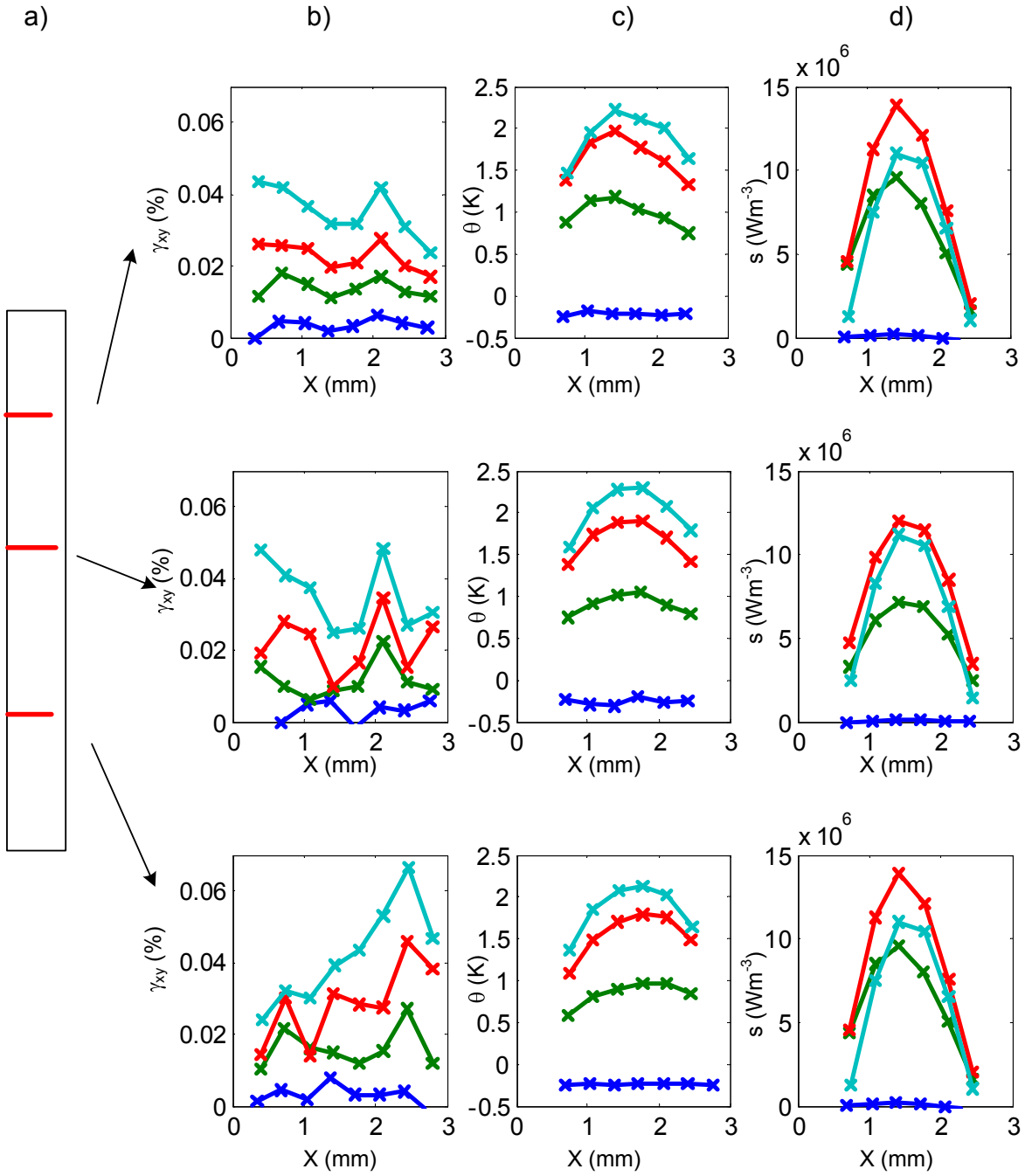

Figure 5.32: *Test cis_2: a) photograph of the shear sample with the position of the selected profiles. For each profile at the four selected times marked in Figure 5.30.b. b) γ_{xy} strain, c) temperature variation θ, d) heat source profiles.*

5.3.2 Macroscopic results and analysis of test cis_2

5.3.2.1 Macroscopic results

As presented in the previous section, the shear test cis_2 was almost homogeneous in the central area of the sample. Therefore the mean shear strain $\overline{\gamma}_{xy}$ and the mean temperature variation $\overline{\theta}$ were estimated with:

$$\overline{\gamma}_{xy} = \frac{1}{s}\int_s \gamma_{xy}\, ds, \tag{5.33}$$

$$\overline{\theta} = \frac{1}{s}\int_s \theta\, ds, \tag{5.34}$$

where s the white section plotted in Figure 5.33.a. The time evolution of the stress $\overline{\tau}_{xy}$, the mean shear strain $\overline{\gamma}_{xy}$ and the mean temperature variation $\overline{\theta}$ are plotted in Figure 5.33.b-d.

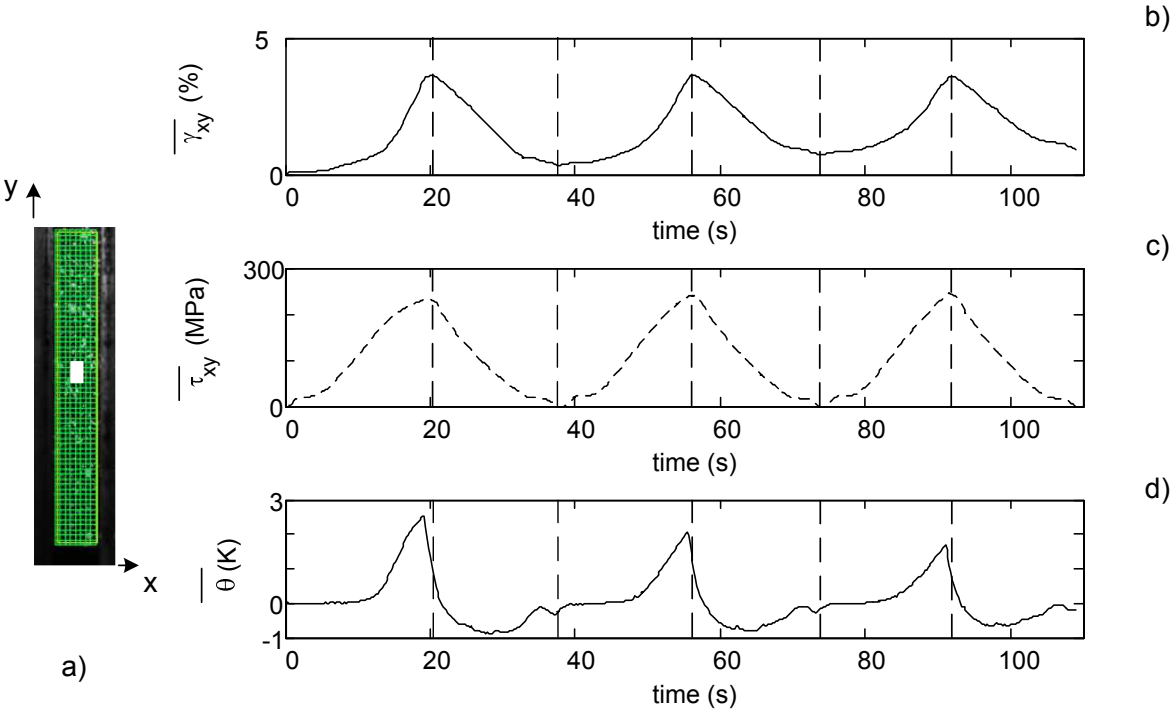

Figure 5.33: *Shear test cis_2: a) position of the selected area s used to estimate the mean values of $\overline{\gamma}_{xy}$ and $\overline{\theta}$. Time evolution of b) the mean shear strain $\overline{\gamma}_{xy}$, c) the shear stress $\overline{\tau}_{xy}$ and d) the mean temperature variation $\overline{\theta}$. The vertical dashed lines represents the beginnings and ends of loadings and unloadings.*

As for tensile tests, the temperature was almost equal to zero at the beginning of each cycle and then decreased and increased up to θ_{max} equal 2.5, 2 and 1.6 K for the first, second and third cycle respectively. At the end of the first cycle the permanent strain was 0.3 %, this value increased to 0.7 % and 0.9% at the end of the second and the third cycle respectively.

5.3.2.2 Heat source estimation

This section will present the macroscopic heat source estimation. The influence of each term of the heat diffusion equation will first be plotted. Then, the latent heat of phase

transformation under shear loading (ΔH_{tr}^{shear}) will be estimated. Finally, using the latent heat value, martensite fraction $f_m(t)$, thermal conductivity $k(f_m(t)) = f_m(t)k_M + (1 - f_m(t))k_A$ and heat sources $\overline{s}$ will be estimated using an iterative process

$$\overline{s}(t+dt) = \rho C \left(\overline{\theta_{,t}}(t+dt) + \frac{\overline{\theta}(t+dt)}{\tau_{th}} \right) - k(f_m(t)) \, \overline{\text{lap}_{2D\ cart}\ \theta}(t+dt), \tag{5.35}$$

with

$$\overline{\theta_{,t}} = \frac{1}{s} \int_s \theta_{,t} \, ds, \tag{5.36}$$

$$\overline{\text{lap}_{2D\ cart}\ \theta} = \frac{1}{s} \int_s \text{lap}_{2D\ cart}\ \theta \, ds, \tag{5.37}$$

Influence of each term of the heat diffusion equation

Figure 5.34 represents the heat sources $\overline{s_A}$ estimated with a thermal conductivity $k = k_A$ and the influence of each term of the heat diffusion equation (2.53) when the thermal conductivity is $k_A = 18$ W m^{-1} K^{-1}. Although, this shear test did not present localization phenomena such as those observed during tensile test, the temperature profiles along the horizontal direction presented strong gradients (see Figure 5.32.b). Those temperature gradients were mostly due to conduction phenomena with the grips. Therefore, as observed in Figure 5.34, the heat sources depended mostly on the term "$-k \, \overline{\text{lap}\,(\,\theta)}$". The Laplacian operator was not negligible and the value chosen for k has a strong influence on the estimated heat source values.

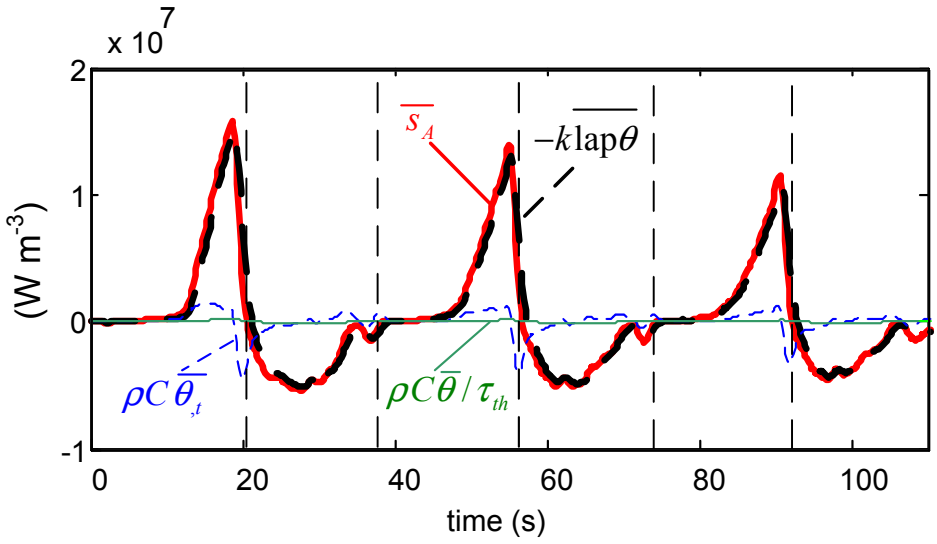

Figure 5.34: *Evolution of the heat sources s_A and its different terms estimated with the austenite thermal conductivity $k_A = 18$ W m^{-1} K^{-1}. The vertical lines represent the beginnings and ends of loading and unloading.*

Estimation of ΔH_{tr} under shear loading

As for tensile test, we assume that each time, the deformation is due to elasticity of the lattice and an additional phenomenon associated with phase transformation; so that:

$$\dot{\overline{\gamma}}_{xy} = \dot{\overline{\gamma}}_{el} + \dot{\overline{\gamma}}_{tr} \qquad \text{with} \quad \dot{\overline{\gamma}}_{tr} = \dot{f}\,\Delta\gamma_{tr}, \qquad \dot{\overline{\gamma}}_{el} = \frac{\dot{\overline{\tau}}_{xy}}{G} \quad \text{and} \quad G = \frac{E}{2(1+\nu)} \tag{5.38}$$

where $\dot{\overline{\gamma}}_{tr}$ the strain due to matensite phase transformation and $\Delta\gamma_{tr} = 12\%$ the shear strain for complete transformation (Orgéas and Favier, 1998). Excluding the heat sources due to intrinsic dissipation ($\dot{\overline{q}}_{plast} \approx 0$) and thermoelasticity ($\dot{\overline{q}}_{thel} \approx 0$), we assume that, heat sources $\dot{\overline{q}} = \dot{\overline{s}}/\rho$ are only due to phase transformation heat sources $\dot{\overline{q}}_{tr}$ so that:

$$\dot{\overline{q}} = \dot{\overline{q}}_{tr} \qquad \text{with} \quad \dot{\overline{q}}_{tr} = \dot{f}\,\Delta H_{tr}^{shear}. \tag{5.39}$$

Therefore,

$$\frac{\Delta H_{tr}^{shear}}{\Delta\gamma_{tr}} = \frac{\dot{\overline{q}}_{tr}}{\dot{\overline{\gamma}}_{tr}} = \frac{\dot{\overline{q}}}{\dot{\overline{\gamma}}_{xy} - \frac{\dot{\overline{\tau}}_{xy}}{G}}. \tag{5.40}$$

ΔH_{tr}^{shear} is plotted as function of the mean shear strain $\overline{\gamma}_{xy}$ during the first cycle in Figure 5.35. At the beginning of loading, we can observe a first plateau around 90 J g^{-1}; then, a second one at $\Delta H_{tr}^{shear}/\Delta\gamma_{tr} = 260$ J g^{-1} when $\overline{\gamma}_{tr} \approx 1.3\%$. After 1.7 % $\Delta H_{tr}^{shear}/\Delta\gamma_{tr}$ started increasing again.

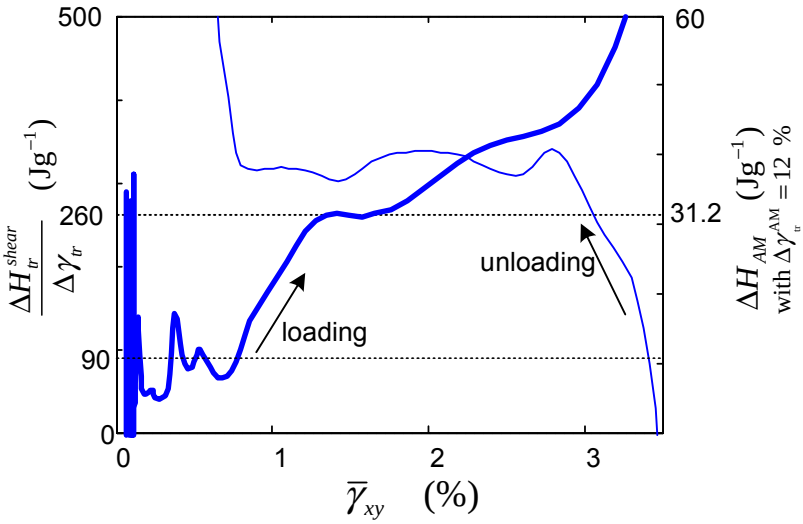

Figure 5.35: *Time evolution of the latent heat of transformation $\Delta H_{tr}^{shear}/\Delta\gamma_{tr}$. The scale on the right shows the value of ΔH_{tr}^{shear} if the phase transformation is assumed to be A-M.*

As noted in the comment of Figure 5.12 during the homogeneous stage of tensile tests, this first plateau when $\Delta H_{tr}^{shear}/\Delta\gamma_{tr} = 90$ J g^{-1} can be associated with the presence of precursor phenomena.

Concerning the second plateau, it is worth noting that in the analysis performed during homogeneous stage of tensile test in Section 5.2.1, the maximum strain was $\varepsilon \approx 1.2\%$ and

we estimated nearly 9 % of martensite fraction transformed at the end of the homogeneous stage. During this shear test, the maximum shear strain at the end is nearly 3.5 %. It is therefore more likely that the martensite fraction is be much higher. Since the heat source estimation is strongly influenced by thermal conductivity, after $\overline{\gamma}_{xy} \approx 1.2\%$, the heat sources are overestimated by using the austenite thermal conductivity ($k_A > k_M$). Therefore, the value of $\Delta H_{tr}^{shear}/\Delta\gamma_{tr}$ should be estimated for strain around 1.3 % rather than 3 %. As shown by the horizontal dashed line, $\Delta H_{tr}^{shear}/\Delta\gamma_{tr} = 260$ J g^{-1}, which leads to $\Delta H_{tr}(shear) \approx 31.2$ J g^{-1}. A similar value of ΔH_{AM} than during tensile test was obtained. This value will be used in the following section to estimate the thermal conductivity, heat sources and martensite fraction.

Estimation of $k(f_m(t))$ and $\overline{s}(t)$

Since the shear test does not present localised phase transformation, it was supposed to be homogeneous. Hence, as presented in Section 2.5.6, the term div $\mathbf{q}(M,t)$ can be estimated without doing any approximation with eq. (2.64):

$$\text{div } \mathbf{q}(M,t) \quad = -\left(f_m(t)\, k_M + (1 - f_m(t))\, k_A\right) \text{lap } T(M,t). \tag{5.41}$$

As presented in Section 5.2.1, the martensite fraction f_m is a function of the heat sources $\overline{s} = \rho\overline{\dot{q}}_{tr}$:

$$f_m(t) = \int_0^t \dot{f}_m(u)du, \quad \text{with} \quad \dot{f}_m(t) = \frac{\overline{\dot{q}}_{tr}}{\Delta H_{tr}^{shear}} \approx \frac{\overline{\dot{q}}_{tr}}{\overline{\dot{\gamma}} - \frac{\overline{\dot{\tau}}_{xy}}{G}}. \tag{5.42}$$

Therefore, $f_m(t)$, $k(f_m(t))$ and $\overline{s}(t)$ were estimated step (dt) by step with the following procedure:

- at time $t = 0$

$$\begin{aligned} \dot{f}_m(0) &= 0 && (5.43)\\ k(0) &= k_A && (5.44)\\ \overline{s}(0) &= \overline{s}_A(0) && (5.45)\\ \overline{s}(0) &= \overline{s}_A(1) && (5.46) \end{aligned}$$

- at each time t,

$$\begin{aligned} \dot{f}_m(t) &= \frac{1}{\rho}\frac{\overline{s}(t)}{\Delta H_{tr}^{shear}} && (5.47)\\ k(f_m(t)) &= (1 - f_m(t))\ k_A + f_m(t)\, k_M && (5.48)\\ \overline{s}(t + dt) &= \rho C(\overline{\theta}_{,t}(t + dt) + \frac{\overline{\theta}(t + dt)}{\tau_{th}}) - k(f_m(t))\ \overline{\text{lap}_{2D\,cart}\ \theta}(t + dt) && (5.49)\\ & && (5.50) \end{aligned}$$

The evolution of the thermal conductivity $k(f_m((t))$ is plotted in Figure 5.36.a. The two horizontal lines stand for the austenite and martensite thermal conductivity. This figure shows that the thermal conductivity was between 15 to 18 W m^{-1} K^{-1}. The material remained

mostly austenitic. The comparison of the heat sources $\overline{\dot{q}}_A$ and $\overline{\dot{q}}$ estimated with the thermal conductivity k_A and $k(f_m(t))$ respectively, plotted in Figure 5.36.b, shows that at the end of the first loading the heat sources were overestimated by 12 % when using the austenite thermal conductivity. The heat sources were constant and nearly equal to zero at the beginning of the test. Then they increased linearly up to $\overline{\dot{q}}_{max} \approx 2.19$ W g^{-1}. This value decreased with cycling: $\overline{\dot{q}}_{max}$(cycle 2)≈1.90 W g^{-1}, $\dot{q}_{max}$(cycle 3)≈1.55 W g^{-1}.

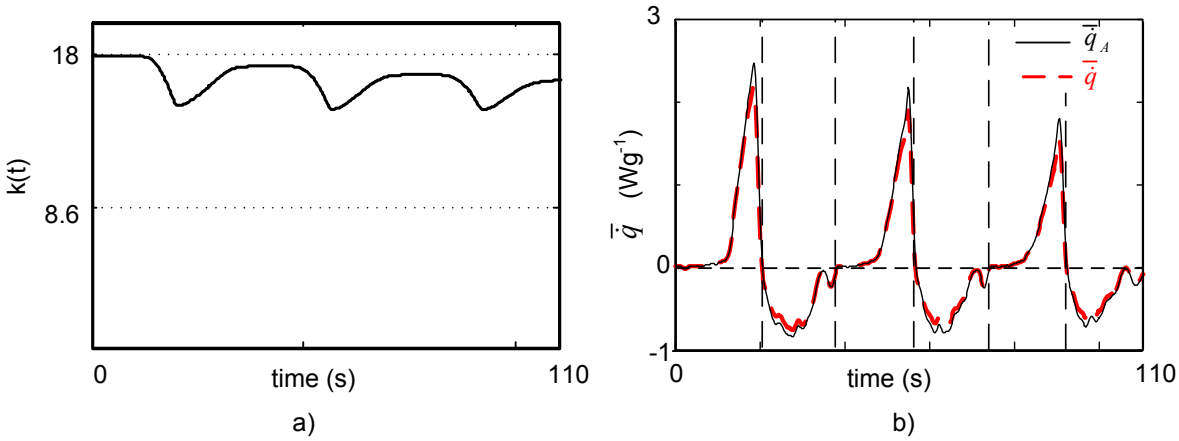

Figure 5.36: *Test cis$_2$: a) time evolution of $k(f_m(t))$. The two horizontal lines are the upper and lower bound, $k_A = 18$ $W.m^{-1}.K^{-1}$ and $k_M = 8.6$ $W.m^{-1}.K^{-1}$ respectively. b) Comparison of the influence of the thermal conductivity on the heat source estimation $\overline{\dot{q}} = \overline{s}/\rho$ obtained with $k(f_m(t))$, the value of heat sources $\overline{\dot{q}}_A$ obtained with $k = k_A$ have also been reported.*

Figure 5.37 shows the change of the heat sources $\overline{\dot{q}}$ and the energy q vs. the mean shear strain $\overline{\gamma}_{xy}$ (a-b) and shear stress $\overline{\tau}_{xy}$ (c-d).

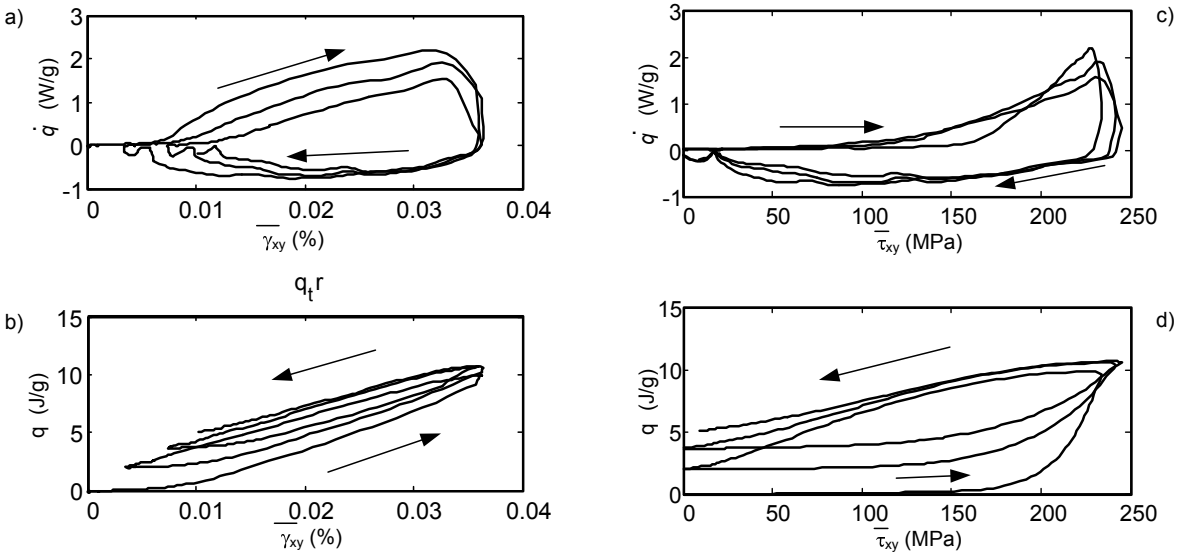

Figure 5.37: *Test P_1. a) Heat sources $\overline{\dot{q}}$ estimated with $k(f_m(t))$ as functions of the mean shear strain $\overline{\gamma}_{xy}$ (a) and the mean shear stress $\overline{\tau}_{xy}$ (c). Energy obtained by time integration of the heat sources as functions of the mean shear strain $\overline{\gamma}_{xy}$ (b) and the mean shear stress $\overline{\tau}_{xy}$ (d).*

The behaviour was much different from that during tensile tests (Figure 5.11). However, as presented in Figure 5.32, the estimated heat sources were not homogeneous along horizontal

profiles. Further studies with a better estimation of the Laplacian operator are necessary to be more confident on those first results.

5.4 Conclusions of Chapter 5

The analysis of **tensile tests** through the analysis of strain, heat sources and energy fields enables us to confirm the nature of the deformation.

- In the homogeneous stage, it leads to homogeneous martensite phase transformation that started as soon as the test starts. Moreover, precursor phenomena of martensitic transformation were detected at the beginning of the homogeneous loading. Since this alloy exhibited no R-phase, it was possible to estimate that, regardless of the test strain rate, the martensite fraction was nearly 9 % at the end of the homogeneous loading and 0.25 % at the end of the first cyclic loading.
- Thermomechanical analysis during the homogeneous stage has confirmed that the latent heat of stress induced martensitic transformation was 30 J g^{-1} and that the dissipated heat was negligible compared to the phase transformation heat.
- Although temperature fields were diffuse, heat sources exhibit narrow peaks in the same location as strain gradients (initiation of a band or band widening). In the remainder of the sample the heat sources were almost equal to zero.
- Due to localization phenomena, both austenite and martensite phases were present within the sample, estimated heat sources using thermal conductivity of austenite and martensite give upper and lower bound values of the heat sources. To better estimate the heat sources and allow a quantitative analysis, a first proposition of weighted heat sources was proposed. Further work is necessary to better estimate those heat sources when the test presents localised phase transformation.
- Energy estimation have been computed by time integration of the heat sources. They were very similar to strain fields and confirmed the nature of the localization, namely, martensitic transformation. Although the phase transformation was not total inside the bands, the energy estimated q_w was around 27 J g^{-1}, which was smaller than the A→M latent heat for a complete phase transformation estimated during the homogeneous stage (30 J g^{-1}).
- Unloading was not localised and was very different from what was observed for tubes (cf Chapter 4). Other experiments are necessary to better analyse and understand the unloading response.

The conclusion of the analysis of the **shear tests** are:

- Analysis of the homogeneity of the shear tests have confirmed that shear tests do not present strong strain localization phenomena like those observed during tensile tests for macroscopic strains below 4 %.
- The latent heat of transformation under shear loading was estimated to be near 31 J g^{-1}. This value is similar to that under tensile loading for the same plate.

- Mainly due to the small gauge length and conduction with the grips, the heat sources was mostly influenced by the term "k lap(θ)". Moreover, although homogeneous in the vertical direction, they presented strong gradients in the horizontal direction. Due to the low number of data in this direction (25 pixels) and error that are induced by the FFT periodic widening, no conclusion can be stated on the homogeneity of the heat sources in this direction and further tests, especially with a better spatial resolution along the horizontal axis would be necessary.
- Considering the heat sources homogeneous in the vertical direction, thermal conductivity depending on the martensite fraction $k(f_m(t))$ was estimated and used to evaluate heat sources with a better accuracy.

CHAPTER 6

Experimental estimation of heat sources to analyse localization

Table of contents

This chapter will present heat source estimation and analysis, using the same method as in Section 5.2.2, on the first test performed on tube T_2. After presenting the heat source results estimated in cylindrical coordinates, we will discuss the impact of thermal conductivity coefficient chosen and estimate "weighted" heat sources using the same approximation as in Section 5.2.2. Finally, the energy will be calculated by time integration of heat sources and compared to the strain fields.

6.1 Results and heat source estimation

Heat source estimations were achieved for the first tensile test (denoted by $T2_1$) performed on tube T_2 at imposed nominal strain rate $\dot{U}/L_0 = 2.3\ 10^{-4}\text{s}^{-1}$. The tube characteristics of this sample are presented in Section 3.1.3.2 and the test was detailed in Section 4.3. Strain fields were calculated from the displacement fields at an acquisition frequency $f_v = 1/3$ Hz,

with a DIC spatial resolution of the order of 0.7×0.7 mm^2 (Figure 6.1.a). Temperature fields were recorded at an acquisition frequency $f_{IR} = 3$ Hz, with a spatial resolution (pixel size) close to 0.4×0.4 mm^2.

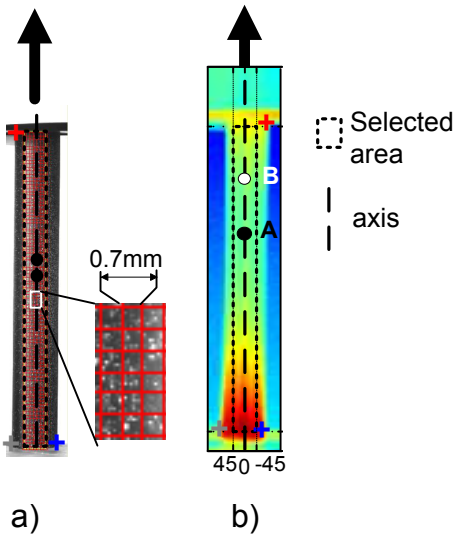

Figure 6.1: *a) Visible photography of tube $T2_1$ with the image correlation grid. b) Infrared image of the same tube and position of the selected area used to estimated the heat sources. The "+" shows the position of the characteristic points used to estimate the transformation matrix and perform the spatial synchronisation. The vertical dashed axis is the position of the tube axis.*

Specific heat sources s_i^0 (in Wm^{-3}) were estimated using image processing presented in Section 2.5.5 from the temperature fields $\theta^0 = T(x,\alpha,t) - T(x,\alpha,0)$ using the diffusion equation expressed in spatial coordinate system[1]:

$$s_i^0 = \rho C(\ \theta^0_{,t} + \frac{\theta^0}{\tau_{th}}) - k\ \mathrm{lap}_{2Dcyl}\ \theta^0, \tag{6.1}$$

with:

$$\mathrm{lap}_{2cyl}\ \theta^0 = \ \theta^0_{,xx} + \frac{1}{R^2}\ \theta^0_{,\alpha\alpha}. \tag{6.2}$$

The characteristic time reflecting heat losses both by convection through the tube surfaces (inner and outer) was estimated using the method presented in Section 2.5.5.1. As shown in Figure 6.2, τ_{th} =102 s. Due to the cylindrical shape of the tube, the observation area was restricted to 45° on each sides of the tube axis, as presented in Figure 6.1.b.

Heat sources were calculated for every particle P using the spatial synchronisation. In order to analyse this test, temperature $\theta(P,t)$, heat sources $s_i(P,t) = \rho\dot{q}_i(P,t)$ and kinematic fields were then estimated for every particle P using the spatial synchronisation explained in Section 2.4 at the infrared frequency f_{IR} on the DIC grid (i.e. at a spatial resolution of 0.7 mm). Figure 6.3 shows, at five different times, Green-Lagrange E_{xx} strain field, temperature variation field θ and heat sources, denoted by s_M, estimated using $k = k_M = 8.6$ W.m^{-1}.K^{-1}.

Figure 6.4 represents the spatiotemporal evolution of E_{xx}, θ and s_M along the vertical axis of

[1]In all this chapter, temperature T, temperature variation θ, heat sources s, and energy q will be indicated with superscript "0" when expressed for spatial point and without superscript when expressed for material point (after performing the spatial synchronisation).

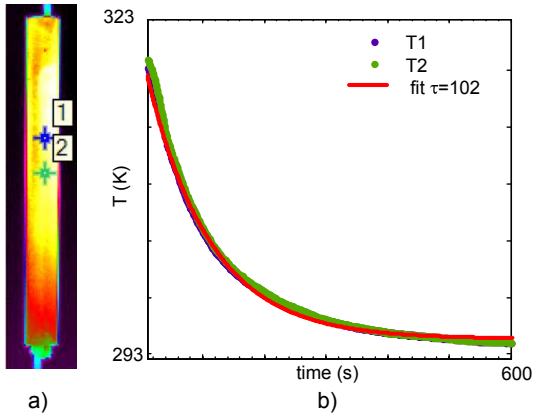

Figure 6.2: *Observation of self cooling of tube T2 held by an insulated rope. a) Infrared image of the tube with the position of the two virtual thermocouples. b) Self cooling and curve fitting using* $\tau_{th} = 102\ s$.

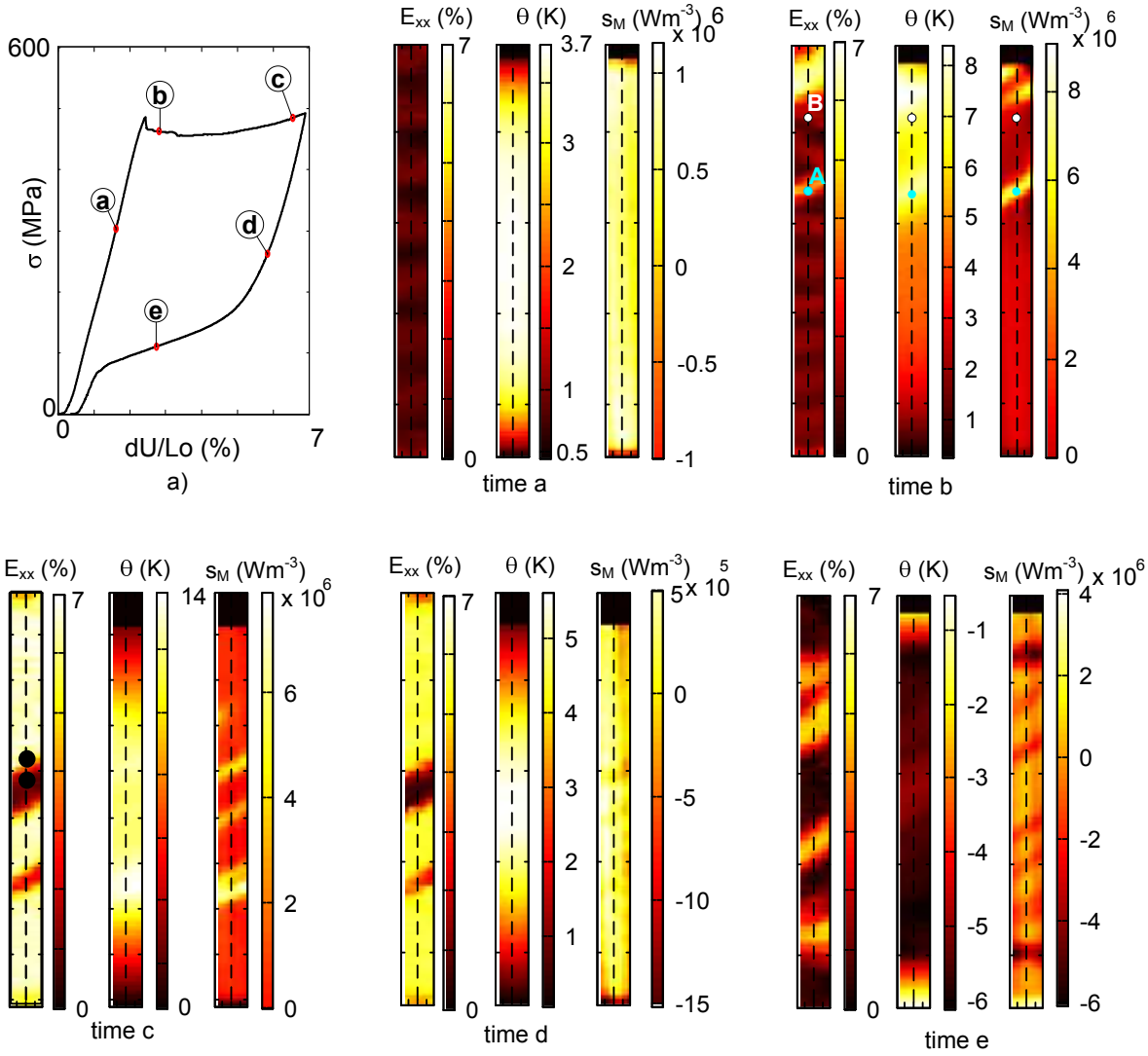

Figure 6.3: *Comparison of the thermal and kinematic fields at several time during test* $T2_1$. *a) Nominal stress strain curve and position of the five selected times. At the selected time marked in a, colored map of the synchronised data: Green-Lagrange* E_{xx} *axial strain field, temperature variation field* θ *and heat sources field* s_M *estimated using* $k = k_M$.

the tube. This representation allows us to have an overview of the test that can be separated into 4 stages depicted in this figure.

Several comments on these first qualitative results can be made (Figures 6.3 and 6.4):

- **stage 1, time** a**:** The heat sources were homogeneous and exothermic in the all sample which confirms the approximations made in Section 4.3 by using a homogeneous formulation;
- **stage 2, time** b **and** c (initiation and propagation of the strain localization): time b corresponded to the beginning of the stress plateau, when the helical band initiated near the upper grip had reached point A. As for plates, the heat source estimation, taking into account heat conduction, increases the contrast and allows to observe better the localised phase transformation, namely, near the top grip, two heat sources fronts emphasise the propagation of the band and its widening (see Figures 6.3, 6.4 and 6.5). Such a localisation of the transformation is detected in the other zones where the helical band passed, but with different velocity as enhanced in scheme of Figure 6.5.b. Time c was at the end of the stress plateau. The temperature variation was about 14 K but very diffuse therefore very difficult to analyse. Like time b, the heat sources allow a better understanding of the kinematics of the transformation.
- **stage 3, time** d**:** in the beginning of unloading, the strain field was heterogeneous but decreased homogeneously. Conversely, heat sources were homogeneous and negative, revealing homogeneous reverse transformation;
- **stage 4, time** e**:** during the unloading stress plateau, the strain field was once again localised. The position of the strain gradients corresponded to negative heat sources localization, whereas the temperature field was below room temperature and again difficult to analyse.

Figure 6.6 shows three axial strain and heat sources profiles, along the vertical axis, during loading (times a, b, c). The heat sources profiles along the vertical axis of the sample are compared to the axial strain profiles in Figure 6.6.b and c at times a, b and c respectively. During the stress plateau (stage 2, time b and c), the strain fields are strongly localised. The heat source profiles show clearly peak values and gradient at the same position as the strain step. Moreover, the heat source peaks have a higher amplitude when the band is propagating rather than widening. Like in plates, the heat source peaks correspond to the position of the more active phase transformations.

6.2 Toward a better heat source estimation

6.2.1 Influence of thermal conductivity on the heat source estimation

During the stress plateau, phase transformation was strongly localised. The less deformed areas were mostly austenitic ($k = k_A$), the highly deformed areas were mostly martensitic ($k = k_M$). The intermediate area were a mixture of both austenite and martensite. Like

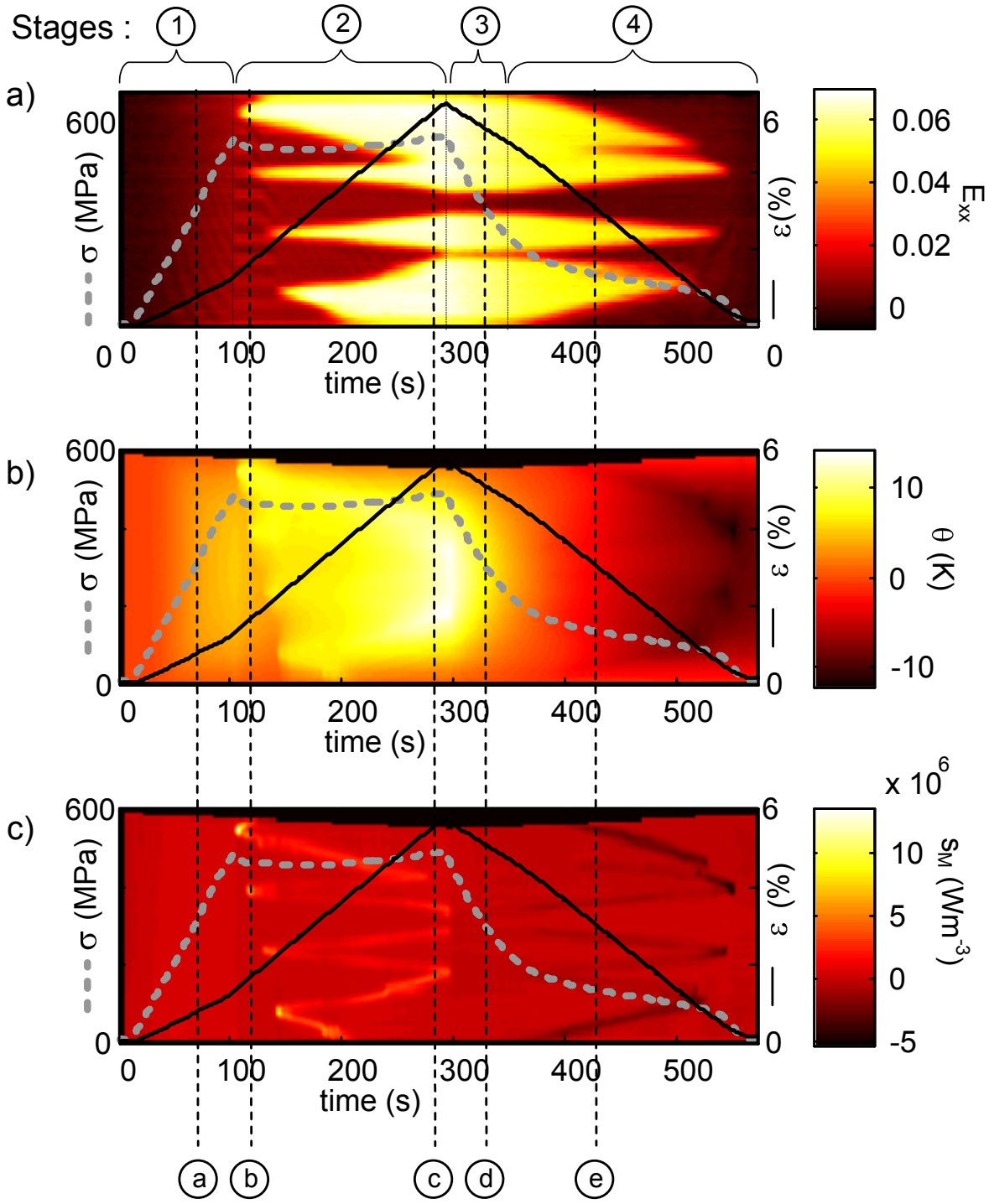

Figure 6.4: *Spatiotemporal representation along the tube axis of: a) Green Lagrange axial strain E_{xx}, b) temperature variation field θ and c) heat sources fields s_M. The grey dotted line represents the nominal stress and the continuous line the strain ε.*

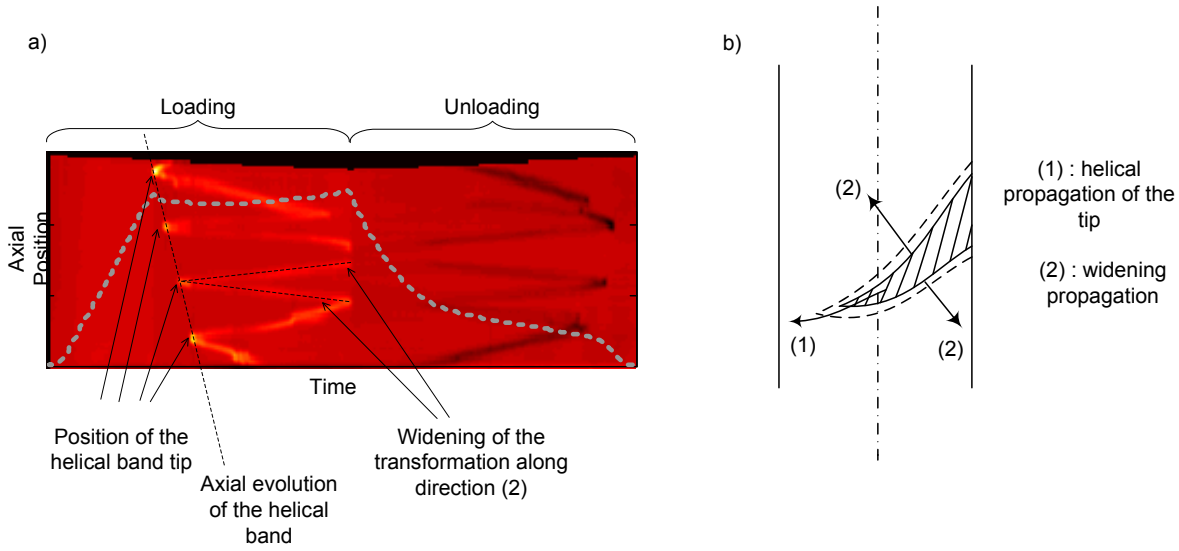

Figure 6.5: *a) Spatiotemporal evolution along the tube axis of the heat sources and evolution of the nominal stress (same images as in Figure 6.4.c. Such a representation clearly enhances the kinematics of the phase transformation. b) Schematic view of the phase transformation showing the two modes: (1) propagation of the tip and (2) widening (see also Figure 4.22).*

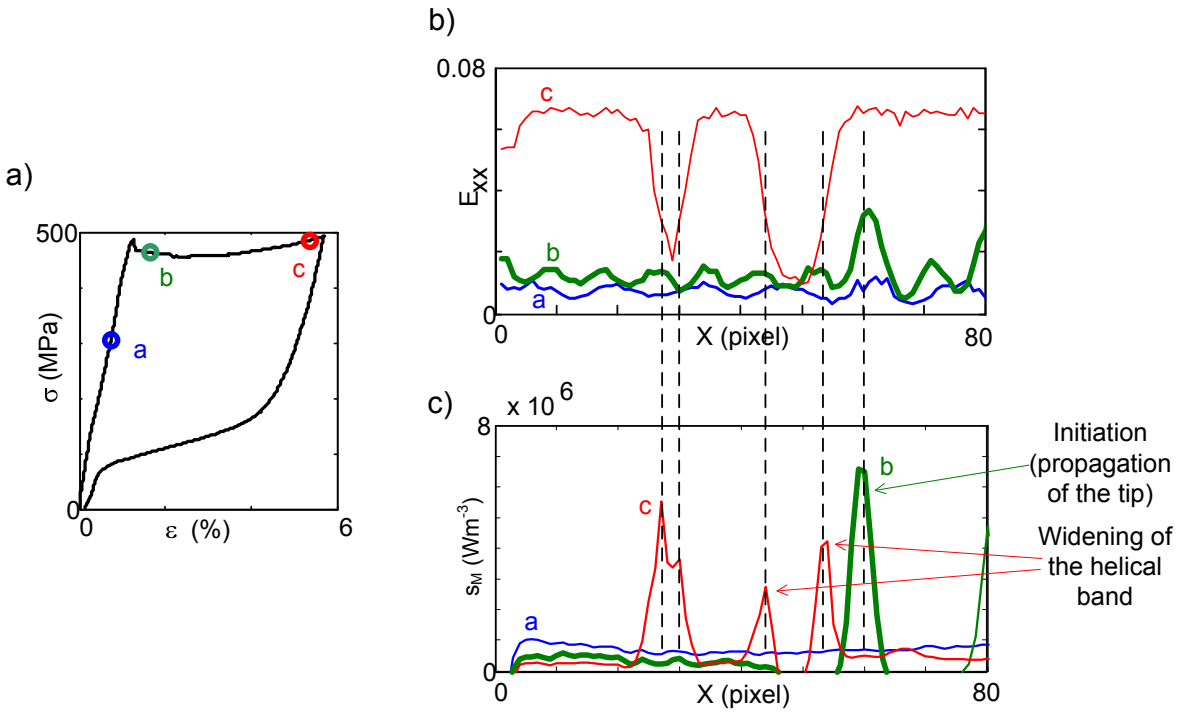

Figure 6.6: *a) Stress-strain response of test $T2_1$ with the position of three selected profiles. b) Axial strain axial profiles (E_{xx}). c) Heat sources profiles (s_M) estimated at the same times.*

for heat sources estimated on plates in Section 5.2.2, heat sources estimated with $k = k_M$, as presented previously in part 6.1, are lower bounds of the real ones and heat sources estimated with $k = k_A$ (remember that $k_A > k_M$) can be considered as upper bound values. It is expected that the real values lie between these two bounds.

Figure 6.7 shows for two selected particles A and B (see position in Figure 6.3 time b), the influence of value of the thermal conductivity coefficient on the heat source estimation. As for plates, the thermal conductivity chosen value k has a strong impact on the heat sources near the strain gradients (Figure 6.7.e) and at the beginning of unloading. In those two cases the temperature profile is strongly heterogeneous, and the Laplacian operator term ($\mathrm{Lap}_{2Dcyl}\ \theta$) is important. Therefore, the value of k chosen strongly affected the heat source estimation. Only heat sources estimated at the beginning of loading were not influenced by the choice of k; as already observed in Chapter 4 the Laplacian was negligible in this stage.

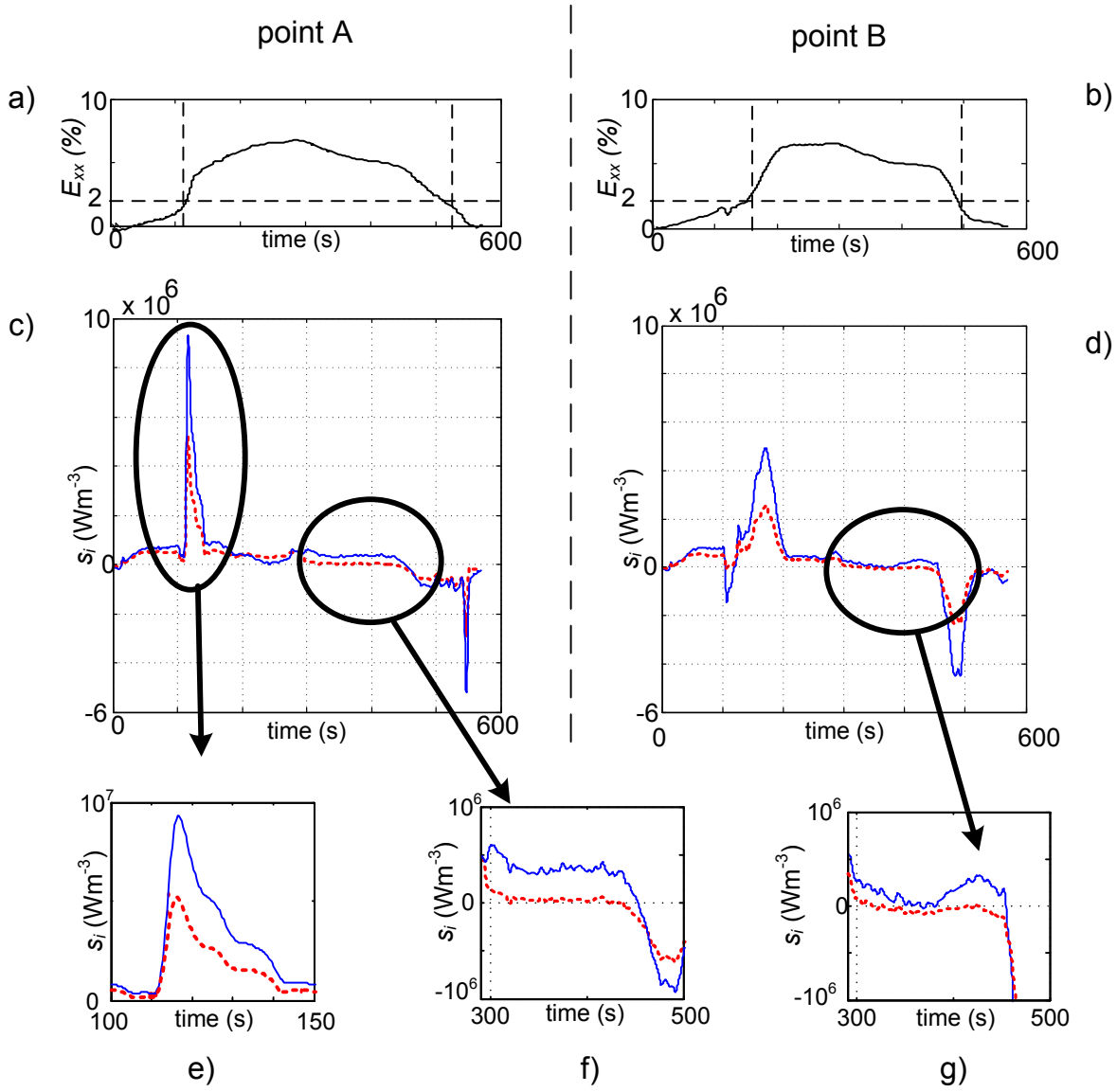

Figure 6.7: *Influence of the thermal conductivity coefficient k on the heat source estimation for two points A and B (see Figure 6.3 time b). a-b) Temporal evolution of the Green Lagrange axial strain $E_{xx}(A)$ and $E_{xx}(B)$. c-g) Temporal evolution of the heat source estimation using $k = k_A$ (solid line) and $k = k_M$ (dashed line).*

6.2.2 Proposition of estimation of "weighted" heat sources

As proposed for plate sample P_3 in Section 5.2.2, depending on the local strain state, the "weighted" heat sources s_w will be estimated with:

$$s_w = s_A \quad \text{if} \quad E_{xx} < 0.04 \quad \text{(white area in Figure 6.8.b)} \tag{6.3}$$

$$s_w = s_M \quad \text{if} \quad E_{xx} \geq 0.04 \quad \text{(grey area in Figure 6.8.b)} \tag{6.4}$$

Figure 6.8 shows the position of the two regions on the sample at time b (beginning of the stress plateau) and on a spatiotemporal representation along the vertical axis of the tube. Due to strong localization phenomena, the two areas were well defined.

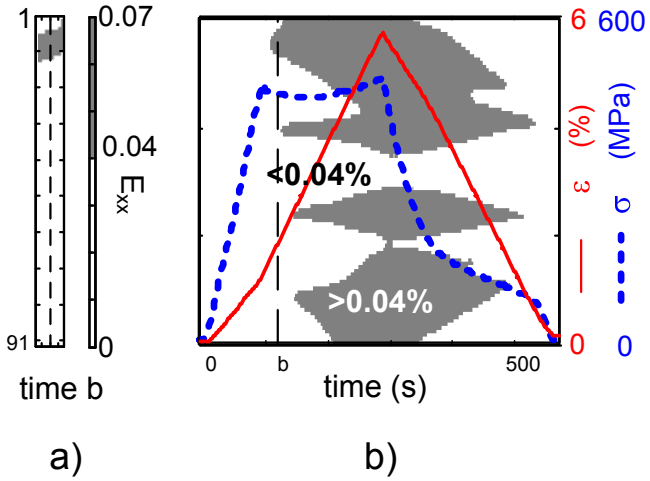

Figure 6.8: *Position of the less deformed region ($E_{xx} < 0.04$, white) associated with austenite phase and the high deformed region ($E_{xx} > 0.04$, grey) associated with martensite phase. View of these positions: a) on the sample at the selected time b, b) using a spatiotemporal representation along the vertical axis of the tube. The stress σ and the strain ε are plotted in dashed and solid lines, respectively.*

6.3 Heat energy estimation

From s_w it is possible, for each particle $P(x, \alpha, t)$ of initial coordinate (X, α_0), to estimate the heat energy ($q_w(P)$ in J g^{-1}) by a time integration, for each particle P of initial coordinates (X, α_0):

$$q_w(P,t) = \frac{1}{\rho} \int_0^t s_w(P,u)\, du. \tag{6.5}$$

Figure 6.9 shows three strain and energy profiles along the vertical axis during loading (time a, b, c). The energy profiles are almost identical to the strain ones and reach, at the end of the stress plateau, a maximum near 36 J g^{-1} in the deformed area.

Spatiotemporal evolutions of E_{xx} and q_w along the same axial profile are plotted in Figure 6.10. Since at the end of the loading the transformation was not completed, a reduced zone in the middle of the sample was still autenitic at time c (Figures 6.9.c and 6.10.b). The energy in this area is around 7 J/g. In spite of these qualitative agreements between these two separate fields, some errors are made during the approximation of two distinct regions with a constant thermal conductivity k (see Section 5.2.2.5).

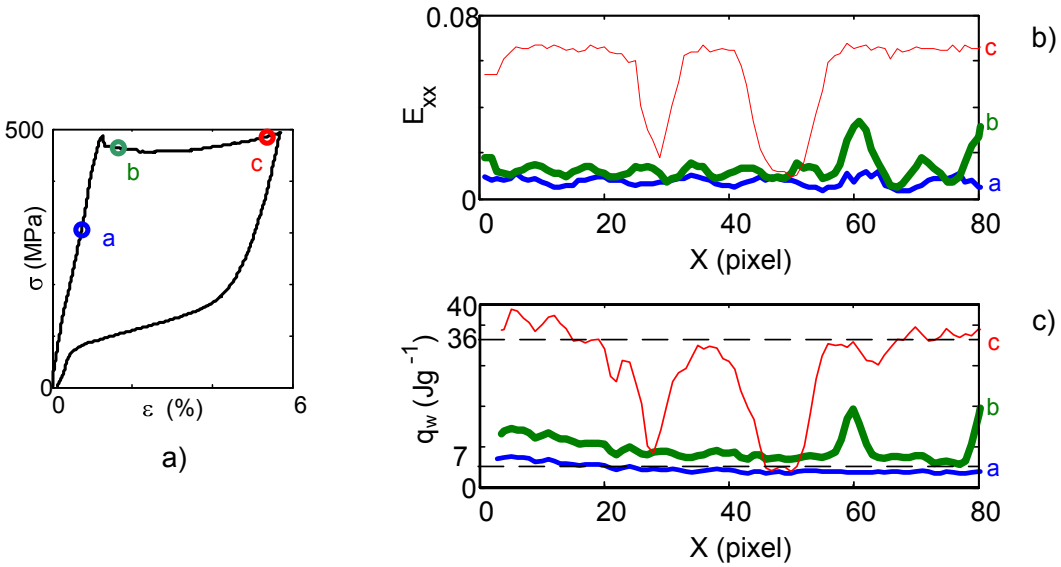

Figure 6.9: *a) Stress strain curve of test $T2_1$ with the time of three selected profiles. b) E_{xx} strain along an axial profile. c) Heat energy q_w estimated on the same profiles.*

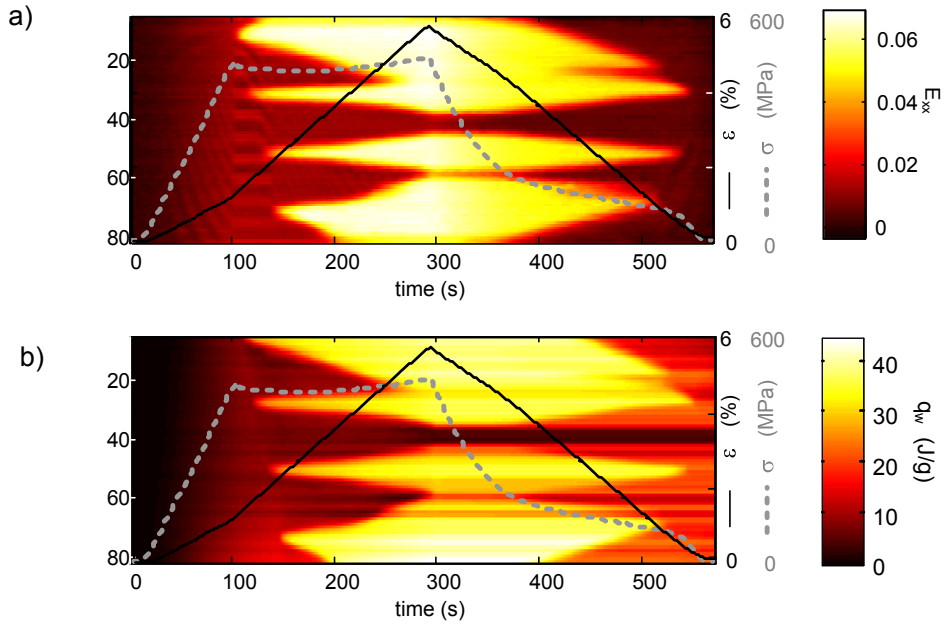

Figure 6.10: *Spatiotemporal representation along the tube axis of a) the Green Lagrange axial strain $E_{xx}(P)$, b) the heat energy $q_w(P)$. The grey dotted line shows the nominal stress and the solid line the nominal strain ε.*

6.4 Conclusion

Heat sources were estimated from the temperature fields during a tensile test performed on an initially austenitic Ti-50.8at% Ni thin walled tube. Temperature and strain fields were synchronised (in time and space) in order to express for each particle P, the temperature variation and the heat sources. They were estimated using the 2D cylindrical formulation of the heat diffusion equation. "Weighted" heat sources were estimated by using the thermal conductivity of the austenite in the less deformed areas ($E_{xx} < 0.04$) and the thermal conductivity of the martensite in the highly deformed areas ($E_{xx} \geq 0.04$). The positions of the heat source peaks correspond to phase transformation areas. The amplitudes of these peaks give information on the kinematics of the phase transformations.

The energy was estimated by integrating, for every particle P, the heat sources during the test. It allows us to perform local DSC during the test. A good correlation was observed between the strain and energy profiles. The energy estimated during the tensile test was 36 J/g for the stress induced A→M phase transformation. For the less deformed area the energy was estimated to 7 J/g.

Due to (i) the existence of the R phase, (ii) a localised R→M transformation and (iii) the difference of the thermal conductivity between austenite and martensite, some errors were made while estimating the heat sources with a constant value of k.

Conclusions and perspectives

Summary

Simultaneous temperature and strain fields measurements during nearly equiatomic polycrystalline NiTi tensile and shear tests have been carried out. Those simultaneous measurements obtained respectively with an infrared camera and digital image correlation were of great interest and have allowed us to better understand the thermomechanical coupling of NiTi for several loading conditions.

One can emphasise the main results about NiTi material obtained in this study. They were of two types. First, tools and software developed to perform mechanical tests and analyse the data; second, understanding of polycrystalline NiTi behaviour.

Tools and software developed:

- Due to conduction phenomena, temperature fields during NiTi tensile tests were very diffuse. Moreover, temperature variations were important due to the localization of the phase transformation. To get around these thermal phenomena and obtain quasi isothermal tests, a new gripping system that controlled the tube temperature and allowed for strain and temperature measurements was designed for tensile tests on tubes.

- In order to compare the data and obtain both strain and temperature for material points, a spatial and temporal synchronisation software has been developed.

- Heat source estimation have been extended, in this work, to the case of thin tubes and have been validated through a numerical benchmark.

- Then, a first model of "weighted" heat sources was proposed. It takes into account the difference of thermal conductivity between martensite and austenite phase.

Understanding of NiTi behaviour:

Mechanical tests with several sample geometries (tube, plate), loading types (tensile and shear tests), macroscopic strain rates and imposed temperatures were performed using the thermomechanical fields and analysed using both synchronisation and heat sources estimation.

Many assumptions were made to estimate heat sources from strongly localized temperature fields induced by a localized phase transformation. However,

- The simultaneous observation of both strain and temperature fields and the heat sources estimation during NiTi mechanical tests are unique and have allowed us to observe and analyse the complex thermomechanical behaviour of NiTi alloys during both homogeneous and localized stages.
- The tensile tests on thin tubes have shown that the stress plateau corresponded to a change in deformation and phase transformation mode, namely, they were homogeneous before the stress plateau (stage 1) and strongly localised thereafter (stage 2). Mixture of homogeneous A-R and A-M phase transformation that started as soon as the test started was observed during the homogeneous loading. NiTi behaviour during the homogeneous loading was not influenced by the macroscopic strain rate.
- The martensite fraction transformed at the end of the homogeneous loading, during tensile test on plates presenting only A-M phase transformation, was estimated to be nearly 9 % using two methods.
- Homogeneous reverse transformation was detected as soon as the unloading started (begining of stage 4).
- Unlike the homogeneous stages, localization phenomena that appeared during the stress plateau were strongly influenced by loading conditions such as macroscopic strain rate and temperature, cycling.
- Several localization morphology (helical, front) have been observed and seemed to be unpredictable.
- Observation of localization morphology during cyclic loading have exhibited modification of the localization mode with the number of cycles. This change of localization pattern can induce variation of the local strain and stress that can influence the macroscopic stress.
- Heat sources were estimated during the stress plateau for both plate and tube samples. Although temperature fields were diffuse, heat sources exhibited narrow peaks in the same place as strain gradients whereas in the rest of the sample, the heat sources were small.
- The latent heat of phase transformation induced by stress was estimated. Its value is higher than the latent heat induced by temperature (commonly obtained by “global” DSC).
- Heat energy fields, estimated from temporal integration of the heat sources, were similar to the axial strain fields. Such energy estimation allows one to perform “local DSC”.

- Comparison of tensile and shear tests on thin plates have shown that shear tests are more homogeneous than tensile tests. Homogeneous heat sources could therefore be estimated as functions of the thermal conductivity that depended on the martensite fraction $k(fm(t))$.

Finally, this work has demonstrated the possibility to use together DIC and IR measurements to better analyse the material behaviour during mechanical test that exhibit localised phase transformations. These set-up and softwares could be used for other material and other applications such as mechanical loadings under large deformation (stamping for instance).

Perspectives

NiTi analysis and investigations

A new field of investigations has been opened to study NiTi and its complex thermomechanical couplings. Despite the large number of experiments done during this work, many results were affected by presence of low acquisition frequency and spatial resolution. The spatial resolution (usually ≈ 0.2 mm to 0.5 mm) was set to allow for observation of the full sample and therefore obtain an overview of the sample behaviour. From those first results other tests should be performed to observe with a higher resolution phenomena of initiation of localization and heat sources along the gauge length direction during shear tests.

Moreover, observation of localization phenomena during ten cycles have exhibited modification of localization phenomena. It has also been shown that the macroscopic stress depends on localization phenomena and morphology. Since the behaviour of NiTi under cyclic loading is very important for commercial applications, further studies, that analyse the localization phenomena are necessary to better understand the cyclic behaviour.

Finally, since shear test is more homogeneous and localization is characteristic of tensile loading, modeling could be investigated using shear tests.

Improvement of the spatial synchronization, heat sources and energy estimations

A lot of time has been spent during this work to implement and develop tools in order to analyse simultaneously strain and temperature fields. Further studies are necessary to characterise errors and better estimate the heat sources and energy:

- The orientation of the cameras can induce some errors during the spatial synchronisation. It should be either quantified in further studies or taken into account by knowing the exact position of the cameras.

- A numerical benchmark has been developed and has shown that the heat sources were underestimated by nearly 20 % in the heat source peaks. This benchmark was useful to adjust the filtering parameters. However, heat source estimation is very sensitive to filtering that still needs to be adjusted manually. Further work is necessary to make this heat source estimation software easier to use in order to enable for its diffusion.

- So far, the heat sources were estimated from the spatial temperature fields and then synchronised with the strain fields. In order to better estimate heat sources, they should be directly evaluated from the synchronised temperature variation field. In this case, it is more likely that the linear interpolations used during the spatial and temporal synchronisation may induce some errors when estimating time derivative and Laplacian operator. Further work is necessary to estimate those potential errors and modify the heat sources software to allow heat source estimation from synchronised temperature fields.
- In the heat diffusion model, the convective term has been neglected. Further studies should be performed to check this hypothesis.
- It was not easy to estimate quantitatively the heat sources since the transformation changes locally the thermal conductivity. A first estimation of "weighted" heat sources was proposed. The impact of such approximation should be investigated for instance by developing another benchmark as done for heat sources.
- Since the energy is calculated from the time integration of discrete heat sources, low temporal or spatial resolution of the data may underestimate the energy when the heat sources are strongly localised in time and space. The impact of spatial and temporal resolution on energy estimation should be investigated in order to quantify the error made.

APPENDIX A

Emissivity estimation

Figure A.1 presents the experimental setup designed to characterise each paint emissivity. Tubular samples were used rather then plates, to easily control the temperature by an insulated fluid circulation. The thickness of the tube was small (0.1 mm) to reduce conduction phenomena and measurements were taken after stabilisation of the temperature along the profile of the tube. The fluid temperature was controlled using a thermocryostat (Julabo FP 50, temperature accuracy 0.03 K).

The sample was linked to the thermocryostat via insulated flexible tubes to limit heat looses (cf Figure A.1.c). In order to avoid the influence of the environment (especially the reflection of external heat sources), the tube was inside a box with only a small open window to allow the observation of the infrared camera. The ambient light sources was turned off and only a cold light was used during the experiment.

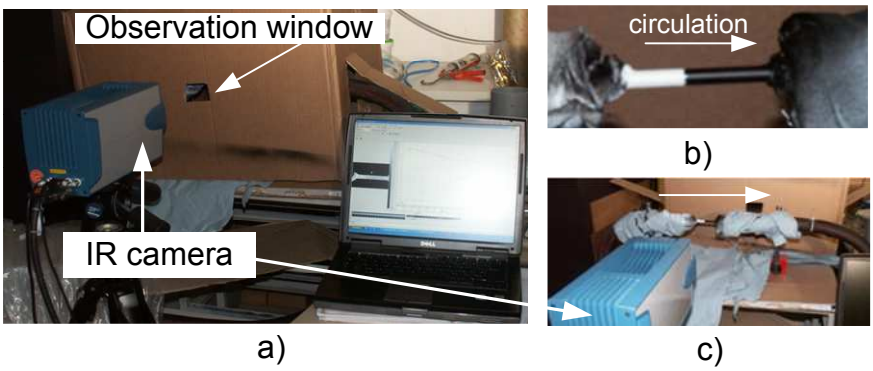

Figure A.1: *Experimental setup of the emissivity measurement: a) Global view of the setup. b) View of the tube surface and the indication of the direction of the fluid circulation. c) Detail without the box cover.*

For each measurement a series of 200 images were taken and averaged for the analysis. This

average operation increased the signal-noise ration by a factor of $1/\sqrt{200}$.

To compare each paint emissivity, the tube was first painted in white on the right end side and in black on the other one (Figure A.2.a). The paint was spread at room temperature until the infrared image of the tube was identical and almost homogeneous for both paints (Figure A.2.c, blue curve). Much more white than black was needed to obtain the same temperature. To easily locate the position of each paint, a small area was not painted between them, this allowed us to check the emissivity of the tube without paint.

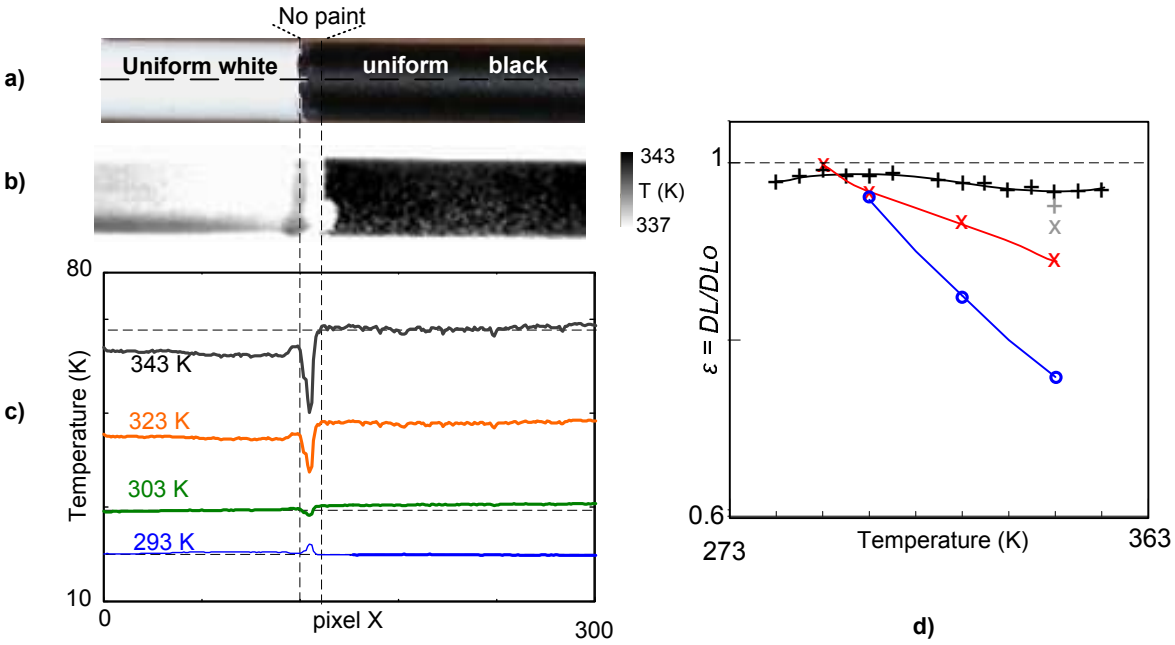

Figure A.2: *a) Visible photography of the observation area of the tube painted in black and white. b) Infrared photography of the same area at imposed temperature 343 K. c) Profiles of the recorded temperatures at 293, 303, 323 and 343 K. d) Evolution of the emissivity ϵ with the imposed temperature for different coating : black paint (+, black), white paint (×, red curve) and a tube without paint (O, blue).*

The profiles of the tube at several temperatures (from 273 to 353 K) are represented in Figure A.2.c. Although the white paint thickness was more important, its emissivity (linked to the apparent measured temperature) was smaller than the black one; especially as the temperature increased. The area without paint gave wrong data due to a very weak emissivity.

The evolution of the emissivity for the three tested configurations are plotted in Figure A.2.d. The emissivity was estimated with the ratio $\epsilon = \frac{DL}{DL_0}$, where DL was the real thermal radiation measured by the infrared camera and DL_0 the thermal radiation given by the calibration law obtained on a Black body surface. The black homogeneous paint had an emissivity of 0.98 that was not influenced by the temperature (grey body) whereas the emissivity of the white paint and the tube without paint decreased as the temperature increased.

The influence of the texture was then tested by spraying black texture on the white area, and a white texture on the black area (Figure A.3.a-b). Figure A.3.c represents the profile of the tube at T_{fluid} =343 K in the two paint configuration. The comparison of the temperature before and after adding the texture (thick red line) on the tube shows that a black texture on a white background will locally change the emissivity (and therefore increase the temperature

noise), whereas, a white texture on a black background gives approximately the same profile as a uniform black background.

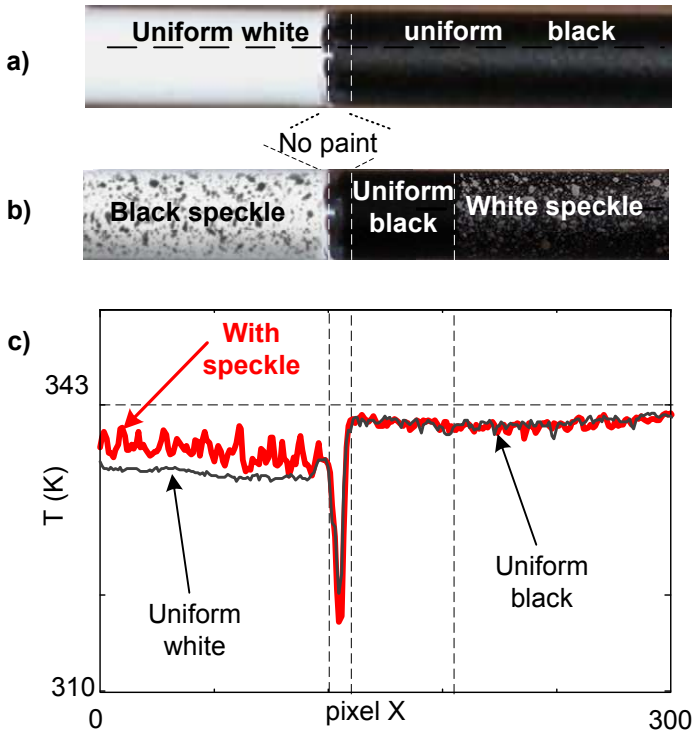

Figure A.3: *a) Visible photography of the tube painted with uniform white and black paint. b) Same tube with textures added, from left to right : a black texture on a uniform white paint, no paint, uniform black paint, a white texture homogeneous black paint. c) Comparison of the temperature profiles before (black, thin) and after the texture was added (red, thick). The imposed fluid temperature circulating inside the tube,* $T_{fluid} = 343$ *K, is represented by the dashed horizontal line*

Bibliography

Amidror, I. (1999). *The theory of the moiré phenomenon.* Kluwer Academic Publishers.

Avril, S., Pierron, F., Sutton, M. A., and Yan, J. (2008). Identification of elasto-visco-plastic parameters and characterization of Lüders behavior using digital image correlation and the virtual fields method. *Mechanics of Materials*, 40(9):729–742.

Besnard, G., Hild, F., and Roux, S. (2006). "Finite-Element" displacement fields analysis from digital images: Application to Portevin-Le Châtelier bands. *Experimental Mechanics*, 46(6):789–803.

Bouc, R. and Nayroles, B. (1985). Méthodes et resultats en thermographie infrarouge des solides. *J. de Méca. Théor. Appl.*, 4(1):27–58.

Boulanger, T. and Chrysochoos, A. (2004). Calorimetric and thermoelastic effects associate with the fatique behavior of steels. *International Journal of Fatigue*, 26:221–229.

Brinson, L. C., Schmidt, I., and Lammering, R. (2004). Stress-induced transformation behavior of a polycrystalline NiTi shape memory alloy: micro and macromechanical investigations via in situ optical microscopy. *Journal of the Mechanics and Physics of Solids*, 52(7):1549–1571.

Brémand, F., Durpré, J., and Lagarde, A. (1992). Non-contact and non-disturbing local strain measurement methods. i. principle. *European Journal of Mechanics, A/Solids*, 11:349–366.

Chambon, L., Congourdeau, F., Galerne, C., Guinard, S., and Thévenet, P. (2005). Application des méthodes optiques pour le suivi global du comportement des structures aéronautiques. In *Proc. Photomécanique 2005, GAMAC*, pages 313–320, Paris, France.

Chang, L. and Read, T. (1951). *Transactions of the American Institute of Mechanical Engineers.*, 189:47.

Chrysochoos, A. and Belmahjoub (1992). Thermographic analysis of thermomechanical couplings. *Arch. Mech*, 44:55–68.

Chrysochoos, A. and Louche, H. (2000). An infrared image processing to analyse the calorific effects accompanying strain localisation. *Int. J. Eng. Sci.*, 38:1759–88.

Chrysochoos, A., Maisonneuve, O., Martin, G., Caumon, H., and Chezeaux (1989). Plastic and dissipated work and stored energy. *Nuclear Eng. and Design*, 114:323–333.

Chrysochoos, A., Pham, H., and Maisonneuve, O. (1996). Energy balance of thermoelastic martensite transformation under stress. *Nuclear Eng. and Design*, 162:1–12.

Chu, T., Ranson, W., Sutton, M., and Peters, W. (1985). Applications of digital-image-correlation techniques to experimental mechanics. *Exp Mech*, 25:232–244.

Coudert, T. (2005). *Reconstruction tridimensionnelle du volume intérieur d'une chaussure : évaluation du chaussant*. PhD thesis, Université de Savoie.

Doudard, C., Poncelet, M., Calloch, S., Boue, C., Hild, F., and Galtier, A. (2007). Determination of an HCF criterion by thermal measurements under biaxial cyclic loading. *Int Jal of Fatigue*, 29:748–757.

Dupré, J. C. (2002). *Traitement et analyse d'images pour la mesure de grandeurs cinématiques, déplacements et déformations à partir de la granularité laser et de réseaux croisés, et pour l'étude de couplages thermomécaniques*. PhD thesis, Université de Poitiers, Poitiers, FRANCE.

Faulkner, M., Amalraj, J., and Bhattacharyya, A. (2000). Experimental determination of thermal and electrical properties of Ni-Ti shape memory wires. *Smart Mater Struct*, 9:622–631.

Favier, D. and Liu, Y. (2000). Restoration by rapid overheating of thermally stabilised martensite of NiTi shape memory alloys. *Journal of Alloys and Compounds*, 297(1-2):114–121.

Favier, D., Liu, Y., Orgéas, L., and Rio, G. (2001). Mechanical instability of niti in tension, compression and shear. In QP, S., editor, *Solid mechanics and its applications*, volume 101, pages 205–212. New York: Kluwer Academic Publishers.

Favier, D., Schlosser, H. L. P., Orgéas, L., Vacher, P., and Debove, L. (2007). Homogeneous and heterogeneous deformation mechanisms in an austenitic polycrystalline Ti-50.8 attemperature and strain fields measurements. *Acta Materialia*, 55:5310–5322.

Feng, P. and Sun, Q. (2006). Experimental investigation on macroscopic domain formation and evolution in polycrystalline NiTi microtubing under mechanical force. *Journal of the Mechanics and Physics of Solids*, 54(8):1568–1603.

Forquin, P., Rota, L., Charles, Y., and Hild, F. (2004). A method to determine the toughness scatter of brittle materials. *Int. J. Fract.*, 125:171–187.

Gadaj, S. P., Nowacki, W. K., and Pieczyska, E. A. (2002). Temperature evolution in deformed shape memory alloy. *Infrared Physics & Technology*, 43(3-5):151–155.

Grabe, C. and Bruhns, O. ((2008)). Path dependence and multiaxial behavior of a polycrystalline NiTi alloy within the pseudoelastic and pseudoplastic temperature regimes. *International Journal of Plasticity*, In Press, Corrected Proof:–.

G'Sell, C., Boni, S., and Shrivastava, S. (1983). Application of the plane simple shear test for determination of the plastic behaviour of solid polymers at large strains. *Journal of Materials Science*, 18(3):903–918.

Hahn, G. T. (1962). A model for yielding with special reference to the yield-point phenomena of iron and related bcc metals. *Acta Metallurgica*, 10(8):727–738.

Hild, F. and Roux, S. (2006). Digital image correlation: from displacement measurement to identification of elastic properties. *Strain*, 42:69–80.

Holst, G. C. (2000). *Common sense approach to thermal imaging*. SPIE Optical Engineering Press, Bellingham WA, ETATS-UNIS.

Iadicola, M. and Shaw, J. (2002a). An experimental setup for measuring unstable thermomechanical behavior of shape memory alloy wire. *Journal of Intelligent Material Systems and Structures*, 13(2):157–166.

Iadicola, M. A. and Shaw, J. A. (2002b). The effect of uniaxial cyclic deformation on the evolution of phase transformation fronts in pseudoelastic NiTi wire. *Journal of Intelligent Material Systems and Structures*, 13(2-3):143–155.

Iadicola, M. A. and Shaw, J. A. (2004). Rate and thermal sensitivities of unstable transformation behavior in a shape memory alloy. *International Journal of Plasticity*, 20(4-5):577–605.

Jacobus, K., Sehitoglu, H., and Balzer, M. (1996). Effect of stress state on the stress-induced martensitic transformation in polycrystalline N-iTi alloy. *Metallurgical and Materials Transactions A*, 27A:3066–3073.

Latil, P. (2008). Caractérisation expérimentale de la loi de comportement du 316LVM pour la simulation du procédé d'étirage à froid de tubes. Master's thesis, Université Joseph Fourier.

Leo, P., Shield, T., and Bruno, P. (1992). Transient heat transfer effect on the pseudoelastic behavior of shape-memory wire. *Acta metall. matter.*, 41(8):2477–2485.

Lexcellent, C. and Vacher, P. (1993). Thermomechanical behavior of polycrystaline shape memory alloys Cu-Zn-Al. *Archives of Mechanics*, 45(1):135–155.

Li, Z. and Sun, Q. (2002). The initiation and groth of macroscopic martensite band in nangrained NiTi microtube under tension. *International Journal of plasticity*, 18:1481–1498.

Liu, Y. and Favier, D. (2001). Stability of ageing-induced multiple-stage transformation behaviour in a Ti-Ni 50.15% Alloy. *J. Phys IV*, 11(Pr8):113–118.

Liu, Y., Liu, Y., and Humbeeck, J. V. (1998). Luders-like deformation associated with martensite reorientation in NiTi. *Scripta Materialia*, 39(8):1047–1055.

Liu, Y., Mahmud, A., Kursawe, F., and Nam, T.-H. (2006). Effect of pseudoelastic cycling on the Clausius-Clapeyron relation for stress-induced martensitic transformation in NiTi. *Journal of Alloys and Compounds*, In Press, Corrected Proof:1173–1176.

Liu, Y. and McCormick, P. (1992). In *Proceedings ICOMAT 92*, page 923, Monterey,CA.

Liu, Y. and McCormick, P. (1994). Thermodynamic analysis of the martensitic transformation in NiTi - I. Effect of heat treatment on transformation behaviour. *Acta Metallurgica et Materialia*, 42(7):2401–2406.

Liu, Y. and McCormick, P. (1996). Criteria of transformation sequences in NiTi shape memory alloys. *Materials Transactions, JIM*, 37:691–696.

Liu, Y. and Xiang, H. (1998). Apparent modulus of elasticity of near-equiatomic NiTi. *Journal of Alloys and Compounds*, 270(1-2):154–159.

Lobel, M. (1995). *Caractérisation thermomécanique d'alliages à mémoire de forme de type NiTi et CuZnAl. Domaine de transition et cinétique de changement de phase*. PhD thesis, Univ. Montpellier II.

Louche, H. (1999). *Analyse par thermographie infrarouge des effets dissipatifs de la localisation dans les aciers*. PhD thesis, These de doctorat Universite de Montpellier. Enter text here.

Louche, H., Bouabdallah, K., Vacher, P., Coudert, T., and Balland, P. (2007). Kinematic fields and acoustic emission observations associated with the Portevin Le Châtelier Effect on an Al-Mg alloy. *Experimental Mechanics*.

Louche, H. and Chrysochoos, A. (2001). Thermal and dissipative effects accompanying Lüders bands propagation. *Mater. Sci. Eng. A.*, 307:15–22.

Louche, H. and Tabourot, L. (2004). Experimental energetic balance associated to the deformation of an aluminum multicrystal and monocrystal sheet. *Materials Science Forum*, 467-470:1395–1400.

Louche, H., Vacher, P., and Arrieux, R. (2005). Thermal observations associated with the Portevin Le Châtelier effect in an Al-Mg alloy. *Materials Science and Engineering: A*, 404(1-2):188–196.

Manach, P. (1989). Analyse par simulations numériques des nonhomogénéités au cours d'essais mécaniques. Master's thesis, Institut National Polytechnique de Grenoble, Grenoble, France.

Manach, P., Favier, D., and Rio, G. (1995). Internal stresses generated during the pseudoelastic deformation of NiTi bodies. In *16-19 May 1995, La Bresse, France* -.

Manach, P.-Y. (1993). *Etude du comportement thermomecanique d'alliage à mémoire de forme NiTi*. PhD thesis, INPG, Grenoble.

Manach, P.-Y. and Favier, D. (1997). Shear and tensile thermomechanical behavior of near equiatomic NiTi alloy. *Materials Science and Engineering A*, 222(1):45–57.

McCormick, P., Liu, Y., and Miyazaki, S. (1993). Intrinsic thermal-mechanical behaviour associated with the stress-induced martensitic transformation in NiTi. *Materials Science and Engineering: A*, 167(1-2):51–56.

McNichols, J., Jr., and J. Cory, S. (1987). Thermodynamics of nitinol. *Journal of Applied Physics*, 61(3):972–984.

Miyazaki, S., Imai, T., Otsuka, K., and Suzuki, Y. (1981). Luders-like deformation observed in the transformation pseudoelasticity of a Ti-Ni alloy. *Scripta Metallurgica*, 15(8):853–856.

Ng, K. and Sun, Q. (2006). Stress-induced phase transformation and detwinning in NiTi polycrystalline shape memory alloy tubes. *Mechanics of Materials*, 38(1-2):41–56.

Olander, A. (1932). An electrochemical investigation of solid cadmium-gold alloys. *J. Am. Chem. Soc.*, 54:3819–3833.

Orgéas, L. (1997). *Etude experimentale et numérique du comportement thermomecanique d'un alliage à mémoire de forme industriel NiTi*. PhD thesis, Université Joseph Fourier - Grenoble 1.

Orgéas, L. and Favier, D. (1995). Application of the beam theory to model the pseudoelastic and ferroelastic bending of SMA beams. *J. de Phys. IV*, pages 519–524.

Orgéas, L. and Favier, D. (1998). Stress-induced martensitic transformation of a NiTi alloy in isothermal shear, tension, and compression. *Acta Meta Inc.lurgica*, 46(15):5579–5591.

Ortin, J. (1992). Thermodynamics and kinetics of martensitic transformation. In *Proceedings of the International Conference on Martensitic Transformation*, pages 305–316, Monterey, USA.

Ortin, J. and Planes, A. (1988). Thermodynamic analysis of thermal measurements in thermoelastic martensitic transformations. *Acta Mater*, 36(8):1873–1889.

Ortin, J. and Planes, A. (1989). Thermodynamics of thermoelastic martensitic transformations. *Acta Metallurgica*, 37(5):1433–1441.

Ortin, J. and Planes, A. (1991). Thermodynamics and hysteresis behaviour of thermoelastic martensitic transformation. *Journal of Physique IV*, 1:C4–13–23.

Otsuka, K. and Ren, X. (2005). Physical metallurgy of Ti-Ni-based shape memory alloys. *Progress in materials science*, 50(5):511–678.

Otsuka, K., Sawamura, T., and Shimizu, K. (1971). Crystal structure and internal defects of equiatomic TiNi martensite. *Physica Status Solidi (a)*, 5:457–470.

Pajani, D. (1989). *Mesure par thermographie infrarouge*. ADD.

Parks, V. (1993). *Geometric moiré. In handbook on experimental mechanics*. Albert S. Kobayashi, seconde edition.

Pastor, M., Balandraud, X., Grédiac, M., and Robert, J. (2008). Applying infrared thermography to study the heating of 2024-T3 aluminium specimens under fatigue loading. *Infrared Physics & Technology*, In Press, Corrected Proof:–.

Patel, J. and Cohen, M. (1953). Criterion for the action of applied stress in the martensitic transformation. *Acta Metallurgica*, 1(5):531–538.

Peters, W. and Ranson, W. (1981). Digital image techniques in experimental stress analysis. *Opt Eng*, 21:427–441.

Pieczyska, Gadaja, and Nowackia (2004). Thermomechanical investigation of martensite and reverse transformation in TiNi shape memory alloy. In *Bulletin of the polish academy of technical sciences*, volume 52-(3).

Rajagopalan, S., Little, A. L., Bourke, M. A. M., and Vaidyanathan, R. (2005). Elastic modulus of shape-memory NiTi from in situ neutron diffraction during macroscopic loading, instrumented indentation, and extensometry. *Applied Physics Letters*, 86(8):081901.

Rajaona, R. D. and Sulmont, P. (1985.). A method of spectral analysis applied to periodic and pseudoperiodic signals. *Journal of Computational Physics*, 61:186–193.

Ramello, S. (2005). Conception du dispositif de traction sur tube. Master's thesis, Grenoble Universités.

Rotinat, R., Tié, R., Valle, V., and Dupré, J.-C. (2001). Three optical procedures for local large-strain measurement. *Strain*, 37:89–98.

Salzbrenner, R. and Cohen, M. (1979). On the thermodynamics of thermoelastic martensitic transformations. *Acta Metallurgica*, 27(5):739–748.

Sandel, A. (2000). Influence des traitement thermomécaniques sur la contraction superélastique des stents en alliages à mémoire de forme NiTi. Master's thesis, UJF Grenoble.

Schlosser, P., Louche, H., Favier, D., and Orgeas, L. (2007). Image processing to estimate the heat sources related to phase transformations during tensile tests of NiTi tubes. *Strain*, 43:260–271.

Schmahl, W. W., Khalil-Allafi, J., Hasse, B., Wagner, M., Heckmann, A., and Somsen, C. (2004). Investigation of the phase evolution in a super-elastic NiTi shape memory alloy (50.7 at.% Ni) under extensional load with synchrotron radiation. *Materials Science and Engineering A*, 378(1-2):81–85.

Shaw, J. and Kyriakides, S. (1995). Thermomechanical aspects of NiTi. *J. Mech Phys. Solids*, 43:1243–81.

Shaw, J. and Kyriakides, S. (1997). On the nucleation and propagation of phase transformation fronts in a NiTi alloy. *Acta Mater*, 45:683–700.

Siddons, D. and Moon, J. (2001). Tensile and compression performance of superelastic NiTi tubing. *Materials Science and Technology*, 17(9):1073–1078.

Sittner, P., Landa, M., Lukas, P., and Novak, V. (2006a). R-phase transformation phenomena in thermomechanically loaded NiTi polycrystals. *Mechanics of Materials*, 38(5-6):475–492.

Sittner, P., Novak, V., Lukas, P., and Landa, M. (2006b). Stress-strain-temperature behavior due to B2-R-B19' transformation in NiTi polycrystals. *Journal of Engineering Materials and Technology*, proof:proof.

Stalmans, R., Van Humbeeck, J., and Delaey, L. (1992). Thermomechanical cycling, two way memory and concomitant effects in CuZnAl alloys. *Acta Metallurgica et Materialia*, 40(3):501–511.

Sun, Q. and Li, Z. (2002). Phase transformation in superelastic NiTi polycrystalline microtubes under tension and torsion from localisation to homogeneous deformation. *Int. J. Solids Structures*, 39:3797–3809.

Sutton, M., Wolters, W., Peters, W., Ranson, W., and McNeill, S. (1983). Determination of displacements using an improved digital correlation method. *Image Vis Comput*, 1:133–139.

Tan, G., Liu, Y., Sittner, P., and Saunders, M. (2004). Luders-like deformation associated with stress-induced martensitic transformation in NiTi. *Scripta Materialia*, 50(2):193–198.

Tong, H. and Wayman, C. (1974). A simplified calorimeter for determining latent heats of martensitic transformations at low temperatures. *Metallurgical and Materials Transactions B*, 5(8):1945–1946.

Tong, W., Tao, H., and Zhang, N. (2005). Time-resolved strain mapping measurement of individual Potevin-Le Châtelier deformation bands. *Scripta Materialia*, 53:87–92.

Vacher, Dumoulin, S., and Morestin, F. (1999). Bidimensional deformation measurement using digital images. *Proc Instn Mech Engrs*, 213:811–17.

Vacher, P. (2003). Apport des techniques de corrélation d'images en mécanique : Analyse de déformations et numérisations 3d, habilitation à diriger des recherches,.

Wack, B. and Tourabi, A. (1993). Cyclic simple shear of metallic sheets: application to aluminium-lithium alloy. . *J. Mater. Sci.*, 28:4735.

Wattrisse, B., Muracciole, J.-M., and Chrysochoos, A. (2002). Thermomechanical effects accompanying the localized necking of semi-crystalline polymers. *International Journal of Thermal Sciences*, 41(5):422–427.

Wollants, P., De Bonte, M., and Roos, J. (1979). A thermodynamic analysis of the stress induced martensitic transformation in a single crystal. *Zeitschrift fur Metallkunde*, 70(2):70–113.

Wollants, P., Roos, J., and Delaey, L. (1993). Thermally and stress induced thermoelastic martensitic transformation in the reference frame of equilibrium thermodynamics. *Progress in Materials Science*, 37(3):227–288.

Zhang, S., Denton, M., and Fariabi, S. (2004). Clausius-Clapeyron equations in different types of nickel titanium shape memory alloy. In *Materials & Processes from Medical Devices Conference 2004; St. Paul, MN; USA; 25-27*, pages 116–119, St. Paul, MN; USA.